Construction and Application of an On-line Flow Cell ICP-OES Setup for Real Time Dissolution Detection

Shahin Nikman

This dissertation is submitted for the degree of

Doctor of Philosophy

July 2020

Department of Chemistry

I dedicate this thesis to my family and friends.

The traveller must train his wits.

All is easy at home. He who knows little

is a laughing-stock

amongst men of the world.

Hàvamàl

Declaration

This thesis has not been submitted in support of an application for another degree at this or any other university. It is the result of my own work and includes nothing that is the outcome of work done in collaboration except where specifically indicated. Many of the ideas in this thesis were the product of discussion with my supervisor Professor Harry Ernst Hoster.

Abstract

By informed design novel high-surface area, low volume flow cells were designed for high-throughput detection of chemical and electrochemical dissolution products of energy storage materials found in zinc-air batteries, including current collectors and bifunctional catalysts. Novel flow cells were fabricated by stereolithography to realise complex flow channels which allowed efficient transport of dissolution products from the working electrode. Due to appropriate construction material selection, the 3D-printed flow cells could withstand concentrated alkaline solutions . Routine analysis in 1 M KOH electrolytes were realised by adapting an ICP-OES to withstand harsh alkaline conditions, providing real-time detection limits below 1 ng s^{-1} cm^{-2}. Positive electrode current collector candidates for alkaline zinc-air batteries were investigated for stability in 1 M KOH as function of potential region and galvanostatic charging currents within relevant for practical energy storage applications. A range of nickel-substituted cobalt oxides $Ni_xCo_{3-x}O_4$ bifunctional electrocatalysts for zinc-air batteries were synthesised and characterised by PXRD, SEM and cyclic voltammetry. With on-line dissolution analysis, the stability of the materials were assessed as a function of potential and pH. Nickel substitution was found to affect the onset of cobalt dissolution, and a correlation between nickel doping, dissolution magnitude of cobalt and catalytic activity towards the oxygen reduction reaction and oxygen evolution reactions was found.

Acknowledgements

First of all, I thank my supervisor Professor Harry Hoster for guiding me through my PhD, and for giving me countless opportunities to travel and connect with researchers and institutions all over the world, for instilling upon me an attitude of knowledge-sharing and engagement.

To the Hoster group at Lancaster University, in particular Mike Mercer for providing me academic guidance, and Violeta Gonzales-Perez for saving me a lot of time with her scripts.

To all the staff at Lancaster Chemistry Department, in particular Steve Holden, David Rochester and Sara Baldock for their invaluable technical insights and assistance with instrumentation, fabrication and general know-how.

To Mathias Kjærgaard Christensen, (Denmark was awesome) and Beatrice Wolff for their much-needed contribution, and for keeping me sane while working on zinc-air batteries and flow cells.

To all the guys in B06, in particular Dhruv, Boblet, Matttthew, Henry and Craig, plus a shout-out to Cindy and Sara in cTap-C for all the great company during my PhD.

Again, to Dhruv for keeping me company during long nights in the office and being a great neighbour.

To the friends I made in Lancaster, especially Assyl who's had my back since the very first day here.

To Claire, for taking care of me with excellent bakery, cards, watering my flowers sorting my jars out and keeping me company.

Last but not least, to my family, to Amme, to Baba who's always supported me through thick and thin. Dige ma har doh doctor astim.

Thank you

Contents

List of Tables

List of Equations

List of Figures

List of Abbreviations and Acronyms

SHE	Standard hydrogen electrode
RHE	Reversible hydrogen electrode
ORR	Oxygen reduction reaction
OER	Oxygen evolution reaction
ICP-OES	Inductive couple plasma optical emission spectroscopy
CV	Cyclic voltammetry
GEIS	Galvanostatic electrochemical impedance spectroscopy
AESEC	Atomic emission spectroelectrochemical cell
FT-SFC	Flow-through scanning flow cell
SDCM	Scanning droplet cell microscopy
FDM	Fused deposition modelling
SLA	Stereolithography
PXRD	Powder X-ray diffraction
SEM	Scanning electron microscopy

List of Appendices

1 Introduction

1.1 Background

With the increase of awareness on climate change issues and demand for electric energy storage battery research has emerged as a multidisciplinary field in its own. The scale of the demand extends from small electric devices, to home storage, microgrids and regional grid regulation[1]. Depending on the application, high power delivery may be preferred over large capacity, or a long shelf life may be more suitable[2]. These qualities are a consequence of the half-cell reactions that takes place at the negative and positive electrodes[3]. Accompanied with these are always side reactions, or parasitic reactions, which degrades the battery either by consumption of active material or by inhibition[4]. These can take place at various stages of operation or storage. With aid of spectroscopic methods these reactions can be identified and reduced to secure efficient long-term operation. Currently in-situ and in-operando techniques are in demand as they couple analytical methods with electrochemistry[5].

1.2 Battery cells

It is important to understand the principle workings of a battery cell in order to investigate the constituent materials for stability. A “battery cell” technically refers to a single cell, while “battery” refers to an aggregate of battery cells. However, “battery” is quite commonly said in daily use for both, and will be used to refer to a single cell of electrochemical energy storage in this work. Here is a compact summary of the primary and secondary elements of a basic battery[3].

A battery is in the essence a two-electrode electrochemical cell in a compact format, a basic schematic representation is provided in Figure 1.1. At each electrode a half cell reaction takes place, which generates electrons and consumes positive charge, or vice versa. The electromotive force the battery can generate depends on the potential difference between the half-cell reactions. The electrode where the half-cell reaction spontaneously give up electrons upon applying an external load is denoted the negative electrode, and the half-cell reaction which receives electrons is denoted the positive electrode.

The electrode which releases negative charge is called the anode. The cathode is the electrode which accepts electrons from the circuit, and that current is cathodic. Therefore, when a battery is discharged by connecting it to a circuit, the negative electrode is the anode, and the positive electrode is the cathode. If the reverse where to happen by injecting energy into the battery in the form of electric current, the negative electrode would be the cathode and the positive electrode would be the anode.

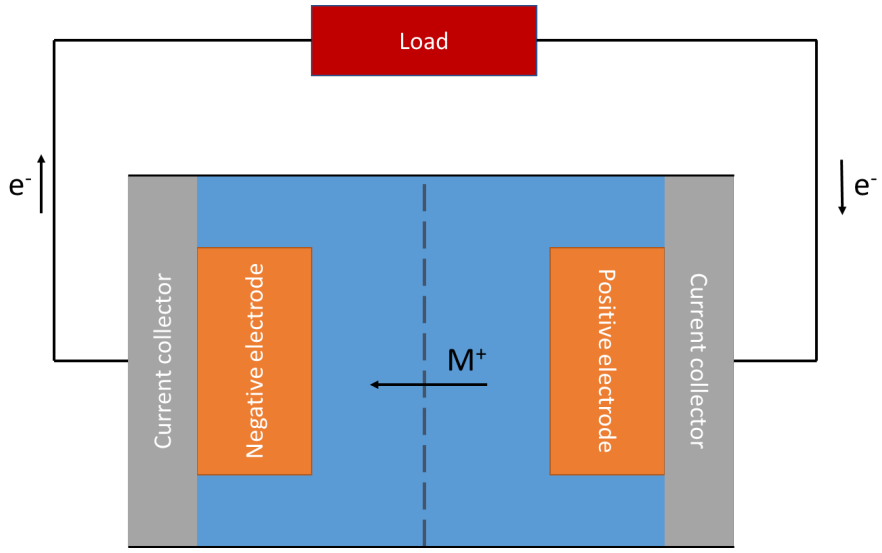

Figure 1.1 A schematic of a sealed battery. The direction of the charge indicates the discharge process. M^+ indicates the transport of charge in the electrolyte

The third fundamental element of a battery is the electrolyte, usually a salt dissolved in a solvent in which the electrodes are immersed in. The electrolyte provides conductivity and overall charge balance to the two half-cell reactions as electrons are donated or

received. A higher electrolyte concentration increases the ionic conductivity which leads to lower resistive losses.

Some secondary elements are usually also present in batteries, which are not strictly necessary, but are employed to minimise space consumption. A separator material is usually placed between the negative and the positive electrode, so that the electrodes can be sandwiched without being in physical contact and undergo internal short circuiting. The separator is usually a thin, insulating membrane of chemically inert plastic with micropores, to let electrolyte ions move between the electrodes for charge balancing.

Lastly, the electrode materials active in the half cell reactions are sometimes placed in front of a conductive backing material, usually a casing which also confines the electrolyte. Typically, they are made of stainless steel, provides pressure and are not supposed to partake in any chemical and electrochemical reactions. They are also the external terminals that one would normally connect a battery to in a circuit.

Batteries where the half-cell reactions are not reversible are called primary batteries. These batteries are not rechargeable. A secondary battery on the other hand can be recharged by applying a reverse current without undergoing a large loss in subsequent discharge performance.

1.3 Zinc-air batteries

The zinc-air battery consists of a zinc anode, electrocatalyst cathode and protic electrolyte. Zinc has historically been used in electrochemical power devices ever since the voltaic pile was invented by Alessandro Volta[6]. In 1886 it was utilised as negative electrode in the alkaline dry cell and the Leclanche cell, with carbon as positive electrode and ammonium chloride electrolyte. By 1930 the positive electrode of the alkaline type battery was replaced with a gas diffusion layer, similar to fuel cells, giving rise to the zinc-air format employed in hearing aids today[7]. In a highly alkaline electrolyte, the negative electrode reaction proceeds as follows[8]:

$$Zn(s) + 4OH^{-}(aq) \rightarrow [Zn(OH)_4]^{2-}(aq) + 2e^{-}$$

The zinc air system stands out as one of few aqueous metal-air batteries. It is the low reactivity of the zinc metal towards water which makes this battery viable[9]. While the energy density of the zinc-air battery is projected to be relatively high, the power density and rechargeability remains problematic, as abrupt cell death usually takes place within few cycles.

Figure 1.2 shows an example of a commercial zinc-air battery, and voltammograms of the (A) negative electrode and (B) positive electrode. Figure 1.2 (C) is a cross-section image of a zinc-air battery.

The zinc-air system is employed in various formats, button cells with the paste zinc electrode/electrolyte are a common commercial format for powering hearing aids, while pumped electrolyte or fuel cell stack configurations (zinc-air fuel cell) are more suitable for larger scale storage. On the other hand, a large variety of commercial and in-house cells are employed in testing of zinc-air batteries[10].

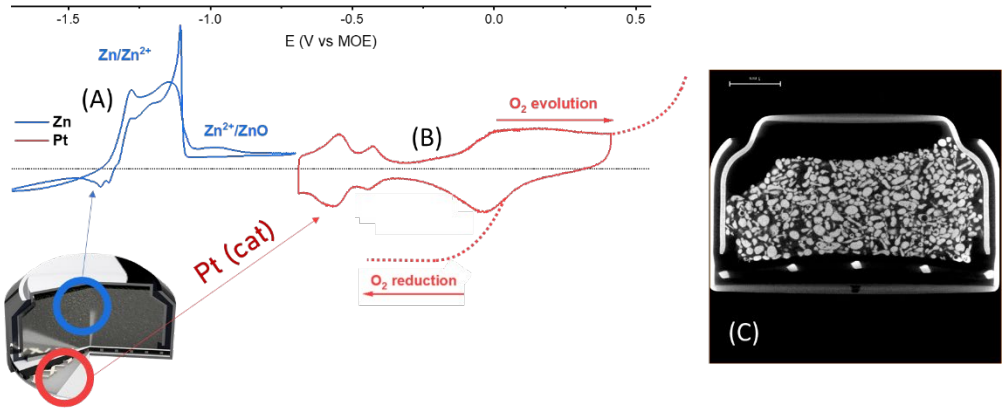

Figure 1.2 A cross-section of a zinc-air battery. The voltammograms display the negative (A) and positive (B) electrode half-cell reactions for zinc and platinum in 1 M KOH. (C) is a cross-section tomograph of a commercial zinc-air battery conducted in collaboration with Drishti Patel (UCL).

Primary batteries have already been used for transport and military applications, and there has also been commercial bus routes operated with mechanically rechargeable cells[11]. In the time of writing, companies like Fluidic[12], EOS Energy[13] and ViZn[14] are claiming or offering large scale secondary zinc-air cells for grid storage. NantEnergy[15] has recently deployed zinc-air batteries to operate in microgrids for villages and other

off-grid sites, with a reported cost of under $100 per kW h, compared to $200-300 kW h for lithium ion batteries. Off-the-shelf available zinc-air batteries are all primary, and most famously deployed for hearing aids, because they are excellent for low current applications, affordable and contains higher capacities compared to sealed battery technologies[16].

The advantages over current lithium ion technologies include higher theoretical energy density, supply of raw materials, lower cost and greener chemistry[17]. Figure 1.3 shows a comparison of commercial zinc-air and lithium ion batteries in terms of charge storage and cost per charge.

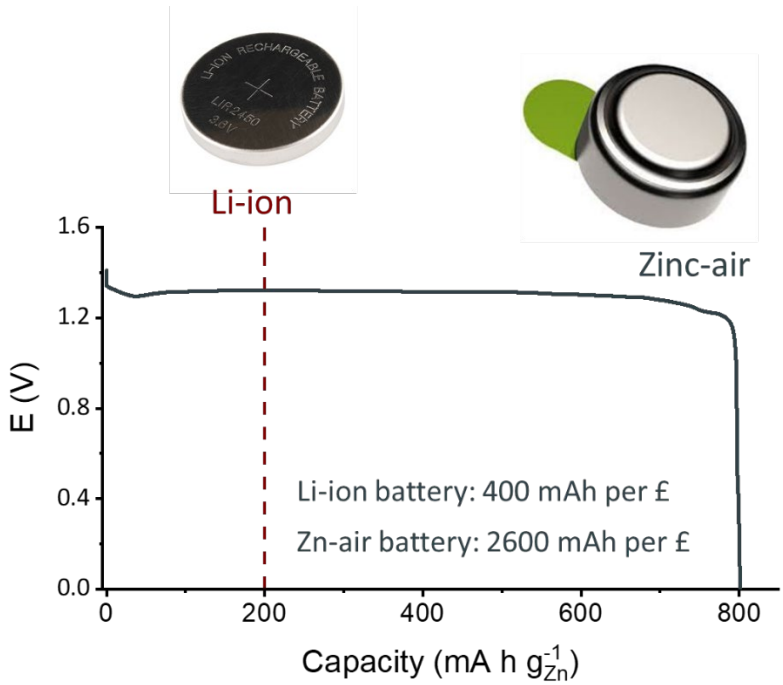

Figure 1.3 Discharge curve of a Varta zinc-air cell. Cost estimation calculated from the cheapest battery packs for the respective battery chemistries available at the time (03/2018) found on Amazon.co.uk.

Much of the safety risks mitigated stems from using aqueous electrolytes as opposed to organic - often volatile and unstable - liquids like cyclic carbonates or ethers. This eliminates the risk of fire, gas evolution, thermal runaway reactions and explosions[18].

1.4 The bifunctional catalyst

Unlike commonly employed positive electrode materials like those in the lithium ion batteries where the half-cell reaction is the intercalation of ions[19], the positive electrode employed in a metal-air battery is an electrocatalyst which facilitates reduction or oxidation of an oxygen or hydroxide molecule at the gas-liquid-solid interface. Since the catalyst can be employed on a membrane, the positive electrode in a zinc battery takes up very little space and weight. In aqueous media the reaction at the positive electrode takes place between the interface of air and electrolyte, which is the reduction of oxygen to water, the oxygen reduction reaction (ORR). In alkaline solutions[20], the overall discharge reaction can be expressed as:

$$O_2 + 2H_2O + 4e^- \rightarrow 4OH^-$$

The charging reaction is the oxygen evolution reaction (OER) and is the reverse of the discharge:

$$4OH^- \rightarrow O_2 + 2H_2O + 4e^-$$

A material that can catalyse both reactions at fast rates is hence “bifunctional”.

In acidic conditions (pH = 0) the equilibrium potential is 1.229V against the standard hydrogen electrode (SHE), as by the Nernst equation[21]:

$$E_{O_2/H_2O} = E^0_{O_2/H_2O} - \frac{RT}{4F} ln \frac{a^2_{H_2O}}{a_{O_2} a^4_{H^+}}$$

Consequentially, for every one-unit increase in pH, the equilibrium potential shifts negative by 59 mV, such that at a pH of 14, it is 0.401V vs SHE. This is an overall model with many intermediate steps: protonation and electron transfer, as well as adsorption and desorption on the surface.

Three main mechanisms have been proposed for this reaction in alkaline media: The dissociation-recombination, which is known as the four-electron mechanism, associative, which is known as the two-electron process, and the peroxo-mechanism[20]. Out of these, the four-electron mechanism is the most energy efficient, as it contains the fewest intermediate steps. In alkaline media it has been seen that the 4-electron pathway (dissociation-recombination) is favoured[22].

Although the first fuel cells and electrolysers employed precious metals like platinum, silver and palladium, manganese dioxide have been a prime choice in primary hearing aid cells, and even graphite has been suggested. Nerbuchilov et al.[23] outlined eight promising classes of ORR materials: MnO_x, CoO_x-MnO_x, Ag, CoTMPP/FeTMPP, metal nitrides, spinels, perovskites and pyrochlore compounds. While they all display promising properties, it is difficult to compare activity and stability across the materials, as preparation and mass loading vary significantly across publications.

Electrocatalysts are employed as particulates or other types of microstructures in order to increase the electrochemical surface area. Hence morphology and size influence number and types of terraces, edges and corner sites, which all may decrease with increased particle size.

1.5 Stability

The common types of performance loss for bifunctional catalysts are activation loss[24], poor electronic conductivity of the electrocatalyst[25] and insufficient transport of oxygen[26]. All these effects combine to energy loss during charge and discharge. While the theoretical voltage for a zinc air battery is 1.65V at pH 14[27], typical discharge currents lead to discharge potentials at 1.1 V depending on the electrode compositions

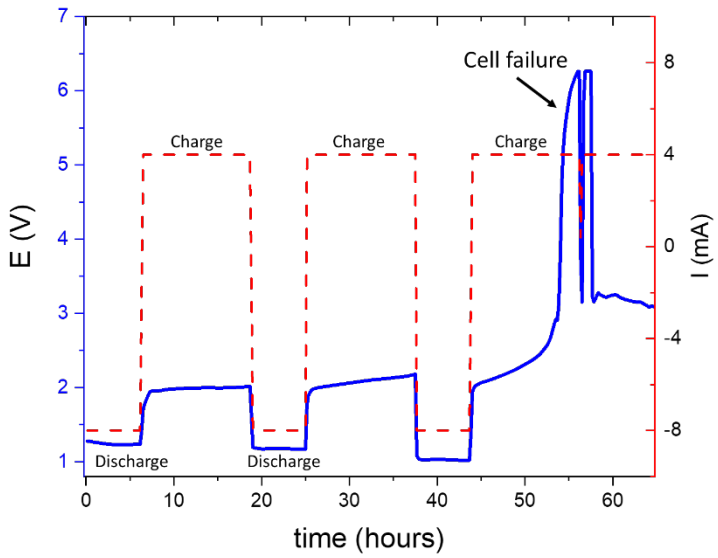

Figure 1.4 Cell failure of a commercial zinc battery during charging.

and the experimental conditions, as seen in Figure 1.3. The poor rechargeability of

commercial zinc-air batteries as shown in Figure 1.4 is in part due to dissolution of the positive electrode material.

According to Katsonauros et al.[20], there are only small gains to reap from efforts in increasing the activity of state-of-the-art catalysts, therefore significant attention has to be directed towards the long term operational stability. Dissolution of active material[528] has been shown to be a significant contributor to premature performance degradation[2930]. Hence, the need to efficiently detect dissolution as a function of material, electrolyte and potential has become increasingly important to inform on stability trends of bifunctional catalysts[3132].

1.6 Research Project Aims and Objectives

1.6.1 Aim

With the background content in mind presented for Chapter 1, the aim for this project is to probe the stability of active and support materials that are used or have been proposed for alkaline zinc-air cells. To achieve this, the dissolution rates as a function of electrochemical potential will be quantified via on-line electrolyte analysis by ICP OES. A set of incremental objectives has been set for the construction, coupling and use of a system consisting of a) a flow cell setup and b) an ICP-OES. The chapters outlined for this thesis follow the objectives chronologically, as this helps in following the thought process behind any design decisions and problem-solving in the stages of construction and testing of the on-line ICP-OES flow cell system.

1.6.2 Scientific Contribution

The contribution of this work is to establish a trend-based analysis of dissolution of materials. To find a dissolution pattern that increases or decreases by material properties such as crystalline structure, morphology, dopant concentration or electrolyte formulation. With such trends established, the wider research community can take advantage of this to make informed decisions in the synthesis of stable, high-performing materials for the next generation high-performance electrochemical energy storage materials. The tools and methods developed in this work will allow the wider community to conduct “fit-for-purpose”-type stability tests in parallel to optimisations of primary properties like electrocatalytic activity.

1.6.3 Objectives by chapter

Chapter 2: Gather comprehensive knowledge of flow cell construction, its use for dissolution studies and data interpretation by reviewing scientific literature.

Chapter 3: Design and construct an electrochemical flow cells by informed parameters, and incremental improvements by rapid prototyping.

Chapter 4: Coupling of the electrochemical flow cell to an ICP-OES as far as possible electronically and by chemical compatibility.

Chapter 5: Investigate inherent corrosion resistance of current collector candidates for the alkaline zinc air battery by dissolution resistance to applied potential.

Chapter 6: Investigate dissolution tendencies of bifunctional electrocatalysts for ORR and OER in alkaline media.

2 Literature Overview

2.1 Introduction

In this section, a brief review will be provided on the development of on-line dissolution analysis, and the cell designs and experimental set-ups that realised transient dissolution detection. The gradual development towards more efficient flow cell designs will be presented. Some approaches towards characterising the flow pattern within the respective flow cells will be presented.

2.2 The need for elemental discrimination

There had been several attempts to couple electrochemical experiments with spectroscopic techniques in the corrosion field in order to investigate phenomena like passivation and dissolution[33,34]. The currents resulting from the various half-cell reactions taking place at the working electrode should be separated in order to understand mechanisms of degradation, this may however be complicated to deduce from electrochemical data alone[35]. Hence, the use of downstream analytics coupled to electrochemical cells could be used to observe selected half reaction independently in order to decouple them. Another important motivation was to discriminate between the partial elemental processes in a multi-element component such as an alloy, as each element might contribute differently to the overall dissolution and passivation process.

In order to solve these problems, hydrodynamic convection has often been utilised, where the mass transport to and from the electrode would be controlled by applied convection as the major contributor, either by utilising a rotating disk electrode design, or having a well-defined electrolyte flow pass over a working electrode. For the latter, a detector is placed downstream of a flow cell in order to monitor the concentration of a species of interest. Cahan and Haynes[36] and Bockris[37] employed polarographic methods where a “collecting electrode” downstream would be held at an electroactive potential to the species of interest, while Tsuru[38] used a double detection electrode system. Rotating ring disk electrodes have an outer ring attached where electrochemical

products would be reduced or oxidised, which has been useful for the measurement of partial elemental currents of iron/chromium alloys[39–41] by generation-collection experiments. Such a set up would become very complex to operate as one increases the number of possible dissolution products in the working electrode. At least one detector per soluble dissolution product would be needed that do not interfere with other electroactive species, otherwise this greatly limits the range of alloys that can be studied. A new experiment could also be conducted per soluble species, but that would also greatly increase the number of experiments per investigation.

Ex-situ ICP-OES has also been employed for flow cells, where the downstream solution would be collected for elemental analysis of dissolution products[42]. The resulting concentration could be related to the total integrated dissolution charge which provides information of the combined chemical and electrochemical dissolution composition, but in order to achieve mechanistic or sequential insights for dissolution, time resolution is necessary.

Flow cells for UV-absorption spectrometry has also been established, although not much used for multielement analysis[43,44]. The necessity of complexing agents to enhance the spectroscopic response, and disturbances from agglomeration and bubble formation again complicates the analysis. In addition, multiple elements and oxidation states would have yielded a multitude of absorption peaks possibly overlapping and complicating the conversion to elemental current.

On-line ICP-OES dissolution testing had been done by 1991 without potential control[45], by dipping a galvanised working electrode into a flow cell and feed the concentration transients downstream by flow injection[46], effectively monitoring chemical corrosion of the working electrode. This had several advantages to the aforementioned techniques: six orders of magnitude linear range, detection limits down to 100 parts per trillion, highly selective towards most elements and relatively insensitive towards matrix effects.

2.3 Electrochemical flow cells for on-line dissolution

2.3.1 AESEC

By 1996 Kevin Ogle built on this idea[47] by integrating potential control to the cell, which allowed for the transient monitoring of the rate of elemental dissolution of the working electrode. The atomic emission spectroelectrochemical cell (AESEC) could now be used to observe elemental dissolution as a function of galvanostatic and potentiostatic programming[48].

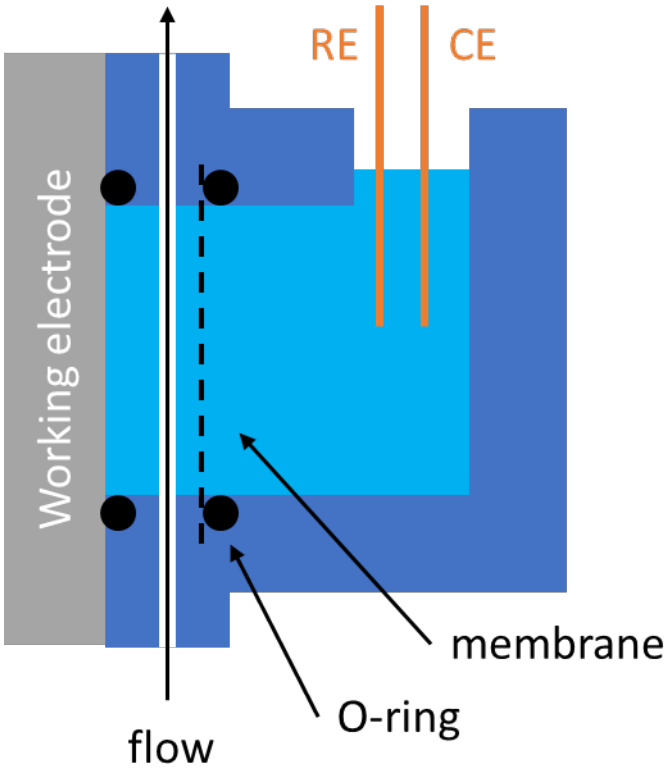

Figure 2.1 A schematic of the AESEC. CE = counter electrode, RE = reference electrode.

The AESEC body as illustrated in Figure 2.1 was machined out of PTFE with a flow compartment for the working electrode sample and a stationary compartment to house the counter and reference electrode. The two compartments were separated by a porous membrane. An O-ring was situated between the working electrode and the casing, which confined the area of the sample exposed to electrolyte. The exposed area was measured to 0.52cm^2, and volume of the working electrode was compartment 0.2 mL.

Flow rates up to 12 mL min^{-1} could be employed before the ICP torch would be extinguished, however 2-3 mL min^{-1} was employed for dissolution experiments, where the lag time between electrochemical and spectroscopic signals was estimated to be 10 seconds from the time difference of the onset of electrochemical and spectroscopic signals.

A heat regulating cooling block module was also created to regulate the temperature of the working electrode sample, hence temperature-dependent experiments could also be conducted. However, no temperature control of the electrolyte was mentioned.

Notably this flow cell has been utilised to investigate the chemical and electrochemical dissolution of zinc in alkaline solutions up to 1 M NaOH[49]. It was found that a more alkaline solution yielded higher dissolution signals despite the high concentration of salt that was injected to the ICP-OES. The rate of zinc forming insoluble oxide products was deduced by subtracting the dissolution current from the electrochemical current, assuming a charge transfer of n=2 for zinc[50].

The AESEC has also been used on drop-cast prepared micrometre sized particles from detaching from dried paint silane binder when exposed to alkaline media[51]. Single point spikes in the transient adsorption signals were not thought to result from electrochemical charge transfer, but shown to relate to corroding binder material.

Further in 2011 the AESEC technique was coupled to electrochemical impedance spectroscopy for the open circuit dissolution of hot dip galvanised steel[52].

2.3.2 The Scanning Droplet Cell

The second type of common downstream analytics coupled to a flow cell was concurrently developed in the fundamental electrochemistry field. A need to analyse samples with fast output and probing processes at the microscale, for example separate the activities at edges and sites of a sample. The scanning electrochemical microscope (SECM) already had such capabilities, but here a redox couple needs to be present, and the entire sample is usually wetted such that the electrode area is less defined, and more samples must be prepared for repeated experiments[53]. Masking techniques had also been used[54,55] from cured photoresin, this is however also time consuming.

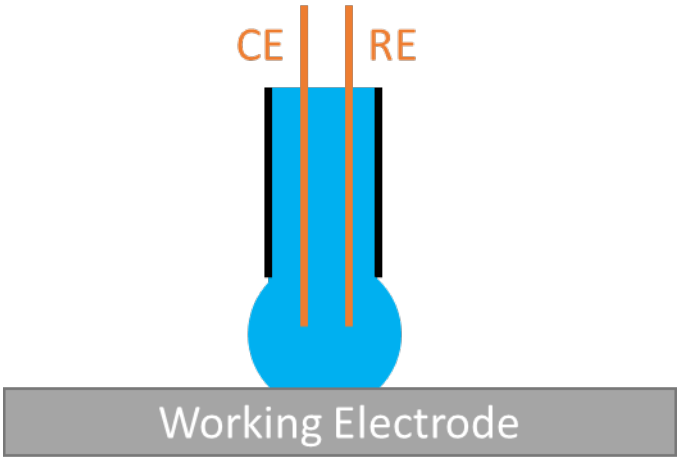

Figure 2.2 A schematic of the droplet cell. CE = counter electrode, RE = reference electrode.

Small capillaries as in Figure 2.2 were first utilised by Böhni[56]. In the earliest example in 1995, a small capillary holding electrodes where the tip was placed upon a working electrode sample. A small wetted area was established, allowing for well-defined electrochemical experiments. One of the first examples includes coupling the cell to an optical microscope with a top-down viewing angle, such that the solvation of microparticles on stainless steel working electrodes could be observed in-situ.

Lohrengel and Hassel built on this concept to develop an automatized rig in which the capillary could be moved translationally to obtain spatially resolved impedance, potentiometric and amperometric data on structured oxide thin films [57]. Selected areas could be probed as the surface tension of the aqueous electrolyte solution retained the integrity of the droplet.

Based on these results the rig was further developed to improve reproducibility by more automation[58]. The capillary cell was mounted on a force sensor such that equal pressure was applied to the hydrophobic silicon gasket for each area investigated. A video microscope observed the wetted area such that the wetted working electrode diameter could be determined by colour recognition software, in addition to any leaks from the gasket that may have taken place. The flow of electrolyte was realised here by a syringe connected upstream of the capillary. During non-contact mode the capillary would be moved to a waste container by an automated head and rinsed with electrolyte before

being positioned on a new spot of interest. The capillary tip could be constructed in the ranges of 100 nm to 30μm, and the total cell volumes that could be obtained was estimated to be less than 1nl.

2.3.3 Flow-Through Scanning Droplet Cell

By 2001 a flow cell configuration was suggested, in the form of a "capillary-within-a-capillary"[58]. The design was never realised because of the complex tubing connections it implied. Instead the theta capillary was created, which got its name because of its likeness of the shape of the Greek letter Θ when looked from top-down[59].

The two compartments, as illustrated in Figure 2.3, join at the lower point, such that one channel can be used as inlet and the other channel as outlet for an electrolyte flow. Downstream analytics capabilities were demonstrated by coupling a spectral flow cell to the theta capillary cell for UV-vis absorption acquisitions. The authors showed that the absorbance and current displayed strong correlation in both current step and potential sweep experiments, despite the relatively large optical flow cell volume (1mL) and long lag time. Results from corresponding flow simulations however indicated that a significant amount of bubbles would remain trapped in the cell [60]. The influence of potentiostatic pulses could be examined by the fast acquisition time of UV-vis spectrometer down to 10 milliseconds, but this was hindered by the large dead volume of the spectroscopic flow cell installed downstream. Therefore, only the mean value of the pulse absorption could be taken[61].

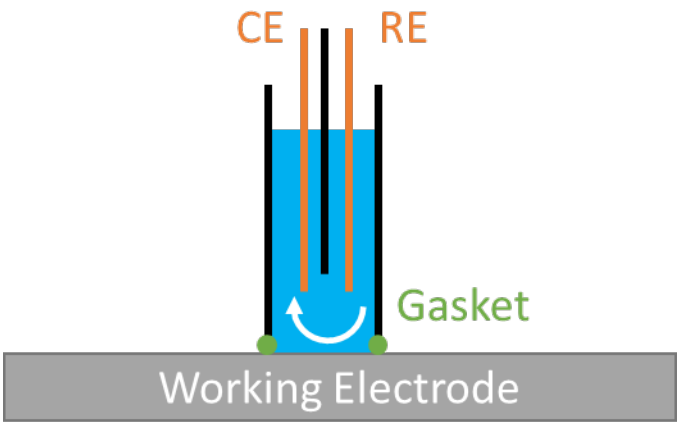

Figure 2.3 A schematic of the scanning droplet cell. CE = counter electrode, RE = reference electrode. White arrow represents the path of the electrolyte flow.

Theta-capillaries have also been machined from blocks of acrylic glass with compartments for a 450nm blue LED light source and a fiberoptic cable leading to a UV-vis spectrometer[62].

In 2007 Homazava et al[63] further developed downstream analytics to include flow-injection ICP methods downstream of the flow cell in order to study downstream dissolution phenomena. Another novelty in the design included use of polypropylene cells to avoid silica contamination from the glass capillary and gasket. The elasticity of the polypropylene tip now provided the sealing. In the study of alloy dissolution ICP methods provided detection limits in the order of 60 ng L^{-1} down to 0.1 ng L^{-1}.

Further elemental analysis was done on the corrosion of Zr-Cu-Ni-Al-Nb alloys [64] to obtain transient and element specific information in acidic media, highlighting the advantage of ICP analysis of multielement dissolution.

The stability of biodegradable magnesium alloys was investigated with an online micro-flow capillary online coupled flow injection analysing system (FIAS) coupled to an ICP-MS for spatial resolution. Capillary diameters in sizes 1000, 800, 600, 400 and 250 micrometres were used with PFA tubing, at a flow rate of 500 microliters per minute. By varying the electrolyte content between NaCl and $CaCl_2$ it was found that the dissolution rate could be controlled[65].

In 2011 Hassel et al coupled a FT-SDC to an UV spectrometer downstream in order to investigate the dissolution of Zn in aqueous media[66,67]. Zincon was added downstream as a complexing agent to increase the molar adsorption coefficient of the ions of interest.

Hassel expanded this work to alloys[68], where flow cells machined out of PTFE to demonstrate the chemical dissolution of zinc from $MgZn_2$ alloys. While possible, UV-vis would not be suitable here, as significant fractions of magnesium ions could have bound to the complexing agent which would make any deconvolution of the respective elements and oxidation states very difficult. Instead an ICP-AAS device was coupled downstream which recorded dissolution concentrations in the order of mg L^{-1}.

On-line ICP-AAS was further utilised in 2015 to quantify the chemical dissolution of aluminium-nickel-copper libraries in acidic media where the total dissolution varied between 4-14 mg mm^{-2} [69]. For more sensitive applications, ICP-MS have been used instead [70] with dissolution rates was measured in ranges of pg $s^{-1}cm^{-2}$.

2.3.4 FT-SFC

An alternative configuration, the flow-through scanning flow cell (FT-SFC) as seen in Figure 2.4, was developed by Mayrhofer et al[71]. Here, two channels (1mm diameter) drilled into a polymer (PMMA) block intersects the bottom surface at an angle of 60 degrees, creating an elliptic opening. The clear advantage here was the ease of manufacturing, and any polymer of choice may be used. The SDC on the other hand was dependent on reproducible elongation of small diameter glass pipettes with the help of a capillary elongating tool.

The FT-SFC was further coupled to an ICP-MS for highly sensitive detection of dissolution products[72]. Here such a set-up was, for the first time, used to address the stability of electrocatalysts under operational conditions. Dissolution of smooth platinum [29,32,73–82], gold[83–86], rhodium[87] and iridium oxide[88–92] surfaces have been investigated to gain comparative insight on pathways for electrocatalyst dissolution.

The effect of dissolved gas in the electrolyte has also been investigated[78], where it was shown that dissolved CO gas in the electrolyte increased the rate of dissolution by a factor of four compared to argon, owing to enhanced surface diffusion of Pt leading to

a decrease in lowly coordinated sites and blocking sites for redepositing of dissolved Pt.

Figure 2.4 A schematic of the v-channel scanning droplet cell. CE = counter electrode, RE = reference electrode. White arrow represents the path of the electrolyte flow.

Quasi-steady-state stability has also been investigated[73]. By applying current or potential in absence of electrolyte flow, to then feed the electrolyte to the downstream ICP-MS and measure the total amount of dissolution.

The stability of bulk and carbon-supported platinum has also been compared[28]. An important distinction between model surfaces and porous materials is the limited mass transport of soluble species within the pores, which can trap ions and increase deposition. Processes like Ostwald ripening and agglomeration becomes significant in such geometries, and a lower observed rate of dissolution is expected. Also, of note is the observed effect of higher catalyst loading leading to lower dissolution rate.

Alloys of $Fe_{50}Cr_{15}Mo_{14}C_{15}B_6$[93,94] and Cu-Al[95], magnesium[96,97], iron based catalysts[98,99], and thin film libraries[100–102] have also been investigated for their chemical and electrochemical stability.

The SFC rig has since been extended to include software controlled electrolyte purging, valve controls and flow rate controls[79] to minimise experimental error.

2.3.5 SDCM

Additive manufacturing techniques have been used by Kollender to further optimise the design of the FT-SDC[103,104], the scanning droplet cell microscope (SDCM) as seen in Figure 2.5. Due to the complex geometry, the cell had to be manufactured by fused

deposition modelling lithography in order to achieve better flow fields over the working electrode area[105].

Figure 2.5 A schematic of the modified scanning droplet cell. CE = counter electrode, RE = reference electrode. White arrow represents the path of the electrolyte flow.

The use of 3D-printing has since been further extended to include multiple flow channels for higher output screening[106].

2.3.6 SPRDE

Markovic created another route to on-line analysis by fixing a probe close to the edge of a rotating disk electrode and connect it to an ICP-MS, hence the name stationary probe rotating disk electrode (SPRDE). By rotating the electrode during electrochemical experiments, dissolution products are transported away from the electrode surface and caught by the probe which feeds it to the ICP-MS at a constant rate[107,108]. Reported detection limits of 0.4 pg s^{-1} cm^{-2} has been achieved by this method.

2.4 Evaluation and characterisation of the flow profile

The respective flow cells have also been evaluated for their fluid transport properties in order to assess or improve the collection efficiency and time resolution of the downstream analytics, which suffers from broadening of the dissolution product concentration transients.

To address the broadening of the dissolution signal of the AESEC once the dissolved products are detected by the ICP-OES, Ogle characterised the residence time distribution (RTD) by fitting the broadening of a near-zero dissolution pulse by Eq. 2.1:

$$H(t) = \frac{I - I^{\circ}}{Q} = \sqrt{\frac{\beta}{\pi t^2}} e^{\beta ln^2\left(\frac{t}{\tau^*}\right)} \qquad \text{Eq. 2.1}$$

Where H(t) is the RTD function for the system, τ relates to the signal maximum, β related to the half-width of the peak, Q is the integral of the transients in arbitrary units, I is the emission intensity and I° is the background emission intensity. By this approximation the experimental and fitted results agreed well[48]. Figure 2.6 shows by how transforming the electrochemical current to account for RDS, good correlation between the electrochemical and dissolution signal can be achieved.

The flow profile of the AESEC flow cell was also assessed by CFD simulations at various flow rates[109], suggesting significant vortex formation at the corners of the flow cell compartments at flow rates above 3 mL min^{-1}, which causes further elongation of the RDS.

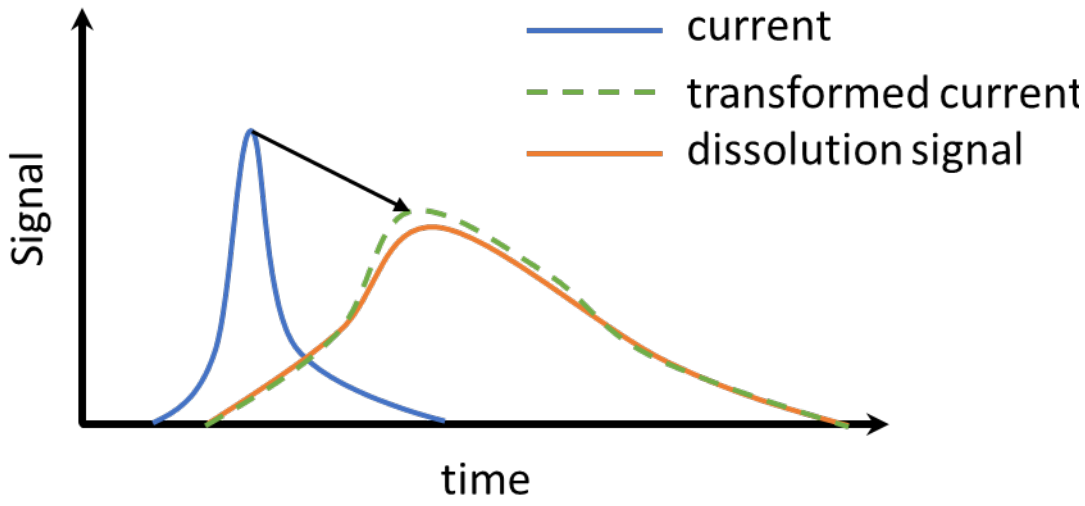

Figure 2.6 A representation of how residence time distribution is imposed on the electrochemical current.

Voith investigated geometry effects on channel flow cells by increasing width of a channel electrode as seen in Figure 2.7, where a clear trend of increasing vortex formation at the corners of the channels with width of the working compartment could be seen[68].

Figure 2.7 Representation of vortexes formed at the corners of a flow cell.

Kulyk characterised the FT-SFC[110] with the Koutecky-Levich relation corresponding with a trend close to unity. It was previously validated by Scherson et al that the relationship also extends to channel-type flow cells under conditions where $k/v_0^{1/3}$ is small. It was also noted that unless small scan rates and high flow rates were used, the depletion or saturation of reactive species would dominate, and the current density would be inhomogeneously distributed over the working area.

Kollender[105] looked to improve the flow field over the working electrode area of the SDCM by constricting the cross-section area over the working electrode. This was found to increase the flow rate of the electrolyte over the working electrode area and improves removal of gas bubbles that may form on the working electrode surface.

2.5 Conclusion and Summary

2.5.1 Conclusion

On-line dissolution detection capabilities have arisen due to the need of characterising multi-element samples where very low detection limits are needed. Through time, by small increments, the designs have become more sophisticated in regard to managing the flow of electrolyte. Today, downstream analysis of dissolution products is routinely performed by a few groups within the field of corrosion and energy conversion materials to inform of transient degradation pathways.

2.5.2 Summary

In previous work, detection of dissolution products on electrodes have been conducted by electrochemical generation-collection experiments, either in rotating ring disk electrodes or channel flow cells. However, where more than one soluble species is generated, discriminating between elements requires very complicated cell designs. Coupling flow cells to spectroscopic instruments is also complicated, due to overlapping absorption signals. Elemental analysers such as ICP-OES and ICP-MS bypasses this problem, in addition to providing very low detection limits. Flow cells for on-line ICP analysis have been concurrently developed in the fields of corrosion and electrocatalysis, but have provided valuable insights in other fields as well. Over time, flow cell designs have incrementally been adapted to minimise volume, increase flow properties and improve workflow. Cells have been manufactured by various plastics and manufacturing techniques, from subtractive machining to additive manufacturing. By additive manufacturing, complex designs are easily realised. There is a transient signal broadening stemming from flow vortexes in the flow cell effectively “trapping” the dissolution products. These can be avoided by minimising dead volume and sharp corners in the flow cell compartment.

3 Flow Cell Design and Fabrication

3.1 Introduction

This chapter will concern the design, construction and stepwise optimisation of a series of flow cells that allow downstream electrolyte analysis. Types of flow cells will be discussed, including geometry, transport properties and electrode arrangement. The construction methods for the flow cell will be discussed, including advantages and drawbacks of the properties of the available materials for alkaline solutions. Finally, the electrochemical performance of the cells will be evaluated by the resistance between the electrodes and by voltammetry of cyanoferrate redox couple at various flow rates. The objective is to create a novel flow cell that will successfully couple with ICP-OES and deliver transport properties within the flow compartment while maximising working electrode surface area while minimising flow compartment volume. The cell must display stable current and potential control, eliminate the risk of bubble entrapment and efficiently transport dissolution products from the working electrode to the channel outlet. To achieve a flow condition that is in compliance with hydrodynamic equations is not an objective in itself, but the establishment of a characteristic flow is seen as an indication of efficient transport. A very brief description of attempts at other flow cell designs are available in Appendix A.

3.1.1 Electrolyte Transport

The transport of soluble species in electrochemical systems is divided into three physical domains[111]. migration, diffusion and convection.

Convection of solution refers to the movement of molecules in the solution when an external force is applied. In a situation where the convection is well-defined, the flux of electroactive species over the working electrode can be modelled and simplified such that parameters like limiting current, diffusion coefficient, electron transfer number etc.

can be related by a single equation. Well-defined convection can be obtained in flooded cells, like in the case of rotating disk electrodes where drag from rotation generates a radial flux over the working electrode. In electrochemical flow cells, flow is achieved by pushing or withdrawing solution through channels, and the flow can either achieve a turbulent state, where the flow of solution is not well-defined, or a laminar state, where the flow of solution is well-defined and kinetic parameters can be derived from equations. Flow cells for downstream analysis are not necessarily used to only derive kinetic information, but in any case a well-defined flow helps efficient transport of products from the working electrode.

3.2 Types of flow cells

In this section, the different types of electrode arrangements and working electrode geometries that was considered will be presented and discussed. The arrangement of electrodes must be considered as it contributes to the internal resistance of the cell, and hence how much current can be passed before the potential compliance limit of the cell is reached. The geometry determines the flow properties, signal strength, and reproducible reference and counter electrode responses.

3.2.1 By electrode arrangement

The arrangement of the working, reference and counter electrode is substantially affecting the resistance and uniformity of the current density distribution onto the working electrode. Eq. 3.3 shows the relationship between the length between the electrodes (l), the resistivity of the electrolyte (ρ) and the total resistance between the cells. Hence, to minimise the resistance R, the electrodes should be situated as closely as is viable.

$$R = \rho \times l \qquad \text{Eq. 3.1}$$

Figure 3.1 depicts the effect electrode arrangement has upon the local resistance exerted upon the working electrode. Improper placement of the electrodes can lead to uneven resistance across the working electrode and hence the current density distribution will not be homogeneous.

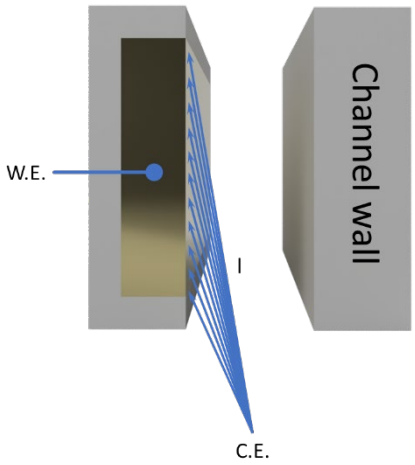

Figure 3.1 Graphical representation of the effect of electrode placement upon local current density distribution on the working electrode. W.E. = working electrode, C.E. = counter electrode, l = distance between counter electrode and working electrode.

Figure 3.2 presents some possible electrode arrangements for a planar thin-film cell[111]. In case (A), the only the working electrode is embedded in the thin-film layer, while the reference and counter electrode is situated downstream of the channel. This is the simplest electrode arrangement. As the counter and reference electrode are situated far away from the working electrode, the resistance in the electrolyte path between the working electrode and the reference will be high, resulting in large overpotentials in the voltammograms, which must be compensated for to provide accurate results. The cell resistance is also high between the working electrode and the counter electrode, which means that large overpotentials must be reached before appreciable currents can be passed. This will result in significant practical issues, as many potentiostats have a potential compliance limit of 10 V between the working electrode and the counter electrode. Lastly, the electrolyte path between the working electrode and the counter electrode is uneven, which means that the edge of the working electrode closest to the counter electrode will experience a higher current density than the edge situated furthest away. Hence, this arrangement should be avoided unless the situation dictates so.

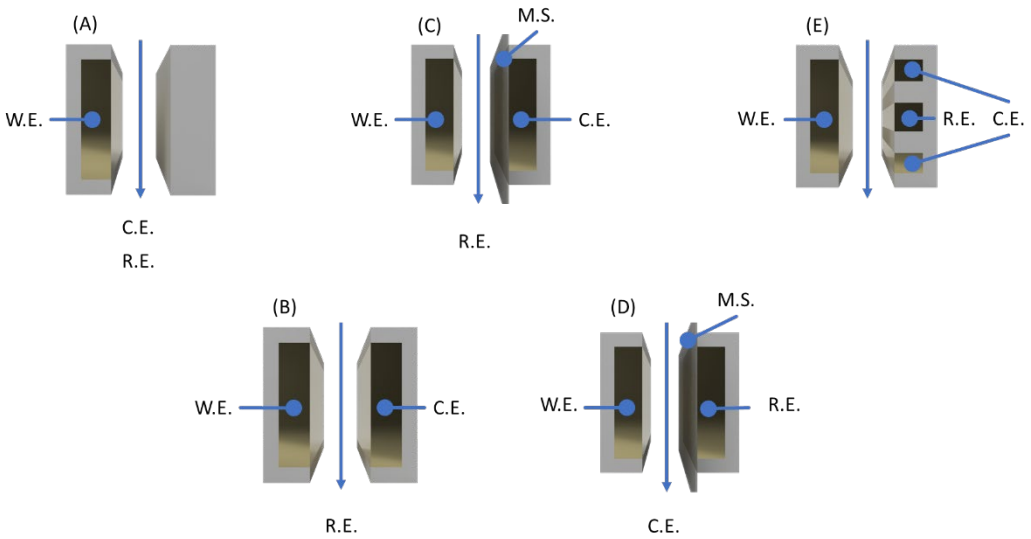

Figure 3.2 Select electrode arrangements for planar thin-film cells. W.E. = working electrode, R.E. = reference electrode, C.E. = counter electrode, M.S. = microporous membrane.

Case (B) of Figure 3.2 the working electrode and the counter electrode are situated opposite each other in the flow compartment, while the reference electrode is situated downstream of the flow cell compartment. As in case (A), since the reference electrode is situated far from the working electrode, the resistances will be large in any measurements and must be compensated for. As the counter electrode is directly facing the working electrode, the cell resistance will be low, and current can be passed without reaching the potential compliance limit of the potentiostat. The current density distribution on the working electrode surface will be uniformly distributed, as the distance between the working and counter electrodes are equal at any point on the surface. The major drawback in this arrangement is that the counter electrode will produce products when current is passed in the circuit, which may interfere with the working electrode, or products in the working electrode may deposit or undergo alteration if transported to the counter electrode, which is not wanted for product detection purposes. This can be avoided by employing a sufficiently high flow rate to remove products from the flow cell compartment, but high flow rates might not be ideal for many experimental scenarios.

Case (C) is similar to case (B), with the addition of a microporous separator membrane on the counter electrode to prevent products from the working electrode and counter electrode to cross over.

In case (D), the working electrode and reference electrode are facing each other in the flow cell compartment, while the counter electrode is situated downstream. This arrangement ensures low resistance between the working electrode and the reference electrode, as the electrolyte path between them are very small, and any measurements will only minutely be affected by potential drops. The cell resistance is very high in this arrangement, as the counter electrode is situated very far away from the working electrode as in case (A), and only small amounts of current can be passed in the cell before the 10 V compliance limit of the potentiostat is reached.

In case (E), the working electrode is sat opposite to both the counter and reference electrodes in the flow cell compartment, with the reference electrode is facing the working electrode across the centre, and the reference electrode surrounding the edges of the working electrode. Here the resistances between both the working electrode and reference electrode, and the working electrode and the counter electrode are minimised as the electrolyte path for both distances are very small, which yields minimal overpotentials during measurement and high currents are easily obtained on the working electrode without reaching the potential compliance limit of the potentiostat. Crossover of species between the working electrode and the counter electrode can be avoided by employing a microporous or ionically conductive membrane separator. However this design is clearly the most complex of all the arrangements presented, and confining the reference electrode and counter electrode together in a small space can cause interferences as the reactions on the counter electrode can alter the pH or form interfering species which may alter the potential at the reference electrode.

None of these cases are optimal for all types of experiments, in other words there is no one-glove-fits-all arrangement of electrodes that can fulfil every requirement for every type of experiment, so it is clear that the particular arrangement chosen must match the expected currents, the potential compliance limit of the potentiostat and avoid contamination from products formed at the working and counter electrodes while only producing negligible overpotentials during measurements.

3.2.2 By geometry arrangement

The geometric layout of the cell affects the rate of transport over the working electrode. Figure 3.3 presents the direction of flow for the RDE (A) and for a channel type flow cell (B) [111]. The corresponding Levich equations[111] are presented in Table 3.1, where i is the limiting current (mA), n is the number of electrons transferred, F is Faraday's constant (96485 C mol^{-1}), A is the electrode surface area (cm^2), D is the diffusion coefficient (cm s^{-1}), w is the angular rotation rate (rad s^{-1}), U is the flow rate (cm s^{-1}), v is the kinematic viscosity (cm^2 s^{-1}), b is the channel height (cm) and C the concentration (mol cm^{-3}) of analyte.

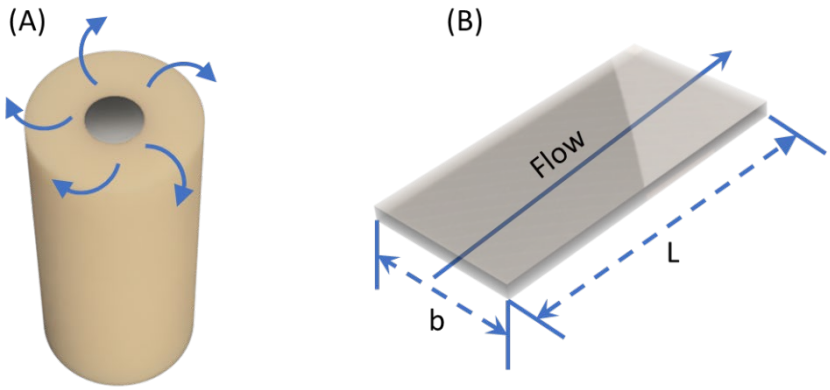

Figure 3.3 A comparison of the flow fields over an RDE and a planar parallel channel-type flow cell. The arrow indicates direction of flow. (A) = RDE electrode flow, (B) = planar parallel type flow cell.

The FT-SFC for example do not strictly conform to the parallel planar geometry, but has been shown to have planar parallel type Levich transport properties under certain hydrodynamic conditions[112]. In both cases, a plot of limiting current against $w^{1/2}$ or $U^{1/3}$ should yield a straight line with a zero-intercept on the y-axis.

Table 3.1 Levich relationships for RDE and planar parallel flow cell.

Cell type	Levich equation	Eq.
RDE	$i = 0.620nFACD^{2/3}v^{-1/6}w^{1/2}$	Eq. 3.2
Planar parallel	$i = 1.47nFC(DA/b)^{2/3}U^{1/3}$	Eq. 3.3

3.3 Design & fabrication requirements

In this section, the practical aspects of the flow cell build will be presented. Issues regarding material compatibility, manufacture process and electrode construction will be discussed.

3.3.1 Material compatibility

The appropriate materials must be used to make the flow cells to avoid contamination and disintegration. Alkaline aqueous electrolyte solution of pH 14 or greater will be used for investigations as it is the most relevant media in literature for zinc-air batteries[113]. Contaminants in solution may also deposit in the walls of the flow cells and tubing, which should be cleaned by immersion of the flow cell components in nitric acid solution. All material in contact with solution should hence be highly chemically resistant. Metals can obviously not be used as they can leech ions and cause interference with both electrochemical and spectroscopic signals and may cause internal circuit shorts.

Table 3.2 Chemical resistance of thermoplastics in alkaline, acidic and neutral salt solutions.

	KOH solution	10% HNO3	KCl
Glass	Moderate effect	No effect	No effect
PTFE	No effect	No effect	No effect
PEEK	No effect	No effect	No effect
PP	No effect	No effect	No effect
Polyacetal	Severe effect	Severe effect	No effect
PVC	No effect	No effect	No effect
PMMA	No effect	No effect	No effect
Nylon	No effect	Severe effect	Minor effect
Epoxy	No effect	No effect	No effect
EPDM	No effect	Minor effect	No effect

Table 3.2 lists some common materials with some key materials properties[114–117]. Glass is commonly used for electrochemistry apparatus, as it has good chemical resistance and low oxygen permeability, but it dissolves in the presence of concentrated basic solutions. Glass is therefore not a suitable candidate as flow cell material.

PTFE and PEEK are all fluoropolymers and are commonly used for applications that require chemical robustness. PEEK is slightly less resistant to concentrated acids. PFA is a fluoropolymer similar to PTFE and is transparent, which is beneficial for troubleshooting bubble entrapment.

Acetal, PVC and Nylon are common engineering thermoplastics, but they are not particularly chemically resistant. PMMA, also known as Perspex or Plexiglass is a transparent polymer with acceptable chemical resistance in a range of pH.

For dependable chemical resistance it is therefore clear that a thermoplastic would be the best choice as construction material. Note that plastics may have a much higher O_2 permeability compared to glass or metal[118], which requires extra consideration for the design process of the cell and electrolyte management system to mitigate oxygen penetration.

Some adhesives were tested for their chemical resistance to KOH, in case the design required combining of component surfaces. A test was designed were an aluminium surface was coated with the respective adhesives, before applying drops of aqueous 38 wt% KOH to the cured adhesive. A chemically incompatible adhesive would decompose in the presence of alkaline solution and expose aluminium to the KOH and rapidly evolve bubbles.

Table 3.3 Outcome of chemical compatibility tests of three adhesives.

Adhesive	38 wt% KOH (aq) compatible?
Nail polish	No
Loctite Universal Superglue	No
RS PRO Quick Set Epoxy	Yes

Table 3.3 presents the results from this test. Only two-component epoxy remained intact following this test. Hence, for flow cell building, it was concluded that only two-component epoxy should be used as adhesion agent.

3.3.2 Additive manufacture consideration

The construction of the flow cells presented in this chapter was made by an additive manufacturing technique referred to as stereolithography (3D-printing). Different techniques and routes were considered, which will be presented, the reasoning for choosing the particular technique will be justified.

3.3.2.1 Additive manufacture techniques

Typically, flow cells have been made by subtractive manufacturing by machining solid blocks of material to the desired shape. While effective, these methods require

expensive equipment with large footprint and expertise in handling, and the time taken to make a flow cell depends on the complexity of the design, material choice and availability of appropriate cutting tools. The complexity of design is also limited due to the type of boring operations that can be performed on a work piece are restricted to strictly linear paths.

Recently 3D printers have become an affordable manufacture alternative both in industry and research for rapid, functional prototyping. The manufacture process involves designing components in CAD software and use software to process movement instructions for the 3D printer to construct solid shapes.

Fused deposition modelling (FDM) 3D printers generally provide resolutions of 0.1 mm in the x- and y-plane, and 0.05 mm in the z-axis. Material is liquified and pushed through a nozzle of 0.4 mm diameter, which sets a lower size limit to features. Complex geometry can be printed, given that it is acceptable to add removable support structures for the printing process. A wide range of thermopolymers are also available to choose from. On the other hand, print quality may be variable. Poor layer adhesion and imperfections on the print surface are common and could cause unknown sources of turbulence in the flow cell compartment, as well as leakage between layers.

SLA 3D printers on the other hand, uses mirror-guided lasers to locally polymerise monomers in resin solution. 25 micron resolution can be achieved in all directions, and this technique does not suffer from poor layer adhesion, imperfections on print surfaces and these machines are generally less complicated to operate. On the other hand, the resin formulations are limited to only a few commercially available options, with differing materials and chemistry properties.

3.3.2.2 Materials choice

The Formlabs Form 2 SLA 3D-printer was used to fabricate the cells. The Form 2 has a minimum specified print resolution of 25 μm in the x, y and z- direction. The Form 2 had a build volume of 14.5 cm × 14.5 cm × 17.5 cm, which would be the maximum permissible component size. Formlabs had several resins commercially available that were compatible with the Form 2. Due to availability, the “Clear” resin[119] was the preferred material option.

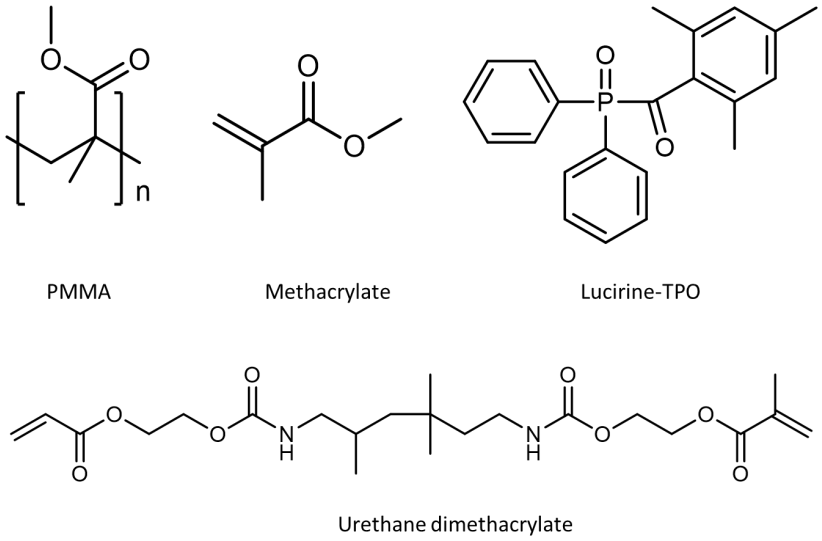

Figure 3.4 Structure of PMMA and listed Formlabs "Clear" resin components methacrylate, urethane dimethylacrylate and Lucirine-TPO.

The main components in the "Clear" resin[120] consists of the monomers methylacrylate and urethane dimethylacrylate[121], and Lucirine-TPO[122] as the photoinitiator, as seen in Figure 3.4. As the functional groups of the monomers closely resembles that of polymethylmethacrylate (PMMA), it was assumed that the cured "Clear" resin should have similar chemical properties to PMMA.

To test for chemical inertness towards alkaline solution, a piece of the "Clear" resin was immersed in aqueous 38% KOH solution and stored at room temperature. In intervals, the piece was weighed after rinsing with water and dried by compressed air blasting. Table 3.4 shows the weight change over time. An incompatible material would be expected to swell and increase in weight over time if alkaline water was absorbed into the compound or decrease in weight over time if the hydroxide would decompose the materials by reacting with the functional groups of the "Clear" resin material.

Table 3.4 weight loss of a "Clear" resin component after immersion in aqueous 38 wt% KOH solution.

Time (days)	Dried weight (mg)	% change	Comment
0	718	-	Initial weight
1	720	0.278	Integrity intact
2	721	0.139	Integrity intact
6	723	0	Integrity intact
7	723	0	Integrity intact
13	723	0	Integrity intact
15	723	0	Integrity intact

There is an initial weight gain of less than 0.5% after 2 days, but subsequent immersion time does not lead to further weight change. It was further noted that the surface of the cured “Clear” resin did not decompose upon touch. The “Clear” resin should hence be a suitable cell material for alkaline solutions. Other cured resins by Formlabs were also tested, but were found to rapidly swell or dissolve, and were not considered for further study.

3.3.3 Arrangement of electrodes & Fast throughput considerations

Elements from other on-line ICP-OES or ICP-MS flow cells as reviewed in Chapter 2 will be borrowed as they are proven to work, and then adapted to maximise surface area and minimise flow compartment volume. For example, the AESEC cell[123] uses a microporous membrane as a wall with great efficiency. A combination of the SDCM and the AESEC was hence thought to deliver both high throughput and high current capability. Further, the AESEC can in theory pass high currents without producing interfering products on the counter electrode, as the electrode arrangement is similar as presented in Figure 3.1 (C) and (D). The SDCM however, has an electrode arrangement

similar to Figure 3.1 (B), where gas evolved on the counter electrode placed at the inlet can block out the working electrode and the reference electrode placed at the outlet. This would cause significant interreference in electrochemical measurements. The cells must also promote efficient transport of dissolution products away from the cells and minimise turbulent flow which may retain products in the cell for extended times.

3.4 Designs

This section will present four cell designs that was fabricated mostly by SLA 3D-printing manufacturing. All cells were modelled in the Fusion360 (Autodesk) CAD software. To ensure that the fabrication methods and materials were sound and that cells performed comparably to literature, the FT-SFC invented by Mayrhofer was first manufactured as it has the simplest geometry, here referred to as "1-Vc". Once the manufacturing process was established, to evaluate the effect of geometry onto hydrodynamic properties, the SDCM cell invented by Kollender[105] was manufactured according to their schematics, and will be referred to as "2-Vc".

These cells however have much smaller working electrode surface areas that would be insufficient for electrode dissolution product detection. Typically, the working electrode opening diameter presented is 1.0 mm, which gives an exposed surface area of 0.0079 cm^2. This may provide a reasonable signal for an ICP-MS, however in comparison the signal intensity for ICP-OES are less sensitive by a factor of 100 to 1000.

Therefore, novel cells combining aspects of the fast throughput capabilities of the FT-SFC with the high current capability of the AESEC were designed. These cells were based on the v-channel design of the FT-SFC, but with a working electrode exposed area nine times the diameter compared to the FT-SDC, resulting in 80 times increase in exposed surface area, in order to amplify dissolution currents. A microporous separator was also employed as a wall in the flow compartment, as utilised in the AESEC. The first draft, the "3-Lc" was first evaluated for its hydrodynamic properties, and an subsequent version, the "4-Lc", had incremental optimisation steps in the geometry to improve the hydrodynamic properties, like optimising the flow compartment to reduce the tendency for turbulence, mitigate dead volume and minimise bubble formation and residency risk.

3.4.1 1 1-Vc

The first flow cell draft was a similar design to the FT-SFC used by Mayrhofer et al. The intersection of the v-shape channels at the bottom of the cell is exposed to contact the working electrode. All ports were modelled to fit 1/4" UNF-28 fittings, and ferrules and 1/8” PFA tubing. Figure 3.5 (A) shows a 3D render of the flow cell. In Figure 3.5 (B), only the cell channels are displayed to give the reader a better appreciation of the internals of the cell.

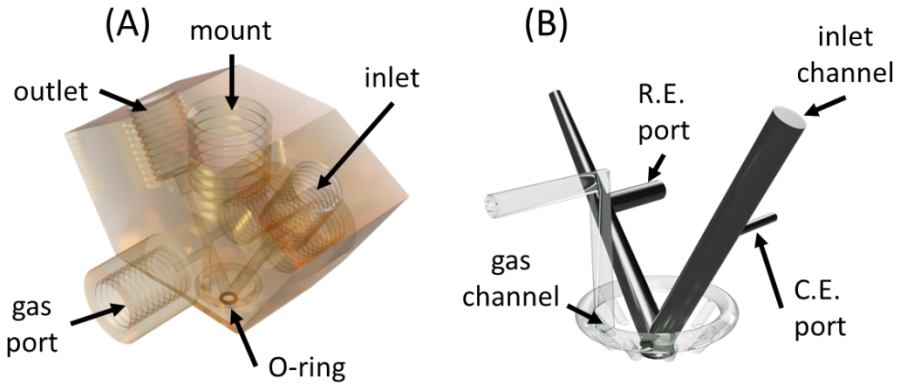

Figure 3.5 A 3D-representation of 1-Vc flow cell (A). In (B), only the internal flow channels are shown in dark, and the shielding gas channels in bright opaque.

Figure 3.6 shows an X-ray style image of the 1-Vc. The inlet (A) is a 1/8” diameter channel that meets the outlet (C) channel at a 60° angle at the bottom of the cell (B). In order to minimise dead volume, the outlet channel was tapered to fit 1/16” tubing on the outlet. The smooth taper was applied in order to minimise vortex creation, and the minimised volume ensures that dissolved products from the working electrode. The intersection point (B) exposes the channel externally with a surface area of 0.031 cm^2. An EPDM rubber O-ring was used as sealing gasket and fixed to the intersection point (B) with two-component epoxy glue. A similar approach to Mayrhofer et al. was first conducted by applying silicone gasketing glue to the edges of the exposed area, but this resulted in poorly defined surface areas, and proved to be more time consuming compared to gluing commercial O-rings. An M8 threaded hole (E) was modelled through the top of the flow cell to allow it to be mounted to a retort stand. The porous EPDM O-ring and sealant epoxy glue is suspected to be a significant source of oxygen

permeability. Therefore, nitrogen flushing channels (D) were introduced to the design by creating a toroid channel around the intersection (B) and have 8 channels extending out from the toroid aimed directly onto the sealing location.

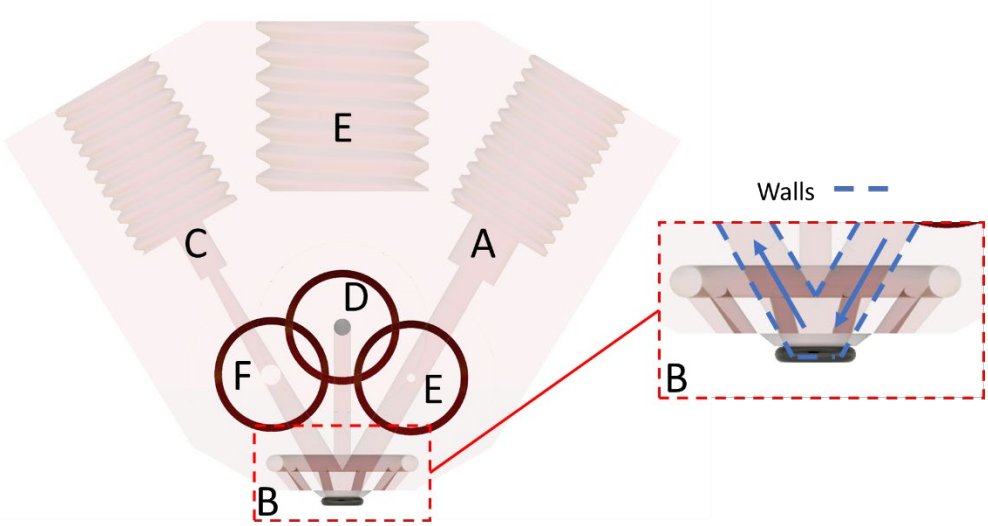

Figure 3.6 Cross-section diagram of the 1-Vc. Red inset is a magnified view of the highlighted area.

An inlet port for nitrogen was added, and the connection between the toroid and the inlet port was placed in a staggered manner with respect to the outlet channels to promote homogeneous distribution of gas pressure.

The electrode arrangement as used by the FT-SFC has the counter electrode placed in the inlet flow channel, and a reference electrode placed on the outlet channel, and a similar approach was taken for the 1-Vc. In the inlet channel, a 1/4" UNF-28 port was added for a counter electrode wire with a 1 mm bore to the inlet channel. As a rule of thumb, it is recommended that the counter electrode surface area should be at least 10 times the surface area of the working electrode[111], in this case 0.31 cm^2. A 20 cm long wire of 0.01 cm thick PtIr (90:10) alloy was folded up and inserted into the cell with both ends extending out of the counter electrode port, which provides 0.63 cm^2 surface area. The port was sealed by wrapping the ends of the wire with PTFE tape and compressed shut with a 1/4" UNF-28 nut. In the outlet channel, a 1/4" UNF-28 port and a 1 mm hole was added to fit a reference electrode. The reference electrode of choice was a Leak Free reference electrode (Innovative Instruments Inc[124]) which is a Ag/AgCl

reference electrode sealed in a 1 mm thick PEEK tubing and a leak-free junction. It was found to be robust and convenient compared to larger reference electrodes with porous glass frits. The reference electrode membrane is claimed to consist of a non-leaking ionically conductive material inert to strong and concentrated acids, bases and organic solvents and electrolytes.

3.4.2 2-Vc

The second flow cell draft was a replica of the SDCM design. The bottom of the v-shape is exposed to contact the working electrode. All ports were modelled to fit 1/4" UNF-28 fittings, and ferrules and 1/8" PFA tubing. Figure 3.7 (A) shows a 3D render of the flow cell, from now referred to as the 2-Vc cell. In Figure 3.7 (B), only the cell channels are displayed to give the reader a better appreciation of the internals of the cell.

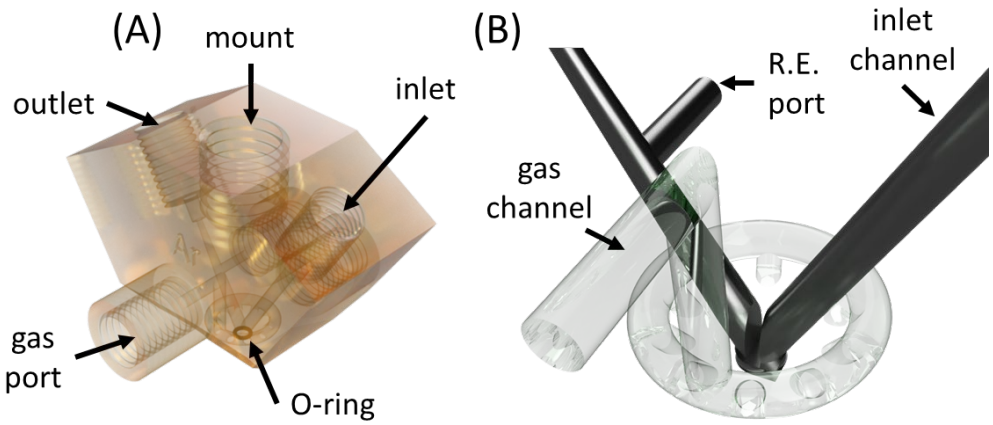

Figure 3.7 A 3D-representation of 2-Vc flow cell (A). In (B), only the internal flow channels are shown in dark, and the shielding gas channels in bright opaque.

Figure 3.8 shows an X-ray style image of the 2-Vc. Similar to the FT-SDC, the inlet (A) is a 1/8" channel that meets the outlet (C) channel at a 60 degree angle (B). The outlet channel was also tapered to minimise dead volume of exiting electrolyte while minimising turbulence. The intersection point (B) exposes the channel externally with a surface area of 0.031 cm^2. An EPDM rubber O-ring was used as sealing gasket and fixed to the intersection point (B) with two-component epoxy glue.

The inset in Figure 3.8 shows a magnified view of the flow compartment (B) of the 2-Vc cell. A wall in the centre of the cell extending all the way down to the O-ring to constrict the cross-section area perpendicular to the flow field. The constricted cross-section greatly increases the flow speed of the fluid at a given mass flow rate. The increased flow will lead to more efficient bubble removal over the working electrode surface and higher flux of transport of ions away from the working electrode surface.

An M8 threaded hole (E) was modelled through the top of the flow cell to allow it to be mounted to a retort stand. Nitrogen flushing channels (D) were introduced to the design by creating a toroid channel around the intersection (B) and have 8 channels extending out from the toroid aimed directly onto the sealing location.

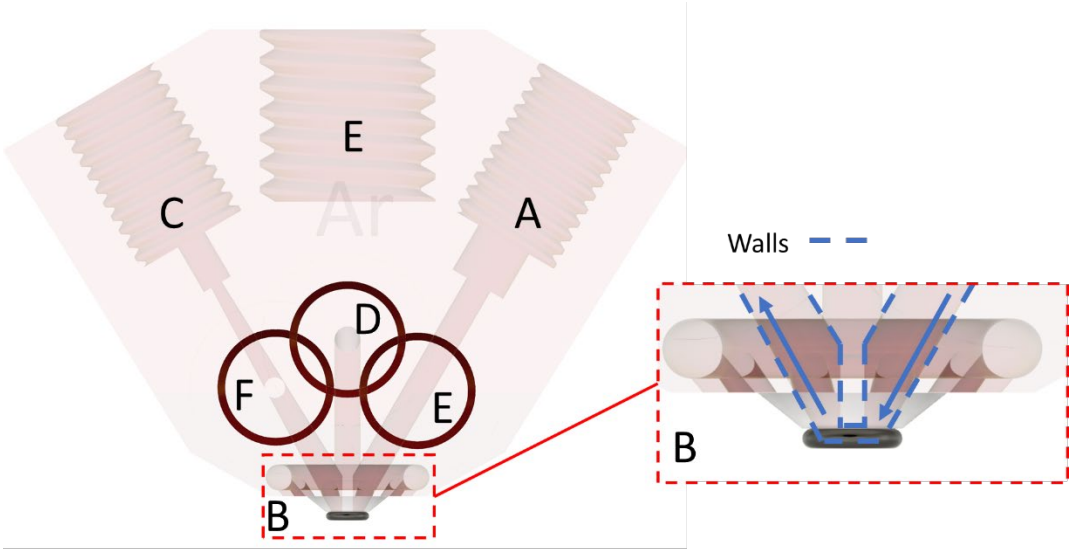

Figure 3.8 Cross-section diagram of the 2-Vc cell. Red inset is a magnified view of the highlighted area.

An inlet port for nitrogen was added, and the connection between the toroid and the inlet port was placed in a staggered manner with respect to the outlet channels to promote homogeneous distribution of gas pressure.

The counter (E) and reference (F) electrode preparation was the same as for the FT-SDC: in the inlet channel, a 1/4" UNF-28 port was added for a counter electrode wire with a 1 mm bore to the inlet channel. A 20 cm long wire of 0.01 cm thick PtIr (90:10) alloy was folded up and inserted into the cell with both ends extending out of the counter electrode port. The port was sealed by wrapping the ends of the wire with PTFE tape

and compressed shut with a 1/4" UNF-28 nut. In the outlet channel, a 1/4" UNF-28 port and a 1 mm hole was added to fit a reference electrode, which was a 1 mm diameter Ag/AgCl reference electrode by Innovative Instruments.

3.4.3 3-Lc

The third flow cell draft in Figure 3.9 (A) was a novel adaptation of the FT-SFC combined with the two-compartment AESEC flow cell, and will be referred to as the 3-Lc cell. The bottom of the v-shape is exposed to contact the working electrode. All ports were modelled to fit 1/4" UNF-28 fittings, and ferrules and 1/8" PFA tubing. In Figure 3.9 (B), only the cell channels are displayed to give the reader a better appreciation of the internals of the cell.

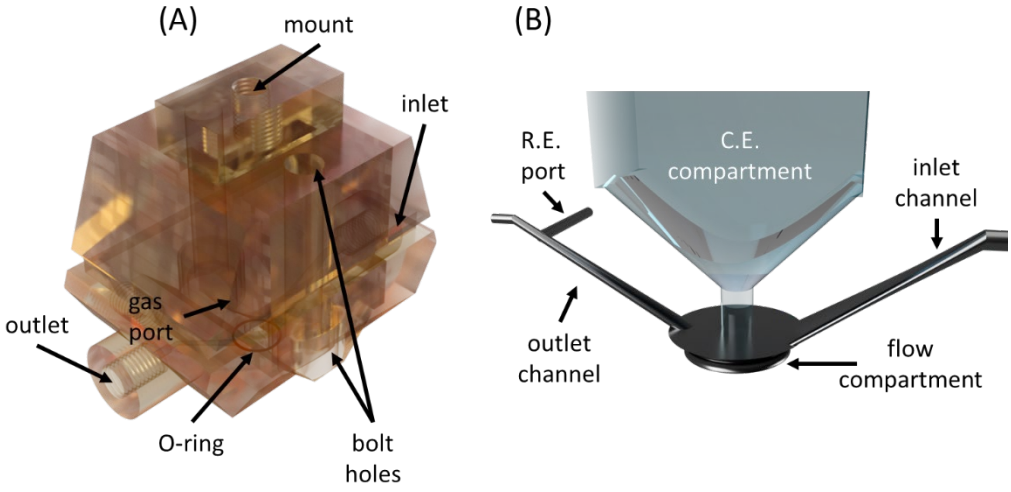

Figure 3.9 A 3D-representation of 3-Lc flow cell (A). In (B), only the internal flow channels are shown in dark, and the shielding gas channels in bright opaque.

Figure 3.10 shows an x-ray style image of the 3-Lc cell. The inlet (A) is a 1/8" channel that meets the outlet (C) channel at a 60 degree angle (B). The cross sectional shape transitions from a circular shape to a wide slot to promote homogeneous flow in the circular shaped flow cell compartment, and avoid the creation of vortexes. The outlet channel in a similar matter starts with a wide slot shape and is transformed to a circular 1/16" channel at the 1/4"-28 UNF port. The outlet channel has a smaller cross sectional diameter to minimise the dead volume of the channel.

The intersection point (B) exposes the channel externally with a surface area of 0.636 cm^2. An EPDM rubber O-ring of 9 mm inner diameter and 1 mm cross-sectional diameter was used as sealing gasket and fixed to the intersection point (B) with two-component epoxy glue. The approach of Mayrhofer et al. was first conducted by applying silicone gasketing glue to the edges of the exposed area, but this resulted in poorly defined electrochemical surface areas, and proved to be more time consuming compared to gluing commercial O-rings.

Figure 3.10 provides a magnified view of location (B). The ceiling of the flow compartment is the interface between the counter electrode compartment and the working electrode compartment. A microporous polypropylene membrane (Celgard 3401[125]) is fixed between the compartments and clamped by a compressed EPDM O-ring in a recess between the compartments (F) to ensure minimal leak rate and homogeneous current density distribution on the working electrode.

The cap for the counter electrode compartment (G) has a 1/4”-28 UNF port to feed the counter electrode contact. The counter electrode was a carbon felt (20 cm^2) which was connected to a gold wire of 1 mm diameter by having it threaded through and bonded with carbon cement for increased conductivity. Carbon was used to avoid leeching of bulk metal at high overpotentials on the counter electrode which could interfere with the electrochemical and spectroscopic signal. Carbon felt is a affordable and highly available option that also provides more surface area, which should further increase the current rate capability of the working electrode before the potentiostat reaches its potential compliance limit. An M6 threaded hole was modelled through the top of the flow cell to allow it to be mounted to a retort stand. The flow compartment is secured to the counter electrode compartment by two nylon M6 bolts on either side of the flow cell opening, secured with nylon nuts.

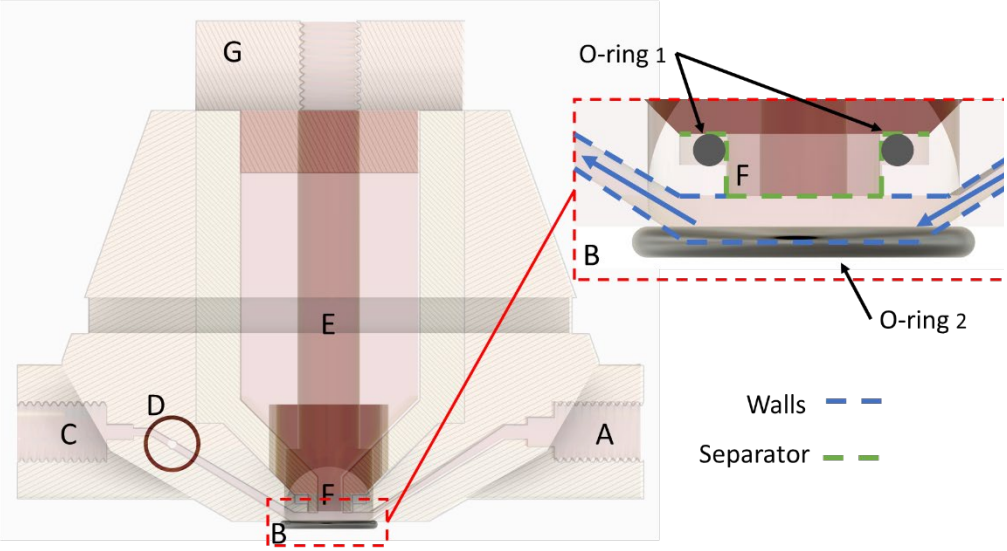

Figure 3.10 Cross-section diagram of the 3-Lc cell. Red inset is a magnified view of the highlighted area.

UNF-28 port and a 1 mm hole (D) was added to fit a reference electrode tip in the outlet flow channel. The reference electrode of choice was the Leak Free Ag/AgCl reference electrode by Innovative Instruments Inc..

3.4.4 4-Lc

The fourth flow cell draft in Figure 3.11 (A) was an optimisation of the 3-Lc presented in Section 3.4.3. The flow-cell compartment is not a converging point of two channels as with previous designs, the flow cell compartment is essentially a thin-film type flow cell. It can be thought of as a combination of the SDCM cell and the AESEC and is from here referred to as the 4-Lc cell. All ports were modelled to fit 1/4" UNF-28 fittings, and ferrules and 1/8” PFA tubing. In Figure 3.11 (B), only the cell channels are displayed to provide the reader a better appreciation of the internals of the cell.

Figure 3.12 shows an x-ray style image of the 4-Lc. The inlet (A) is 1/4"-28 UNF port that is connected to the flow compartment by a channel. The channel starts with a circular cross-section profile at the port with a diameter of 1/16” and ends with a slot-like profile at the flow cell compartment to even out flow fields and prevent creation of vortexes. Similarly, a channel is extended from the flow cell compartment to a 1/4"-28

UNF outlet port, with the slotted profile at the flow cell compartment and a circular profile at the port. Both channels are slightly curved to open up space for nitrogen shielding channels.

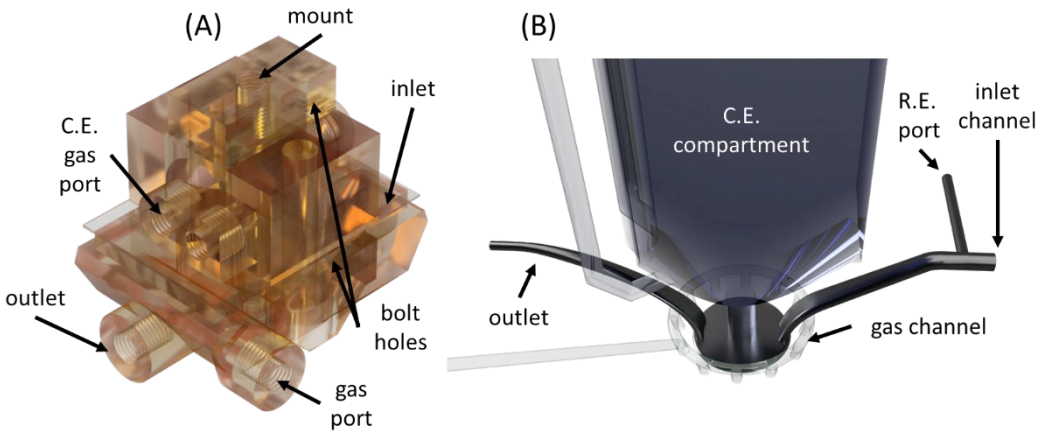

Figure 3.11 A 3D-representation of 4-Lc flow cell (A). In (B), only the internal flow channels are shown in dark, and the shielding gas channels in bright opaque.

The intersection point (B) exposes the channel externally with a surface area of 0.636 cm^2. An EPDM rubber O-ring of 9 mm inner diameter and 1 mm cross-sectional diameter was used as sealing gasket and fixed to the intersection point (B) with two-component epoxy glue. A groove was modelled for the O-ring for improved adhesion and further limiting the effective height of the flow cell compartment. The O-ring was attached by applying a thin coating of epoxy glue to the groove, carefully placing the O-ring on the groove, placing a PTFE sheet and a flat stainless steel surface on top of that to ensure even pressure and a flat O-ring profile as the glue hardened overnight. This procedure was found to be essential to obtain practically flat O-ring profiles.

Figure 3.12 provides a magnified view of location (B). The ceiling of the flow compartment is the interface between the counter electrode compartment and the working electrode compartment. A microporous surfactant-coated membrane (Celgard 3401) is fixed between the compartments and clamped by a compressed O-ring in a recess between the compartments (D) to ensure minimal leak rate and homogeneous current density distribution on the working electrode.

The counter electrode compartment (F) has a volume of 20 cm^3 and a direct interface to the flow cell compartment. Two 1/4"-28 UNF ports (J) with channels leading to the bottom of the counter electrode compartment were modelled in, one for oxygen purging the electrolyte solution, and for potential removal of electrolyte solution without disassembly of the cell. An electrolyte inlet (K) was also fitted at the top of the counter electrode compartment for potential electrolyte exchange.

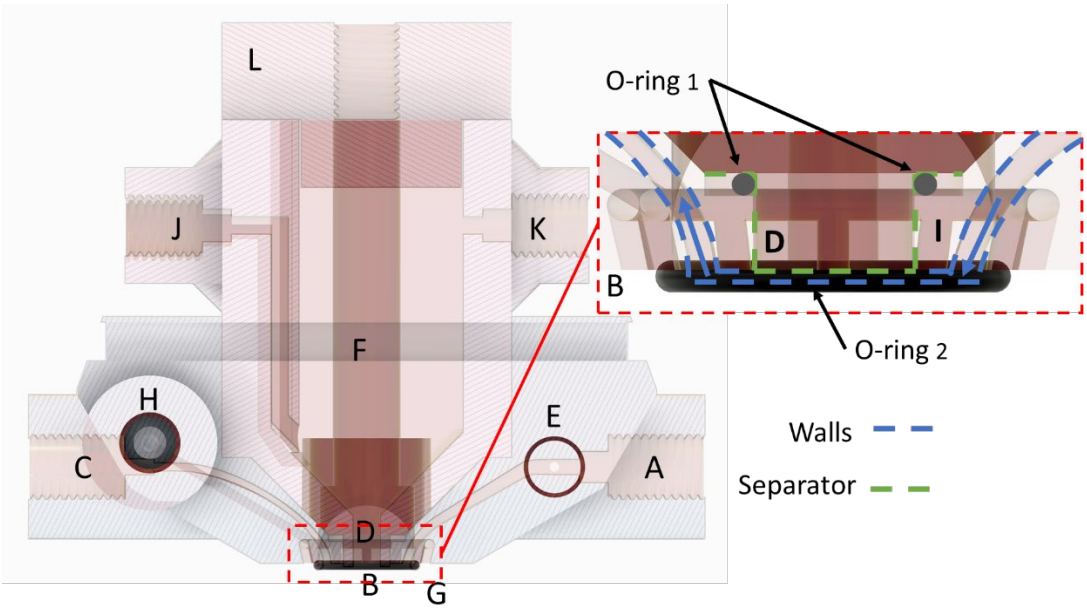

Figure 3.12 Cross-section diagram of the 4-Lc cell. Red inset is a magnified view of the highlighted area.

The cap for the counter electrode compartment (L) has a 1/4”-28 UNF port to feed the counter electrode contact. The counter electrode was a carbon felt (20 cm^2) which was connected to a gold wire of 1 mm diameter by having it threaded through and bonded with carbon cement for increased conductivity. An M6 threaded hole was modelled through the top of the flow cell to allow it to be mounted to a retort stand. The flow compartment is secured to the counter electrode compartment by two nylon M6 bolts on either side of the flow cell opening, secured with nylon nuts.

An inlet port for nitrogen gas (H) was added, and the connection between the toroid cavity (I) surrounding the flow compartment and the inlet port was placed in a staggered manner with respect to the outlet channels (G) to promote homogeneous distribution of gas pressure.

The electrode arrangement of the 4-Lc cell was modified to prevent instability from bubble generation. In the inlet channel, a 1/4"-28 UNF-28 port and a 1 mm hole (E) was added to fit a 1 mm diameter Leak Free Ag/AgCl reference electrode by Innovative Instruments.

3.5 Performance testing

In this section, aspects of the hydrodynamics of the cells will be characterised by estimating the Reynolds numbers, the effect of dead volume on the transport of dissolution products, and by linear sweep voltammetry. The differences in hydrodynamic properties will be evaluated against the geometry of the flow compartment. The ability to prevent oxygen penetration into the electrolyte will be tested by cyclic voltammetry on polycrystalline platinum, and strategies to minimise signal instability caused by the potentiostat will be presented. The impact of electrode arrangement will be assessed by electrochemical impedance spectroscopy (EIS). The practical aspects around additive manufacturing and how its limitations affected the design process will be discussed.

3.5.1 Potentiostat instability, settings, oxygen exclusion

To verify the cell response upon polarisation, cyclic voltammograms of polycrystalline platinum were taken in 1 M KOH. Since the cyclic voltammogram of platinum is well characterised in the scientific literature[126], sources of incorrect potentiostat operation can easily be identified and addressed by troubleshooting.

The potentiostat used for all measurements was a Nordic Electrochem ECi200 with an internal resistance compensation module. An Iviumstat (Ivium) and an SP-200 (Biologic) was also used in similar tests, however noise could not be fully cancelled during measurements from these instruments, with the Iviumstat being the least stable option.

Figure 3.13 (A) and 3.14 (A) presents the results of the 2-Vc cell and the 4-Lc cell respectively, with the default manufacturer potentiostat settings as is. Oscillations are introduced in the voltammograms as a result of the potentiostat not being able to set the correct voltage under the potential scan. The essential component in the potentiostat is the negative feedback loop, which seeks to set the potential of the potentiostat to a

desired input potential. When the internal resistance between the working electrode and reference electrode approaches zero, the negative feedback loop acts like a comparator, producing either maximum or minimum compliance voltage, which causes these oscillations[127]. The ECi200 is quite stable compared to Iviumstat and Biologic, so these oscillations are not very pronounced from the outset.

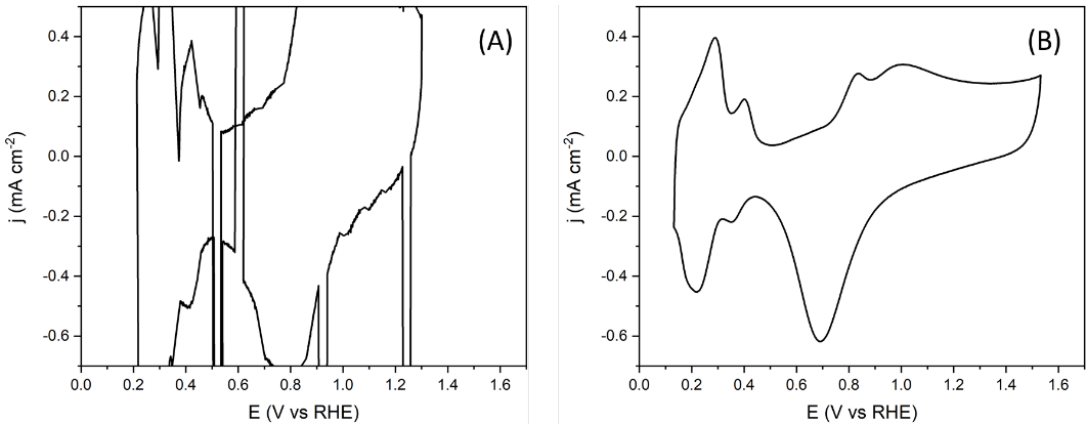

Figure 3.13 Cyclic voltammograms of polycrystalline platinum with the 2-Vc cell in 1 M KOH. Left hand side without stability settings applied. Right hand side with 100 Ohm resistor, increased bandwidth, increased current range and power line filtering. Scan rate 100 mV s^{-1}.

The most effective way to increase stability is hence by artificially introducing internal resistance. Figure 3.13 (B) and Figure 3.14 (B) shows the cyclic voltammograms of polycrystalline platinum when a 100 Ohm resistor is added in series between the working electrode lead wire and the working electrode contact. Oscillations produced by potentiostat instability is completely removed in both cases, and the characteristic regions of the platinum cyclic voltammograms are clearly distinguishable. The artificially introduced internal resistance distorts the current response. This can be mended by enabling the potentiostat control software to compensate for the internal resistance digitally or analogous to a certain extent, but this re-introduces the oscillation problem. A negative impedance device by Nordic Electrochemistry was fitted inline between the potentiostat and the cell. This device can be thought of as adding energy, or "negative impedance" to the circuit to restore the lost potential drop due to internal resistance[127].

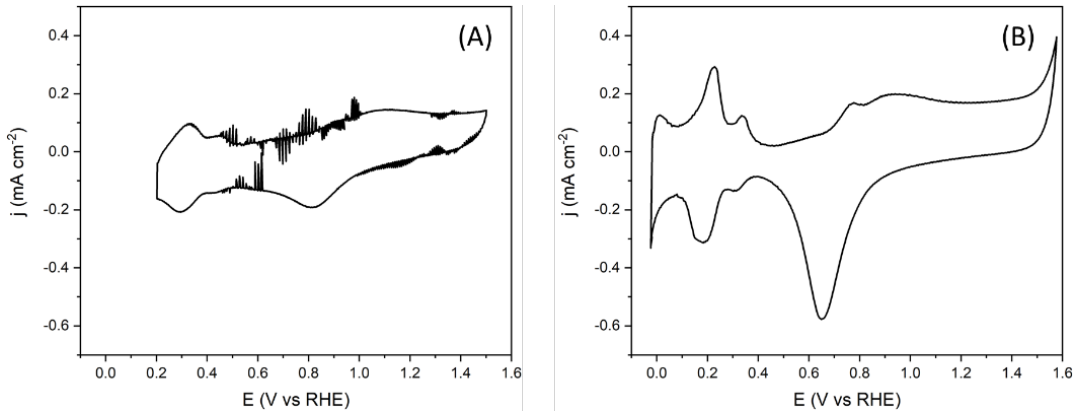

Figure 3.14 Cyclic voltammograms of polycrystalline platinum with the 4-Lc cell in 1 M KOH. Left hand side without stability settings applied. Right hand side with 100 Ohm resistor, increased bandwidth, increased current range and power line filtering. Scan rate 100 mV s^{-1}.

Other settings were applied to increase potentiostat stability. The ECi200 had options to sync sampling rate with the 50 Hz powerline, and to filter out the power line frequency, to minimise effects from electromagnetic noise. The bandwidth setting was increased by one increment which proved to reduce noise, however at very high bandwidth settings the voltammograms appeared clearly distorted. Increasing the experimental current range setting to the highest setting viable without overstepping the signal-to-noise ratio also lessened the chance of oscillations. The typical resolution of each current range for any given potentiostat is usually 0.1% of the maximum specified current. Therefore, this setting must be chosen carefully depending on the expected current magnitude, for example a 10 mA current range is appropriate for expected current responses between 10 µA and 1 mA.

3.5.2 Estimation of the flow quality

As the cells do not conform to any of the traditional geometries presented in Section 3.2, a mathematical treatment of the flow will not be feasible. However, approximation by Reynold's number calculations by solving Eq. 3.4 will be used to estimate the transition limit from laminar to turbulent flow[111]:

$$Re = \frac{Inertia\ force}{Viscous\ force} = \frac{\rho v L}{\mu} \qquad \text{Eq. 3.4}$$

where ρ is the density of the fluid, ν is the flow velocity of the fluid, L is the characteristic length and μ is the dynamic viscosity. The characteristic length L will be taken as the cross-section of the flow over the working electrode for each cell. The critical Reynolds number for a tube is 1500. For estimated Reynolds numbers below 1500, the movement is dominated by the fluid viscosity and produces a laminar flow profile. For estimated Reynolds numbers above 1500, the movement is dominated by the flow forces and produces turbulences[128].

Table 3.5 Calculated Reynolds numbers for the flow cells between flow rates 1-3 mL min^{-1}. The flow rate is set by a peristaltic pump (volume per time), and is not the same as the flow speed (distance per time)

Flow rate	1-Vc	2-Vc	3-Lc	4-Lc
Cell height (mm)	4.0	0.25	3.1	0.5
1 mL min^{-1}	4.4×10^{1}	7.0×10^{2}	5.6×10^{1}	3.5×10^{2}
1.5 mL min^{-1}	6.6×10^{1}	1.0×10^{3}	8.3×10^{1}	5.2×10^{2}
2 mL min^{-1}	8.7×10^{1}	1.4×10^{3}	1.1×10^{2}	7.0×10^{2}
3 mL min^{-1}	1.3×10^{2}	2.1×10^{3}	1.7×10^{2}	1.0×10^{3}

Table 3.5 shows the calculated Reynolds numbers for the flow cell designs. The dynamic viscosity of 1 M KOH aqueous solution was taken as 0.000998 Kg m^{-1} s^{-1}[129], density to 104.652 kg m^{-3}, the characteristic length was taken as the distance between the cell entries (the cell compartment diameter) which is limiting for non-developed flows, and the fluid velocity the flux of fluid at the cross-section, diameter times height, of the middle of the cell.

The obvious result for these calculations is that as flow rate increases, so does the Reynolds number. The Reynolds number also changes with the cell geometry. Considering the cells with the same distance between the channel entrances, the 2-Vc cell has Reynolds numbers 1-2 orders of magnitude larger than the 1-Vc. This is due to the significantly smaller cross-section area above the working electrode compared to the 1-Vc. This raises the fluid velocity and that may introduce turbulence at flow rates

above 2 mL min^{-1}. The 4-Lc has Reynolds numbers around 1 order of magnitude larger than the 3-Lc due to the same reason. The Reynolds numbers do not change much when the cell entrance distances are altered, the calculated Reynolds numbers are similar for the 1-Vc and the 3-Lc, and similar for the 2-Vc cell and the 4-Lc. This is because the cell height becomes the dominating factor for solving Eq. 3.5 when the cell entries distance (the diameter) is small.

Another way to characterise the performance of the cells is to calculate the time it takes for the cell to be completely replenished with electrolyte assuming 100% efficiency. Eq. 3.5 is used to calculate replenishing time *t*, by dividing the flow cell compartment volume V (cm^3) by the flow rate v (cm^3 s^{-1}).

$$t = \frac{V}{v} \qquad \text{Eq. 3.5}$$

A smaller replenishing time would indicate that the transport of product generated at the working electrode out of the flow compartment, and a lower replenishing time would indicate better signal quality in terms of time distribution when they reach the ICP-OES. As the highest datapoint generation frequency of the ICP-OES is roughly 1 Hz, it is desirable for the cells to have a replenishing time equal to or lower than this, but for more discussion of the signal quality the reader is referred to Chapter 4. Table 3.6 displays the flow cell compartment volumes and calculated replenishing times for the cells.

Table 3.6 Calculated replenishing times of the flow compartment of the cells.

	1-Vc	**2-Vc**	**3-Lc**	**4-Lc**
Volume (mL)	7.1×10^{-3}	4.0×10^{-4}	2.0×10^{-1}	3.2×10^{-2}
Flow rate	**Cell replenishing time *t* (s)**			
1 mL min^{-1}	4.2×10^{-1}	2.7×10^{-2}	1.2×10^{1}	1.9×10^{0}
1.5 mL min^{-1}	2.8×10^{-1}	1.8×10^{-2}	8.0×10^{0}	1.3×10^{0}
2 mL min^{-1}	2.1×10^{-1}	1.3×10^{-2}	6.0×10^{0}	9.5×10^{-1}
3 mL min^{-1}	1.4×10^{-1}	8.8×10^{-3}	4.0×10^{0}	6.4×10^{-1}

The replenishing time obviously decreases as the flow rate increases. For the small cells 1-Vc and 2-Vc, the replenishing time is below 0.5 seconds and 0.03 seconds respectively even at the lowest flow rate considered for this calculation. The short replenishing times should correspond to excellent dissolution signal authenticity between the product generation at the flow cell compartment and the signal measurement in the ICP-OES. For the larger 3-Lc and 4-Lc, the replenishing times are orders of magnitude larger. The 3-Lc having the largest volume, never reaches a replenishing time below 1 second for any of the flow rates considered here, which suggests that the signal authenticity once the dissolved products reaches the ICP-OES is poor. The 4-Lc has a replenishing time of 1.9 seconds at 1 mL min^{-1} flow rate, which is longer than the desired replenishing time. With increasing flow rate however, the replenishing time decreases to 0.95 s, which is acceptable and comparable to the replenishing time of the 1-Vc at 1 mL min^{-1} flow rate. These calculations show that increasing the flow rate is sufficient to make any flow cell suitable for on-line analysis, however it does not take into account the chance of turbulence generation previously discussed or how the flow rate affects the signal quality of the ICP-OES, which will be discussed in Chapter 4.

3.5.3 Linear sweep response of the 3D-printed cells

Each cell was tested by linear sweeps of oxidation of 10 mM potassium hexacyanidoferrate(II) in 1 M KOH electrolyte in varying flow rates set by the peristaltic pump attached to the ICP-OES. The response, diffusion or convection controlled, may inform about the internal fluid mixing and residence time distribution within the cell.

Figure 3.15 shows the linear sweeps for the 1-Vc flow cell. The curve at 0.0 mL min^{-1} shows the result for the purely diffusion-limited case. As the flow rate increases, the current density increases, but never achieves a convection-limited state, even at very high applied flow rates. This may translate to a widening of the signal in the ICP-OES, as the residence time distribution of the system is increased.

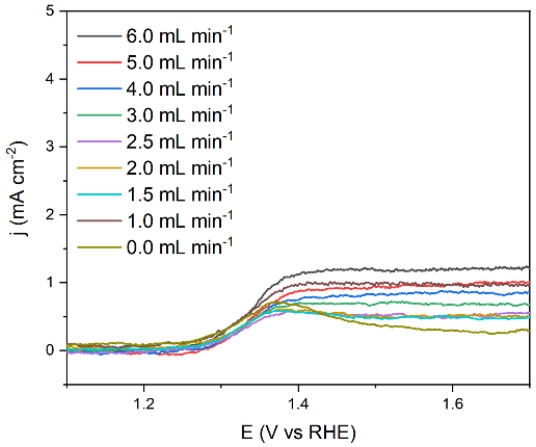

Figure 3.15 Linear sweep voltammograms for the 1-Vc in 1 M KOH + 10 mM Fe(II) electrolyte and 10 mV s^{-1} scan rate.

Figure 3.16 shows the linear sweeps for the 2-Vc cell. The curve at 0.0 mL min^{-1} shows the result for the purely diffusion-limited case. As the flow rate increases, the current increases and reaches a limiting plateau region. The limiting current further increased as a function of the flow rate. This suggests that the flow over the working electrode is very efficient and the degree of internal mixing is low, and may translate to well defined peaks for the ICP-OES signals. The apparent noise in the linear sweep data under flow conditions may stem from peristaltic pump pulsation.

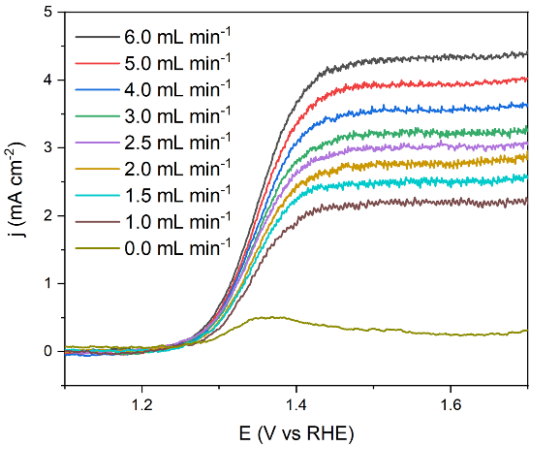

Figure 3.16 Linear sweep voltammograms for the 2-Vc in 1 M KOH + 10 mM Fe(II) electrolyte and 10 mV s^{-1} scan rate.

Figure 3.17 shows the linear sweeps for the 3-Lc cell. The curve at 0.0 mL min^{-1} shows the result for the purely diffusion-limited case. As the flow rate increases, the current density increases, but never achieves a convection-limited state, even at very high applied flow rates, which suggests the hydrodynamic transport over the working electrode is not very efficient.

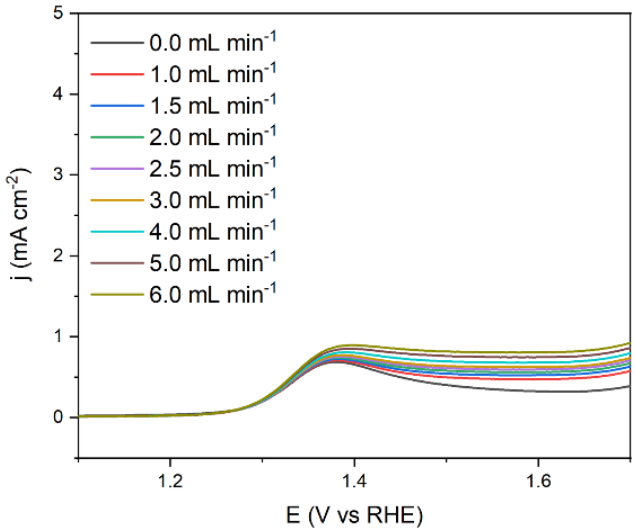

Figure 3.17 Linear sweep voltammograms for the 3-Lc in 1 M KOH + 10 mM Fe(II) electrolyte and 10 mV s^{-1} scan rate.

Figure 3.18 shows the linear sweeps for the 4-Lc cell. The curve at 0.0 mL min^{-1} shows the result for the purely diffusion-limited case. As the flow rate increases, the current

increases and reaches a limiting plateau region. The limiting current further increased as a function of the flow rate. This suggests that the flow over the working electrode is very efficient and the degree of internal mixing is low.

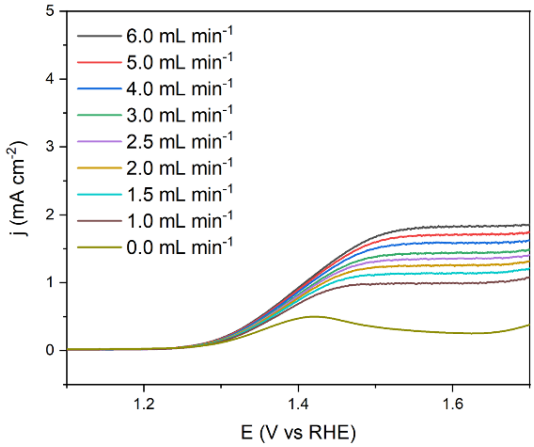

Figure 3.18 Linear sweep voltammograms for the 4-Lc in 1 M KOH + 10 mM Fe(II) electrolyte and 10 mV s^{-1} scan rate.

Figure 3.19 shows the relationship between the reciprocal current density and the reciprocal flow rate of the limiting current density at 1.5 V. To adhere to a channel type geometry[130], the relationship should be linear, and the y-intercept should be at 0 as per Eq 3.3. Of the cells, 2-Vc and 4-Lc show intercepts close to 0 and linear slopes. The 3-Lc and the 1-Vc with their lower flow speeds on the other hand, show poor linearity in the slopes and y-intercepts significantly deviating from 0, which indicates that the hydrodynamics do not adhere to a Levich relationship, possibly because the flow rate over the working electrodes are not high enough to develop a convection limited condition. That does not mean that the design of the original FT-SFC is flawed, since the channel diameters and the gasket thickness was significantly scaled up in the design presented in this chapter.

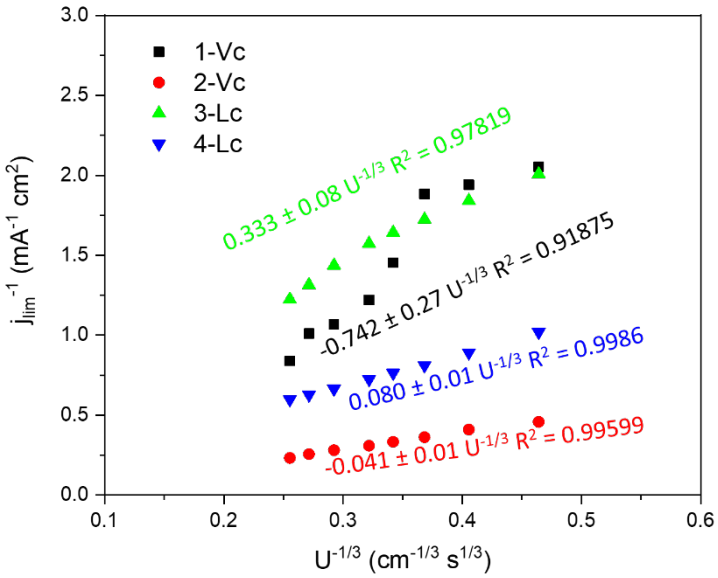

Figure 3.19 Koutecky-Levich relationship for the four flow cells at 1.5 V vs RHE, solved for Eq 3.3.

The flow cells 3-Lc and 4-Lc utilise microporous membranes on the top side walls to allow electrolyte diffusion between the flow compartment and the counter electrode cell compartment. This may however allow dissolution products or other impurities to be introduced in the flow compartment which may interfere with the electrochemically active surface of the working electrode or introduce interferences or false signals in the ICP-OES. To test for ion transmission in the 4-Lc, the counter electrode compartment was filled with a solution of 10 mM potassium hexacyanidoferrate(II) in 1 M KOH, while a 1 M KOH solution free of Fe(II) was flowed through the flow compartment. Figure 3.20 displays display the results. In test (A), the flow is completely arrested after flowing the 1 M KOH solution at 3 mL min^{-1} for 5 minutes. The moment the flow was arrested, 100 cyclic voltammograms were taken at 100 mV s^{-1}. In test (B) the flow has been completely arrested for 30 minutes before a flow of 0.5 mL min^{-1} is applied. 100 cyclic voltammograms at 100 mV s^{-1} was again commenced the moment the flow was applied.

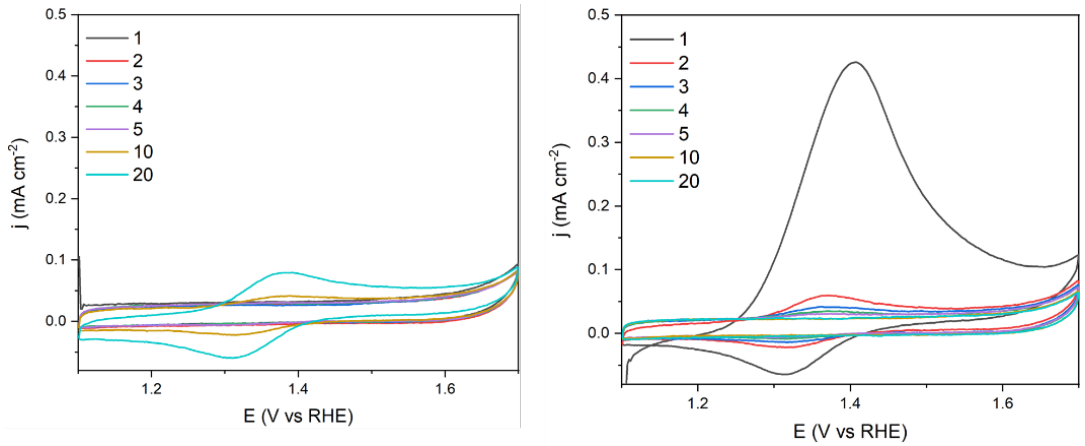

Figure 3.20 Cyclic voltammograms at 100 mV s^{-1} with 1 M KOH in the flow compartment and 10 mM Fe(II) + 1 M KOH in the counter electrode compartment after flow arrest following a rinsing period of 3 mL min^{-1} applied flow (left) and flow initiation at 0.5 mL min^{-1} after 1200 s in stagnant condition (right).

In test (A), only the background current from the platinum working electrode is visible on the first few cycles. Fe(II) oxidation is visible upon the 10^{th} cycle, and the current magnitude increases upon the subsequent cycles. The time for the first oxidation or reduction to be electrochemically visible was 120 s, which is within the timeframe of cyclic voltammogram s or galvanostatic experiments that could reasonably be planned with the ICP-OES. Test (A) has shown that the membrane is indeed permeable for transition metal ions and that could interfere with experiments.

In test (B), the current magnitude of the iron redox couple is decreased the moment 0.5 mL min^{-1} flow is applied. After 10 cycles, the current from the redox couple is completely vanished from the electrochemical signal, which corresponds to 120 s. Hence, test (B) proves that even moderately small flows are sufficient to keep the electrolyte solution in the flow compartment pure. Since the 4-Lc utilises carbon cloth as the counter electrode, the concentration of leeched impurities in the counter electrode compartment should remain low. On the other hand, tests (A) and (B) proves that the electrolyte composition in the counter electrode compartment and the flow compartment should be identical to avoid crossover artefacts, for example, the same electrolyte species and concentration should be used in both compartments.

3.5.4 Internal resistance

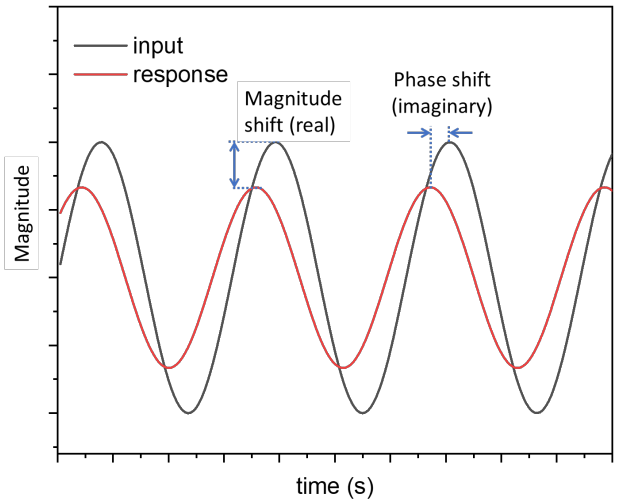

Figure 3.21 Illustration of phase and magnitude shift when sinusoidal perturbation is imposed on an electrochemical system.

The resistance of the electrodes was tested by galvanostatic electrochemical impedance spectroscopy (GEIS)[111]. In this technique, a sinusoidal current is imposed on between the working and counter electrode, while the potential response is measured between the working and reference electrode. The potential response is manifested in either a change in magnitude (real impedance) or in phase shift of the sinusoid wave (imaginary impedance).

When the impedance is measured as a function of frequency of the imposed sinusoid wave, the impedance changes depending on the physical processes that impedes the response at that given frequency. The result is often plotted in a Nyquist plot, with real impedance on the x-axis and the imaginary impedance on the y-axis.

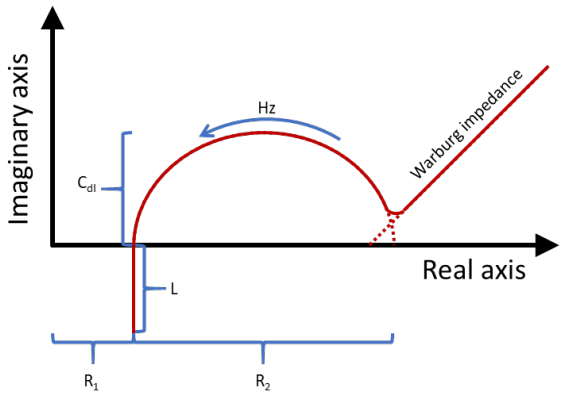

Figure 3.22 Example of a Nyquist plot representation for a 1-electron transfer.

In most electrochemical systems, the typical impedance result looks like the illustration in Figure 3.22. As the frequency of the imposed sinusoidal perturbation is decreased, the datapoints usually shifts positive in the real axis. The processes are represented by analogue circuit elements, for example by Randles circuit in Figure 3.23, with the addition of an inductor L_1.

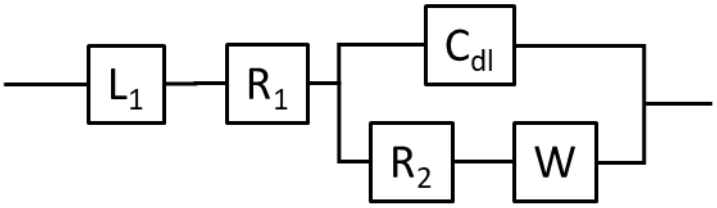

Figure 3.23 Randle's equivalent circuit for a reversible 1-electron transfer. L_1 is added to represent electrode contact and lead wire inductance.

A mathematical treatment of GEIS interpretation is out of scope for this investigation. The point is that R_1 represent contact resistances in wiring and resistance in the electrolyte, which will cause either the potentiostat to reach the potential compliance limit between the working and counter electrode for small currents, or the measured potential between the working and reference electrode to be skewed. The intersection of the Nyquist plot with the x-axis corresponds to R_1, therefore GEIS can be used to find the value of R_1. In the case of R_1 between working and reference electrode, it can be compensated for by software or by using a NID device presented earlier in the chapter. In the case of high R_1 between working and counter electrode, measures can be taken to reduce this value.

Table 3.7 presents the obtained R_1 values for the cells in this investigation both between the working and counter electrode, and between working and reference electrode. For the 1-Vc and 2-Vc, the resistance between working and counter electrode is between 10^1-10^2 Ohm in 0.1 M KOH, and for the 3-Lc and 4-Lc 10^3 Ohm. This decreases by at one order of magnitude when the ionic strength is increased by one order of magnitude. Increasing the ionic strength is hence necessary for experiments where high current densities are expected.

Table 3.7 R_1 values for the four flow cells derived from GEIS in 0.1 M KOH and 1 M KOH argon saturated electrolyte. Frequency range: 10^5-10^{-1} Hz, 0.1 mA current perturbation at open circuit of a platinum working electrode.

	0.1 M KOH (Ohm)		1 M KOH (Ohm)	
Cell	W.E.-C.E.	W.E.-R.E.	W.E.-C.E.	W.E.-R.E.
1-Vc	234	59	36	13
2-Vc	1037	8.5	258	16
3-Lc	1343	2.4	142	2.1
4-Lc	3520	3.5	1371	0.025

The resistance between the working electrode and reference electrode is low in all cases except for the 1-Vc, which could be due to the positioning of the reference electrode in that particular cell. The potential reading should therefore be an accurate representation in the 2-Vc cell, 3-Lc and 4-Lc. However, the low resistance between the working and reference electrode causes instability issues in the potentiostat. As the strategies outlined in Section 3.5.1 resolves these issues, no further modification is needed.

3.5.5 Limitations of SLA fabrication

With the four cells characterised by their hydrodynamic and electrochemical response, some words will be said about the findings from utilising SLA-based 3D-printing techniques for flow cell manufacture.

By 3D-printing, designs that would be impossible to make even by professional workshop machinists are now available for production within 24 hours from the moment of idea conception. However, the 3D printing techniques have their own limitations which are technique and machine dependent, and Formlabs include a guide which outlines minimum scales for some shape features that may limit the scope of use for certain flow cells[131].

The minimum hole diameter should not be modelled smaller than 0.5 mm. Even larger holes were found to be printed clogged if longer than a few centimetres or if it contained right angles, and this was a particular challenge for the 3-Lc and the 4-Lc which has many intricate channels. In some cases, it was found better to drill out holes with a PCB drill bit which can be as narrow as 0.1 mm. The minimum groove or embossed feature should be 0.4 mm. This imposes a limitation to for example O-ring grooves, slots or channels.

The minimum supported wall thickness should not be less than 0.4 mm. The O-ring that separates the counter electrode compartment from the flow compartments in the 3-Lc and 4-Lc required significant thicker walls to both print properly and remain intact when pressure is added. It was further found that mating surfaces between different components would not print accurately. At small tolerances, this error was found to be difficult to predict. The solution was to print mating surfaces slightly oversized and polish them down to a snug fit by 8000 grit sand paper and 1 μm polishing compound. SLA 3D-printed parts had to be washed rigorously with isopropanol and detergent after printing to avoid leftover residue polymerise and clog channels or deform other features.

Threads as small as M4 (4 mm between threads) were printed successfully by adding 0.4-0.6 mm tolerance to the holes, due to components slightly shrinking post printing. Manual threading with tools was also attempted by tapping pre-modelled holes, but would leave the threads fragile and rendering the threads unusable after replacing fittings 2-3 times. The ‘’Clear’’ resin by Formlabs produced translucent objects, but after polishing with 1 μm alumina polishing compound they were found to be transparent, so channels and compartments could be inspected for bubble generation and entrapment.

The final design of the flow cell is a compromise of desired channel and wall thicknesses and printing limitations, however due to the rapid prototyping workflow that the SLA 3D-printing technique enabled, print inaccuracies could quickly be rectified by modifying design features.

3.6 Conclusion and Summary

3.6.1 Conclusion

3D-printing is a viable technique for rapid manufacture of electrochemical flow cells, producing well-defined hydrodynamics. When connected to a potentiostat, artificial resistance and modifications to potentiostat settings may be added to achieve stable operation. Using a thin, microporous separator to separate electrodes may be a viable strategy to reduce cell resistance, but continuous flow must be applied to avoid cross-contamination of ions dissolved in the electrolyte. Scanning droplet cells enable higher experiment throughput, but additional precautions must be taken to fully shield the electrolyte from oxygen gas around the sealing O-ring.

3.6.2 Summary

By rapid 3D-printing manufacturing, four electrochemical flow cells for use with on-line ICP-OES dissolution analysis were designed, fabricated and characterised electrochemically and hydrodynamically. Two of the cells were completely novel, with design optimised for high dissolution signal capability by maximising electrode are and minimising flow compartment volume, and high throughput capability by adopting scanning droplet cell design elements. The scanning droplet cell design was further improved by adapting the AESEC design by installing a microporous separator between working and counter electrode compartments. Artificial solution resistance had to be added to the potentiostat circuit, as well as increasing bandwidth and current range in order to remove current oscillations due to potentiostat instability. The hydrodynamics depended significantly on cell geometry, where small flow compartments are excellent for dissolution product removal but may introduce turbulence above flow rates of 2 mL min^{-1}. Informed design lead to optimal positioning of electrodes to minimise resistance between them for high current capability and minimal introduction of iR drop.

4 On-line ICP-OES Configuration and Verification

4.1 Introduction

The work in this chapter was done in collaboration with Dr. Violeta Gonzales-Perez, who authored a code to automate the timestamp alignment of the potentiostat and ICP-OES.

This chapter will elaborate on the coupling and signal verification of the flow cells from Chapter 3 with an inductively coupled plasma optical emission spectroscopy (ICP-OES) instrument. Before discussing the on-line setup, it is first necessary to understand how the ICP-OES operates. Following this, results and discussion will be presented on modifications to make the ICP-OES operate with increased stability for the flow cell electrolyte. There will also be a section which elaborates on the maintenance procedures for the ICP-OES and flow cell in order to maintain accuracy of results.

Hence the aim of this chapter is to illustrate and document the process of creating a spectroelectrochemical on-line flow cell ICP-OES setup. The setup must be compatible with 1 M KOH electrolyte and possess detection limits comparable to other systems in literature (less than 1.0 ng s^{-1} cm^{-2})[93] for real time elemental analysis of electrolyte content.

The objectives of the chapter will be to understand the working principle of the ICP-OES, modify or exchange parts as necessary, couple the flow cell downstream to the ICP-OES, process and combine the electrochemical and spectroscopic data by calibration standards. A maintenance procedure to minimise impurities and avoid instabilities will be presented.

4.2 ICP-OES Principle of Operation

In this section, the principles of the inductively coupled plasma optical emission spectrometer (ICP-OES) will be explained. The information presented in this chapter will later be applied to adapt the ICP-OES to be compatible with flow cell electrolyte contents.

4.2.1 Overview and purpose of the ICP-OES

An ICP-OES is an elemental analyser with sub-parts per million concentration detection limits of elements dissolved in a liquid, referred to as a "matrix"[132]. This instrument consists of two main parts, the sample introduction system (ICP), and the sample measurement system (OES). The introduction system accepts liquid samples only, in which the analyte is fully dissolved. Briefly described, the instrument heats up the sample to a plasma in a confined space, such that the molecules in the sample is broken down to individual atoms and ions. A large energy influx from an induction coil causes the elements in the sample to heat up to 6000-9000 K and emit radiation corresponding to the atomic emission line wavelengths, which are characteristic to each element. By placing an optical sensor in the path of the emitted radiation, the elements in the sample can be determined from the emission wavelength, and the concentration of the elements in question can be determined from the signal intensity.

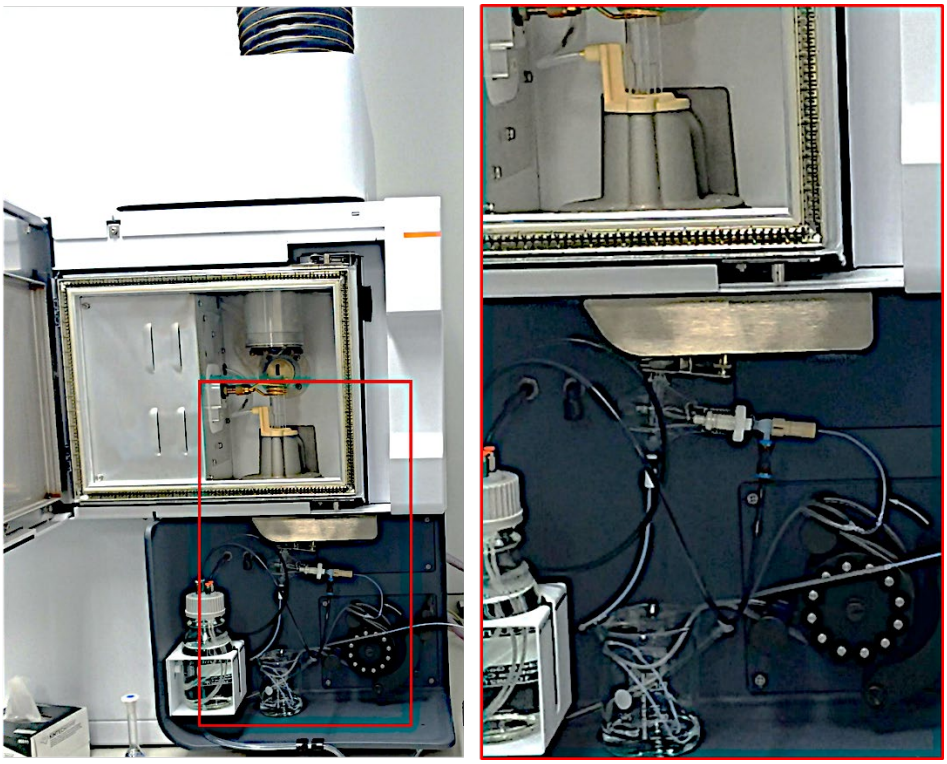

Figure 4.1 Agilent 5100 ICP-OES system

4.2.2 Introduction system

This section will elaborate on the role of the individual components for the ICP introduction system.

4.2.2.1 Nebuliser

The nebuliser is one of the critical components for the sample introduction system, as it converts the liquid sample into a fine aerosol mist. This is necessary, as heating an atomised sample to plasma is much more efficient than bulk liquid. A small droplet size and small droplet size distribution in the aerosol is important for a stable signal measurement[132].

The most common nebuliser is the concentric nebuliser which operates on Bernoulli's principle. High gas flow through an outer tube causes underpressure at the tip of a smaller tube which carries liquid, situated within a larger tube which carries the gas. The inner tube has a very fine nozzle tip, and the turbulence from the mixing of the water and flowing gas causes the liquid to rupture into an aerosol. Figure 4.2 depicts a

schematic of a concentric nebuliser. The diameters of the two tubes, the flow rate of the carrier gas and the physical properties of the liquid matrix determines the droplet size and size distribution. Although these nebulisers are preferred for general use due to their versatility and ease of use, they have certain limitations. Small precipitates could build up in the thin inner tube over time, causing a blockage of the sample introduction line. If the matrix contains a high degree of total dissolved solids (TDS), precipitates can form at the dry nozzle tip from salts in the matrix, also causing a blockage which will terminate the measurement. The diameters of the tube nozzles can be increased to reduce the chance of blockages happening.

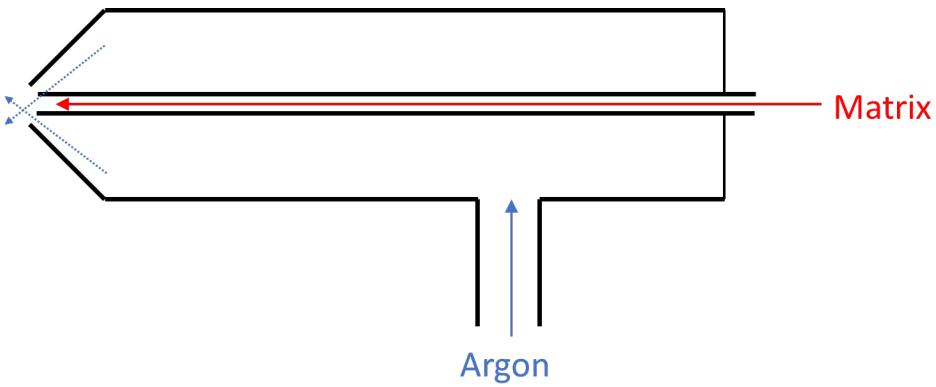

Figure 4.2 Cross-section schematic of a concentric nebuliser.

Another type of commercially available nebuliser is the flow blurring nebuliser[133]. It promises more consistent atomisation of tough samples (samples with high total dissolved solids). As opposed to the concentric nebulisers, the flow blurring nebuliser utilises pneumatic atomisation. Liquid is introduced into the gas stream by pressure, which causes a turbulent mixing of the gas and liquid phase which results in small droplets.

To reduce the risk of dissolved salts in the matrix precipitating and forming nozzle blockages, the argon gas supplied to the nebuliser can be humidified by passing it through a solution of ultrapure water prior to entering the nebuliser[134]. The thought is that a H_2O saturated gas slows down the drying effect of replenishing gas over the ICP components. Some commercial solutions have the argon gas humidified by passing through submerged tubes of hydrophilic material, and the moisture is absorbed by the gas from the internals of the wetted tubes. This is safer for operation as opposed to

bubbling the argon gas, as droplets from the water reservoir are not accidentally collected by this method, and risk of spillage is minimised.

4.2.2.2 Spray chamber

Once the sample has been atomised, it enters and is contained in the spray chamber, which is the last step before being introduced to the torch. The spray chamber not only contains the mist, but it also ensures that excessively large droplets are filtered out.

The most common spray chamber type is the cyclonic spray chamber, where the mist is forced into a vortex pattern that is collected by the torch inlet port at the top of the chamber. Spray chambers are made in "single pass" or "double pass" configurations[132]. The extra pass ensures that droplets excessively deviating in size are hindered from being collected by the torch carrier gas flow. This causes signal stability to increase, which is beneficial when low deviation of emission signal is desired, but on the other hand leads to an overall loss in the amount of sample reaching the torch, which lowers the sensitivity. A schematic of single pass and double pass cyclonic spray chambers are depicted in Figure 4.3.

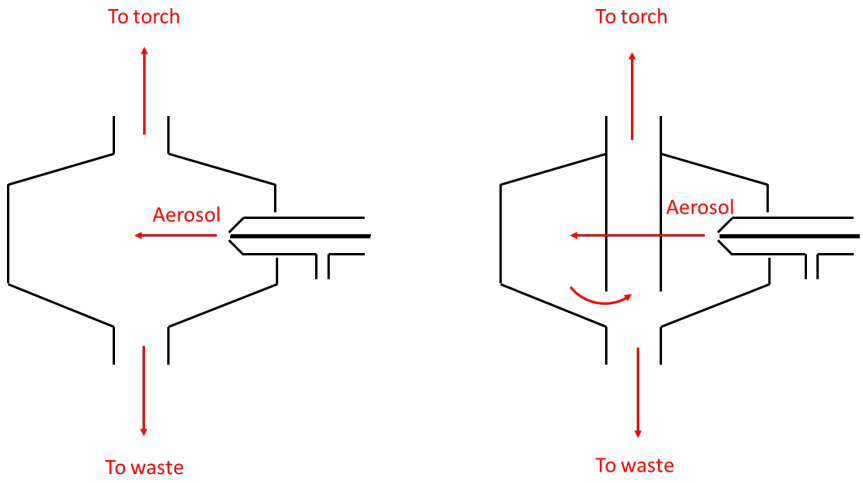

Figure 4.3 Cross section schematic of a single pass (left) and double pass (right) spray chamber.

Other types of spray chambers are available for strongly nucleophilic solutions like hydrofluoric acid digests, where glass components would otherwise wear out. Spray chambers for organic matrices are also common, with a temperature control to keep the mist below their flash points[135].

Uncollected aerosol mist is removed from the spray chamber through a port at the bottom of the spray chamber leading to waste collection. Typically, 70% of the sample introduced to the spray chamber is directly routed to the waste from the spray chamber. It must also be noted from a practical perspective, that if the waste extraction system is not removing liquid at a sufficient rate, the excessive amount of liquid may be introduced to the torch and cause the plasma to extinguish due to flooding.

In conclusion the spray chamber is the last filter between the sample introduction system and the plasma torch. Its role is to filter out deviating droplets from the sample aerosol mist and ensure that the aerosol that is introduced into the torch is as homogeneous as possible.

4.2.2.3 Plasma Torch Assembly

This section discusses the component and process that generates, contains and maintains the plasma.

4.2.2.4 Torch

The torch component consists of a concentric outer wall surrounding an inner capillary tube, similar in principle to the concentric nebuliser[132]. Gas flow across the outer tube generates a pressure differential at the opening of the inner capillary, which is connected to the outlet of the spray chamber, as depicted in Figure 4.4. Given a constant and even concentric gas flow, sample aerosol is extracted from the spray chamber at a constant rate. The amount and containment of the mist being taken up depends on the outer tube gas flow, the bore of the inner capillary of the torch, and the physical properties of the sample aerosol.

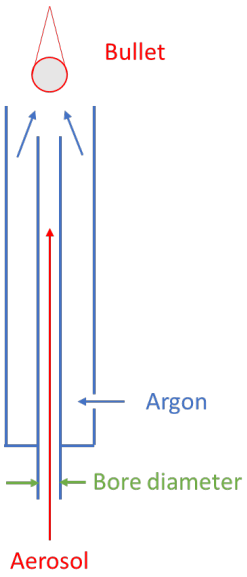

Figure 4.4 Cross-section schematic of an ICP-OES Torch.

4.2.2.5 Radio Frequency Coil

To successfully convert aerosol to plasma, an ignition spark is briefly applied across the gas-aerosol mixture which provides the initial ionisation of the molecules in the aerosol. After that, a high-power radio frequency (RF) coil surrounding the outer wall of the torch supplies electromagnetic energy to the aerosol by induction to maintain the ignited plasma at a constant temperature[132]. The plasma phase is contained to a location directly above the inner capillary outlet and is referred to as a "bullet" due to its shape.

Elements that have higher first and second ionisation energies also require more power from the radio frequency coil to excite in sufficient amounts to be detected. These are classified as "hard" and "soft" elements, and therefore the power for the radio frequency coil should be set in consideration for the known elements in the sample[132]. Figure 4.5 provides an overview of elements and their first and second ionisation energies. Chromium for example, require less energy compared to an element like Zn. When a sample consist of both hard and soft elements, the supplied energy should be in between the requirement of both elements.

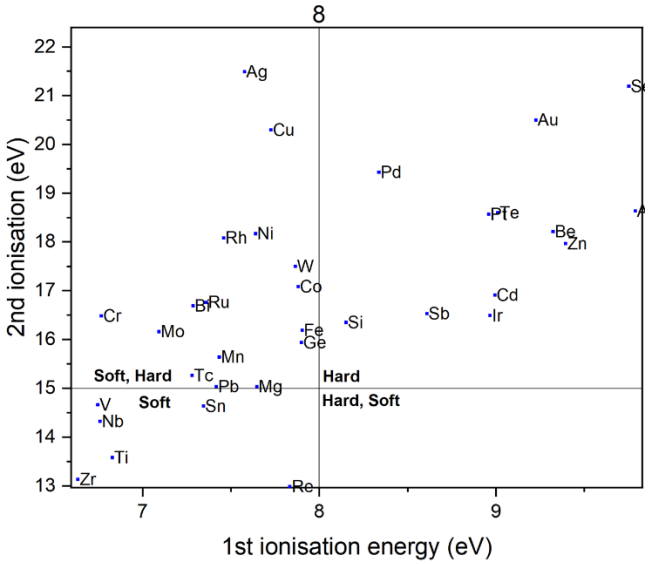

Figure 4.5 First and second atomisation energies for selected elements.

Applying too much power to the torch can lead to rapid damage by deformation of the glass component of the torch. For hard element samples in high total dissolved solids matrices where a high power is required to excite the sample in sufficient amounts, the gas flow of the outer tube must therefore be increased to maintain a sufficient cooling rate of the glass component of the torch. On the other hand, samples containing easily ionisable elements (EIE) only in the matrix require very little power before higher order excitations become significant and cause increased background signal. For these types of samples, it is important to supply the radio frequency coil low power without extinguishing the plasma.

Lastly the rate of sample being introduced to the torch must also be considered for the rate of power required to maintain a plasma bullet. In cases where an unusually high rate of sample is delivered to the torch, the power to the radio frequency coil must naturally be increased in order to sufficiently convert the sample aerosol into plasma.

4.2.2.6 Other components

This section provides an overview of miscellaneous components that were found to be important during testing and troubleshooting of the ICP-OES.

4.2.2.7 Peristaltic Pump

The sample matrix is usually transported from the original container the nebuliser by a peristaltic pump. During operation the suction power of the nebuliser far exceeds the required driving force to inject the sample at a reasonable rate for the torch, and therefore the main purpose of the peristaltic pump is to regulate the mass uptake to a constant rate. No adjustments should therefore be made to the peristaltic pump tubing once the ICP torch is ignited, since any exposed paths between the peristaltic pump and the nebuliser would cause excess air or liquid to be taken by the nebuliser and cause an overload of atmospheric gas in the ICP chamber, which would cause an automated shut down of the ICP-OES instrument. ICP-OES instruments are commonly supplied with a multichannel peristaltic pump, with at least one channel reserved for the inlet flow and one channel to extract surplus sample liquid from the spray chamber. Since the rotation rate of the peristaltic pump is fixed across all channels, the flow rate is instead adjusted by choosing different tube diameters supplied from the manufacturer. For example, the outflow channel from the spray chamber has a larger internal diameter compared to the inlet tubing to ensure that the spray chamber never floods over. Additional channels can also be utilised for sample introduction. Internal standards (IS)[132] can for example be mixed in to the sample matrix downstream from the peristaltic pump by a y-connector such that signal intensity later can be corrected for drift or background noise. Here the relative ratio of sample to internal standard can be set by choosing the appropriate peristaltic pump tubing diameters, since the peristaltic pump will ensure that consistent mass flow is delivered.

4.2.3 Optics

In this section the sensory part of the inductively coupled plasma optical emission spectrometer will be presented.

4.2.3.1 Viewing configuration

The intensity of the emission spectra observed from the bullet depends on the viewing orientation of the sensor, presented in Figure 4.6. The bullet can be observed from the side, which is called the radial configuration. For radial mode, one must be careful to

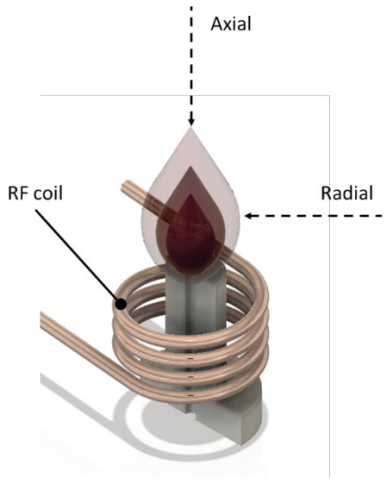

Figure 4.6 Representation of the two viewing configurations (axial and radial) onto the plasma bullet.

optimise the point on the bullet of which a spectrum is taken, as there will be a temperature gradient and hence a change in emission intensity of the sample.

The bullet can also be observed in a top-down orientation, which is the axial configuration. Since the axial configuration observes the whole bullet from above, no optimisation of viewing position is necessary. Since the bullet is elongated in the viewing axis of the axial view, the path length for this mode is longer compared to radial view, and a better detection limit is achieved. However, in the axial view orientation there is an increased risk of interferences and noise.

4.2.3.2 Pre-optics window

Between the bullet and the sensory device there are pre-optics windows which protects the electronics from the plasma heat. In the axial configuration, it also physically shields the sensory device from overshooting aerosol.

4.2.3.3 CCD detector

The emission spectra from the sample can be observed either with a monochromatic sensor, which observes a very fine wavelength range, or a polychromatic sensor which can observe several wavelength ranges at once. The Agilent ICP-OES 5100 is installed with charge coupled device (CCD) sensors, which consist of an array of sensors referred to as pixels on a. Each pixel can be dedicated for observation at a fine wavelength range simultaneously. It is therefore a convenient tool to perform multielement analysis of samples or observe several emission wavelengths of the same element in order to increase the linear range of emission intensity.

4.2.3.4 Acquisition

The acquisition time can be varied to optimise the signal-to-noise ratio. Measurements can also be repeated to increase the quality of the spectra. For routine off-line analysis, the recommended settings for the Agilent ICP-OES 5100 is 3 measurements of 30 seconds each. However, for on-line transient analysis, reasonable time resolution is desirable in order to correlate features from a transient event like a cyclic voltammogram. Therefore a 10 second acquisition time for a cyclic voltammogram with a 1 mV s^{-1} sweep rate would yield more accurate signal, but with a potential resolution of 10 mV, which would be too low to reasonably observe and correlate finer features of the electrochemical and elemental dissolution signals. The Agilent 5100 ICP-OES lowest acquisition interval is 1 s, and this was used for all measurements throughout this project.

4.2.3.5 Elemental Standards

To correlate intensity outputs from the ICP-OES to sample concentration, it is necessary to use calibration standards to measure the intensity of a sample with a known concentration of element in in an identical matrix[136]. A calibration standard series must be made in the expected concentration range of the sample, to ensure that the concentration to intensity ratio is linear throughout the measured intensity range.

Chemical compatibility to the matrix also influences what kind of standards can be used. Most standards found commercially available come in a 5 wt% nitric acid matrix. Depending on the element there may be additional ligands in the elemental standard solution to increase solubility. Using samples with other matrices can then be

challenging due to solubility limits and cause precipitation, which would lead to inaccurate calibrations. One can circumvent this problem by adding complexing agents to stabilise the dissolved species[132].

Figure 4.7 10 mmol complexing agents for 10 ppm multielement standard in 0.1 M KOH from left: no complexing agent, Na_2SO_3, K_3EDTA, $Na_2S_2O_3$, glycine, Na_4EDTA.

For routine off-line analysis it is common to use multielement standards, which usually contains a variety of common elements by the discretion of the supplier. However, these elements do not address issues related to emission line interferences, which cannot be excluded, and the chemical incompatibility of only one element in an exotic matrix would render the entire calibration standard useless. Figure 4.7 shows a multielement standard (Alfa Aesar) in 0.1 M KOH. The insolubility of one or more of the elements have caused precipitation. Trials with 10 mmol of either Na_2SO_3, K_3EDTA, $Na_2S_2O_3$, glycine or Na_4EDTA complexing agents did not solve the insolubility issue. For these cases it is better to use single element standards instead. The advantage of this approach is that the chemical incompatibility of one element will not affect the measured precision of the other elements, and one can effortlessly see if the concentration increase of one element would cause emission interferences at the observed wavelength of another element in the matrix.

A calibration plot with the known concentration on the x-axis and the raw signal returned from the ICP-OES should yield a linear trendline by regression fitting as per Eq. 4.2

$$I = slope \times C + c \qquad \text{Eq. 4.1}$$

Where I is the measured intensity, "slope" is the counts of the raw signal per unit concentration, C the concentration of the calibration standards in ppm, and c the y-intercept. Figure 4.8 shows the calibration curve for a zinc single element standard in 1 M KOH.

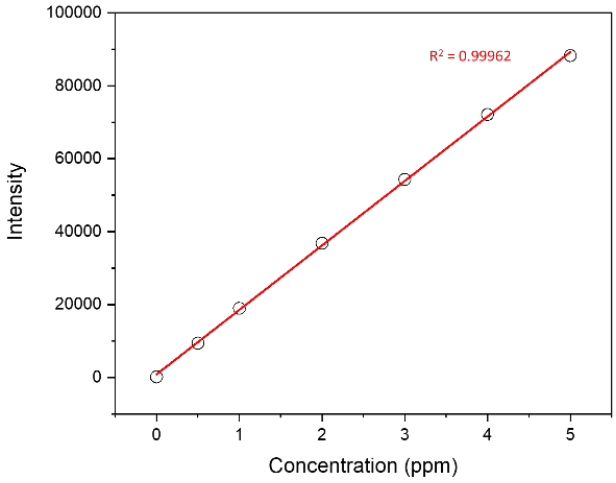

Figure 4.8 Calibration curve of observed (Zn) wavelength 213.857 nm in a 1M KOH matrix and 1 mL min^{-1} flow rate.

From the calibration standards limit of blank (LoB), limit of detection (LoD) and limit of quantification (LOQ) can be estimated. There are no universally agreed way to calculate these values, and the most appropriate method to calculate these would depend on the type of instrument and type of measurement[132,136–142]. For calculations in this work, the following definitions have been used:

Limit of blank: The standard deviation of 10 blank measurements of the observed wavelength as per Eq. 4.2:

$$LoB = SD \times 1.3 \qquad \text{Eq. 4.2}$$

Limit of detection: 3 times the limit of blank as per Eq. 4.3:

$$LoD = LoB \times 3 \qquad \text{Eq. 4.3}$$

Limit of quantification: 10 times the limit of blank as per Eq. 4.4:

$$LoQ = LoB \times 10 \qquad \text{Eq. 4.4}$$

These intensity signals are converted to concentration by dividing the number with the gradient of the calibration curve as per Eq. 4.5:

$$C = \frac{Intensity}{slope} \quad \text{Eq. 4.5}$$

For an applied case of the flow cell, further calculations can be done to convert the elemental signal into mass per second (Eq. 4.6), mol per second (Eq. 4.7) and an equivalent current (Eq. 4.8), given that the charge number z is known:

$$m_e = C \times f \quad \text{Eq. 4.6}$$

Where m_e is the dissolution rate in mg s^{-1} and f is the flow rate in kg s^{-1}.

$$N_e = \frac{C \times f}{M_r} \quad \text{Eq. 4.7}$$

Where N_e is the rate of atoms dissolved per seconds in mol s^{-1} and M_r is the atomic mass of a given element in the sample and given as mg mol^{-1}.

$$j_e = \frac{C \times f}{M_r} \times n \times F \quad \text{Eq. 4.8}$$

Where j_e is the equivalent dissolution current in mA, F is Faraday's constant 96485 C mol^{-1} and n is the number of electrons involved in the half-cell reaction of interest.

4.3 ICP Optimisation for High Total Dissolved Solids

This section will elaborate on the modifications made to the Agilent ICP-OES 5100 in order to be compatible with 1 M KOH, which is a high total dissolved solids matrix. The effect of 3 components will be demonstrated. The Agilent ICP-OES 5100 was supplied with a 1.8 mm bore torch, a SeaSpray concentric nebuliser and a double pass cyclonic spray chamber. Best practice for routine sample analysis in 1 M KOH matrix could not be readily found in scientific, technical literature or by technical enquiry to Agilent support staff. However, it was recommended to use similar settings as with brine water analysis. Since the nebuliser, spray chamber and torch were optimised for 5 wt% nitric acid matrices, modification was thought necessary to increase signal

stability and durability of the parts, since the components in a large degree consist of glass and should be exchanged with equivalent components made of alkaline solution resistant materials.

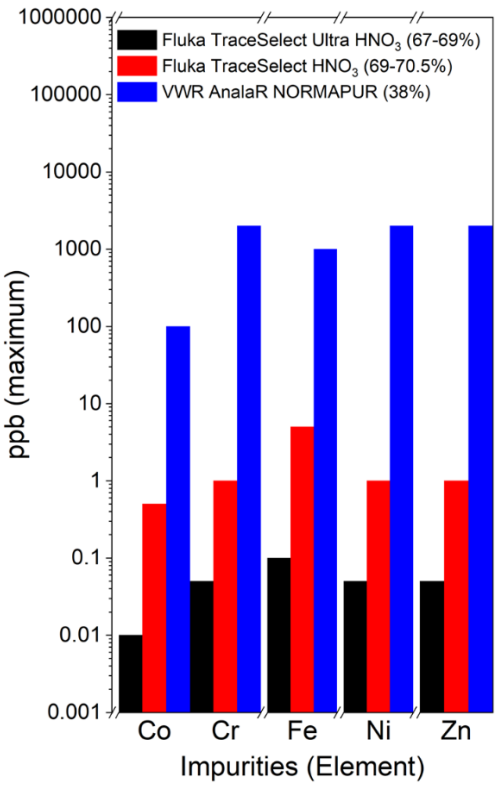

Figure 4.9 Selected manufacturer-specified impurity levels of three undiluted matrixes.

Another consideration the ICP-OES is the purity of the matrix. Figure 4.9 shows the relative concentration of impurities as stated by manufacturer in ultrapure HNO_3, high purity HNO_3 and the KOH solution used here. The impurities may give rise to interferences and increased noise during measurement. However, apart from an elevated background signal and possibly an increase in noise levels, the KOH matrix did not cause interference issues during measurements.

4.3.1 Nebuliser

The as-supplied nebuliser was a SeaSpray concentric type nebuliser suitable to provide better signal stability with high total dissolved solids samples, however, the glass walls may dissolve from KOH exposure[143]. A OneNeb2 flow-blurring nebuliser was procured, due to the potential of more stable operation signals and high chemical

compatibility with alkaline matrices as the main components consist of PEEK polymer or fluoropolymers.

Comparisons were made between the two nebulisers by running a zinc standard in 1M KOH matrix through the Agilent ICP-OES 5100. Noise in this test is defined as the magnitude of standard deviation in one minute of continuous measurement. Zinc was chosen, as zincate ions have high solubility in 1 M KOH[144]. However, the OneNeb2 nebuliser does not provide less noise than the SeaSpray nebuliser in this test, as seen in Table 4.1.

Table 4.1 Standard deviation of signal obtained from 1 ppm Zn in 1 M KOH for the SeaSpray and OneNeb2 nebuliser.

Nebuliser	Standard deviation (Intensity)
SeaSpray	129.033
OneNeb2	133.823

Although the SeaSpray nebuliser consists of glass, which is known to dissolve in alkaline solutions, the overall stability gain compared to the OneNeb2 nebuliser was considered to be significant due to the high back-pressure from flow-blurring nebulisers may misplace electrolyte in the flow cell. The SeaSpray nebuliser was hence chosen for all further work. No degradation of the SeaSpray nebuliser glass walls and orifice has since been observed with alkaline solutions.

4.3.2 Spray Chamber

As with the nebuliser, the spray chamber component supplied with the Agilent 5100 was a glass double pass cyclonic spray chamber. Such spray chambers provide excellent signal stability, because the collected aerosol droplet sizes are more homogeneous compared to single pass[132]. However, since the spray chamber was made of glass, there was concern over long term degradation of the component leading to weakening of the walls[143]. A single pass fluoropolymer spray chamber supplied by Agilent Technologies was acquired to replace it. Although the single pass spray chamber in theory could produce lower detection limits, no significant impact on the performance was seen and

the glass spray chamber originally supplied was used for the rest of this work without any observed damage.

4.3.3 Torch

As the torch component is exposed to the most heat, it was assumed to be the component under the most risk of damage from exposure of 1 M KOH, particularly because glass dissolution is accelerated by both increase in OH^- concentration and temperature[143]. The as-supplied torch was a 2.2 mm bore all-in-one component supplied from Agilent Technologies, and severe damage on the outer glass wall was made after just one experiment as shown in Figure 4.10.

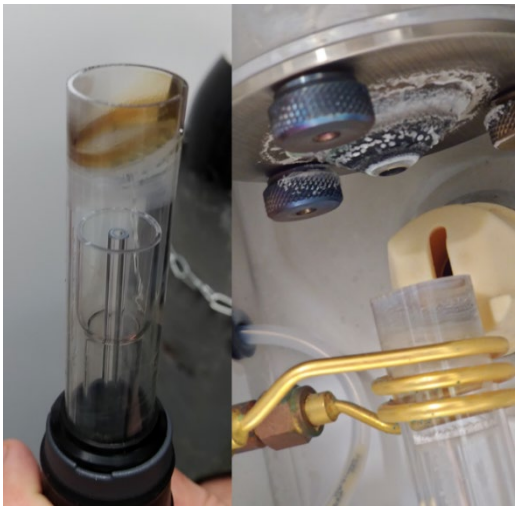

Figure 4.10 Damage on torch and precipitates on ICP-OES components after 5 hours of continuous operation with 1 M KOH matrix.

A ceramic torch with alumina walls was therefore tested. The main purpose of this product is to be compatible with hydrofluoric acid digests that dissolves glass at high rates.

Table 4.2 Standard deviation of signal obtained from 1 ppm Zn in 1 M KOH for the 1.8 mm, 2.2 mm and 2.4 mm diameter bore torches.

Torches and bore diameter (mm)	Standard deviation (Intensity)
Alumina 1.8	2633.94
Glass 2.2	132.64
Glass 2.4	255.11

As shown in Figure 4.11 and Table 4.2, trials with 1 M KOH 1 ppm zinc standards showed that not only was the signal noisier with the alumina torch, the signal was also fluctuating. Maintenance work on the ICP-OES was necessary as the protective glass disk separating the bullet from the axial optical sensors became coated with water-soluble crystals. Most likely some of the sample was not properly combusted in the plasma and was transported past the torch in its aerosol state.

A wide bore, demountable torch was acquired, as wider bore was recommended to better combust high total dissolved solids matrices. Although this torch has glass walls and bore, the outer glass walls were replaceable in case of damage. A test run with zinc standard solution displays stable signal. The calculated the standard deviation of the signal from a 1 ppm Zn standard in 1 M KOH shows that the standard deviation is somewhat higher in magnitude compared to the 2.2 mm bore standard torch, at a lower intensity. However, maintenance of the pre-optics glass window after this was unnecessary as no residue was found using the wide bore torch. The 2.4 mm wide bore torch was therefore used for all investigation.

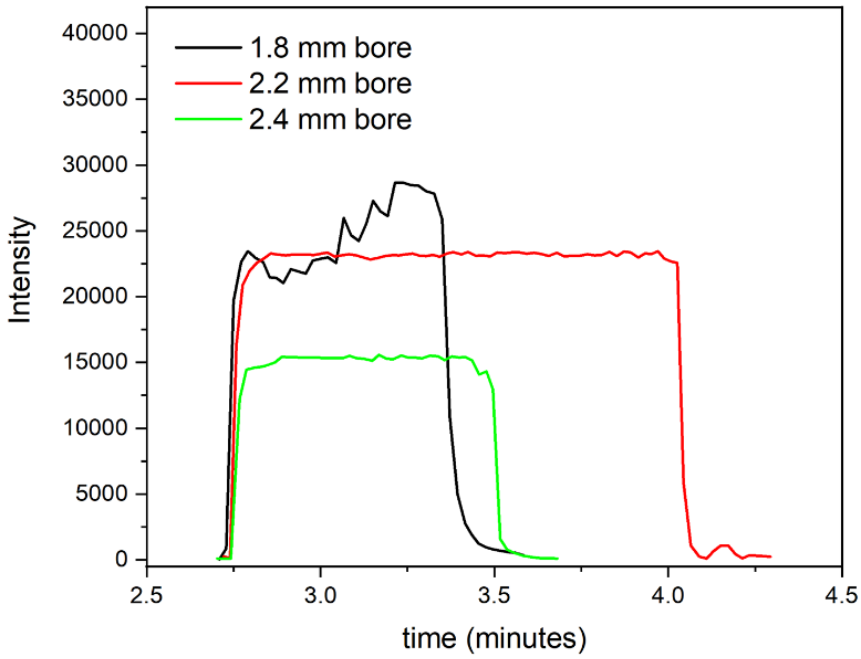

Figure 4.11 Intensity signals of 1 ppm Zn in 1 M KOH with torches of 1.8 mm, 2.2 mm and 2.4 mm bore. Double-pass cyclonic spray chamber, SeaSpray concentric nebuliser, 3 mL min^{-1} flow rate.

4.3.4 Other components

An argon humidifier was installed between the argon supply and the nebuliser, to prevent build-up of salt deposits from the matrix.

A 1:1 dilution of the 1 M KOH with ultrapure water was used, by adjoining a supply to ultrapure water by a Y-connector. The idea was that by lowering the total dissolved solids content by half, more stable operation would be achieved. However, it made no difference to the signal stability, apart from decreasing the sensitivity by half.

4.4 Maintenance Considerations

During prototype testing, some maintenance protocols were developed for the flow cell to operate optimally, remove precipitates and contaminant signals from the cell and retain stable operation of the ICP-OES[145]. Here the most common problems associated with operation and the solutions found described.

4.4.1 ICP-OES Maintenance

Pulsation or back-and-forth rocking of the matrix through the peristaltic pump tubing instead of a steady flow, even after mild tightening of the peristaltic pump clamps, suggested that the peristaltic pump tubing had been worn out from tear and wear. To check for tubing degradation, the peristaltic pump would be activated, and the tubing would then be gradually tightened by the peristaltic pump tubing fastener until an even flow was achieved. This method decreased long term tear of the peristaltic pump tubing and ensured steady flow.

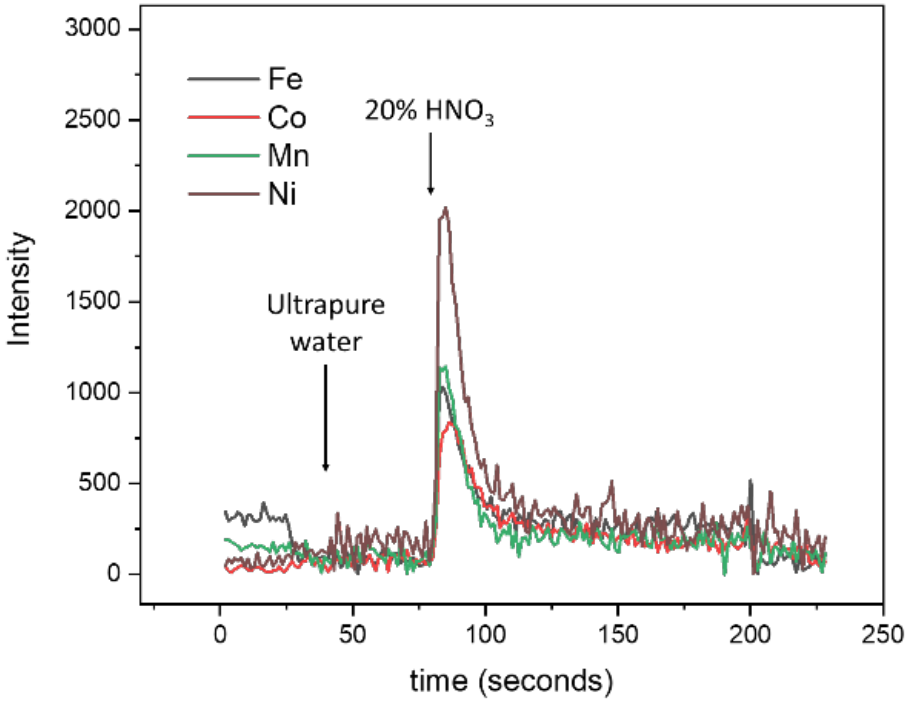

Figure 4.12 Chemical dissolution of deposits from tubing and ICP-OES component walls after switching from ultrapure water to 20% HNO_3 solution.

The plugging of the nebuliser could occur from deposits building up around the tip, especially for drop-casted powder samples, which would cause the flow of mass to the ICP-OES to completely stop. Under these scenarios the nebuliser tip would be blasted with nitrogen according to manufacturer instructions, to remove built up precipitates. To remove any contamination from routine measurements, nitric acid solutions would be fed to the ICP-OES. The spikes in transition metal signals concurrent with acid solution were indicating that precipitates were forming.

In cases of high amounts of dissolved transition metals, there is an increased chance of metals in the matrix depositing on the glass walls of the spray chamber and leaving a background signal in the emission spectra. To remove the residue, the spray chamber would be immersed in either a nitric acid solution or as according to manufacturer recommendations an alkaline glass cleaning solution (RBF-25).

The tip of the torch glass walls forms a crust of black residue and white precipitate after use. To remove the residue from the outer glass walls it was suggested to either heat the outer glass wall of the torch with a blow torch, or to leave it in a furnace at 600 ^{o}C to remove carbon residue. This however would either prove to be ineffective or distort the shape of the glass wall. To fully remove the crust, the tip of the torch was rather immersed in an aqua regia solution overnight, which proved to be effective. Otherwise the torch tip would be left in a solution of RBF-25 when not under operation.

In cases where the pre-optics glass would be covered in residue, it was removed and wiped with a wet lint free paper towel until visibly clean.

With the 1 M KOH matrix the pre-optics cooling cone, a nickel plate, would end up covered in a crust white residue after each day of operation. To make sure the surface remained clean and did not obstruct the path of the perpendicular argon stream surrounding the bullet, the pre-optics cone would be demounted and scrubbed under ultrapure water to retain a pristine surface.

4.4.2 Flow Cell Maintenance

The following procedures were adopted in order to remove contaminants from the cell that would cause background signal in the emission measurements or replacement of parts damaged by tear and wear.

The membrane separating the working and the counter electrode compartment of the 3-Lc and 4-Lc cells would be replaced together with the O-rings every few weeks as the polymer would stretch out and to make sure contamination was not building up. New membranes were punched out by a 10 mm diameter punch-and-die tool.

On occasion, dissolution products would leave a permanent background signal in the emission spectra, in particular for high dissolution rate samples. For example, after many zinc or steel dissolution experiments, the background signal for the emission lines

for zinc, iron and chromium would remain elevated from the cell compared to the blank signal determined from calibration standards. It was thought that some of the dissolution products may have formed deposits on the cell walls, fitting ferrules or tubing. The cell was regularly disassembled and placed in an acid bath of 2-5% nitric acid for a few hours, before being thoroughly rinsed with ultrapure water. Care was taken to not leave the cell in the acid bath for too long, as it could damage the cured resin polymer.

On occasion the ferrules for the compression fittings would be damaged and cause leaks due to the strain from the tubing and would have to be replaced. Downstream of the working electrode, PTFE tape would sometimes be used as a replacement for Delrin ferrules with similar results. This was not though to affect the electrochemistry as since oxygen is not a concern once the matrix leaves the electrochemical cell. Parafilm was also found to work very effectively as ferrule material.

To ensure that the counter electrode compartment containment was minimised, it was replenished every experimental day with 1 M KOH. pH differences between the counter electrode compartment and the flow compartment could otherwise increase due to CO_2 absorption of alkaline solutions[146].

4.5 On-Line Assembly

This section will introduce the complete on-line ICP-OES set-up and expand on the methods developed to couple the data from the potentiostat and the ICP-OES, and finally assess the flow efficiency of the cells and determine the final parameters like flow rate.

4.5.1 Overview of the ICP assembly with gas line, reservoir, droplet, jack, ICP-OES.

The on-line ICP-OES set-up is presented in Figure 4.13 (A). It features a flow-through droplet cell with a sample stage, an electrolyte inlet port and an electrolyte outlet port. Following is a description of the design features of the line components, following the electrolyte path.

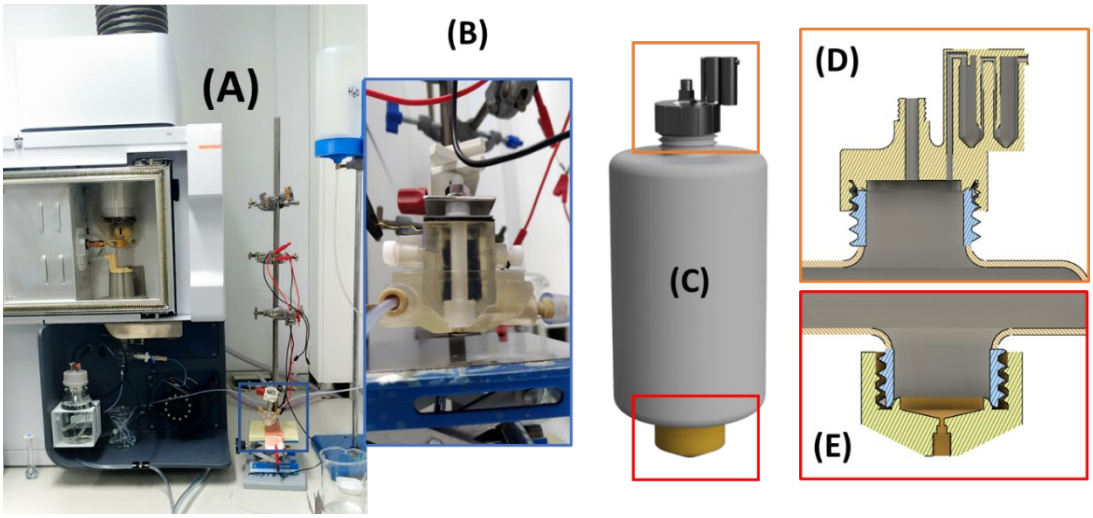

Figure 4.13 Finished ICP-OES assembly. From left: on-line flow cell assembly with the 2-Vc cel (A)l, the 4-Lc cell connected to the jacketed tubing (B), A render of the electrolyte reservoir (C), the inlet (D) and outlet (E) caps for the electrolyte reservoir.

4.5.1.1 Electrolyte reservoir and argon gas line

For the electrolyte reservoir, a container (E) suspended above the cell was chosen. As opposed to a container level with the cell, the elevated reservoir provides gravity feed to the cell, such that no pump or overpressure control is needed to maintain inlet flow. Another advantage is that since the electrolyte outlet can be placed at the bottom of the reservoir, the risk of bubbles entering the electrolyte tubing during sparging is greatly reduced. Since the electrolyte reservoir would be in contact with the cell walls over a long period, polypropylene was chosen as it has excellent chemical resistance to alkaline solutions, as seen in Chapter 3. Polypropylene bottles were sourced from Fisher and modified by Bay Plastics ltd for cutting and plastic welding. Bespoke lids for top and bottom openings were made by FDM 3D printing with ASA filament. The top lid contained an inlet for gas sparging through the central axis such that the lid could be rotated without removing the gas line. A double bubbler relief (D) was designed for it to minimise back pressure effects. The bottom lid (E) was designed with one outlet compatible with 1/4”-28 UNF threads to connect 1/8” tubing. The internal surfaces of the lid in contact with electrolyte were polished with sandpaper (grits 240-8000) and then coated with two-component epoxy glue to ensure that the lid was leak tight. Two such electrolyte containers were installed at approximately one meter above the flow

cell assembly. A three-way, two-opening switching valve connected the cell and the two electrolyte reservoirs, for instant switching between electrolytes. Between the three-way valve and the flow cell a high-impact polystyrene adjustable microvalve was placed to manually control the flow rate of the electrolyte upstream of the cell. Finally, the entire electrolyte tubing assembly was jacketed in 10 cm diameter PVC tubing. The outer walls of the electrolyte tubing could then be maintained by a constant flush of nitrogen gas to further minimise oxygen diffusion into the electrolyte while being transported into the flow cell. The PVC jacket tubing would terminate at the respective fitting ports of the tubing channels and provide a constant stream of nitrogen over the fittings.

4.6 Zinc pulsed experiments

To align the timestamps of the potentiostat and the ICP-OES instrument, a pulse protocol was devised. The aim is to ensure that the timestamps of the ICP-OES and the potentiostat can be aligned, and to align the elemental dissolution signal observed at the ICP-OES of the sample with the half-cell reaction taking place in the flow cell. As the Agilent 5100 ICP-OES has no communication interface, this had to be done manually post-experiment.

4.6.1 Time alignment – tube delay and internal clock

To align the timestamps of the potentiostat and the ICP-OES instrument, a pulse protocol was devised at one-minute intervals. Comparing the last point pre-dissolution pulse of sample element from the two datasets should yield a plot with a trendline of y = 1x, and a negative y-intercept corresponding in the delay of mass transport from the flow cell to the plasma torch. The magnitude of each step was also varied to test if the ICP-OES concentration calibration corresponded well to the anodic release of ions from the sample. For the last case it was important to choose a sample that only produced one half cell reaction during anodic pulses. Zinc was chosen, because in alkaline media above 1 M KOH concentration the half-cell reaction

$$Zn \rightarrow Zn(II) + 2e^-$$

Proceeds to form zincate $Zn(OH)_4^{2-}$ only[147]:

$$Zn + 4OH^- \rightarrow Zn(OH)_4^{2-} + 2e^-$$

Zincate is soluble up to 0.8 M in 1 M KOH. Assuming that the faradaic efficiency is 100%, the quantitatively converted ICP signal for wavelengths emitted from zinc should correspond to 2 mol of electrons per 1 mol of detected zinc.

The untreated data for a timestep test conducted with the 1-Vc cell is presented in Figure 4.14. There is an obvious time delay between the current steps observed by the ICP-OES and programmed by the potentiostat. The pulse maximum of the ICP-OES appears after significant rise time. The last pulse observed by the ICP-OES ends before it has commenced at the potentiostat. Hence, it seems that the ICP-OES observes time at a faster rate than the potentiostat and thus assigns wrong timestamps to the data points. To confirm this, a video was taken of a step experiment, which showed that the time between the video recording device and the potentiostat were in agreement.

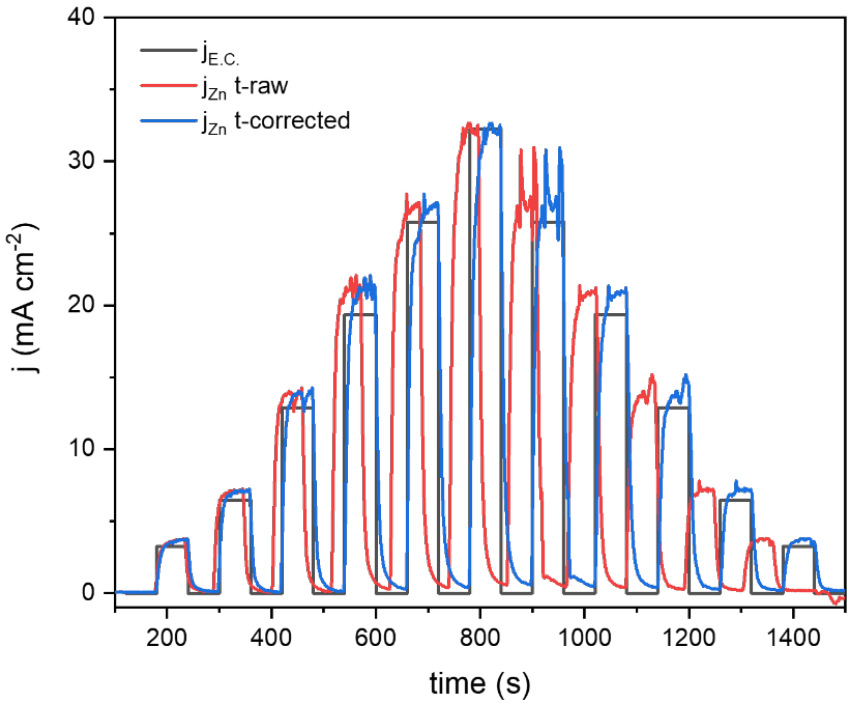

Figure 4.14 Dissolution signal as is (red) and corrected for time dilation (blue). Dissolution signals are converted to equivalent current j_{Zn} assuming a 2-electron transfer half-cell reaction.

To align the timestamps of the ICP-OES and the potentiostat, the time of the last datapoint before the steps was compared. Figure 4.15 and Table 4.3 shows the resulting relationship for flow rate 1.0, 2.0, and 3.0 mL min^{-1} for the 1-Vc flow cell. The intercept onto the ICP-OES time axis is proportional to the transport time of dissolution products from the working electrode surface to the ICP torch, and naturally decreases with increasing flow rate. But the slope value was found to not be constant day-by-day. Through troubleshooting it was ultimately found to depend on how many wavelengths were being recorded by the ICP-OES. Therefore, it was decided that a galvanostatic step protocol similar to Figure 4.14 be executed at the start of each experimental day, and to not change any ICP-OES settings within each day of operation. This protocol yielded reasonable correlations between electrochemical and ICP-OES data throughout the project.

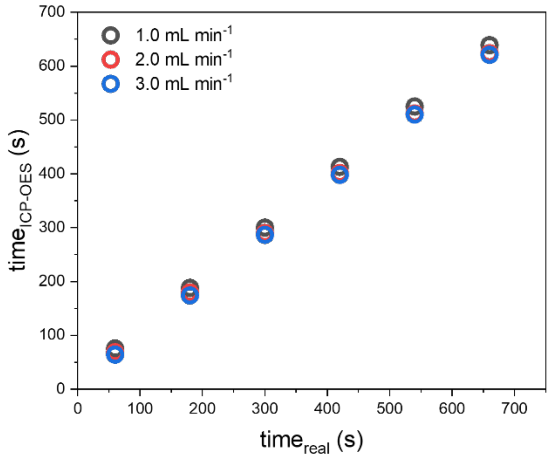

Figure 4.15 1-Timestep response for the Vc flow cell using a zinc electrode in 1 M KOH.

Table 4.3 Delay times and time dilation between the electrochemical flow cell and the ICP-OES.

Flow rate	1.0 mL min^{-1}	2.0 mL min^{-1}	3.0 mL min^{-1}
Slope (ICP/Real)	0.938452	0.925357	0.929643
Intercept	18.9 s	12.8 s	7.58 s

Apart from the "time dilation" issue, the results of the time step protocol in Figure 4.14 showed that the conversion calculation Eq. 4.8 gave reasonable equivalent currents.

4.6.2 On-line ICP-OES Cell response evaluation

To compare the properties of the flow cells presented in Chapter 3, on-line ICP-OES galvanostatic timestep experiments were performed with each flow cell under identical conditions. The aim here was to compare the rise time and signal intensity of the zincate concentration generated from each cell (triggered by a current step). A desirable flow cell would have efficient transport of working electrode dissolution products and hence a short rise time response. An undesirable or poorly designed cell would have a long rise time for a current step and lower signal intensity due to inefficient transport of dissolution products.

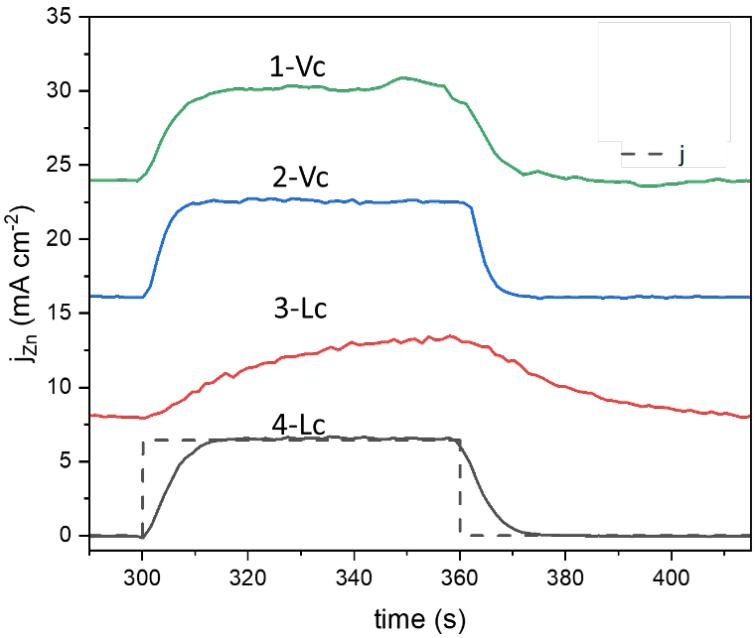

Figure 4.16 Galvanostatic step response for the four flow cells presented in Chapter 3. All experiments were performed in 1 M KOH at 1 mL min^{-1}, on a zinc sheet working electrode, Ag/AgCl reference electrode and a PtIr (90:10) wire or graphite felt counter electrode.

Figure 4.16 shows the galvanostatic step response of the four cells 1-Vc, 2-Vc, 3-Lc and 4-Lc under identical electrochemical protocols. The 3-Lc cell has the longest rise time, and never reaches a j_{Zn} plateau. The 1-Vc and 4-Lc cells response are similar,

which could be expected from their similar Reyonlds numbers and replenishing time calculations in Chapter 3. The 2-Vc cell has the sharpest rise curve and decrease once the current step is arrested. The results presented in Figure 4.146hence seem to agree with the calculations in Chapter 3. The 4-Lc cell, which was the final and novel prototype in Chapter 3 produces similar response to cell designs already published in literature while maintaining a much larger working electrode surface area[105,148]. The 4-Lc cell was therefore used for all further on-line dissolution testing.

4.6.3 Flow rate evaluation

To evaluate the effect of flow rate on the quality of mass transport response time, the time step protocol was repeated at various flow rates for the 4-Lc cell.

The Agilent ICP-OES interface provides manual control of the peristaltic pump revolution rate between 0.5 to 9.0 mL min^{-1}. However, since the on-line experiments are conducted with high total dissolved solids, it is of interest to keep the flow rate as low as reasonable, to decrease the rate of salt deposits forming on the torch assembly which may partially block the orifices and decrease the apparent measured concentration. It must be noted that the recommended revolution rate for off-line routine analysis is 1 mL min^{-1} with white/white peristaltic pump tubing, which corresponds to 1 mL min^{-1}, and that higher flow rates are used for fast rinsing between sample analysis. The damage and instability issues onto the ICP-OES by applying too high flow rates have already been presented in earlier sections of this chapter. In the other scenario where to flow rate is too slow, the widening of the dissolution signal due to slow transport may cause the spectroscopic signal to be too obscured to conduct a meaningful comparison with the electrochemical data. Therefore, flow rates in increments of 0.5 mL min^{-1} from 1.0 mL min^{-1} to 3.0 $min^{-1}$was chosen for comparison.

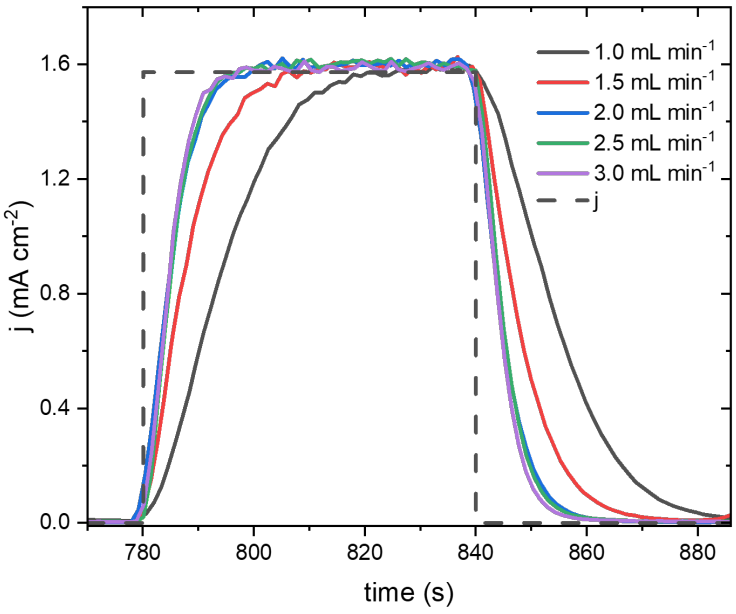

Figure 4.17 Galvanostatic step response for the 4-Lc flow cell at various flow rates. Conducted in 1 M KOH on a zinc sheet working electrode, Ag/AgCl reference electrode and either PtIr (90:10) wire or graphite felt.

Figure 4.17 presents the variation in dissolution signal response time with the flow rate. The spectroscopic data series reach a plateau corresponding to an equal current density to the electrochemical data within the one-minute step at all flow rates. By visually comparing the results in Figure 4.17 to pulsed experiments by other investigators with similar on-line capabilities, the 4-Lc flow cell yields a very favourable response[105,148]. The data from this test display a clear trend of more rapid plateau formation as the revolution rate of the peristaltic pump increases. However, beyond 1.5 mL min^{-1} the rise time only provides diminishing returns, and no significant gain is seen with increased flow rate. By considering the response time in the isolated case, 20 mL min^{-1} would be a suitable option. However, this is an increase of 33% of mass flowing through the torch compared to 1.5 mL min^{-1}, which may increase the risk of solid deposits and blocking of the torch and nebuliser orifices, which may further decrease the spectroscopic signal during experiments. Experiments may also last for several hours and cleaning the ICP-OES components between each experiment would require significant down time. 15 mL min^{-1} was therefore chosen for all further studies to make sure that the risk for unstable operation remained minimised.

4.7 Conclusion and Smmary

4.7.1 Conclusion

ICP-OES can be adapted to analyse matrixes of 1 M KOH by employing a wide bore torch and humidification of nebuliser argon gas. Multielement standard solutions must be avoided in alkaline solutions as it is probable that at least one species will be insoluble in 1 M KOH. The emission signal from the ICP-OES can be converted to equivalents of mass, moles and charge by single element standard calibration curves. Time resolved dissolution signals downstream from a flow cell working electrode can be correlated to equivalent charge. The response time and spread of dissolution signal measured by the ICP-OES depends on the flow cell internal geometry, volume and flow rate of electrolyte.

4.7.2 Summary

In this chapter, the principle of operation of the Agilent 5100 ICP-OES has been described. Components have been changed to suit a high total dissolved matrix, and an evaluation of ICP-OES parameters have been made and compared to expected outcomes. A protocol was developed to align electrochemical data obtained from the potentiostat with time-dependent spectroscopic data from the ICP-OES. Spectroscopic emission signals were successfully converted to equivalent currents of the Zn/Zn(II) half-cell reaction that matched the electrochemical data. Lastly, the efficiency of mass transport between different flow cell geometries were compared by downstream analytics and the effect of flow rate on the time-dependent observed signal of the ICP-OES. The 4-Lc cell was found to provide good response time at flow rates of 1.5 mL min^{-1}.

5 The Dissolution Tendency of Current Collectors for Aqueous Batteries

5.1 Introduction

The work in this chapter was done in collaboration with Dr. Mathias Kjærgaard Christensen as part of a collaboration initiative between DTU and Lancaster University Department of Chemistry. Mathias provided partial assistance in both electrochemical and dissolution testing of positive and negative electrode current collectors, however the latter was sadly not included in this thesis.

In this chapter, the stability of current collectors for aqueous electrolyte batteries will be tested and evaluated by downstream spectroscopic metal detection in a flow cell. The novelty and relevance of this investigation will be justified in the introductory section, followed by an explanation of methods. Results will then be presented from the combined potentiostat/ICP-OES experiments and discussed in the context of aqueous batteries.

5.1.1 Current Collector Materials

Current collectors are the backing material upon which the active materials rests and connects them to the external circuits. As their function is vital to the battery it is inferred that they must remain inert to electrochemical and chemical processes that may cause loss in contact to the active material. The potential window of bifunctional oxygen electrocatalysts spans a potential window of over 0.8 V, and in this potential range a current collector must show excellent resistance to side reactions. Considering the brief literature summary in the introduction, very little attention has been directed to the stability of the current collector materials commonly used for alkaline zinc-air batteries. A clear opportunity window is therefore found to investigate the stability and

dissolution tendency of materials commonly utilized as the positive electrode current collector for zinc-air batteries and report the findings to the wider battery science community to aid them develop longer-lasting alkaline zinc-air battery prototypes. For this investigation, the stainless-steel alloy AISI 304, silver, nickel and titanium are examined as they often reoccur in publications. Hastelloy C276 was also included in this investigation, to see whether nickel alloy specified for corrosion prevention further increases dissolution resistance of the material in 1 M KOH.

5.1.2 Aqueous Zinc-air Cells

Zinc-based aqueous batteries have gained more traction recently as cheap energy storage devices with specific energy densities competing with or exceeding that of lithium ion. The capacity retention of aqueous batteries however, are not on par with lithium ion, typically reaching 200 cycles as opposed to 2000 for li-ion. This is attributed to parasitic side reactions in the active components of the battery. While current collector materials have been established for lithium-ion as copper for the negative electrode, and aluminum for the positive electrode (due to anodic dissolution of copper)[149], there is a discrepancy in the aqueous battery community. For example, throughout various zinc-air battery reports in the literature, materials like unspecified types of stainless steel[150], nickel[151], titanium[152], silver[153–156] and carbon[30] have been used as current collectors for the positive electrode.

5.1.3 Previous Studies

Recent investigation into the stability of negative current collectors have been made byWei et al[157], which concluded on copper and bismuth as the most suitable negative electrode current collectors by voltammetry and columbic efficiency calculations in a flooded type cell. Krebsz et al[158] investigated the passivation film properties of tungsten as current collectors for PEM-type fuel cells, while Geiger [159] explored dissolution resistant backing materials as alternatives for glassy carbon electrodes. An early attempt can also be tracked to Dahn[160], who compared the capacity retention of nickel-zinc batteries by coating stainless steel coin cell casings with tin, copper or nickel.

5.2 Methods

5.2.1 Materials

Foils of nickel (99.994%, Alfa Aesar), titanium (99.5% Alfa Aesar), silver (99.995%, Mateck), Hastelloy C276 (Ni 57%, Mo 17%, Cr 16%, Fe, W, Mn; Goodfellow) and AISI 304 (Fe 70%, Cr 19%, Ni 11%; Alfa Aesar), were obtained. Prior to testing, the foils were polished with sandpaper (2000 grit and 8000 grit), and 1.0μm and 0.3μm de-agglomerated alumina polishing compound (Buehler) until a mirror surface finish was obtained. Samples were then thoroughly rinsed with ultrapure water (18.2 MOhm) before being dried by nitrogen gas blasting.

Electrolyte solution of 1 M KOH was prepared by diluting aqueous stock 38 wt% KOH (9.6 M) (VWR). The batch certificates of analysis were always checked to confirm that the KOH concentration was correct. Preparing the electrolyte from stock solutions were preferred to increase reproducibility of the pre-experimental procedures as opposed to rely on low weight measurement variance by dissolving solid KOH pellets. Despite the relative high impurity level of the stock 1M KOH solution as provided by manufacturer data sheet compared to that of ICP grade nitric acid (parts per trillion vs parts per million), little to no significant background signal or interreferences were observed.

Single element standards for nickel, titanium, silver, tungsten, iron, chromium, manganese, molybdenum and cobalt were purchased from Sigma Aldrich at 1000 ppm with and error of +/- 0.3 ppm. Single element standards were preferred over multielement standards, as some analytes had very low solubility in 1 M KOH and would form precipitates even at sub-ppm concentrations. Each element standard calibration series were conducted in isolation to ensure that false positive signals were not caused by interferences in the emission spectra.

5.2.2 Instrumentation, Settings and protocols

In order to maximise the signals from trace metal dissolution, the 4-Lc flow cell with large surface area but small cell volume was chosen, as discussed in chapters 3 and 4. The working area constricted by the sealing O-ring was 0.636 cm^2. A silver/silver chloride reference electrode in 3.5 M KCl was used (Leaf Free series, Innovative Instruments Inc.) and the potentials are reported against RHE as by equation 5.1

$$E_{RHE} = E_{Ag/AgCl} + E^{\circ}_{Ag/AgCl} + 0.059 \times pH \quad \text{Eq. 5.1}$$

Where $E_{Ag/AgCl}$ is the measured potential against the reference electrode, $E^0_{Ag/AgCl}$ is the formal potential of the reference electrode against SHE and pH is the pH value of the solution. The Ag/AgCl reference electrode was compared to the RHE by a platinum cyclic voltammogram in 1 M KOH.

The counter electrode was a carbon cloth bound to a gold wire of 1 mm diameter with conductive carbon cement. Carbon cloth was chosen to increase counter electrode surface area and to minimise the risk of metal dissolution from the counter electrode. The electrolyte in the counter electrode reservoir was nitrogen saturated.

The ICP-OES was utilised in axial mode, and at the beginning of each experimental day a wavelength calibration was performed. The built-in feature to track carbon and argon emission lines for signal drift correction was enabled in the ICP Expert software. The RF coil power was set to 1.4 kW, the argon flow set to 14 L min^{-1}, and the nebuliser flow to 0.7 L min^{-1}. Flow rate of the direct injection was set to 1.5 mL min^{-1}. Emission line intensities were recorded every 1 second, which consisted of an average of 9 measurements every 100 ms, presumed by a 100 ms recording step to determine appropriate gain level of the ICP-OES CCD detector.

The spectroscopic intensity values were converted to dissolution rates as presented in Chapter 5.

For convenience, the dissolution rates are also displayed as equivalent monolayers per second (ML) through equation 5.3:

$$ML = \frac{Diss}{MM \times p_d} \quad \text{Eq. 5.2}$$

Where MM is the molecular mass of the specific element and p_d is the packing density in mol per surface area of the specific element, and Diss the dissolution rate in ng s^{-1} cm^{-2}.

A Biologic ECi200 was used to carry out the electrochemical protocols. All cyclic voltammograms were conducted at a 2 mV s^{-1} sweep rate. The current range was set to

10 mA for increased stability of the potentiostat negative feedback loop. Electrochemical impedance spectroscopy was taken at OCP with a 10 mV excitation potential at open circuit potential to measure iR drop.

5.2.3 Elemental Dissolution at Open Circuit Conditions

Materials can exhibit dissolution during open circuit conditions, i.e. without any applied current. This can originate from chemical reactions with the electrolyte, or an electrochemical corrosion process where the anodic reaction and cathodic reaction take place on the same surface. By measuring the open circuit dissolution of the working electrode in a given electrolyte, an approximation of the stability in application specific scenarios can be made, for example in stored batteries. In the case of corrosion, the concentration of dissolved O_2 would have a significant effect, as many surfaces catalyse the cathodic oxygen reduction reaction, which would provide a current source for the anodic dissolution. However, all open circuit dissolution tests were performed in argon saturated electrolyte, so any dissolution would be caused from chemical reactions with the electrolyte, or from a corrosion process not involving dissolved O_2.

In these tests, the ICP-OES and potentiostat open circuit recording were initiated with the cell in non-contact mode, such that the working electrode was not exposed to the electrolyte as shown in Figure 5.1a. Then the sample was raised up to the electrolyte droplet until a compact seal was formed with the flow cell O-ring, as displayed in Figure 5.1b. The resulting data will display the open circuit potential drift from the moment the electrochemical cell circuit is closed, and also the resulting open circuit dissolution from the very moment the electrolyte is in contact with the working electrode. The potential recording prior to the working electrode contact point is essentially noise, as the reference electrode and the working electrode are not physically connected by the electrolyte.

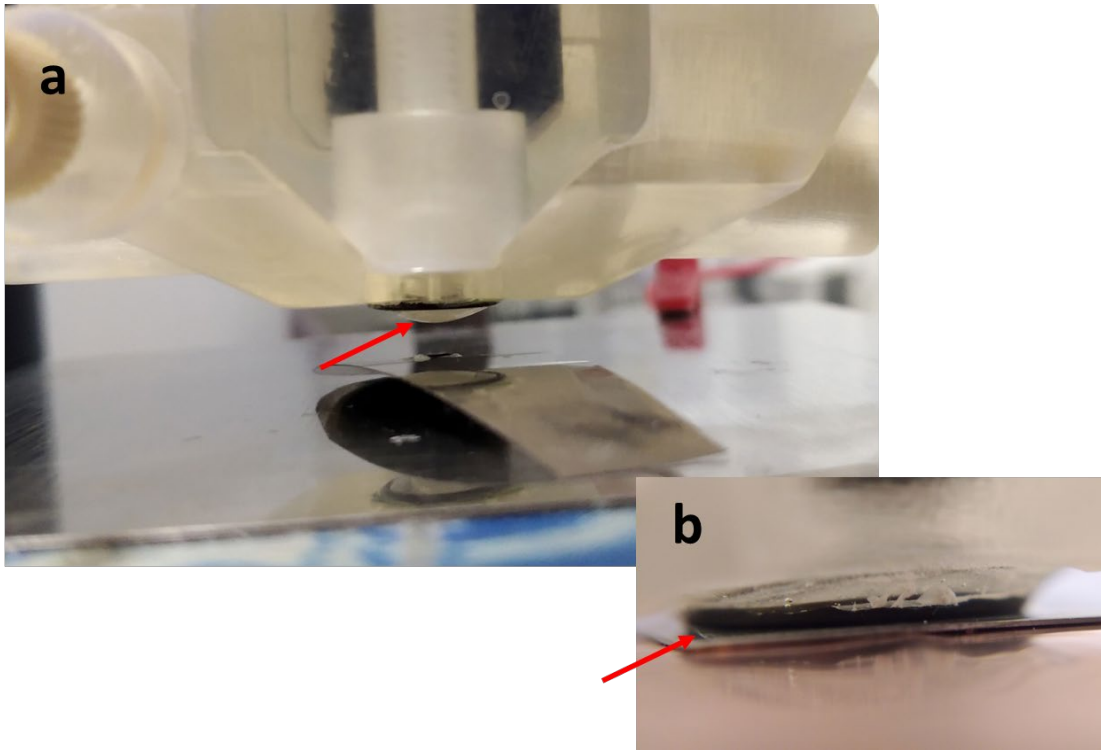

Figure 5.1 a) cell in non-contact mode. note the hanging meniscus. b) Cell in contact mode, where a compressed O-ring seals the electrochemical cell.

5.2.4 Dissolution Voltammetry

As significant dissolution may rise from electrochemical half-cell reactions, and since one material often exhibits more than one half cell reaction within the electrochemical window of aqueous electrolytes, it is important to capture elemental dissolution rates as a function of potential. Hence, cyclic voltammograms were applied to the samples in the on-line ICP-OES setup, applying scan rates of 2 mV s^{-1} in the potential range -0.2 to +1.5 V vs RHE. Since metal-air batteries can reach very positive potentials during charging depending on the applied current density and the local concentration of reaction products, it was decided to scan to the most positive potential that the potentiostat could comply with for each sample. This measurement procedure would allow to detect dissolution products at very aggressive charging conditions for applied aqueous metal-air batteries, where the driving force for anodic dissolution may be large. The purpose of the sweep is to determine the dissolution free potential window of the current collector candidates.

5.2.5 Dissolution Under Constant Charging

The dissolution voltammograms displayed the instantaneous dissolution tendencies of the current collector samples at a given potential. However, to get an idea of the long-term dissolution, it was decided to perform a galvanostatic charging protocol on each sample. This simulated charging protocol was applied in the form of 300 s long galvanostatic steps at 0.1, 1.6, 7.9 and 15.7 mA cm^{-2}, respectively. This covers the range of moderate to very aggressive charging of a metal-air battery. As some of the current collectors exhibit relatively low overpotentials to oxygen evolution, it could be argued that these materials would contribute to a charging step in a metal air battery.

In contrast to insertion chemistry positive electrodes, the potential of a metal-air battery is not governed by the proportion of inserted ions in the cathode, but by the standard potential for the oxygen reduction / evolution reaction, the overpotential for the oxygen evolution reaction, and the surface concentration of starting material and products, in this case hydroxyl anions and O_2 molecules, conductivity of catalyst and the quality of the gas diffusion layer, which can vary widely for different lab-made batteries. Therefore, an upper limiting potential for the charging of metal-air batteries is not easily set but depends on the variables listed above. In light of this reasoning, no potentiostatic control was incorporated into this protocol. If the sample only undergoes minute dissolution, gradually stepping up the anodic potential may not reveal appreciable dissolution above the detection limit.

On the other hand, this could risk running unrealistically high potentials at the samples. The samples analysed may have different oxygen evolution kinetics, in which case a small change in oxygen evolution onset potential will result in an exponentially higher oxygen evolution current and risk hitting the potentiostat compliance limit and ruin any comparison. Lastly, charging in a applied batteries are done with galvanostatic protocols, hence a galvanostatic comparison would be relevant.

5.3 Results and Discussion

5.3.1 Calibration Standards

Calibration curves were performed of all elements of interest in the range of 0.1-1.0 ppm, with a minimum of 10 averaged measurements per point. From the single element standards, no interference was found for between wavelengths of differing elements. The slope of the calibration curve is expressed in intensity ppm^{-1}. Table 5.1 presents typical obtained detection limits expressed in dissolution rate ng s^{-1} cm^{-2}. Standards deteriorated quickly in 1 M KOH and would therefore had to be made fresh for each day. The detection limits were defined as 3 times the standard deviation of the blank signal multiplied by 1.3, and the average blank signal was subtracted from the spectroscopic signal of each emission wavelength dataset.

Table 5.1 Values of calibration slopes and limits of detection for selected wavelengths.

Element	λ / nm	Counts ppm^{-1}	S_{DEV} Blank	LoB (ng s^{-1} cm^{-2})	LoD (ng s^{-1} cm^{-2})
Silver	238.068	52874.45	41.57	0.03091	0.09272
Nickel	352.453	9923.46	32.40	0.1283	0.38510
Titanium	334.941	99153.68	52.41	0.02078	0.06234
Iron	238.204	16607.79	25.64	0.06070	0.18210
Chromium	283.563	52329.79	39.42	0.02962	0.08885
Manganese	257.610	114970.37	34.25	0.01171	0.03513
Molybdenum	379.825	9810.60	54.73	0.2193	0.65800

5.3.2 Dissolution of Silver

Upon contact with the electrolyte, small concentrations of silver were detected from the silver sample. The open circuit potential rested at 0.73 V vs RHE, which corresponds to early stages of silver oxidation in alkaline solution[161].

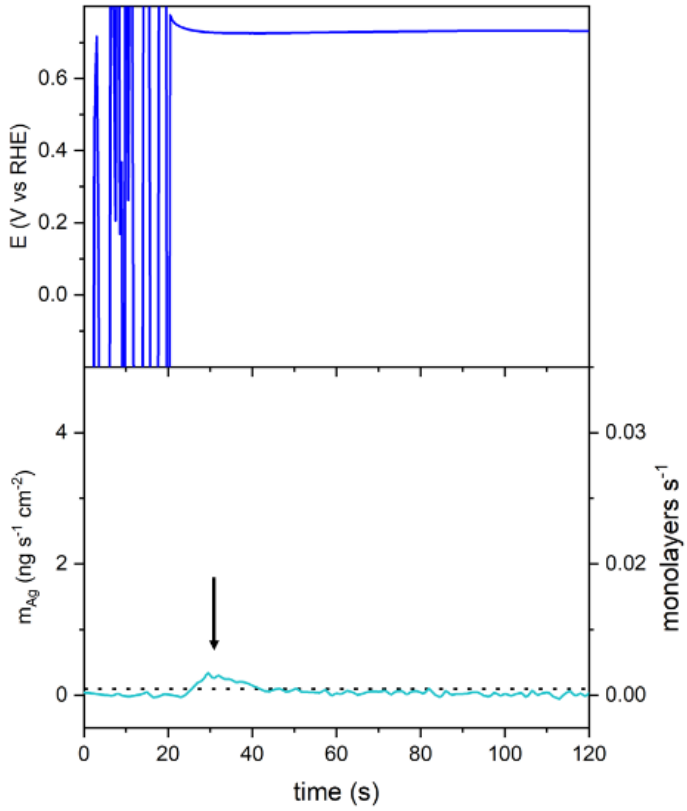

Figure 5.2 Open circuit dissolution of silver in 1 M KOH. The dashed line represents the detection limit estimated from calibration standards.

After a short period of time, the dissolution rate decreases to below the pre-defined detection limits, which suggests that no significant corrosion mechanism takes place in de-aerated solution, and that a thin oxide layer was produced in contact with atmosphere prior to electrolyte contact.

Fig. 5.3a shows the electrochemical cyclic voltammogram of the silver foil sample. The voltammogram is feature rich, so a breakdown of the electrochemical features will be provided. This voltammogram exhibits four anodic peaks A, B, C and D, and two cathodic peaks E and F. These peaks were described by Stonehart as follows[162]:

Following the anodic direction, at 1.05 V vs RHE the first anodic peak reflects the formation of surface adsorbed Ag(OH). Following that, a much larger peak at 1.15 V vs RHE corresponds to the formation of surface Ag_2O. At 1.35 V vs RHE a sharp peak form, which corresponds to the conversion of Ag2O to AgO. At more anodic potentials, the faradaic current increases again, corresponding to the production of non-

stoichiometric Ag(III) species Ag_2O_3, which has a surface structure of 1 Ag(III) for every 6 Ag(I), or 2 Ag(II) for every 3 Ag(I). This process coincides with the evolution of molecular oxygen.

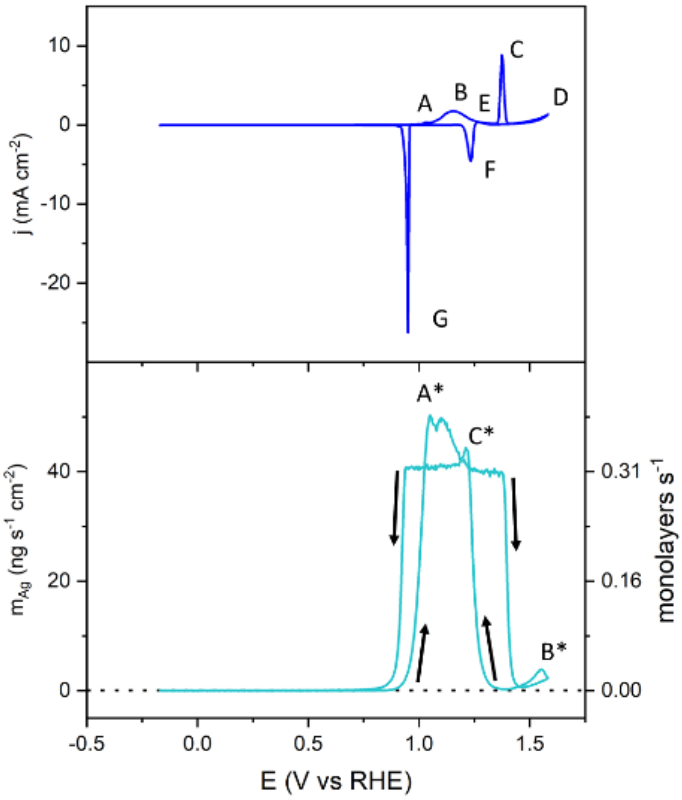

Figure 5.3 Cyclic voltammogram of silver in 1 M KOH.

On the cathodic sweep, at 1.27 V there is yet another anodic peak (E), which is explained as oxidation of "leftover" Ag_2O which was not oxidised further during the anodic sweep. At 1.20 V the first cathodic peak (F) is seen which corresponds to the reverse reaction of peak C, the reduction of AgO to Ag_2O. The final cathodic peak (G) at 0.92 V is the reduction of Ag_2O to Ag^0. As the features in the silver voltammogram obtained here closely resembles that of Stonehart, it is assumed that the electrochemical processes observed here accurately represents silver.

It has been claimed that initial peak A corresponds to the oxidation of Ag to AgOH, which subsequently dissolves into solution as $Ag(OH)_2^-$, and contributes to the precipitation of an $Ag(OH)_2$ film on the electrode [163]. It has also been expected that the theoretical Ag(III) species formed at positive potentials is soluble [164], however this has not been supported by some investigations[165].

Fig 5.3b shows the dissolution rate voltammogram for the silver foil sample. It contains three anodic peaks at 1.05 V (A*) at 50 ng s^{-1} cm^{-2}, 1.60 V (B*) at 10 ng s^{-1} cm^{-2} and 1.25 V (C*) at 45 ng s^{-1} cm^{-2}. No cathodic features exist, as the electrolyte flowing into the cell contained no dissolved silver ions, hence features originating from deposition of silver ions cannot take place. Nevertheless, some correlation between the electrochemical and dissolution rate voltammograms are immediately obvious: Peak A* seem to coincide with electrochemical peak A, and is followed by a dissolution rate plateau which abruptly ends coinciding with the electrochemical peak C. Peak B* and peak D overlap together. Peak C* appears simultaneously with the cathodic peak F, and is followed by a dissolution rate plateau, which abruptly ends in the cathodic direction with the appearance of peak G.

By performing bipotentiostatic experiments on a rotating ring-disk electrode, Miller et al[165] was able to observe dissolution of silver by generation-collection experiments and discriminate between dissolved silver oxidation states. They in deed concluded that the initial rise in current around peak A corresponds to direct electrochemical dissolution of Ag to $Ag(OH)^{2-}$[166], and that once supersaturation of dissolved Ag(I) ions is reached at the electrode surface, a silver oxide film precipitates, and that all subsequent anodic current contributes to the build up of this film. The top layer of the film facing the electrolyte is thereafter dissolved according to the solubility limit of Ag(I), which is why the dissolution rate after peak A* settles to a steady state. When the surface Ag(I) is converted to Ag(II) the dissolution is “switched off”, because the solubility of Ag(II) is much lower than Ag(I). They argue therefore that it is the solubility and convection rate that controls the dissolution rate of silver ions.

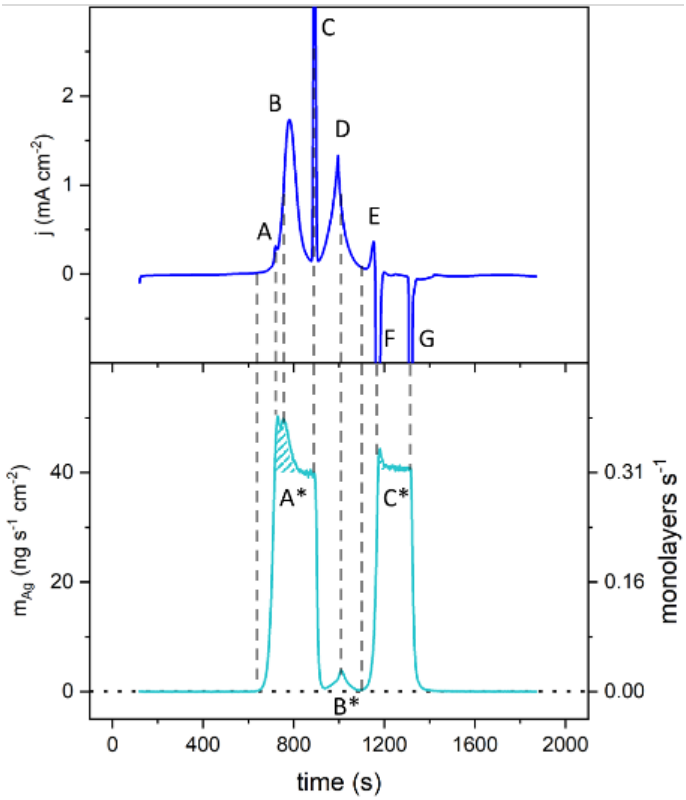

Figure 5.4 Dissolution voltammogram of silver in 1 M KOH.

Fig 5.4 display the same data as Fig 5.3, but it is plotted against time for convenience, and stippled lines are drawn to connect features from the electrochemical and spectroscopic data. Peak A* is actually a doublet, and the first peak of this doublet coincides perfectly with peak A, while the second peak coincides with the incline of peak B. The supersaturated Ag(I) dissolution rate is the shaded area under peak A*. The abrupt end of the dissolution rate plateau, which was found to be 40 ng s^{-1} cm^{-2} coincides with the peak of C, and in agreement with Miller, the silver dissolution rate almost completely vanishes, due to the much lower solubility of Ag(II). However, at peak D, which coincides with oxygen evolution, silver commences dissolution again, which could not be reliably confirmed by reported generator-collector experiments of silver dissolution. The cathodic scan of the dissolution rate voltammogram is almost a mirror image of the anodic scan, except the supersaturation peak C* takes place before the plateau, which is another indication that supersaturation precedes film formation.

Further it has been argued that the initial dissolution rate equals the rate of Ag_2O formation, but that from 1.2 V vs RHE the faradaic current contributes to film

formation, and that the dissolution rate observed at more positive potentials is from chemical dissolution of the Ag_2O oxide film[167] and that the dissolution rate depends on the film thickness[168].

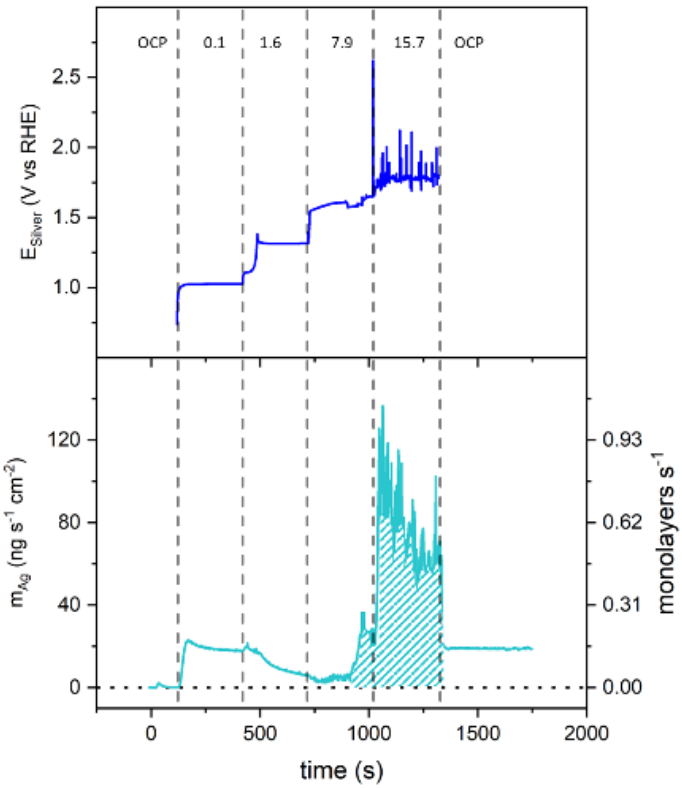

Figure 5.5 Anodic charging of a silver electrode at j = 0.1, 1.6, 7.9 and 15.7 mA cm^{-2}.

It has been reported that Ag(I) on the form of Ag_2O and Ag(II) in the form of AgO has near similar solubilities[169], [170], while other have reported that the solubility of AgO is near 1/16th that of Ag_2O [165]. If the latter is the case, it makes sense that the observed steady dissolution rate of 40 ng s^{-1} cm^{-2} drops and reappears with the formation and reduction of AgO.

The galvanostatic step experiment of charging silver is shown in Fig 5.5. The anodic current density is stepwise increased until 15.7 mA cm^{-2}. The potential profile in Fig 5.5a is initiated by two plateaus preceded by a peak each, corresponding to nucleation of Ag(I) and Ag(II) respectively. After 1000 seconds the potential rises to 1.8 V and irregular spikes due to oxygen evolution appear, which causes random temporary blockage of the electrode surface. The resultant dissolution of the first plateau is a

supersaturation peak at 20 ng s^{-1} cm^{-2}, which after 300 seconds settles at a plateau of constant dissolution of 18 ng s^{-1} cm^{-2}. On the second electrochemical plateau, the dissolution rate is constantly decreasing to a steady state of 5 ng s^{-1} cm^{-2}, which is due to the lower solubility of the AgO formed. As the experiment reaches the oxygen evolution stage, the dissolution rate of silver dramatically increases to between 80 and 120 ng s^{-1} cm^{-2}, which is on average an increase of a factor of 4. The irregularity in dissolution could be due to agitation from bubbles formed on the electrode surface and in the tubing between the flow cell and the ICP-OES assembly. Once the cell returns to open circuit voltage, the dissolution rate quickly settles at 20 ng s^{-1} cm^{-2}, which is equal to the dissolution rate of the Ag(I) covered electrode surface. This suggest that the surface now contains a permanent layer oxidised silver.

Since on-line ICP-OES can effortlessly discriminate between currents rising from oxygen and silver dissolution without any need for correction, this is one of the few definite evidences that silver does in deed dissolve into solution in potentials beyond oxygen evolution. Continuous loss of silver current collector could lead to capacity fade as seen with AgZn-type batteries[170], and complete loss in performance for alkaline electrolysers[171].

5.3.3 Dissolution of Titanium

Figure 5.6 shows the open circuit potential and dissolution rate of titanium. Upon contact, the titanium dissolution rate increased to 2 ng s^{-1} cm^{-2}, before settling to above detection limits. Simultaneously, a small jump in the open circuit potential of 0.10 V took place. The potential of the titanium sample rested around 0.05 V vs RHE once in contact with the electrolyte.

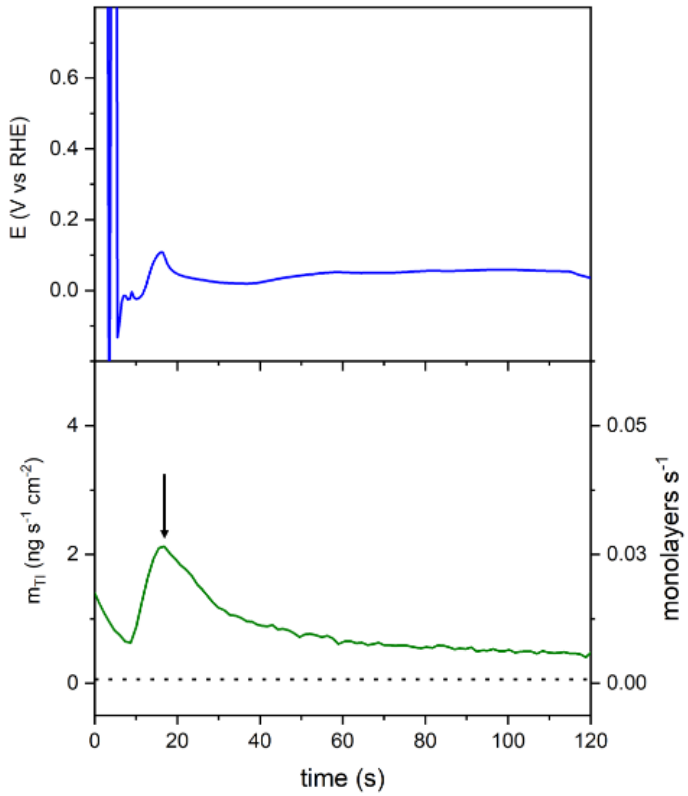

Figure 5.6 Open circuit dissolution of titanium in 1 M KOH. Arrow points to dissolution maximum.

The titanium sample also displayed measurable open circuit dissolution which settled above the detection limit of the ICP-OES. As the potential rested around 0.05 V vs RHE, which is close to hydrogen evolution, the dissolution rate may be explained as a corrosion reaction where hydrogen evolution is the cathodic reaction, and the oxidation of titanium as the anodic reaction. However, $Ti(OH)_3$ species are shown to form spontaneously upon contact with alkaline electrolyte, which may cause the above detection limit signals[172].

The titanium sample was scanned to an anodic potential of 3.0 V vs RHE, as no oxygen evolution current was observed. Titanium is known to form passivating oxide layers. The voltammogram in Figure 5.6a the small "hump" at 0.2 V (A), probably corresponds to the oxidation of titanium to hydrated titanates $[Ti(OH)_2]_{ads}$[173]. Commencing at 0.9 V (B), the current density increases to 0.08 mA cm^{-2} and then sharply increases at 1.6 V, corresponding to a phase transformation of TiO_2 to Ti_3O_5 (C). This is known to inhibit oxygen evolution at titanium surfaces at potentials negative of 10 V[174]. Peaks D and E were not identified with any published data, but presumptuously it corresponds to either oxide growth or phase transformation.An anodic current is maintained also during the cathodic scan down to the phase transformation point at 1.6 V (F). No cathodic peaks are observed.

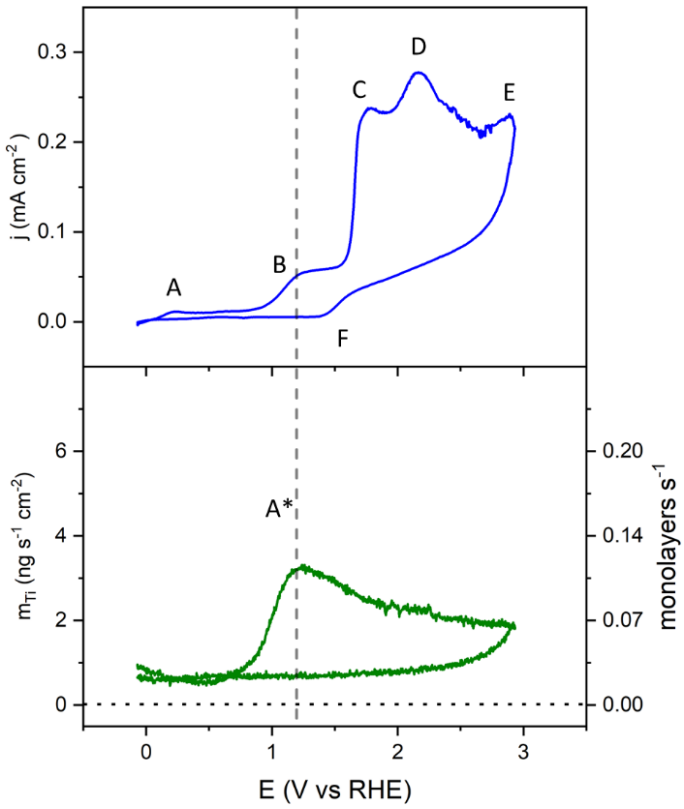

Figure 5.7 Electrochemical and dissolution voltammogram of titanium in 1 M KOH.

The titanium dissolution rate remains well above the detection limit during the entire scan, albeit relatively low at 1 ng s^{-1} cm^{-2}. It has been reported that oxide films $Ti(OH)_3$ form spontaneously in alkaline solutions, and there may be a chemical dissolution of this that caused the constant background signal[172]. Appearing with the current plateau

from 0.9 V vs RHE is an increase with of the dissolution rate with a maximum peak A* of 3 ng s^{-1} cm^{-2}, but the dissolution rate decreased to 2 ng s^{-1} cm^{-2} at the vertex point. No change in the dissolution rate could be associated with the phase transformation at 1.6V vs RHE on the cathodic sweep, and the dissolution rate remained at 0.5 ng s^{-1} cm^{-2} until 0.0 V vs RHE, suggesting that the oxide film is reduced at lower potentials[173].

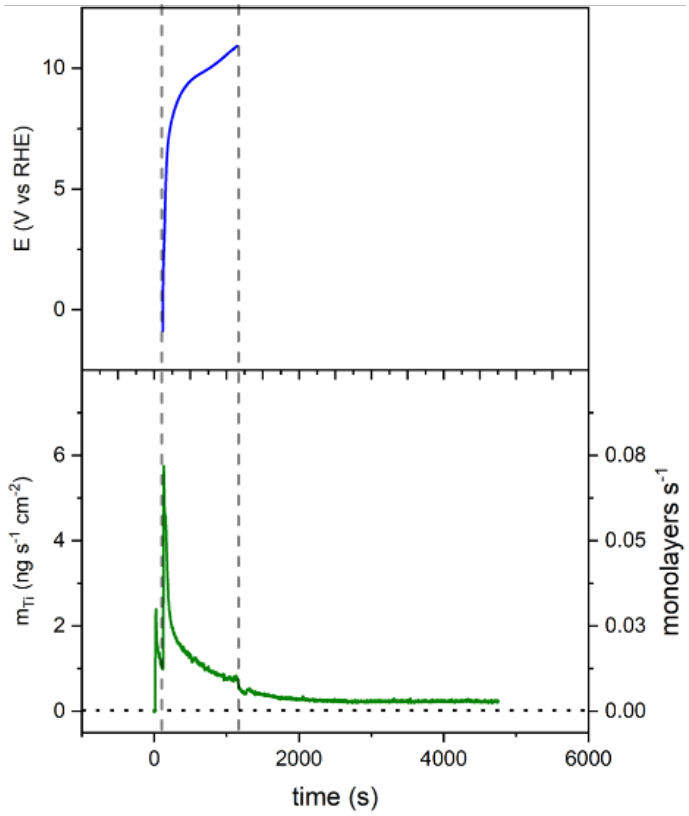

Figure 5.8 Anodic charging of a titanium electrode at j = 1.0 mA cm^{-2}.

In Figure 5.8, a current density of only 1.0 mA cm^{-2} was applied for the duration of the galvanostatic step protocol, as higher current densities caused the potential between the working and counter electrode of the flow cell to reach compliance limits. At this current density, the potential rapidly increases to above 5.0 V vs RHE, which is unrealistically high for a metal air battery, even during aggressive charging.

During the first 200 seconds, a dissolution signal is seen with a peak after 15 seconds at 6 ng s^{-1} cm^{-2}. The dissolution signal then decreased, but still above detection limit levels between 1-2 ng s^{-1} cm^{-2}, while the potential of the titanium electrode reached 9 V vs RHE. Once the protocol was concluded, the cell relaxed to open circuit conditions,

and a dip in the titanium dissolution rates followed. However, after 1000 s the dissolution rate was still at 0.2 ng s^{-1} cm^{-2}. Interestingly, titanium can reach very high potentials without passing significant currents or promote large rates of metal dissolution. From this result it may be appropriate to suggest that titanium remains relatively chemically and electrochemically passive when high potentials or currents are applied, and that very little dissolution takes place at high potentials or very small currents passed.

5.3.4 Dissolution of Nickel

Figure 5.9 shows the open circuit potential and dissolution rate of nickel. The open circuit potential of the electrode rested at 0.3 V. No dissolution rate above the detection limit was observed, suggesting that the surface remains pristine at open circuit.

Figure 5.10 shows the cyclic voltammogram of the nickel foil sample. It produced two

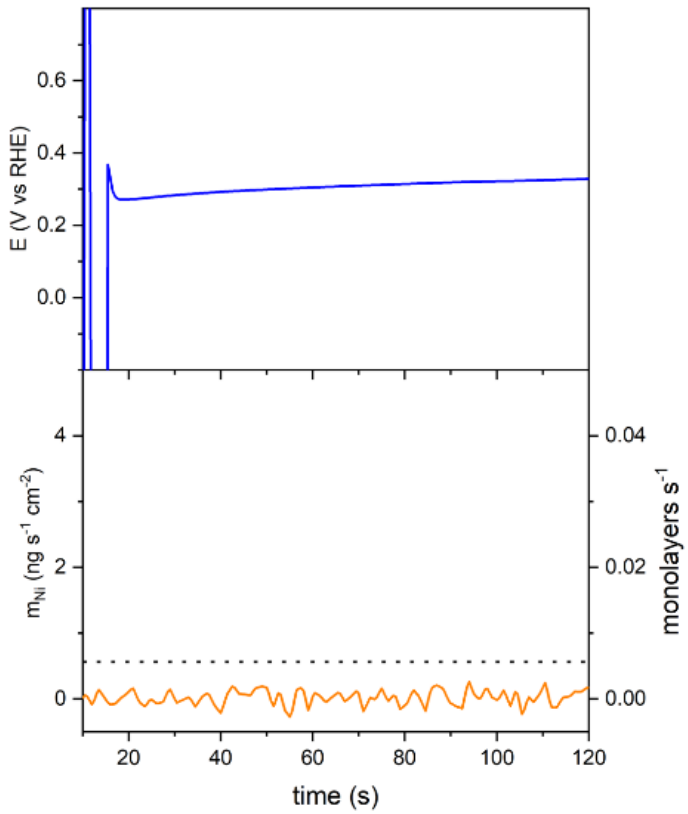

Figure 5.9 Open circuit dissolution of Nickel in 1 M KOH.

anodic and one cathodic feature features at 0.9 V (A), 1.2 V (B) and 1.15 V (C). Feature A corresponds to the oxidation the beta-hydroxide β-$Ni(OH)_2$ to γ-NiOOH[175]. It has

been reported that this peak could also stem from the formation of NiO. NiO has a lower gravimetric density, and it has been hypothesised that some of the film is mechanically detached from the surface, hence causing a columbic efficiency below 100% for the reduction peak [176]. Others have suggested that the NiOOH film is not reduced during the reduction peak [177].

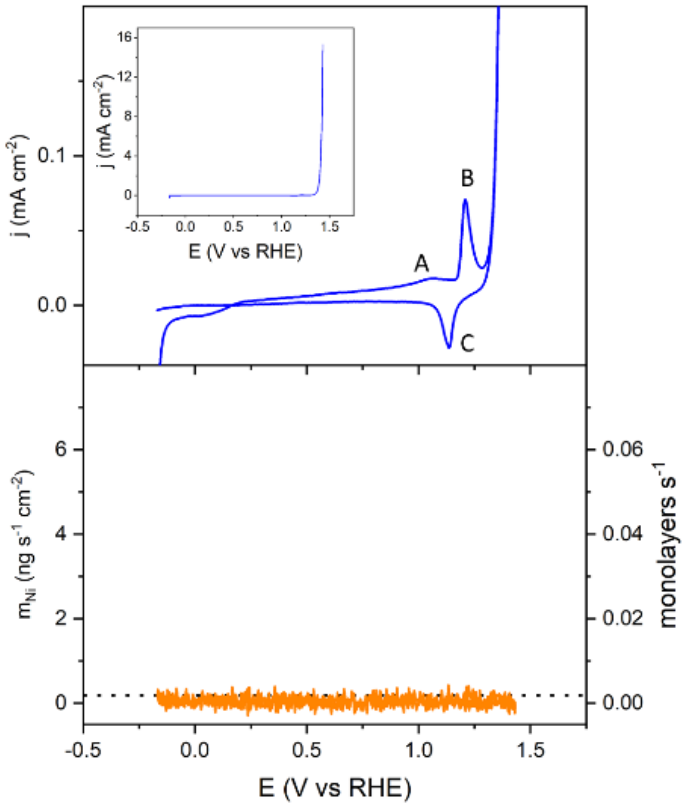

Figure 5.10 Electrochemical and dissolution voltammogram of nickel in 1 M KOH.

The dissolution rate voltammogram however, revealed that no dissolution was observed above the detection limits, even at very high anodic current densities, which suggest that the oxide film formed on the electrode surface is stable and does not detach under these conditions as claimed in some publications.

Figure 5.11 shows the galvanic charging experiment for the nickel foil sample. The potential response to the galvanostatic steps are flat, and probably corresponding to oxygen evolution, in contrast to silver and titanium which displayed potentials corresponding to oxidation of the surface species. At the highest current density of 15.7 mA cm^{-2} some noise appears in the potential readings, which may be due to rapid bubble

formation on the surface of the nickel foil electrode which cause random blockage of the electrochemically active surface. This observation affirms the results from the dissolution voltammetry experiments, that the nickel oxide films remains dissolution resistant in alkaline media, and that the oxidation of the surface may act as a protective barrier.

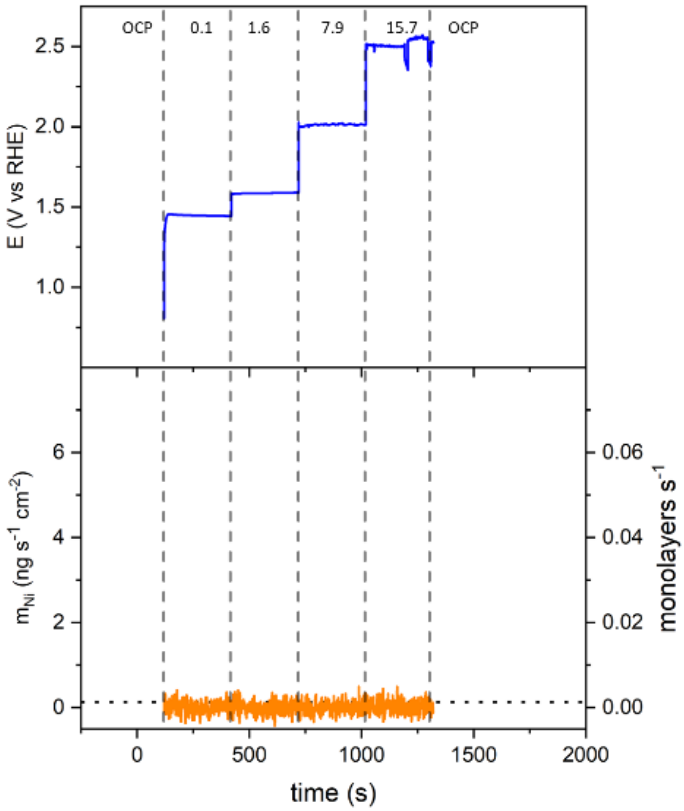

Figure 5.11 Galvanostatic charging of nickel foil sample.

5.3.5 Dissolution of AISI 304 Stainless Steel

Figure 5.12 depicts the open circuit conditions for AISI 301 stainless steel. Once the electrochemical circuit is closed, the potential rests at 0.47 V. The corresponding dissolution rate data reveals that upon contact with the alkaline electrolyte, iron spontaneously dissolves from the surface of the stainless steel sample at a maximum of 3 ng s^{-1} cm^{-2}, but decreases to barely above detection limits within one minute. Dissolution from other element constituents of stainless steel, like chromium or manganese, was not found during open circuit conditions.

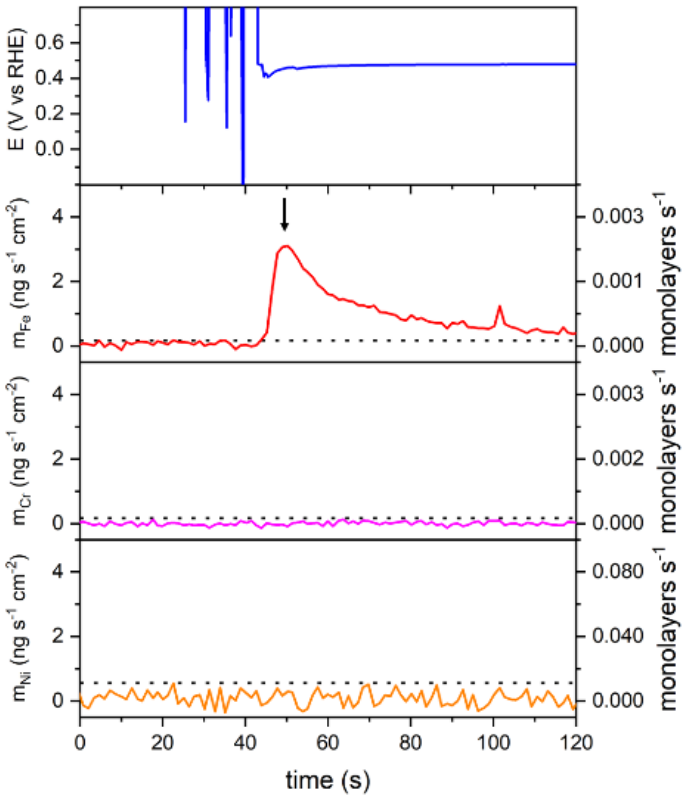

Figure 5.12 Open circuit dissolution of AISI 304 stainless steel in 1 M KOH.

Figure 5.13 depicts the electrochemical and dissolution voltammograms of the AISI 304 stainless steel sample. The electrochemical data reveals two electrochemical features: an anodic peak at 0.80 V (A) and a cathodic peak at 1.3 V (B). Note that any faradaic process negative of 0.4 V is obscured by hydrogen evolution currents.

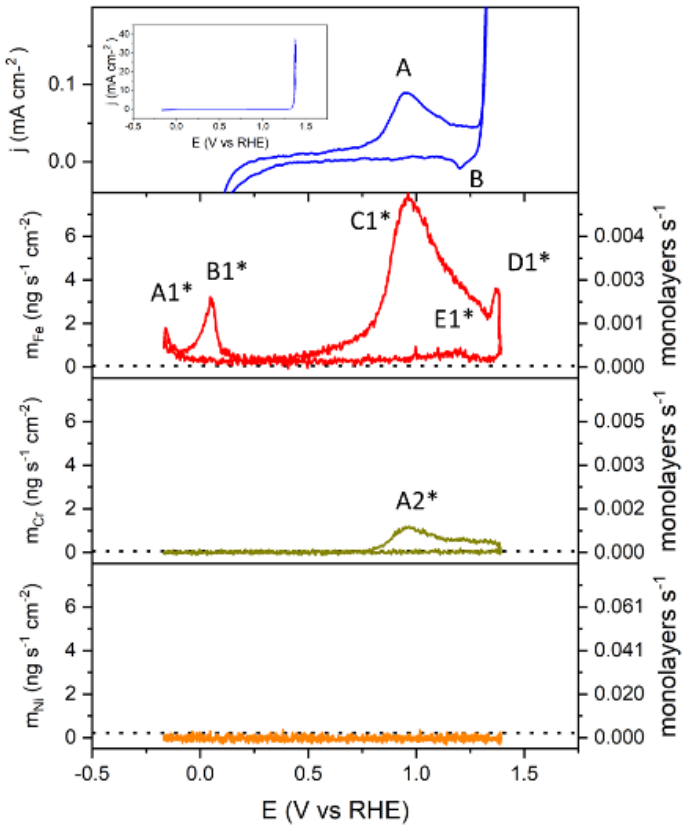

Figure 5.13 Electrochemical and dissolution voltammogram of AISI 304 stainless steel in 1 M KOH.

The dissolution voltammogram in Figure 5.13 only depicts the elements with dissolution rates above the respective detection limits. The iron dissolution rate displays five active regions: below -0.1 V (A1*), 0.0 V (B1*), 1.0 V (C1*), above 1.4 V (D1*), and 1.2 V (E1*). In addition to this, there is a constant dissolution rate of iron throughout the scan at 0.5 ng s-1 cm-2. Apart from iron, only chromium dissolution was detected within the full range of the cyclic voltammogram, with a peak at 1.0 V. Iron dissolution is visible even at the lower potential limit, peaking with 3 ng s^{-1} cm^{-2} at 0.0 V.

The dissolution voltammogram starts and ends with the dissolution feature A1*, which is reported to be the reduction of Fe(II) film to Fe^0 [178]. Peak B1* corresponds well with the oxidation of Fe^0 to $Fe(OH)_2$ as seen in voltammograms of both pure iron and AISI 304 stainless steels[178–182].

The dissolution rate of both iron and chromium increase to peak C1* and A2* respectively, corresponding to peak A of the electrochemical voltammogram on the

return scan the dissolution peak E1* for iron may correspond to the reverse process. There is no agreement about the origin of the anodic peak A for AISI 304 stainless steel. It was suggested to reflect simultaneous iron and chromium dissolution[183] producing a chromium enriched passivating film, or that it is the oxidation of Cr(III) to Cr(VI) [184].

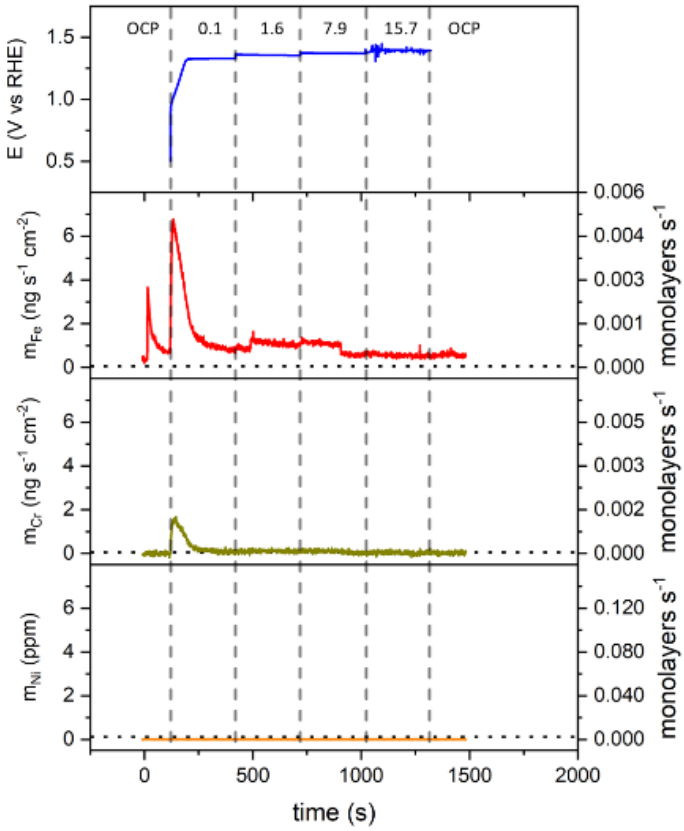

Figure 5.14 Anodic charging of an AISI 304 stainless steel electrode at j = 0.1, 1.6, 7.9 and 15.7 mA cm^{-2}.

By performing cyclic voltammetry of pure elemental electrodes, Tiwari suggested that the oxidation peak corresponds to the oxidation of Ni(II) to Ni(III) [185], however no corresponding dissolution rate of nickel is observed here.

The iron dissolution feature D1* may correspond to further oxidation beyond the limits of the cyclic voltammogram in Figure 5.13. Figure 5.14 depicts the galvanostatic step experiment for the AISI 304 stainless steel foil sample. After the initial open circuit dissolution as seen in Figure 5.12, simultaneous dissolution of iron and chromium take place when an anodic current density of 0.1 mA cm^{-2} is applied. Once the potential reach steady-state around 1.3 V, the chromium remains just above detection limits,

while iron dissolution progresses at 1 ng s^{-1} cm^{-2}. Accelerating this test by increasing the current density does not yield appreciably higher dissolution rates, the iron dissolution rate remains constant throughout the experiment. At open circuit after the protocol, the iron dissolution rate is unchanged. It is possible that this is due to chemical dissolution of an iron-rich film on the electrode surface. Again, no nickel dissolution was observed. The total dissolution rate however, seem to be higher than thought, as it is observed throughout all potentials and under prolonged anodic current.

5.3.6 Dissolution of Hastelloy C276

Figure 5.15 displays the elemental dissolution rates of Hastelloy C-276 upon contact with the electrolyte. The potential of the working electrode rested at 0.32 V vs RHE.

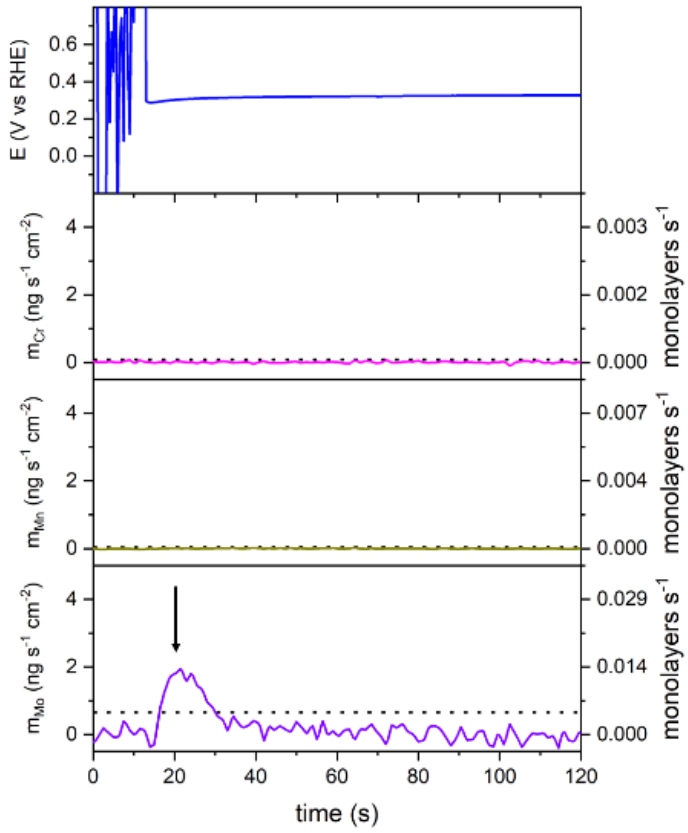

Figure 5.15 Open circuit dissolution of Hastelloy C276 in 1 M KOH.

The only detectable dissolution signal is a short transient peak reflecting molybdenum dissolution. No nickel, chromium or manganese signals were measured above detection limits.

Little electrochemical corrosion work has been done on Hastelloy C276 in alkaline media. Corrosion studies suggest it is relatively dissolution resistant compared to stainless steel[186–188].

The electrochemical voltammogram remained featureless on the anodic scan until 0.8 V, were the current density increased to a plateau at 0.03 mA cm^{-2} (A). At 1.2 V an anodic peak appeared (B), which coincides with the oxidation of Ni(II), before oxygen evolution takes place. On the cathodic scan, a reduction peak appeared at 1.15 V (C).

The dissolution voltammogram in Figure 5.15 displays the chromium dissolution rate of chromium, manganese and molybdenum, however dissolution was only seen for chromium. The dissolution rate increases from 0.8 V vs RHE and a plateau of 2 ng s^{-1} cm^{-2} is established before a maximum that co-incides with the electrochamical peak at 1.2 V (A*). Once the oxygen evolution region was reached, no further dissolution rate above the detection limits were observed.

The dissolution of chromium is similar to that of reported for stainless steels, and most likely contributes to the formation of a passivating film[189].

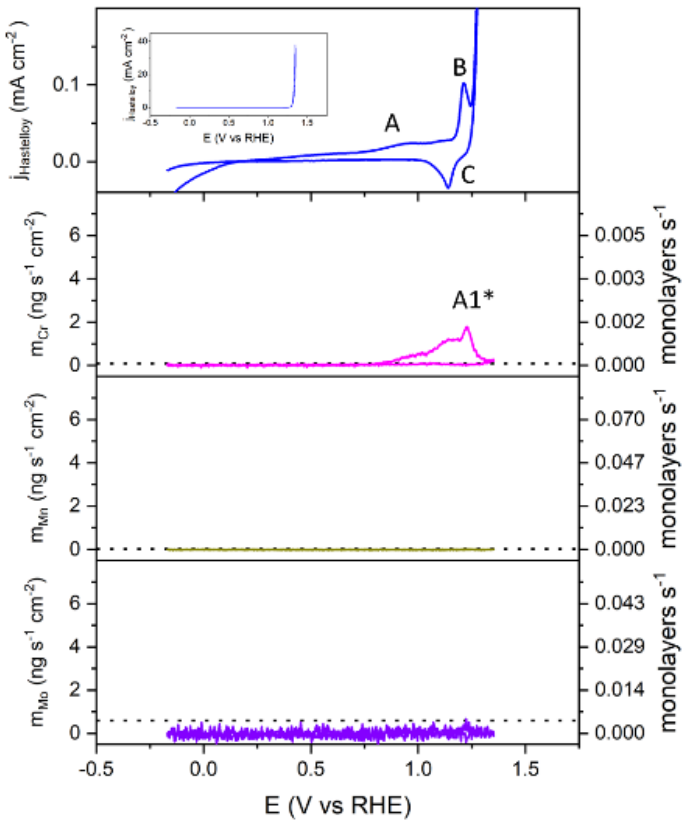

Figure 5.16 Electrochemical and dissolution voltammogram of Hastelloy C276 in 1 M KOH.

For Hastelloy, the dissolution trend is somewhat similar to that of the stainless-steel alloy. At the first charging step of 0.1 mA cm-^{2}, the dissolution rate of chromium rises to approximately 2.0 ng s^{-1} cm^{-2}, before decreasing to a rate above the detection limit. Simultaneously, molybdenum also increases to a rate of approximately 0.9 ng s^{-1} cm^{-2}, but never above detection limits as defined from the calibration standards section. The soluble molybdenum species are reported to contribute to the formation of a passivating film on marine grade stainless steel [183], and a similar effect may have taken place here.

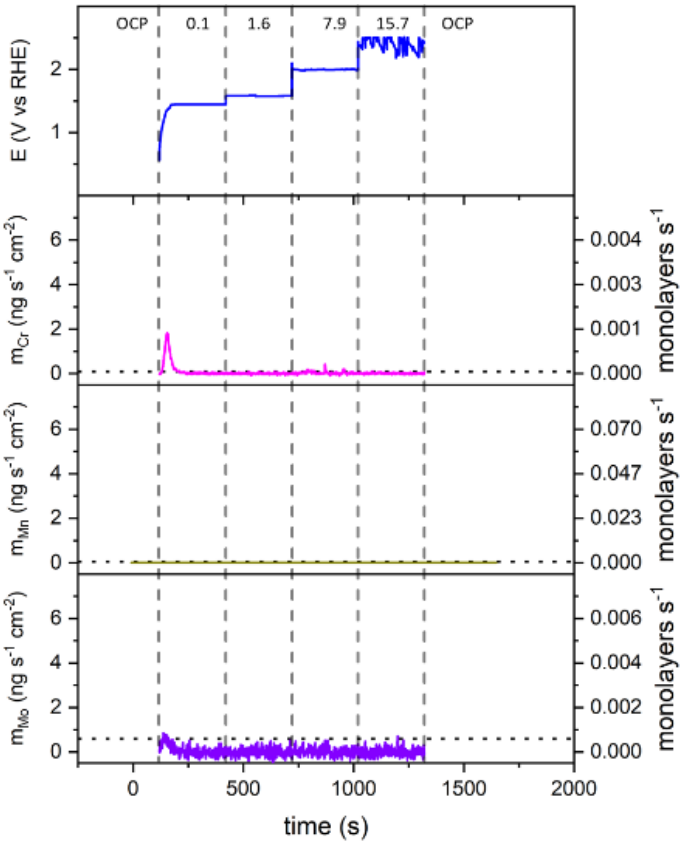

Figure 5.17 Anodic charging of a Hastelloy C276 electrode at j = 0.1, 1.6, 7.9 and 15.7 mA cm^{-2}.

Subsequent increases in the current density did not yield an increase in the dissolution rate of any element. No dissolution of nickel was observed, suggesting that co-alloying nickel with the other materials do not reduce the stability of nickel.

5.4 Discussion and Evaluation of Results

The suitability of these materials as current collectors for zinc-air batteries will now be discussed. Referring to the potential range of the positive electrode earlier in the chapter, where platinum was used as an example for the oxygen reduction reaction and the oxygen evolution reaction, the following criteria must be met.

First, the material should not pass any faradaic current within the practical potential range that the oxygen electrocatalyst operates in. Defining a potential limit for the positive electrode of the zinc-air battery is not as trivial compared to intercalation

materials, as the potential does not vary with state of charge, but with applied current density, which can vary widely, based on application and battery design. For the sake of argument, the potential range of interest for further discussion will be 0.4-1.5 V, or an overpotential of 300 mV for the onset of ORR and OER on the platinum electrode.

From 0.8 V to 1.4 V vs RHE, an oxidation process takes place on all materials tested, correlated to the oxidation of either chromium, nickel or titanium for AISI 304, Hastelloy C276, nickel and titanium. The current densities obtained from the voltammograms were comparatively low at 0.08 mA cm^{-2}, which is not large in applicable terms where current densities in order of 10 mA cm^{-2} is passed. For the silver sample, the voltammograms pass current densities in the order of 1 mA cm^{-2}, which would mean that a significant part of the charging or discharging current would be passed to oxidise or reduce silver oxides.

Table 5.2 Electrode potentials at j = 1 mA cm^{-2} during anodic scan. Values taken from cyclic voltammograms.

Material	E / V vs RHE at j_{OER} = 1 mA cm^{-2}
Hastelloy C276	1.296
AISI 304	1.340
Nickel	1.386
Silver	1.559
Titanium	N / A

The potentials for oxygen evolution for each sample displayed in Table 5.3. Nickel, AISI 304 and Hastelloy display relatively early onset to the oxygen evolution reaction, whereas this reaction has a much higher overpotential for silver and not observed on titanium. As the oxygen evolution is the main reaction of the positive electrode during charging of zinc-air batteries, this may be beneficial as the current collector would partially aid the bifunctional electrocatalyst, and hence may reduce overpotential for charging. On the other hand, excessive bubble formation on the current collector may lead to bubbles mechanically displacing the electrocatalyst powder bound to the surface.

The current collector material should not dissolve chemically or electrochemically. That could cause overall contact loss to the bifunctional catalyst particles. Furthermore, dissolved metal ions could diffuse to the negative electrode and deposited with the zinc active material. Certain elements are proven to cause an increase in hydrogen production, a parasitic side reaction on the negative electrode of zinc air batteries. This was demonstrated for nickel and silver ions added as dopants in the electrolyte[190].

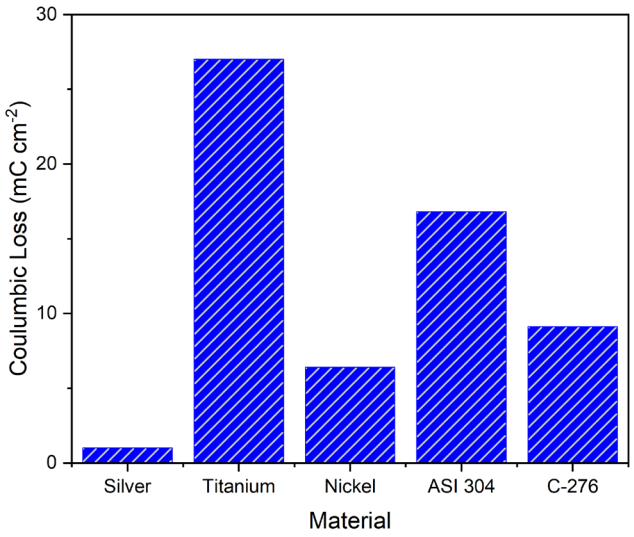

Figure 5.18 Net Coulombic loss from the electrochemical cyclic voltammograms of the current collector materials.

Figure 5.18 shows the "coulombic loss" of the electrochemical cyclic voltammograms for each of the samples, where the charge passed during the cathodic scan is subtracted from the charge passed during the anodic scan within the water splitting window. The surplus charges can inform if some of the oxidised species during the anodic scan has not been reduced during the cathodic scan. To be accounted for, these surplus oxidised species would either stay on the electrode surface as a permanent film, or dissolved into solution and observed in the ICP-OES. Assuming an atomic mass of 100 g mol $^{-1}$, the equivlant current of 1 ng s^{-1} cm^{-2} is approximately 1 µC s^{-1} cm^{-2}. A total Coulombic loss of above 1 mC cm^{-2} must obviously have a significant proportion of its charge contributed to a film formation rather than dissolution.

All of the materials tested have some surplus charges in the voltammogram, which agrees well with the ICP-OES observations. Silver, despite the large dissolution currents seemingly recovers most of its oxidised species, as only 1 mC cm^{-2} was lost.

Titanium on the other hand, had the lowest relative of charge recovery. As only a very small dissolution current was observed in Figure 5.7, it is reasonable to assume that most of the lost charge of 27 mC cm^{-2} has been converted to a permanent titanium oxide film. The dissolution rate voltammogram of nickel from Figure 5.10 shows no measurable dissolution rate, but there is a surplus of lost charge in the electrochemical voltammogram of 6 mC cm^{-2}. This suggest that there is an oxidised nickel on the electrode surface that does not dissolve in alkaline media. The AISI 304 foil electrode had a coulombic loss of 17 mC cm^{-2}, while the dissolution rate cyclic voltammogram in Figure 5.13 only had a moderate rate of 8 ng s^{-1} cm^{-2} of iron dissolution. This suggests that a non-reversible oxide film was established on the electrode surface during the voltammogram. The Hastelloy C-276 foil electrode had a Coulombic loss of 9.1 mC s^{-1} cm^{-2}, while the dissolution rate cyclic voltammogram in Figure 5.16 only appreciable dissolution of chromium at a maximum of 2 ng s^{-1} cm^{-2}.

Of the pure elements, silver exhibits the highest dissolution rates at positive potentials, related to the electrochemical dissolution of $Ag(OH)_2^-$ from 0.8 V vs RHE, and subsequently the chemical dissolution of the Ag_2O film. The dissolution rate of silver, compared to the other dissolving samples, is in general one order of magnitude larger, and spans a wider potential range. In addition, the passivation of silver seems to be reversible and the dissolution rate of silver oxide only depends on the degree of AgO surface coverage. The galvanostatic tests also revealed that silver as the only sample displayed prolonged dissolution at higher dissolution rates, and an elevated level of background dissolution rates were recorded after this stress test. The ready dissolution of silver could be a serious problem for electrocatalyst adhesion. It is then clear that silver should be avoided as a current collector material for the positive electrode. In addition, AgO is a strong oxidising agent, which could significantly alter other components in a battery, like a polymer separator[170]. Indeed, the stability of silver as a current collector or conductive additive has been under recent scrutiny, and it is suggested that even carbons provide better longevity than silver at anodic potentials due to the tendency of silver to erode rapidly in alkaline media[171].

Table 5.3 Published solubility values of relevant metal species.

Species (s)	Species (l)	Solubility	K_{sp}	Solution	Ref
Ag_2O	AgO^-	1×10^{-4} M	3.8×10^{-8}	1 M KOH	191
AgO	$Ag(OH)_3^-$, $Ag(OH)_4^{2-}$	2×10^{-4} M		1 M KOH	170
Ag_2O	AgO^-		2×10^{-8}	alkaline	192
Ag_2O	AgO^-	2×10^{-4} M			169
AgO	$Ag(OH)_2^-$, $Ag(OH)_4^-$			alkaline	193
AgO	Ag(II)	2.5×10^{-5} M		10 M KOH	165
$Cr(OH)_3$	$Cr(OH)_4^-$	1×10^{-5} M	Log β=-27.4 Log K=-18.25	0.1 M $NaClO_4$,NaOH	194
Cr_2O_3	Cr(III)	2×10^{-9} M		Phosphate, pH=9-11	195
Fe_3O_4	$Fe(OH)_3^-$,$Fe(OH)_4^-$	1×10^{-7} M	logK2=8.23, logK3=-11.05	NaOH	179
$Fe(OH)_2$	$HFeO_2^-$		$1\times10^{-18.3}$	1 M KOH	180
Fe_2O_3	Fe(III)	5×10^{-5} M	lnK=-19	1 MKOH	196

K_2FeO_4	Fe(VI)	1×10^{-3} M		Sat KOH	197
$Ni(OH)_2$	$HNiO_2^-$	6×10^{-6} M	6.5×10^{-18}	1 M NaOH	198
$Ni(OH)_2$			2.0×10^{-15}	6 M KOH	199
NiO	Ni(II)	6.3×10^{-10} m		3 mmol NaOH	200
TiO_2	titania	$< 4\times10^{-5}$ M		pH12	201
TiO_2	$Ti(OH)_4$, $Ti(OH)_5^-$	$1\times10^{-5.1}$m	logK=-7.72, -10.11	pH12	202
TiO_2	$[Ti(OH)_6^{2-}]$		10^{-5}	pH14	203
TiO_2		1×10^{-3} to 1×10^{-7}	pK_s^0=64-67	1 MNaOH	204

Table 5.3 lists soluble species found in literature that are found in the current collector samples. It is clear that the elements incorporated in the samples will form thermodynamically stable oxides even at quite cathodic potentials of the oxygen reduction reaction on platinum, in particular oxides of iron, chromium and titanium.

Table 5.4 Prevalence speciation obtained from published Pourbaix plots.

Element	Species	V vs SHE	V vs RHE	Predominance	Source
Ag	Ag_2O	-0.3-0.6	0.526-1.426		205
	AgO	0.6-0.7	1.426-1.526		
	Ag_2O_3	0.7-1.2	1.526-2.026		

	AgO_+	1.2-2.2	2.026-3.026		
Ag	AgO^-	0-0.5	0.826-1.326		[206]
	Ag_2O_2	0.6	1.426		
	Ag_2O_3	0.6-1.5	1.426-2.326		
Cr	Cr_2O_3	-1.0-0	-0.174-0.826		[207]
	CrO_4^{2-}	0.0-2.0	0.826-2.826		
Fe	$Fe(OH)_3^-$	-1.0	-0.174		[207]
	Fe_30_4	-1.0	-0.174		
	$Fe(OH)_4^-$	-0.5-1.0	0.326-1.826		
	FeO_4^{2-}	1.0-2.0	1.826-2.826		
Mo	MoO_4^{2-}	-0.5-1.0	0.326-1.826		[207]
Mo	MoO_2	-0.75- -0.5	0.076-0.326		[208]
	MoO_4^{2-}	-0.5-1.5	0.326-2.326		
Ni	$NiH_{0.5}$	-2.0- -1.0	-1.174- -0.174		[209]
	Ni	-1.0- -0.75	-0.174-0.076		
	$Ni(OH)_3^-$	-0.75-0.6	0.076-1.426		
	γ-NiOOH	0.6-2	1.426-2.826		

	$Ni(OH)_2$			$Ni(OH)_3^-$ 50%	[210]
				$Ni(OH)_4^{2-}$ 50%	
Ti	TiO	-2.2- -2.0	-1.374- -1.174		[211]
	Ti_2O_3	-2.0 - -1.3	-1.174- -0.474		
	TiO_2	-1.3-0.2	-0.474-1.026		
	$HTiO_3^-$	0.2-1.8	1.026-2.626		
	TiO_2^{2+}	1.8-2.4	2.626-3.226		

The solubilities of the most prevalent oxides are listed in Table 5.4. A general trend can be seen in the solubility were $AgO^- > Fe_2O_3 > TiO_2 > Cr(OH)_3 > Ni(OH)_2$. These values predict that materials containing silver, iron and titanium would be more prone to dissolution than chromium or nickel. The dissolution test show that trace concentrations of iron and chromium are continuously dissolved from AISI 304 under constant charge, while the iron-free Hastelloy C276 has a much better dissolution retention. However, both materials have a similar weight percentage of chromium, which suggests that the dissolution of one element, iron in the case of AISI 304, can cause other co-alloying elements to co-dissolve. On the microscale, this could be due to change in surface pH, as iron(II)/(III) complexes are acidic, or it could be that the erosion of the surrounding atoms cause the chromium to also detach[208]. Although the dissolution rates from the stainless steel was far below that of silver under galvanostatic charging, if one looks beyond the short timeframe of the dissolution experiments, a battery operated for months with stainless steel as current collectors may see more dissolution from these current collectors. As mentioned above, that could lead to undesired metal deposition, e.g., on a zinc electrode and thus promote parasitic hydrogen evolution. On the other hand, it has been shown that passivation of stainless steels improves under prolonged cycling[212]. Longer-term potentiostatic experiments with steel electrodes are thus in preparation in our laboratory.

In alkaline media, the solubility of titanium oxides is in the same order to that of iron oxides, and despite forming an electrochemically passivating layer upon contact with the electrolyte, continuous dissolution rates were observed during anodic and cathodic scans. However, this film prevents oxygen evolution at positive potentials. On one hand this could be beneficial as the film may contribute to the inertness of the titanium. On the other hand, titanium oxides are known to have an electric resistivity close to technically being insulators. Titanium applied in a battery may hence see increased resistivity under operation due to such layers formed. However, there may be a good case for use of titanium in sealed alkaline batteries due to its very high overpotential to oxygen evolution.

The most dissolution inert material found in this test is the nickel current collector. Neither in the voltammogram or in the galvanostatic charging protocol were there any observable dissolution above the detection limits. That does not suggest there is no dissolution at all, as one must consider the path dissolved ions must take from the working electrode surface to the plasma torch. The thermodynamic solubility of the nickel oxides and nickel oxyhydroxides are the lowest of all species in this test, but it is possible for them to form and precipitate in the inner walls of the tubing of the flow cell setup. With a more sensitive elemental analysis instrument such as an ICP-MS, much smaller dissolution rates may be detected. However, the ICP-MS is much less compatible with high total dissolved solids; on-line analysis with ICP-MS is usually not conducted in alkaline media with a KOH or NaOH concentration above 0.05 M[213], where the speciation of nickel oxides and hydroxides may be very different from 1 M KOH. Nevertheless, the resistance to dissolution displayed by nickel suggests that it would be an excellent current collector for bifunctional oxygen catalysts in alkaline media.

5.5 Conclusion and Summary

5.5.1 Conclusion

In conclusion, nickel was found to be the most and only dissolution resistant material in the potential ranges of the positive electrode of a zinc air battery during charging, while titanium was thought to have formed a lowly soluble, electrochemically inhibiting film that prevented oxygen evolution and may be the best choice for sealed battery chemistries, or where bubble formation causing mechanical detachment of catalyst material on the positive current collector is undesirable for alkaline zinc-air batteries. Silver was found to be highly unsuitable as a current collector for any type of aqueous battery due to its high dissolution rates, while stainless-steel alloys and the nickel alloy Hastelloy were found to dissolve trace amounts of hydrogen evolution-inducing agents that are undesirable for zinc-based negative electrodes and should be avoided.

5.5.2 Summary

With a high-surface area flow cell coupled on-line to an ICP-OES the dissolution tendencies of current collector candidates for zinc-air batteries were investigated by voltammetry and galvanostatic protocols. Stainless-steel alloy AISI 304 and the nickel alloy Hastelloy all exhibited limited dissolution within the potential range of the charging reaction in the zinc air battery, while galvanostatic tests showed that this effect was temporary only. Silver readily dissolved into solution at potentials above 0.9 V vs RHE, which was coupled to the oxidation to soluble Ag(I), and further dissolution in the onset of the oxygen evolution reaction due to formation of Ag(III). Nickel and titanium both had desirable abilities as current collector materials. Nickel under no circumstance displayed dissolution within detection limits and is suggested as an excellent current collector. Titanium, while displaying limited dissolution rates coupled to the precipitation of the film formed due to the formation of TiO_2 and Ti_3O_5, remained inert to the oxygen evolution reaction and seem to be passivated due to this film. It was suggested that titanium may be an excellent current collector for sealed battery chemistries where gas evolution is highly undesirable.

6 Stability of Nickel Substituted Spinel Cobalt Oxides

6.1 Introduction

The work in this chapter was done in with the aid of Beatrice Wolff as part of her Erasmus placement. Beatrice contributed with the synthesis, electrochemical and materials characterisation of the materials presented here.

In this chapter, the stability of spinel nickel cobalt oxides will be investigated by on-line metal dissolution detection and electrochemical benchmarking. Samples with a varying amount of nickel content will be synthesised and examined by common material science methods to characterise the resulting particle structure and morphology. Electrochemical benchmarking methods will be used to characterise the effect of dissolution upon the oxygen reduction reaction and the oxygen evolution reaction, and the instability dependence on nickel content will be examined. The discussion and interpretation of the results will be presented at the end of the chapter.

6.1.1 Background

The positive electrode of the electrochemically rechargeable zinc-air battery contains a bifunctional catalyst that can reduce oxygen to hydroxide ions and oxidise the hydroxide ions back to oxygen reversibly. These are also found in fuel cells and electrolysers. Typically, platinum and platinum alloys have been used for the oxygen reduction reaction[214 215], whereas iridium oxide and ruthenium oxide are the state-of-the-art catalysts for oxygen evolution[216 214 217 218 219 220].

These elements however, are costly due to their low abundance on the earth's crust, and are prone to side reactions such as oxide formation, dissolution particle agglomeration and Ostwald ripening[217 219]. Scientific research effort is directed towards affordable and

abundant alternatives. Such materials include transition metal oxides such as MnO_2, Co_3O_4, $MnCo_2O_4$ and $NiCo_2O_4$[23]. Transition metal oxides are promising bifunctional catalyst because they easily shift between oxidation states and are easily mixed to tune catalytic properties[214]. Investigations typically focus on discovery and performance of new variations of these materials that increase catalytic activity of the more affordable materials to approach the state-of-the-art noble element materials[220]. On the other hand, the long-term stability of the catalysts is difficult to quantify, and although less studies pay attention to this, turnover ratio (catalyst loss compared to product generation) is an important metric in the economic assessment of battery investment.

6.1.2 Motivation and previous studies

Historically there has been a few ways to assess long-term stability. The simplest method has been to cycle energy materials either as half cells or full batteries and observe increase in overpotential or capacity loss[221 216 222]. These methods provide a benchmark for performance longevity, but does not provide mechanistic insight as to why, unless post-mortem analysis is made, in which temporal information is lost. By elemental analysis of the electrolyte, mass loss of catalyst material can be estimated.

In the last 10 years more effort has been put to temporal observation of catalyst degradation. On-line ICP analysis has been used to reveal potential and history dependent dissolution of noble metal bifunctional catalysts and their alloys to better understand dissolution mechanisms and synthesise novel materials by informed, bottom-up approaches. However, these tests are usually performed on flat thin-films and hence the scope of materials that can be tested are limited[77].

Recently on-line dissolution analyses have been conducted on abundant materials such as transition metal oxides synthesised conventionally and prepared as electrode by drop-casting. Materials have been tested for dissolution under a constant current oxygen evolution current, and assessed against each other by a spiderweb plot, but no investigation is made as to why dissolution takes place[223].

Co_3O_4 has a spinel structure with a close-packed face-centred cubic configuration of Co^{2+} in tetrahedral sites, Co^{3+} in octahedral sites and $2O_4$ on edge sites[224, 225, 218, 220] and is known as an efficient oxygen evolution catalyst. However, by substitution of nickel to form inverse spinel $NiCo_2O_4$, which increases its catalytic activity due to increased

conductivity, atomic structure modifications, formation of oxygen vacancies[226] and surface atom rearrangement[220 227 224 220]. The actual formula of nickel cobalt oxide can be written as $Co^{2+}_{1-x}\ Co^{3+}_{x}\ [Co^{3+}\ Ni^{2+}_{x}Ni^{3+}_{1-x}]O_4$, with octahedral sites occupied by Ni^{2+}, Ni^{3+} and Co^{3+}. Ni(Oh) and Co(Td) exchange takes place easily, causing more disorder in the structure[228 226]. As nickel doping decreases the band gap due to creation of oxygen vacancies, conductivity increases and is thought to contribute to increased catalytic activity[214, 215, 224].

It has been suggested that with an increase in nickel content there is an increase in oxygen reduction[214] and oxygen evolution[229] performance. However, little work has

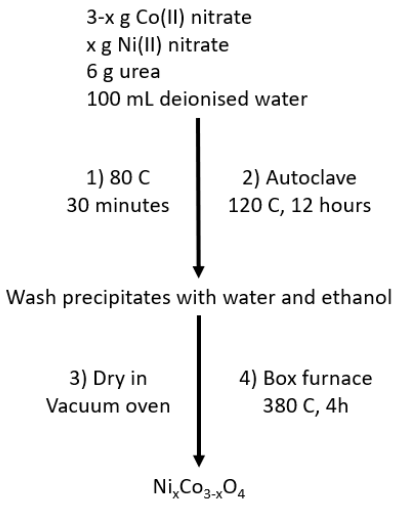

Figure 6.1 Synthesis scheme for spinel nickel cobalt oxides.

delved into how the nickel content affects the stability of the catalyst.

In this work, the change in stability of increased nickel content in spinel Co_3O_4 by on-line metal detection from catalyst leeching. The electrochemical performance will be assessed before and after dissolution to note if dissolution alters performance, and if it is related to increase in nickel content.

6.2 Experimental

6.2.1 Synthesis route of $Ni_xCo_{3-x}O4$ oxide samples

Nickel substituted cobalt oxides were synthesised by the procedure outlined in Figure 6.1:

2-x g $Co(NO_3)_2.6H_2O$ and x g $Ni(NO_3)_2.6H_2O$ (Alfa Aesar) with x = 0, 0.4, 0.5, 0.8 and 1.0 was dissolved in water (50 mL) and stirred under reflux (80 C). Urea (Alfa Aesar) (6 g) dissolved in ultrapure water (50 mL) was added dropwise. After 30 minutes, the pink solution was transferred to an autoclave and left under heat (120 ^oC) for 12 hours. The solids from the obtained suspension was extracted by centrifuging at 5000 RPM for 20 minutes and decanting clear solution. To remove further residue, ethanol and water was added to the solids for another round of centrifuging. The solids were subsequently dried in a vacuum oven (40 ^oC) overnight, before calcination at 380 ^oC for 4 hours.

6.2.2 Materials characterisation

The samples were characterised by powder x-ray diffraction (PXRD) by a Rigaku SmartLab diffractometer with a 9 kW Cu Kα source equipped with the High-Speed Position Sensitive Detector System for accurate alignment between sample scans. Scans were taken in reflection mode for 10 hours between 10 and 110 2θ angles. Sample size and morphology was inspected by field emission scanning electron microscopy (FE-SEM) with a JEOL JSM-7800F at 5 kV accelerating voltage.

6.2.3 Electrochemical equipment and electrode preparation

Electrochemical characterisation was conducted in a three-electrode cell, consisting of a glassy carbon rotating disk working electrode (0.196 cm^{-2}), Hg/HgO reference electrode in 1 M KOH, and a nickel mesh counter electrode. The 1 M KOH electrolyte was prepared by diluting concentrated 38 wt% aqueous KOH solution (VWR). Nickel mesh was used an inexpensive substitute for platinum, as no rate of nickel dissolution could be observed in previous on-line dissolution experiments in 1M KOH solutions at any potential (Chapter 5). All potentials are reported against RHE. Conversion of potentials were done by conducting cyclic voltammograms of platinum in identical media, and comparing the hydrogen absorption and desorption peak potentials with a cyclic voltammogram of platinum in NHE conditions.

To examine the samples, an ink consisting of 1 mg catalyst, 1 mL H_2O, 1 mL isopropanol and 50 µL 1% Nafion solution was prepared. 4 aliquots of 5 µL was drop-casted onto the glassy carbon working electrode to reach a loading of 100 µg cm^{-2}. An IR-lamp was used to accelerate the evaporation rate of the ink.

6.2.4 On-line dissolution detection set-up

On-line dissolution observation was conducted with the 4-Lc flow cell as described in previous chapters. The counter electrode compartment was filled with 1 M KOH and contained a carbon felt counter electrode. The reference electrode was a leak free Ag/AgCl 1 mm diameter electrode.

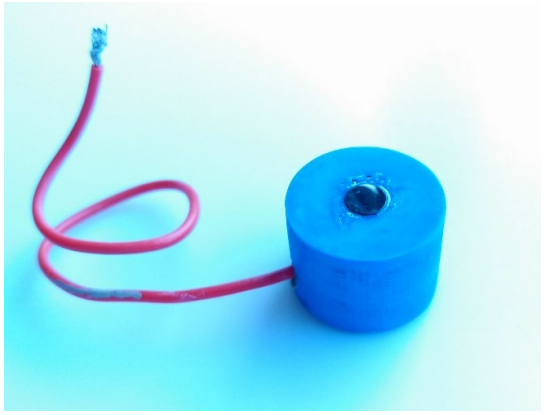

Figure 6.2 Fabricated glassy carbon electrode for powder-deposited on-line ICP electrochemical analysis.

To properly mount the powders, glassy carbon electrodes were fabricated by additive manufacturing, displayed in Figure 6.2. The housing was 3D-printed by fused deposition modelling with ABS thermoplastic. On one side, a glassy carbon rod was inserted and fixed with epoxy glue, and on the other side a stainless-steel wire lead was connected to the backside of the glassy carbon rod mechanically and electrically by silver glue. The glassy carbon rod was then sanded and polished down to be level with the surface of the housing. Similar to the three-electrode cell electrochemical experiments, ink was drop-casted to each a loading of 100 μg cm^{-2} [218].

The ICP-OES instrument was configured to a 1.4 kW power the RF-coil, 14 L min^{-1} argon gas rate, 0.7 L min^{-1} nebuliser flow rate, and a sample matrix a flow rate of 1.5 mL min^{-1}. The argon gas line to the nebuliser was moisturised by an argon humidifier to minimise salt deposits on the surfaces of the torch assembly.

Time alignment step protocols to synchronise spectroscopic data with electrochemical data as developed in Chapter 4 were performed at the start of each experiment day, and calibration standards of cobalt and nickel were measured at the end of every experiment day in concentrations 100-1000 parts per billion. For cobalt a limit of detection of 1.3 ng s^{-1} cm^{-2} was achieved, and for nickel a limit of detection of 2.0 ng s^{-1} cm^{-2} was achieved. The observed wavelengths for cobalt was 238.892 nm, and for nickel 352.453 nm, which corresponds to the most intensely emitting wavelengths according to the ICP

Expert software. Due to the time-consuming nature of the on-line ICP-OES measurements, only the first cycle of the dissolution voltammograms were taken.

6.2.5 Protocol for determination of dissolution impact upon catalytic activity

To test for changes in performance caused by elemental dissolution from the samples, a testing protocol was made as seen in Figure 6.2. 10 cycles of cyclic voltammograms were initially taken to characterise sample-specific electrochemical peaks and magnitude. Then a series of cyclic voltammograms were taken at increasing scan rate to get a relative measure of the capacitance of the double layer by plotting the non-faradaic current[230]:

$$C = \frac{\Delta j}{v} = \frac{j_{a(1.1V)} - j_{c(1.1V)}}{v} \qquad \text{Eq. 6.1}$$

Where C is the capacitance in mF cm^{-2}, $j_{a(1.1\ V)}$ and $j_{c(1.1\ V)}$ is the anodic and cathodic current density at 1.1 V in mA cm^{-2}, and v is the scan rate in V s^{-1}. Scans were not taken too far in the anodic direction in order to avoid dissolution, however the current at 1.1 V is not truly non-faradaic in all cases. Hence this test serves only as an indication on surface property changes.

An anodic linear sweep was then taken of the sample to find the Tafel slope [229]:

$$\eta = A \times log_{10}\left(\frac{i}{i_0}\right) \qquad \text{Eq. 6.2}$$

Where η is the overpotential, A is the Tafel slope, i the current and i_0 the exchange current. Overpotential to reach the oxygen evolution current density at j = 1 mA cm^{-2} was also noted. Following that, the cell was oxygen saturated for 20 minutes before performing linear sweep voltammograms at increasing rotation rate at the rotating disk electrode to extract the inherent kinetic current i_K from Koutecky-Levich analysis:

$$\frac{1}{i_m} = \frac{1}{i_K} + \frac{1}{i_{MT}} \qquad \text{Eq. 6.3}$$

Where i_m is the total current and i_{MT} is the mass transport limiting current. The kinetic current density at 0.5 V was considered for this calculation. The kinetic current is related to the inherent catalytic activity of the sample and was used to minimise mass transport effects from stirring or electrode preparation.

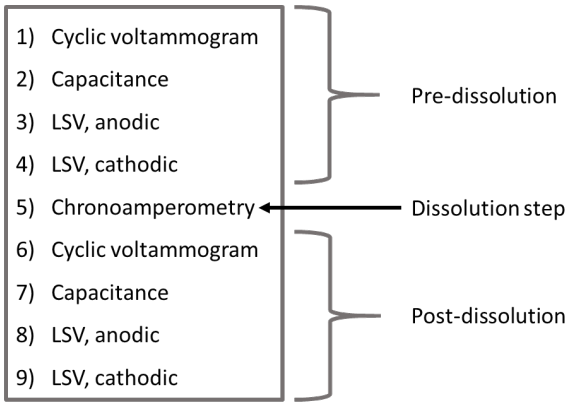

Figure 6.3 Electrochemical test protocol for dissolution effects.

The sample would then be held at a potential were dissolution was found to take place for 20 minutes, before the analysis procedure steps 1-4 was repeated to find if any changes in electrochemical half-cell peaks, surface area, oxygen reduction current or oxygen evolution rate had occurred as a consequence.

6.3 Results & discussion

In this section, the results from off-line experiments will be presented where the samples x = 0.0, x = 0.4, x = 0.5, x = 0.8, x = 1.0 will be characterised by PXRD, SEM and cyclic voltammetry in stagnant solution. After that, on-line ICP-OES will be conducted to identify and quantify the order and potential range of dissolution. The results from the as outlined protocol in Figure 6.3 will be presented. Lastly, discussion and interpretation will be conducted at the very end of this section. Form hereon, the samples will be referred to as $x_{0.0}$, $x_{0.4}$, $x_{0.5}$, $x_{0.8}$ and $x_{1.0}$.

6.3.1 Powder X-ray diffraction results

Figure 6.4 (A) displays the background-subtracted powder x-ray diffractogram (PXRD) of sample $x_{0.0}$ before and after the calcination step. Pre-calcination, no diffraction peaks were recorded. After calcination, diffraction peaks at 2θ corresponding to the reflections of planes (111), (220), (311), (222), (400), (422), (511), (440), (533) and (731) were clearly visible[225], and in agreement with the ICDS #28158 card for Co_3O_4. No evidence of other cobalt oxide phases could be distinguished from the diffractogram[220].

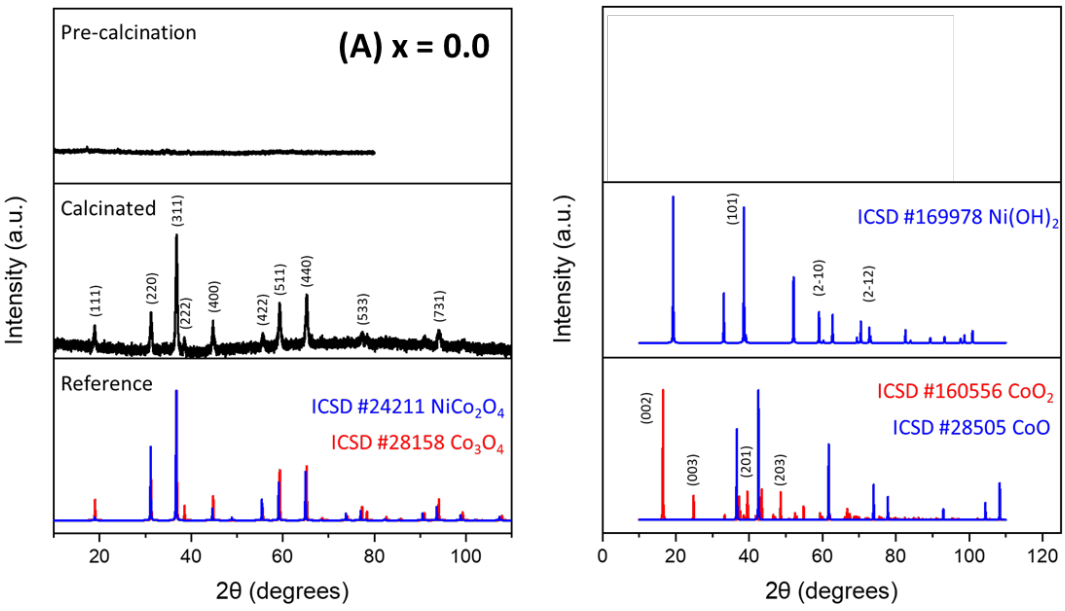

Figure 6.4 (A) PXRD of sample $x_{0.0}$ before and after calcination. PXRD of possible side products displayed on the right.

Similarly to $x_{0.0}$, figure 6.5 displays the powder x-ray diffractogram (PXRD) of samples (A) $x_{0.4}$, (B) $x_{0.5}$, (C) $x_{0.8}$ and (D) $x_{1.0}$ before and after the calcination step. Pre-calcination, no diffraction peaks were recorded. After calcination, diffraction peaks at 2θ corresponding to the reflections of planes (111), (220), (311), (222), (400), (422), (511), (440), (533) and (731) were clearly visible, and in agreement with the ICDS #24211 card for $NiCo_2O_4$. No additional diffraction peaks are visible, which suggests that nickel oxide side products were not formed during sintering.

The diffractograms of the samples are visibly broader as nickel content is increased in the starting material. Scherrer's equation[218] (Eq. 6.4) relates the full width at half maximum (FWHM) of the reflection peaks to the average size of the crystallites in the sample, as a measure of the crystallinity:

$$D = \frac{K\lambda}{\beta cos\,(\theta)} \qquad \text{Eq. 6.4}$$

Where D is the average size of the crystallite, K is a unitless shape factor, λ is the wavelength of the copper Kα X-ray source and β is the FWHM value of the (311)

reflection peak[214]. K was taken as 0.9[220]. The average crystallite sizes were calculated to 48 nm, 30 nm, 29 nm, 23 nm and 25 nm for $x_{0.0}$, $x_{0.4}$, $x_{0.5}$, $x_{0.8}$ and $x_{1.0}$ respectively.

The diffractograms confirm that the heteroatom doping has visibly taken place[231]. Figure 6.6 displays the shift in 2θ degree values as nickel content is added in the starting material[224]. The negative shift of reflection peaks are the result of lattice expansion from heteroatom doping, which indicates that the nickel has been incorporated into the cobalt oxide structure[216]. The reflection peak shifts also increase with increasing concentration of nickel in the starting material, which means that the lattice expands to accommodate more nickel in the cobalt oxide structure.

The signal-to-noise ratio of the diffractrograms was too small to confidentily determine if a single phase was successfully synthesised, as no doublet peaks appear. However the (222) reflection from Co_3O_4 is still present in the diffractograms of the nickel doped samples, but with reduced intensity.

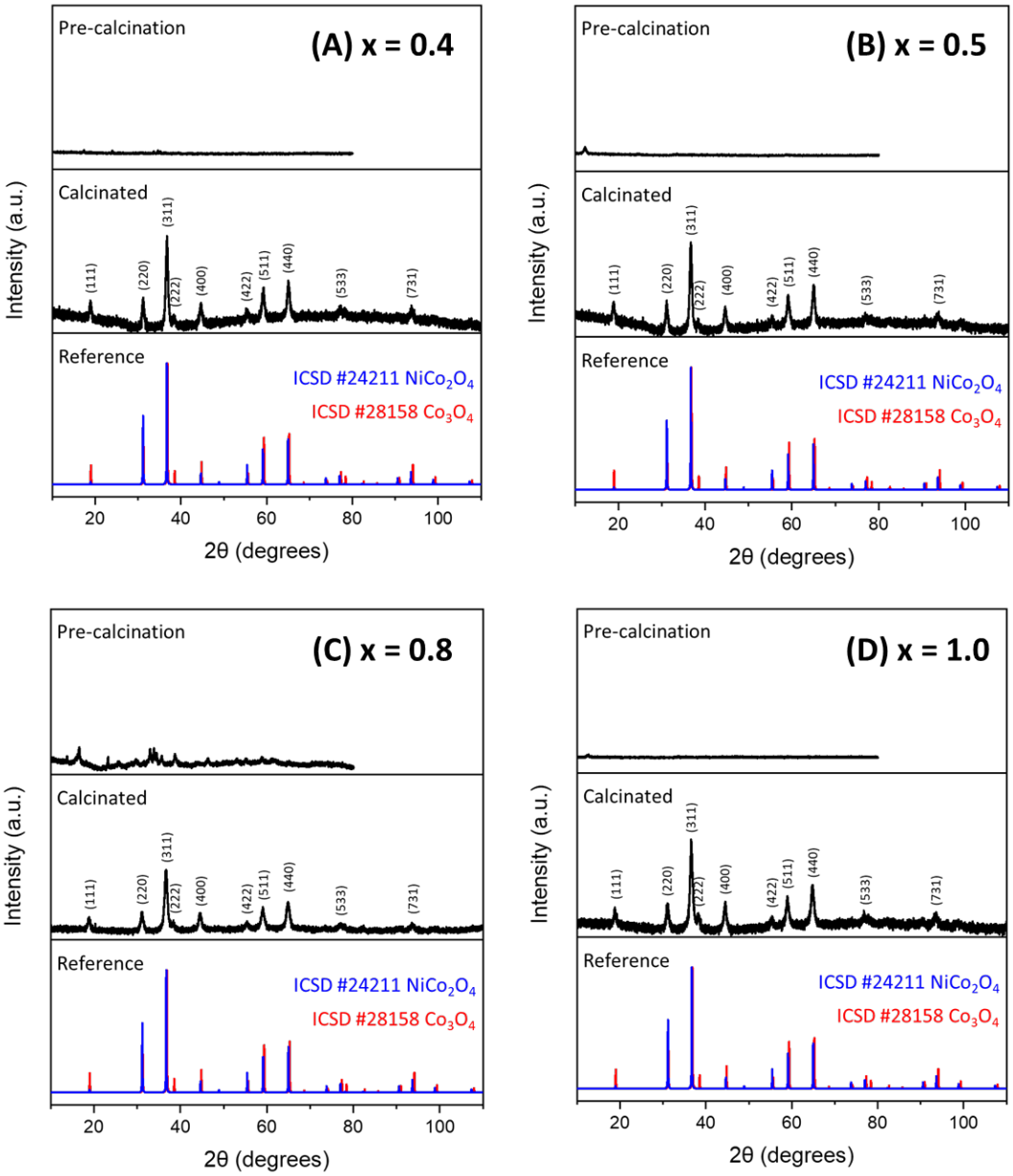

Figure 6.5 A) PXRD of sample $x_{0.4}$ (A), $x_{0.5}$ (B), $x_{0.8}$ (C) and $x_{1.0}$ (D) before and after calcination. PXRD of possible cobalt oxide and nickel cobalt oxide provided for reference.

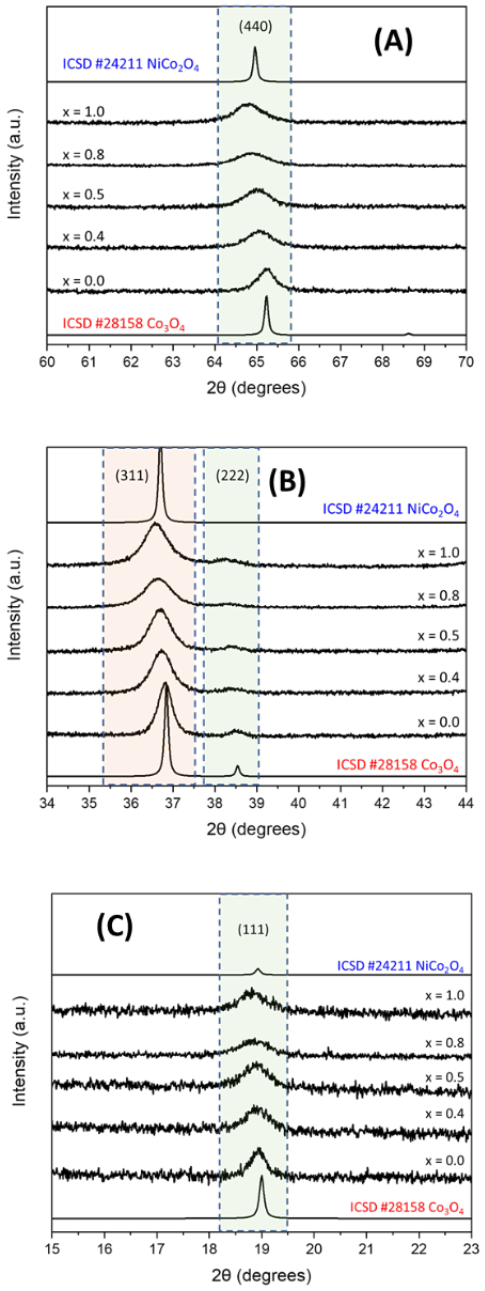

Figure 6.6 PXRD shift of reflection peaks (A) (440), (B) (311) and (222), and (C) (111) for the synthesised samples.

A diffractogram of commercial nickel oxide was also taken, to see if the nickel had separated out as a second phase in the prepared samples. In the commercial nickel oxide samples, significant peaks appeared at 35, 42, 51, 62, 74 and 79 degrees diffraction angle. Comparing that to the calcinated samples and the commercial spinel cobalt oxide, none of the peaks from the nickel oxide overlap. Hence, no observable nickel oxide phase was detected from powder x-ray diffraction. These findings suggest that the nickel has been incorporated into the cobalt oxide phase.

6.3.2 FE-SEM imaging

The $x_{0.0}$ sample consists of mainly two morphologies that make up a hierarchical rosette morphology. FE-SEM images obtained for sample $x_{0.0}$ is presented in Figure 6.7. The macroscale image shows that the particle morphology is arranged in rosette-like clusters consisting of flakes, with each flake having a length of a few micrometres, and thickness of 70 nanometres. A magnified image however reveals that the flakes are lodged into sub-micron sized particles of roughly 60 nanometres diameter, which is 10 nm larger than the crystallite sizes calculated from the Scherrer's equation.

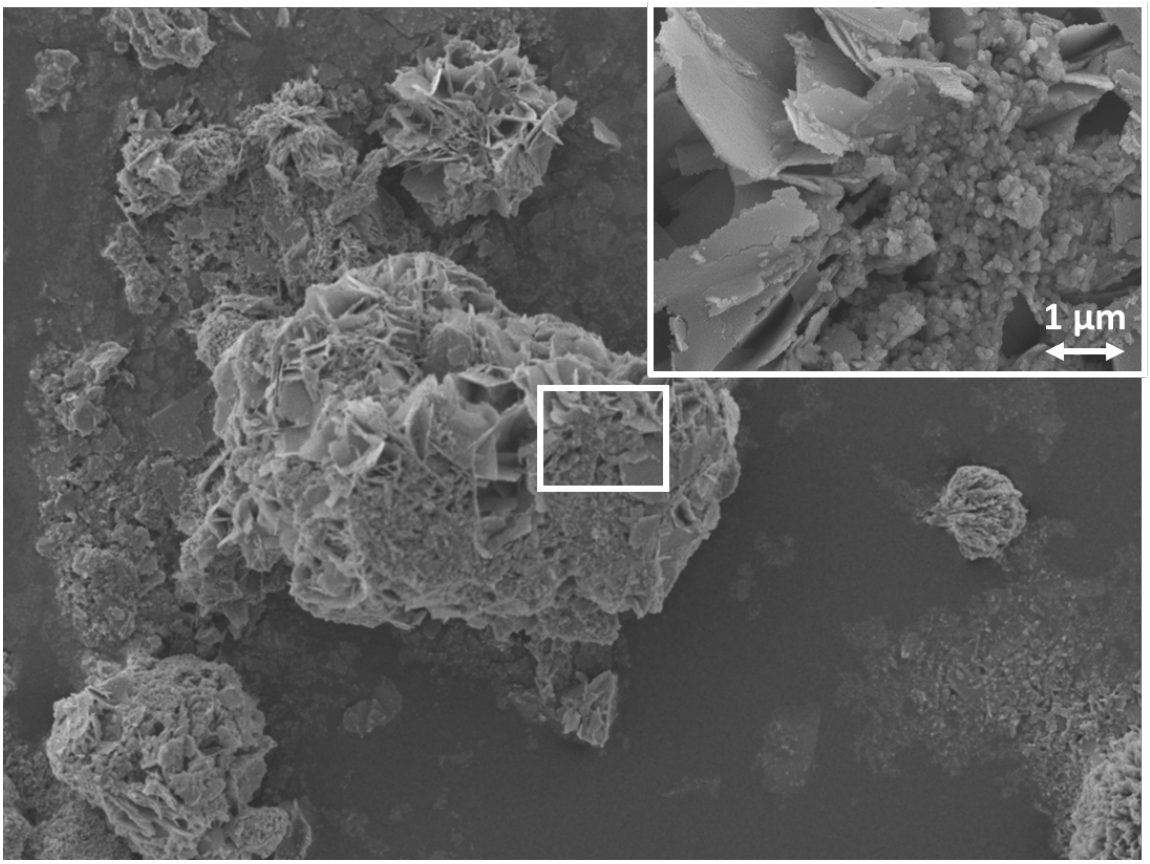

Figure 6.7 FE-SEM image of sample $x_{0.0}$. Inset displays magnified view of the white square.

The $x_{0.4}$ sample has an apparent hierarchical morphology where rosette-like clusters are made up of mainly 3 particle morphologies. FE-SEM images for sample $x_{0.4}$ is presented in Figure 6.8. The macroscale image shows that the particle morphology consists of clusters of interconnected flakes, where each flake has a length of a few micrometres. A magnified image shows that sub-micron particles of around 40 nanometres diameter, which is 10 nanometres larger than the average diameter found from Scherrer's equation, are covering the surface of these flakes. Rod-shaped structures with lengths around 500 nanometres and widths of around 60 nanometres were found to cover the surfaces of the larger flake clusters as well.

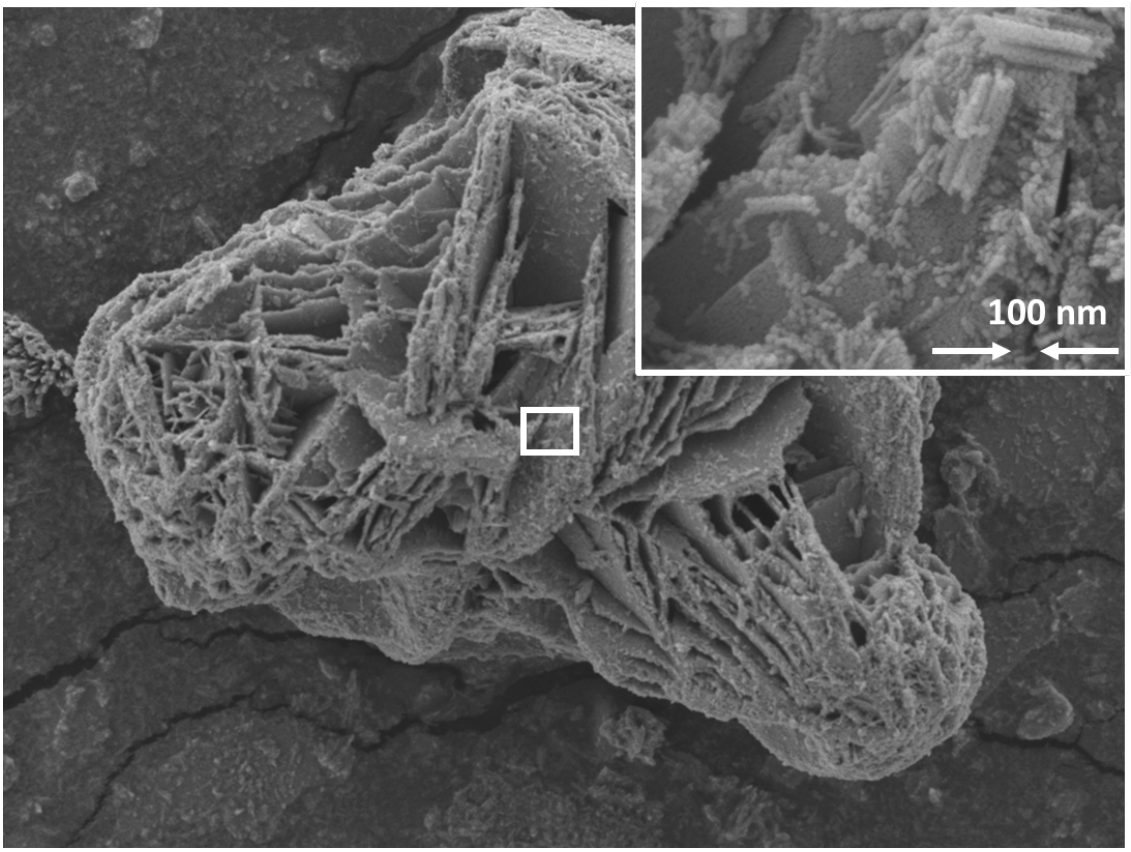

Figure 6.8 FE-SEM image of sample $x_{0.4}$. Inset displays magnified view of the white square.

The $x_{0.5}$ sample consist of two small-scale particle morphologies which make up two morphologies on the micrometre range FE-SEM images for sample $x_{0.5}$ is presented in Figure 6.9. The macroscale image shows that the material appears as lumped clusters with an apparent smoother surface compared to the $x_{0.0}$ and $x_{0.4}$ samples. The clusters have an apparent size in the order of tens of micrometres. The magnified image reveals a section with an apparent mossy structure, but which contains rods with apparent lengths of 400 nanometres, and widths in the range of 35 nanometres, as well as particles with diameters of 35 nanometres, which is 7 nanometres more than estimated by the Scherrer's equation applied to the (311) reflection peak of the diffractogram.

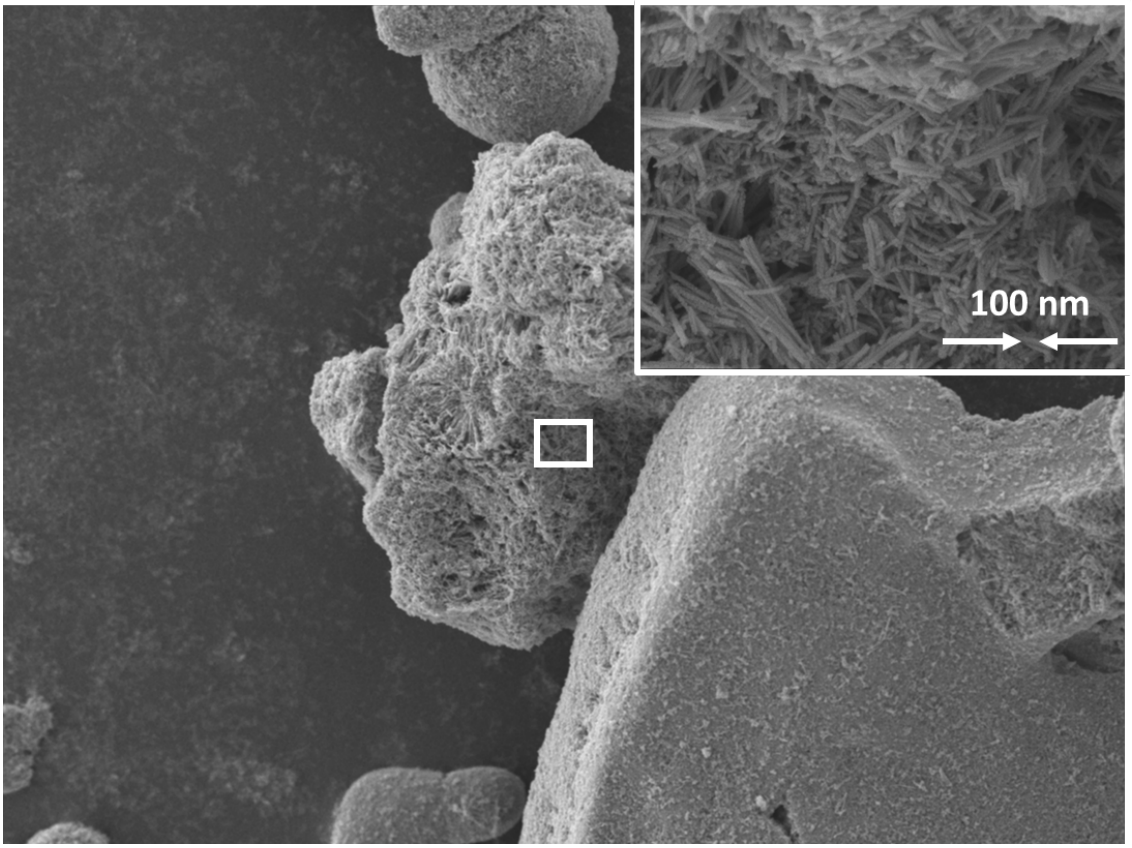

Figure 6.9 FE-SEM image of sample $x_{0.5}$. Inset displays magnified view of the white square.

The $x_{0.8}$ sample is made up of particles of mixed sizes and morphologies. FE-SEM images for sample $x_{0.8}$ is presented in Figure 6.10. The macroscale image shows particles in the shape of spherical balls, in the order of tens of micrometres, with an apparent rough surface. A magnified image shows that the surface of the spheres consists of a mixture of mossy structures and rods where the length is in the order of 500 nanometres, and the width in the order of 35 nanometres. Particles were also found scattered on these surfaces with diameters around 28 nanometres, which is close to the estimated particle size from Scherrer's equation.

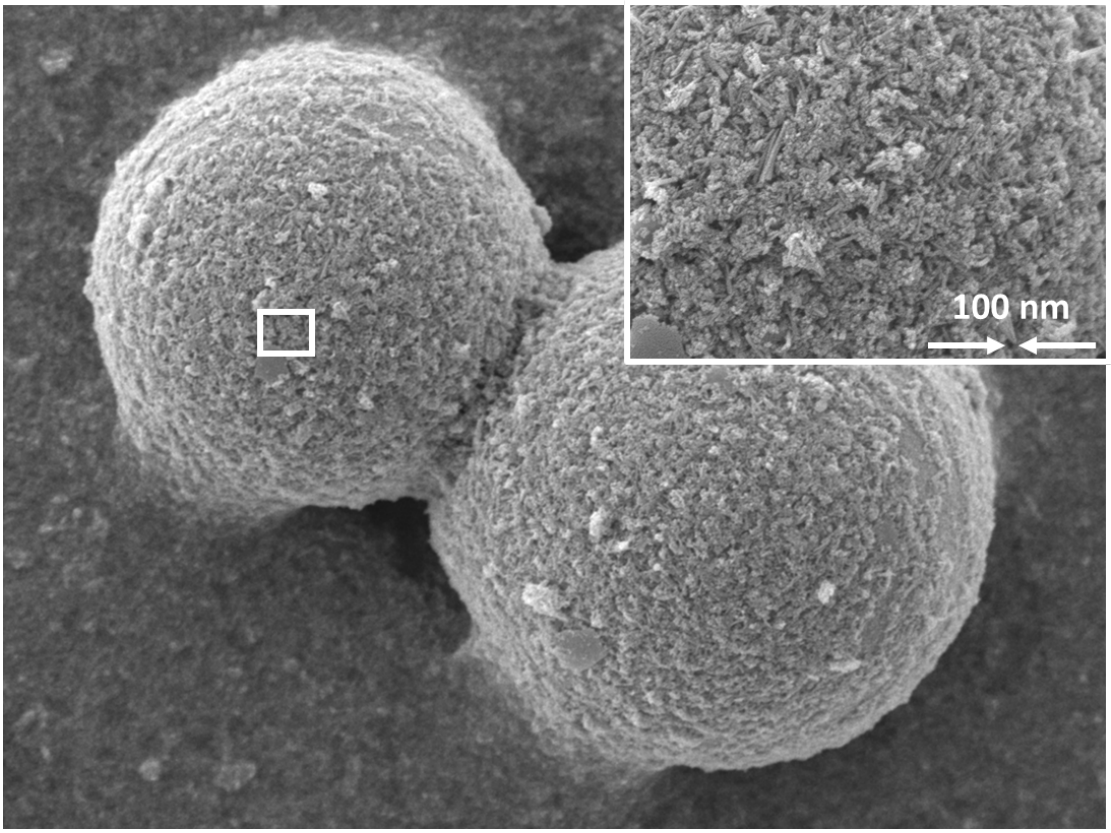

Figure 6.10 FE-SEM image of sample $x_{0.8}$. Inset displays magnified view of the white square.

Sample $x_{1.0}$ is made up of small particles of varying morphologies. The FE-SEM images for sample $x_{1.0}$ is presented in Figure 6.11. The macroscale image shows particles in the shape of spherical balls, in the order of tens of micrometres, with an apparent rough surface. A magnified image shows that the surface of the spheres consists of a mixture of mossy structures, particles with diameters in the order of 25 nanometres which is close to the estimated diameter from the Scherrer's equation and rods where the length is in the order of 400 nanometres, and the width in the order of 40 nanometres. Some flakes were also found with a length and width in the order of 100 nanometres on the surface of the spheres.

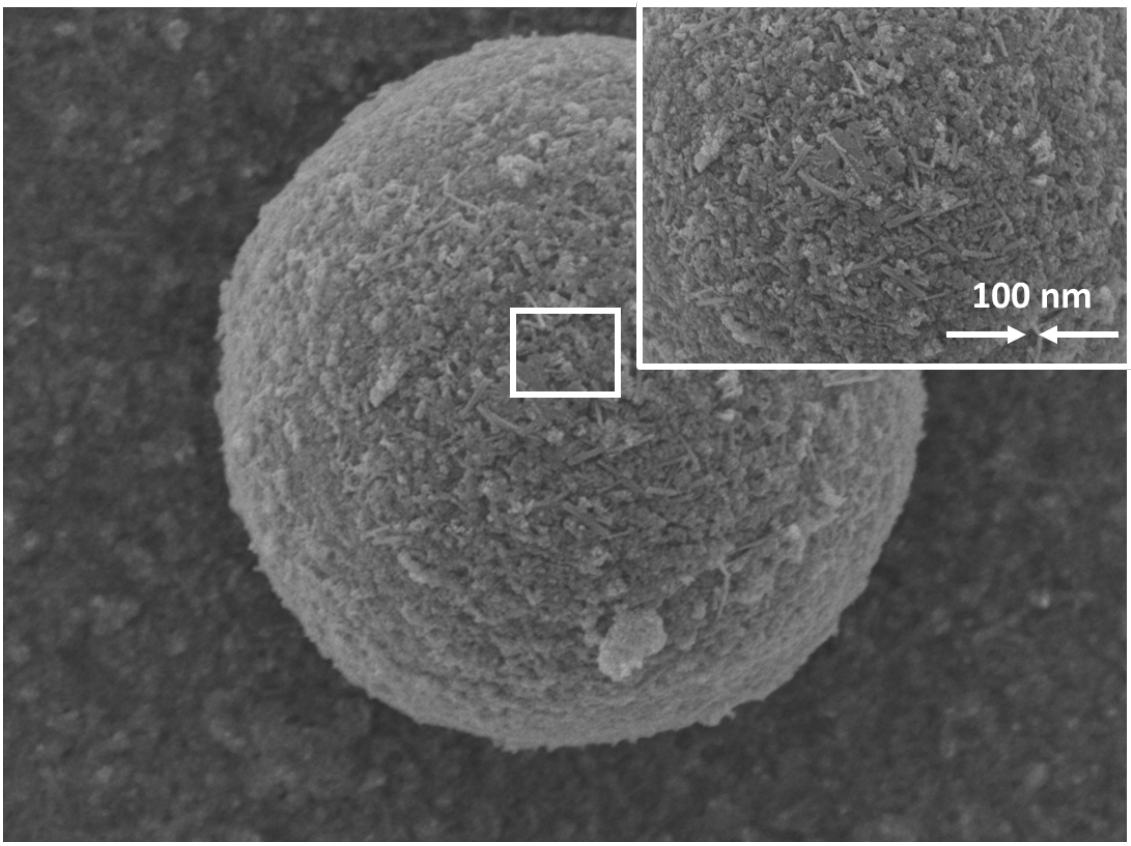

Figure 6.11 FE-SEM of sample $x_{1.0}$. Inset displays magnified view of the white square.

In summary, the FE-SEM images of the prepared materials show that at the macroscale the samples are lumped together in clusters, but that on the surface a variety of morphology appears[214]. In general, samples $x_{0.0}$ and $x_{0.4}$ contain more flakes as part of their morphology, and as the proportion of nickel increases with the samples, less flakes and sub-micron particles appear. As nickel content increases, more rods and mossy structures in the sub-micron range is formed instead[224]. Particles found in the micrographs decrease in size with increasing nickel content[219], in agreement with the estimated crystallite sizes calculated from the Scherrer's equation[232 229].

6.3.3 Cyclic voltammetry characterisation

The samples were electrochemically characterised by stationary cyclic voltammetry with the RDE setup. The result is shown in Figure 6.12. sample $x_{0.0}$ The electrochemical half-cell reactions will be discussed in Section 6.3.7, However, a negative shift is imposed on the peaks as the nickel content is increased. Sample $x_{0.8}$ have a much larger geometric current density magnitude compared to the other samples, and will be used to initially investigate instability tendencies due to its pronounced features.

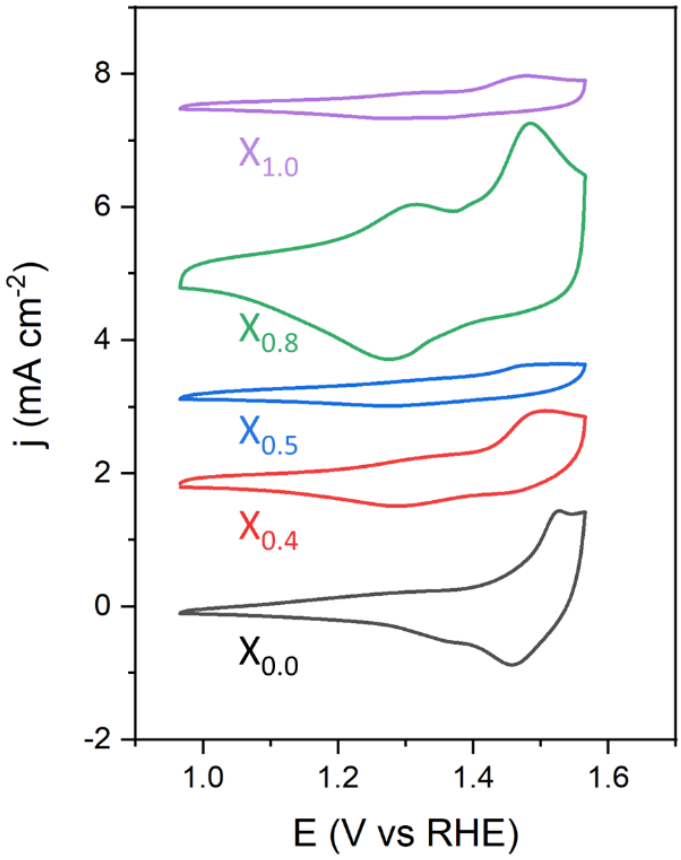

Figure 6.12 Stationary cyclic voltammograms taken at scan rate of 200 mV s^{-1} for all synthesised samples in 1 M KOH electrolyte.

The nickel-containing catalysts undergo irreversible change as the potential range is expanded in the cathodic direction. Figure 6.13 shows the voltammogram of sample $x_{0.8}$ within the water splitting window of 0.1-1.6 V. Sample $x_{0.8}$ was chosen as it had the most visible signature peaks for cobalt oxidation, and hence any surface changes would be most obvious for this sample. The voltammogram starts at the open circuit potential of 1.0 V and is scanned in the anodic direction. Upon the first cycle, two anodic peaks

a and b appear at 1.35 V and 1.5 V respectively. On the return sweep a cathodic peak c at 1.3 V and a peak d at 0.3 V. On the subsequent cycles peak a, b and d disappear, while an increase in current density above 1.5 V is recorded. In the two subsequent scans all peaks disappear, and the current density magnitude decrease further.

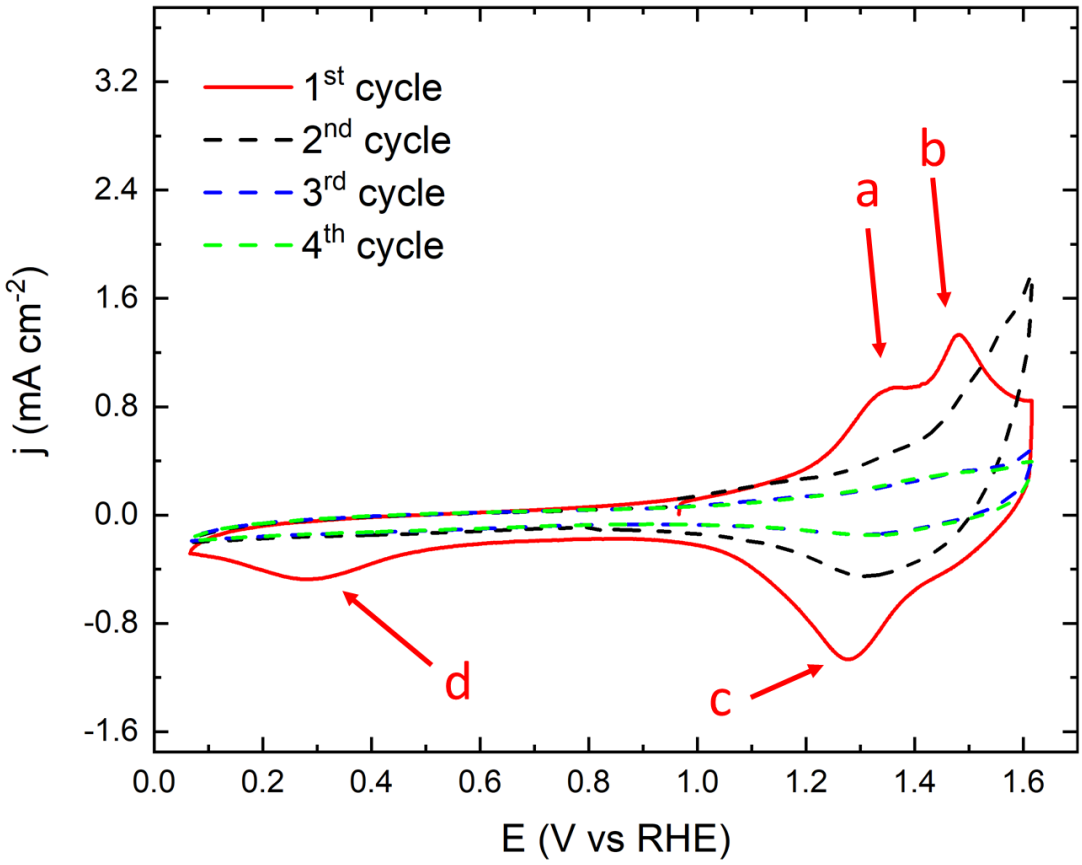

Figure 6.13 Stationary cyclic voltammogram of sample $x_{0.8}$ in 1 M KOH at a scan rate of 10 mV s^{-1}.

Cyclic voltammograms for the bare glassy carbon substrate and nickel oxide with similar loadings were taken for reference and displayed in Figure 6.14 It is clear that the signals in the cyclic voltammograms in Figures 6.12 and 6.13 are actually arising from the nickel cobalt oxide, and not from nickel oxide side products.

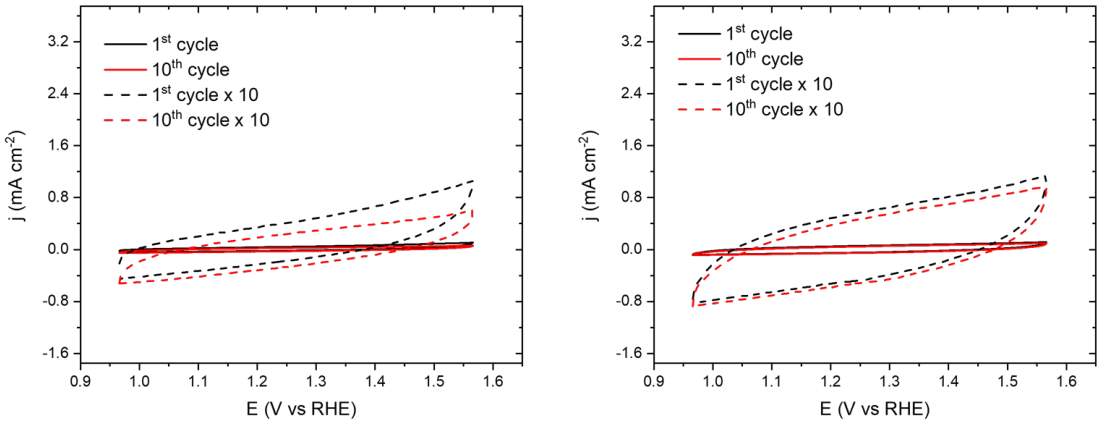

Figure 6.14 Stationary cyclic voltammograms of glassy carbon (left) and drop-casted NiO (right) in 1 M KOH at a scan rate of 10 mV s^{-1}. Dashed lines represent 10 times magnification of current densities.

Since the peak signatures from the nickel cobalt oxide disappear on the first wide scan, it was thought that one of the peaks from the voltammogram correspond to an electrochemical degradation process, possibly due to changes of the surface structure[229].

Sample $X_{0.8}$ was probed by on-line ICP-OES analysis. Figure 6.15 shows cycle 1-4 of an expanding window per cycle during on-line analysis. Towards positive potentials, "spikes" of cobalt and nickel signal was observed, while the scan in the negative direction a consistent increase of dissolution was seen upon the third scan. Upon the fourth scan, the potential scan window was extended in both directions. The dissolution onset in the negative direction was shifted further negative.

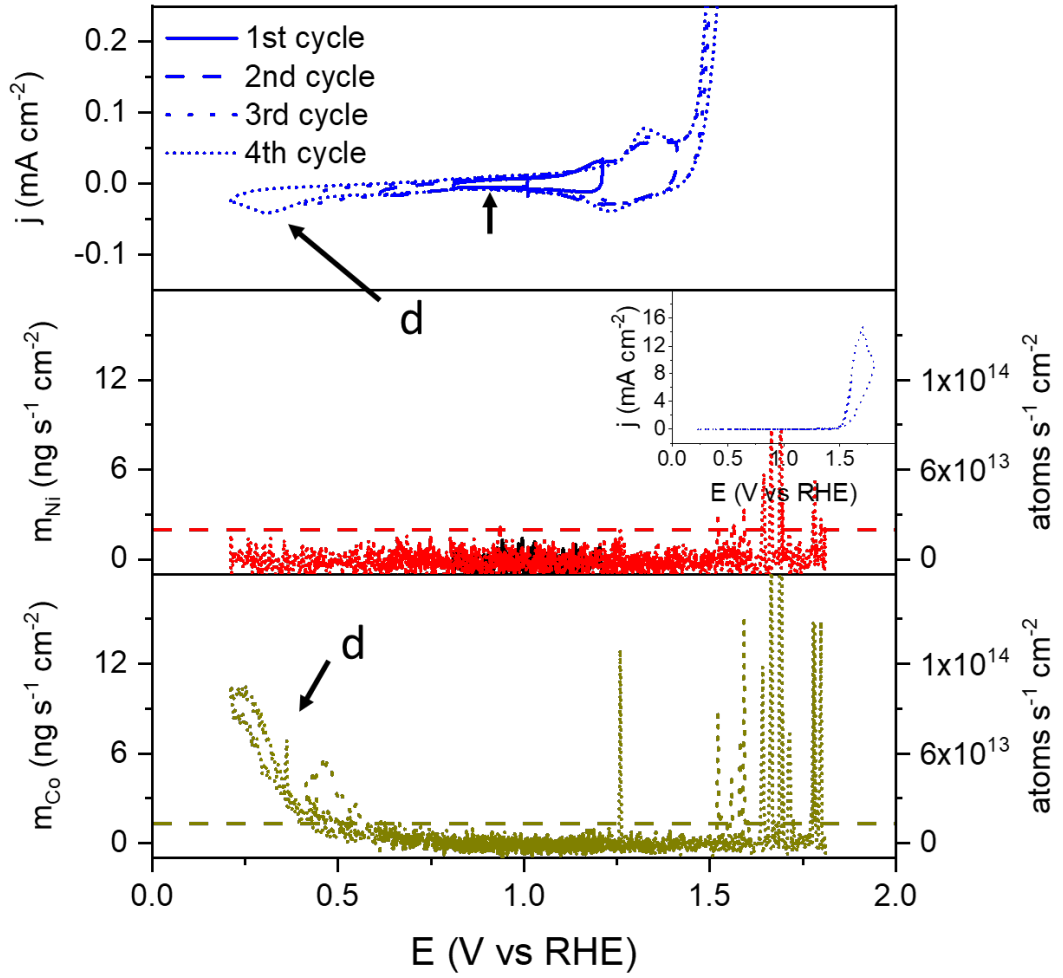

Figure 6.15 Cyclic voltammogram of sample $x_{0.0}$ in 1 M KOH conducted with the on-line flow cell-ICP setup taken at 2 mV s^{-1}. Top panel and inset displays the electrochemical current, middle panel displays the cobalt dissolution rate, and bottom panel the nickel dissolution rate. Dashed lines represent detection limits.

In the subsequent on-line measurements, only one cycle of cyclic voltammetry was measured.

6.3.4 Dissolution testing by on-line flow cell ICP-OES

In this section, the voltammograms taken with the on-line ICP-OES setup for all samples will be presented. To investigate whether any of the electrochemical peaks of the cyclic voltammograms corresponded to a dissolution process, each sample was examined in the on-line ICP flow-cell set-up for real time metal detection.

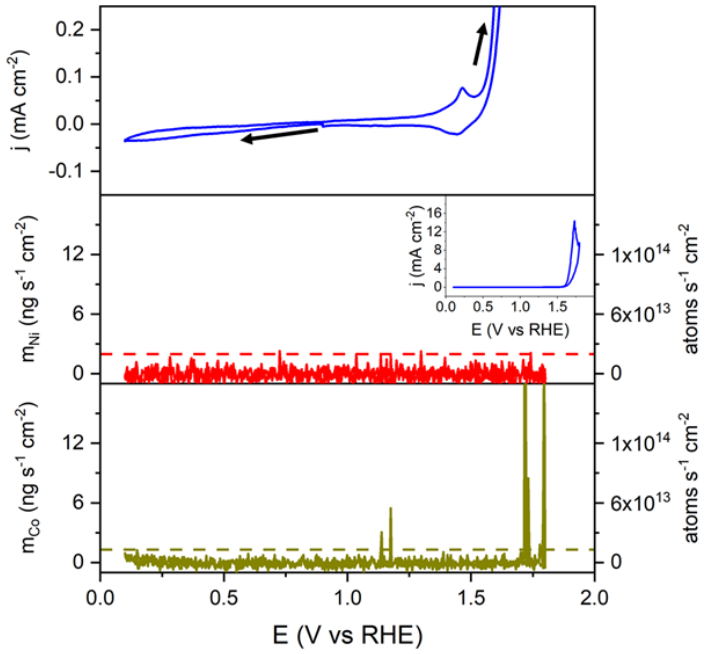

Figure 6.16 Cyclic voltammogram (first cycle) of sample $x_{0.0}$ in 1 M KOH conducted with the on-line flow cell-ICP setup taken at 2 mV s^{-1}. Top panel and inset displays the electrochemical current, middle panel displays the cobalt dissolution rate, and bottom panel the nickel dissolution rate. Dashed lines represent detection limits.

Figure 6.16 presents the electrochemical and dissolution rate voltammogram of sample $x_{0.0}$. The potential is scanned in the cathodic direction from the open circuit potential of 0.9 V. In the electrochemical voltammogram, only peak b and c are present, which may correspond to the oxidation and reduction of the Co^{4+}/Co^{3+} redox couple prior to oxygen evolution. The inset shows that the oxygen evolution current density reaches over 10 mA cm^{-2}. The dissolution voltammogram for nickel in Figure 6.16 shows that no dissolution rate above the detection limit was observed within the entire potential range scanned. In the dissolution rate voltammogram for cobalt, the dissolution rate never increases to above the detection limit threshold. On the anodic scan, spikes of cobalt dissolution rate signals appear as the potential enters the oxygen evolution region at 1.65 V.

Figure 6.17 presents the electrochemical and dissolution rate voltammogram of sample $x_{0.4}$ (A), $x_{0.5}$ (B), $x_{0.8}$ (C) and $x_{1.0}$ (D). The potential is scanned in the cathodic direction from the open circuit potential of 0.9 V. In the electrochemical voltammogram (A),

peak d is present on the cathodic sweep at 0.223 V. On the anodic sweep, a wide oxidation feature which may correspond to peak a and b are present, and a wide

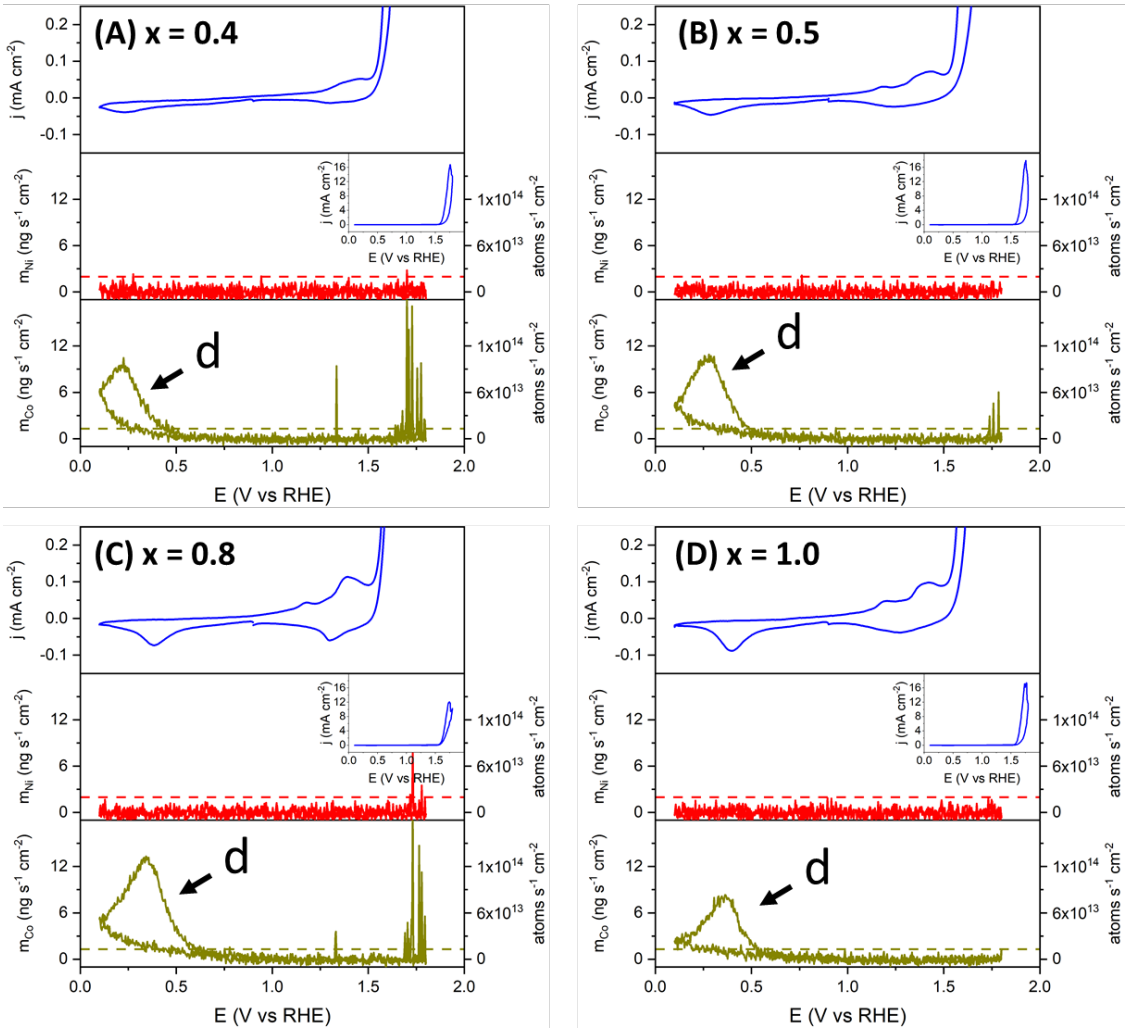

Figure 6.17 Cyclic voltammogram (first cycle) of sample $x_{0.4}$ in 1 M KOH conducted with the on-line flow cell-ICP setup taken at 2 mV s^{-1}. Top panel and inset displays the electrochemical current, middle panel displays the cobalt dissolution rate, and bottom panel the nickel dissolution rate. Dashed lines represent detection limits.

reduction feature on the cathodic sweep after the second vertex potential which may correspond to peak c. peak a, b and c may correspond to the oxidation and reduction of the Co^{4+}/Co^{3+} redox couple prior to oxygen evolution. The inset shows that the oxygen evolution current density reaches over 10 mA cm^{-2}.

The dissolution voltammogram for nickel in Figure 6.17 shows that no dissolution rate above the detection limit was observed within the entire potential range scanned. Dissolution of cobalt was observed in the cathodic scan with a maximum of 9 ng s^{-1} cm^{-2} at 0.226 V, which coincides with peak d of the electrochemical voltammogram. On the anodic scan, inconsistent spikes of cobalt dissolution were observed in the potential region positive of 1.65 V corresponding to oxygen evolution.

Figure 6.17 (B) presents the electrochemical and dissolution rate voltammogram of sample $x_{0.5}$. The potential is scanned in the cathodic direction from the open circuit potential of 0.9 V. In the electrochemical voltammogram, peak d is present on the cathodic sweep at 0.286 V. On the anodic sweep, a oxidation features which may correspond to peak a and b are present, and a wide reduction feature on the cathodic sweep after the second vertex potential which may correspond to peak c. Peak a, b and c may correspond to the oxidation and reduction of the Co^{4+}/Co^{3+} redox couple prior to oxygen evolution. The inset shows that the oxygen evolution current density reaches over 10 mA cm^{-2}.

The dissolution voltammogram for nickel in Figure 6.17 (B) shows that no dissolution rate above the detection limit was observed within the entire potential range scanned. Dissolution of cobalt was observed in the cathodic scan with a maximum of 10 ng s^{-1} cm^{-2} at 0.280 V, which co-insides with peak d of the electrochemical voltammogram. On the anodic scan, inconsistent spikes of cobalt dissolution were observed in the potential region positive of 1.65 V corresponding to oxygen evolution.

Figure 6.17 (C) presents the electrochemical and dissolution rate voltammogram of sample $x_{0.8}$. The potential is scanned in the cathodic direction from the open circuit potential of 0.9 V. In the electrochemical voltammogram, peak d is present on the cathodic sweep at 0.385 V. The inset shows that the oxygen evolution current density reaches over 10 mA cm^{-2}.

The dissolution voltammogram for nickel in Figure 6.17 (C) shows that no dissolution rate above the detection limit was observed within the entire potential range scanned, apart from a few small spikes in the potential region corresponding to oxygen evolution in the electrochemical voltammogram. Dissolution of cobalt was observed in the cathodic scan with a maximum of 12 ng s^{-1} cm^{-2} at 0.342 V, which co-insides with peak

d of the electrochemical voltammogram. On the anodic scan, inconsistent spikes of cobalt dissolution were observed in the potential region positive of 1.65 V corresponding to oxygen evolution, some of which overlaps with the signal spikes seen for the nickel dissolution rate voltammogram.

Figure 6.17 (D) presents the electrochemical and dissolution rate voltammogram of sample $x_{1.0}$. The potential is scanned in the cathodic direction from the open circuit potential of 0.9 V. In the electrochemical voltammogram, peak d is present on the cathodic sweep at 0.399 V. The inset shows that the oxygen evolution current density reaches over 10 mA cm^{-2}.

The dissolution voltammogram for nickel in Figure 6.17 (D) shows that no dissolution rate above the detection limit was observed within the entire potential range scanned. Dissolution of cobalt was observed in the cathodic scan with a maximum of 8 ng s^{-1} cm^{-2} at 0.362 V, which co-insides with peak d of the electrochemical voltammogram. On the anodic scan, the inconsistent spikes of cobalt dissolution were not observed.

In summary, peak d was observed for all samples bar the nickel-free sample $x_{0.0}$. Dissolution was found to coincide with the emergence of peak d, and Peak d shifted to more positive potentials for both the electrochemical and dissolution rate voltammogram of cobalt as the nickel content of the samples increased.

6.3.5 The effect of dissolution on catalytic activity

In this section, the test protocol described in the experimental section was used to test if the dissolution rate seen from 0.6 V vs RHE. The protocol was conducted with the RDE setup. The hold potential was set to 0.425 V vs RHE for 20 minutes. Although this potential only corresponds to the initial stages of dissolution in the dissolution voltammograms, the potential was held for a longer time, and would be more relevant for applied zinc-air scenarios. A more negative potential would correspond to a higher load on the battery, which would be less likely to happen. Therefore, any changes in electrochemical performance post-dissolution would signify that even moderate dissolution rates can be relevant for long-term stability.

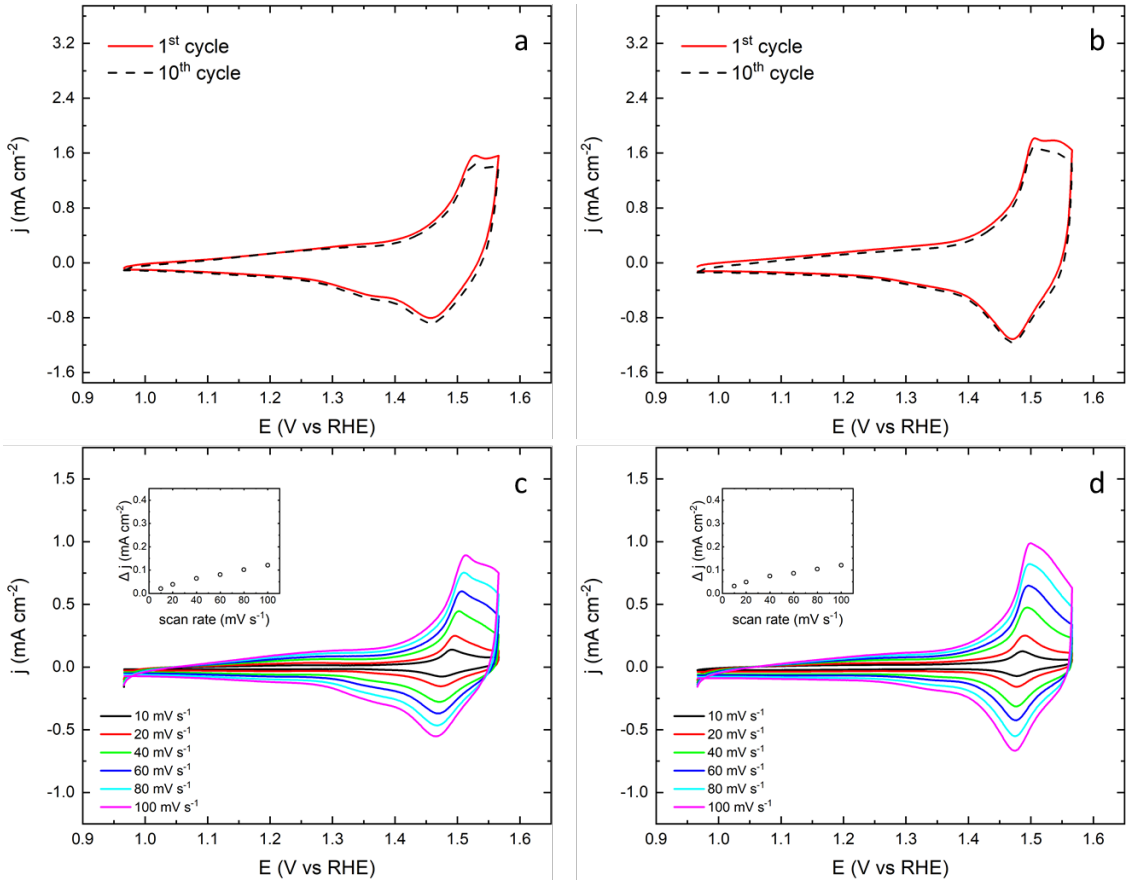

Figure 6.18 Stationary cyclic voltammograms of sample $x_{0.0}$ before (a) and after (b) dissolution step at 10 mV s^{-1} in 1 M KOH. Stationary cyclic voltammograms at various scan rates for sample $x_{0.0}$ before (c) and after (d) dissolution step in 1 M KOH. Inset plots the double layer current at 1.1V versus the scan rate.

The cyclic voltammograms for sample $x_{0.0}$ is presented in Figure 6.18 a and b, prior to and after dissolution respectively. The voltammogram prior to dissolution exhibited an anodic peak at 1.52 V and cathodic peaks at 1.45 V and 1.36 V.

After dissolution, two anodic peaks were found at 1.50 V and 1.53 V, and one cathodic peak at 1.47 V. The characteristic peaks have altered significantly, suggesting that the material surface properties have changed.

The capacitance measurements are presented in Figure 6.18 c and d, prior to and after dissolution respectively. The non-faradaic currents for capacitance determination were

taken at 1.1 V, and the capacitive current display a linear trend against scan rate (inset). The capacitance prior to dissolution was found to be 1.08 μF cm^{-2}.

The capacitance after dissolution had a slope of 0.950 μF cm^{-2}. The relative surface area from capacitance measurements have decreased by 12%, which suggests that the material have either undergone surface restructuring or dissolution.

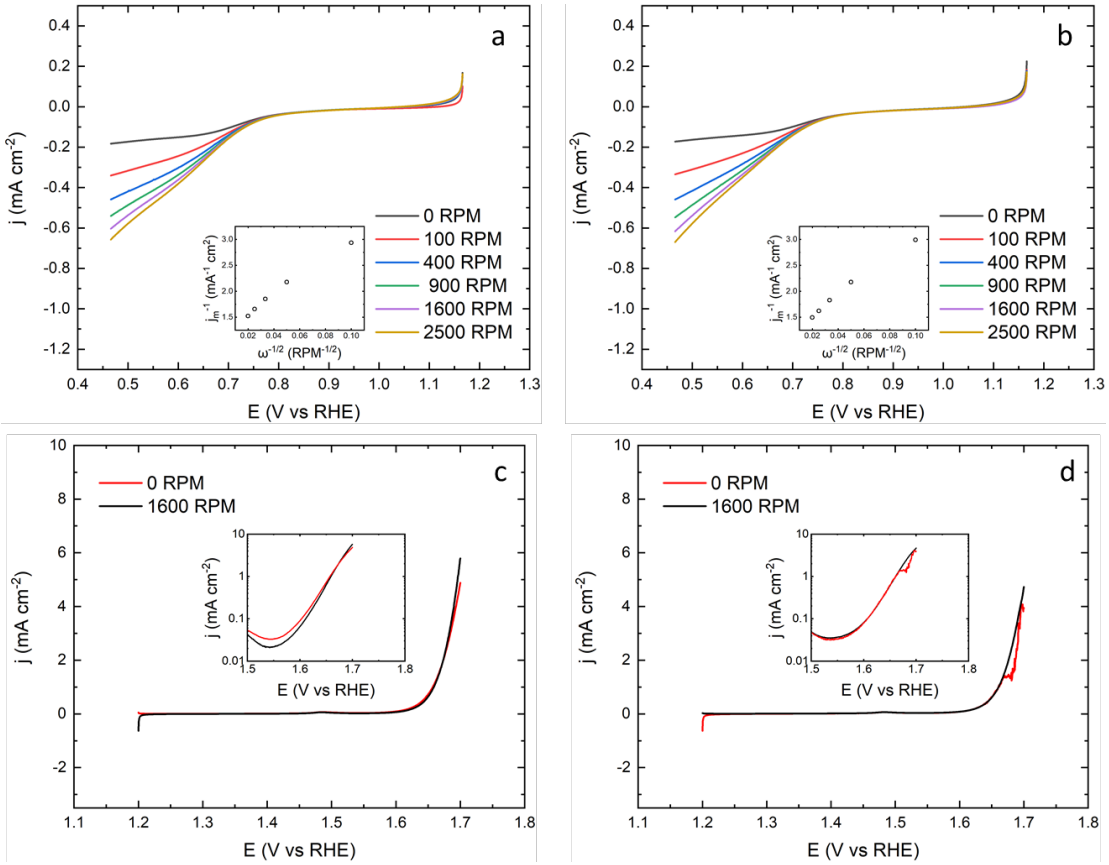

Figure 6.19 Cathodic linear sweeps at 5 mV s^{-1} for sample $x_{0.0}$ in 1 M KOH before (a) and after (b) dissolution step at various rotation speeds. Insets displays the Levich analysis plots at 0.5 V vs RHE. Linear sweeps in the OER region taken at 5 mV s^{-1} before (c) and after (d) for sample $x_{0.0}$ in 1 M KOH. Insets displays the exponential relationship between current and overpotential.

The linear sweeps for determination of oxygen reduction reaction kinetics for sample $x_{0.0}$ prior and after dissolution are displayed in Figure 6.19 a and b respectively. In both instances, an increase of net current with electrolyte convection was observed. The insets display the corresponding Koutecky-Levich analysis at 0.5V, which was found

to yield a linear relationship. Prior to dissolution, the mass transport current determined from the slope was 57.8 μA cm^{-2}, and the kinetic current determined from the intercept was found to be 0.81 mA cm^{-2}.

After dissolution, the mass transport current determined from the slope was 54.3 μA cm^{-2}, and the kinetic current determined from the intercept was found to be 0.85 mA cm^{-2}. This correspond to a 4.9 % decrease in the kinetic current and a 6.1 % decrease in the diffusion controlled current after dissolution.

The linear sweeps for estimation of oxygen evolution reaction activity are displayed in Figure 6.19 c and d prior to and after dissolution respectively. Linear sweeps for both 0 and 1600 RPM are presented for easy comparison with literature values, but only results at 0 RPM will be considered. All linear sweeps clearly display much higher currents compared to the glassy carbon blank in Figure 6.14. Tafel slopes taken for the 0 RPM instances reveals values of 54 mV/decade prior to dissolution, and 50 mV/decade after dissolution. However, as seen in the inset of Figure 6.16 d, the current density of the oxygen evolution reaction after dissolution does not follow a Butler-Volmer relationship with overpotential, hence a Tafel slope value was difficult to determine. However, this data suggests that the activity for oxygen evolution has increased after dissolution.

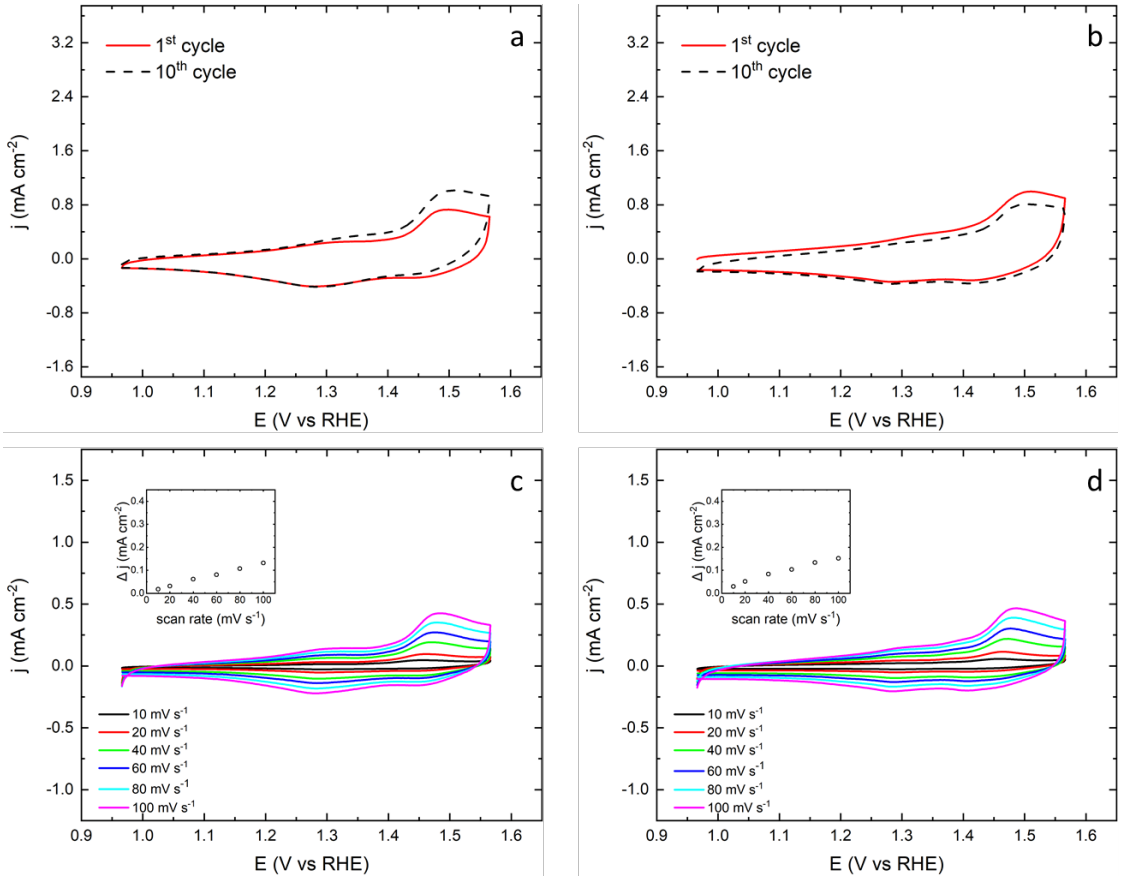

Figure 6.20 Stationary cyclic voltammograms of sample $x_{0.4}$ before (a) and after (b) dissolution step at 10 mV s^{-1} in 1 M KOH. Stationary cyclic voltammograms at various scan rates for sample $x_{0.4}$ before (c) and after (d) dissolution step in 1 M KOH. Inset plots the double layer current at 1.1V versus the scan rate.

The cyclic voltammograms for sample $x_{0.4}$ is presented in Figure 6.20 a and b, prior to and after dissolution respectively. The voltammogram prior to dissolution exhibited an anodic peak at 1.32 V and 1.50 V, and cathodic peaks at 1.45 V and 1.28 V.

After dissolution, two anodic peaks were found at 1.32 V and 1.50 V, and cathodic peak at 1.41 V and 1.28 V. The characteristic peaks have altered significantly.

The capacitance measurements are presented in Figure 6.20 c and d, prior to and after dissolution respectively. The non-faradaic currents for capacitance determination were taken at 1.1 V, and the capacitive current display a linear trend against scan rate (inset). The capacitance prior to dissolution was found to be 1.26 µF cm^{-2}.

The capacitance after dissolution had a slope of 1.34 μF cm^{-2}. The relative surface area from capacitance measurements have increased by 6.3%, which suggests that the material have either undergone surface restructuring or dissolution.

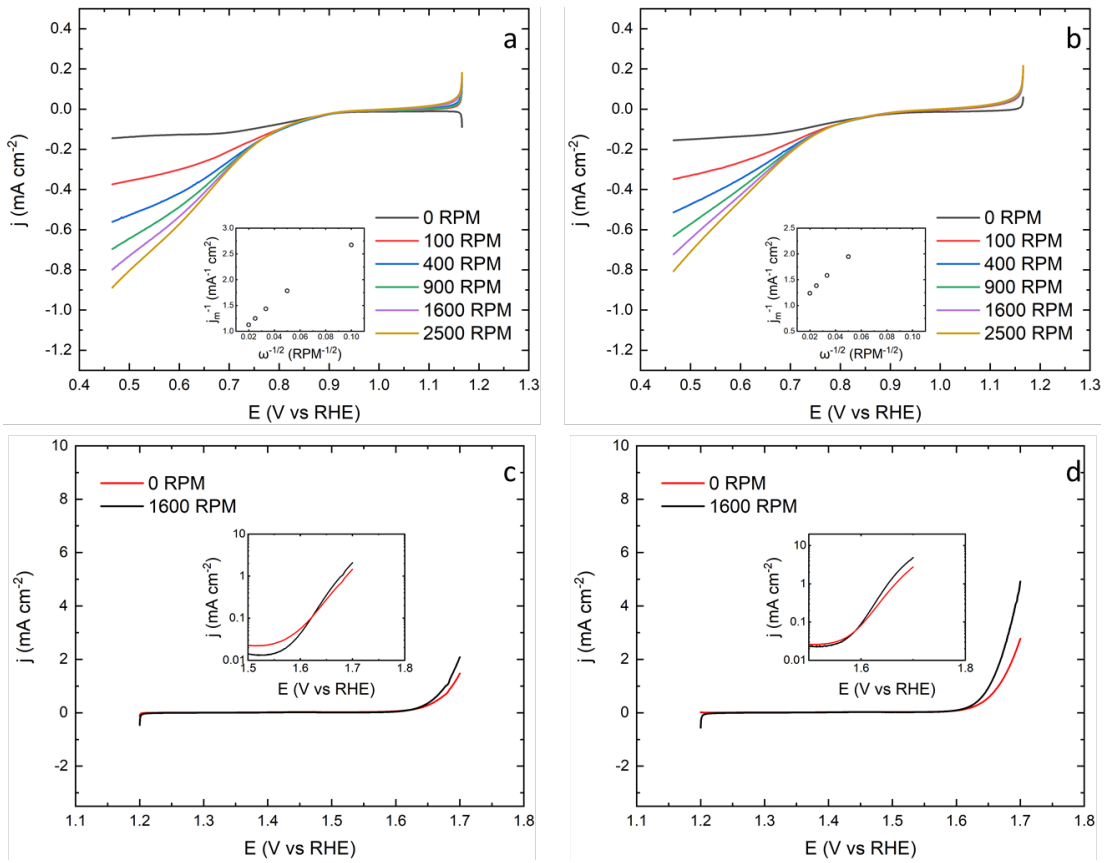

Figure 6.21 Cathodic linear sweeps at 5 mV s^{-1} for sample $x_{0.4}$ in 1 M KOH before (a) and after (b) dissolution step at various rotation speeds. Insets displays the Levich analysis plots at 0.5 V vs RHE. Linear sweeps in the OER region taken at 5 mV s^{-1} before (c) and after (d) for sample $x_{0.4}$ in 1 M KOH. Insets displays the exponential relationship between current and overpotential.

The linear sweeps for determination of oxygen reduction reaction kinetics for sample $x_{0.4}$ prior and after dissolution are displayed in Figure 6.21 a and b respectively. In both instances, an increase of net current with electrolyte convection was observed. The insets display the corresponding Koutecky-Levich analysis at 0.5V, which was found to yield a linear relationship. Prior to dissolution, the mass transport current determined

from the slope was 52.4 μA cm^{-2}, and the kinetic current determined from the intercept was found to be 1.28 mA cm^{-2}.

After dissolution, the mass transport current determined from the slope was 50.0 μA cm^{-2}, and the kinetic current determined from the intercept was found to be 1.12 mA cm^{-2}. This correspond to a 12 % decrease in the kinetic current and a 4.6 % decrease in the diffusion controlled current after dissolution.

The linear sweeps for estimation of oxygen evolution reaction activity are displayed in Figure 6.21 c and d prior to and after dissolution respectively. Linear sweeps for both 0 and 1600 RPM are presented for easy comparison with literature values, but only results at 0 RPM will be considered. All linear sweeps clearly display much higher currents compared to the glassy carbon blank in Figure 6.14. Tafel slopes taken for the 0 RPM instances reveals values of 70 mV/decade prior to dissolution, and 68 mV/decade after dissolution. However, as seen in the inset of Figure 6.16 d, the current density of the oxygen evolution reaction after dissolution does not follow a Butler-Volmer relationship with overpotential, hence a Tafel slope value was difficult to determine. However, this data suggests that the activity for oxygen evolution has increased after dissolution.

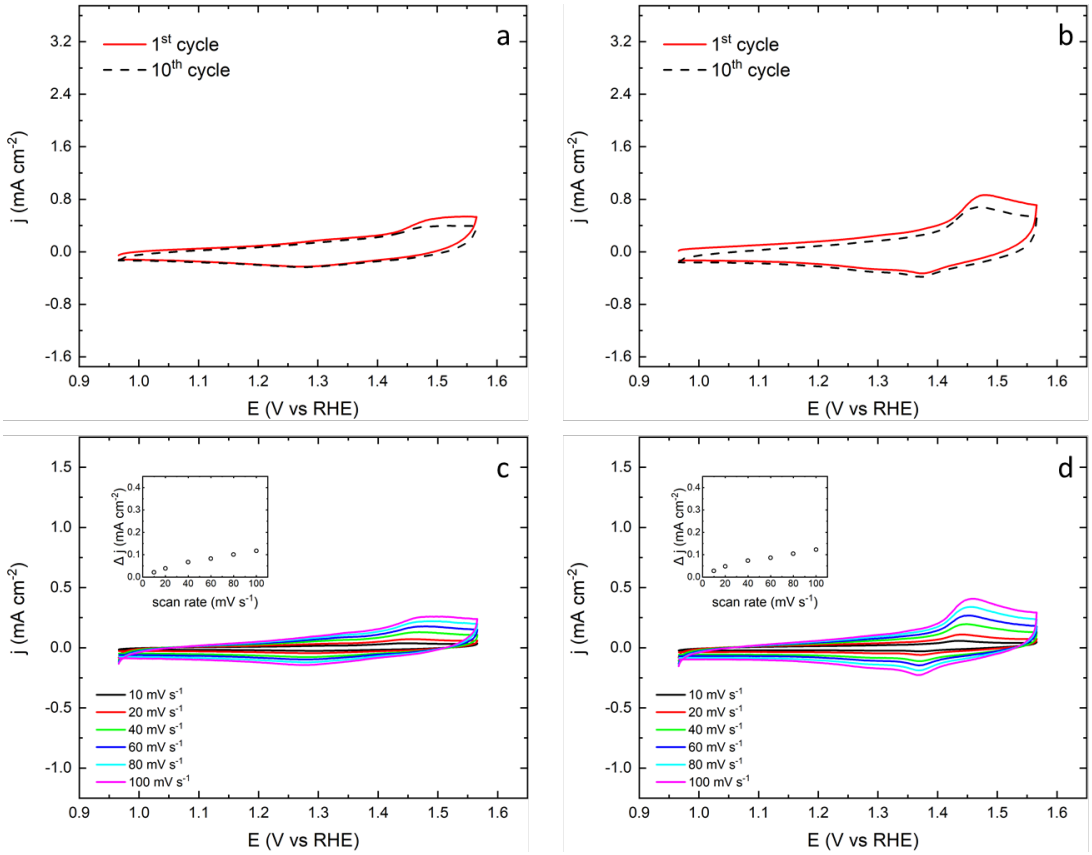

Figure 6.22 Stationary cyclic voltammograms of sample $x_{0.5}$ before (a) and after (b) dissolution step at 10 mV s^{-1} in 1 M KOH. Stationary cyclic voltammograms at various scan rates for sample $x_{0.5}$ before (c) and after (d) dissolution step in 1 M KOH. Inset plots the double layer current at 1.1 V versus the scan rate.

The cyclic voltammograms for sample $x_{0.5}$ is presented in Figure 6.22 a and b, prior to and after dissolution respectively. The voltammogram prior to dissolution exhibited an anodic peak at 1.31 and 1.46 V, and a cathodic peak at 1.27 V.

After dissolution, two anodic peaks were found at 1.31 and 1.51 V, and a cathodic peak at 1.37 V. The characteristic peaks have altered significantly, suggesting that the material surface properties have changed.

The capacitance measurements are presented in Figure 6.22 c and d, prior to and after dissolution respectively. The non-faradaic currents for capacitance determination were taken at 1.1 V, and the capacitive current display a linear trend against scan rate (inset). The capacitance prior to dissolution was found to be 1.04 µF cm^{-2}.

The capacitance after dissolution had and a slope of 1.00 µF cm^{-2}. The relative surface area from capacitance measurements have decreased by 3.9%, which suggests that the material have either undergone surface restructuring or dissolution.

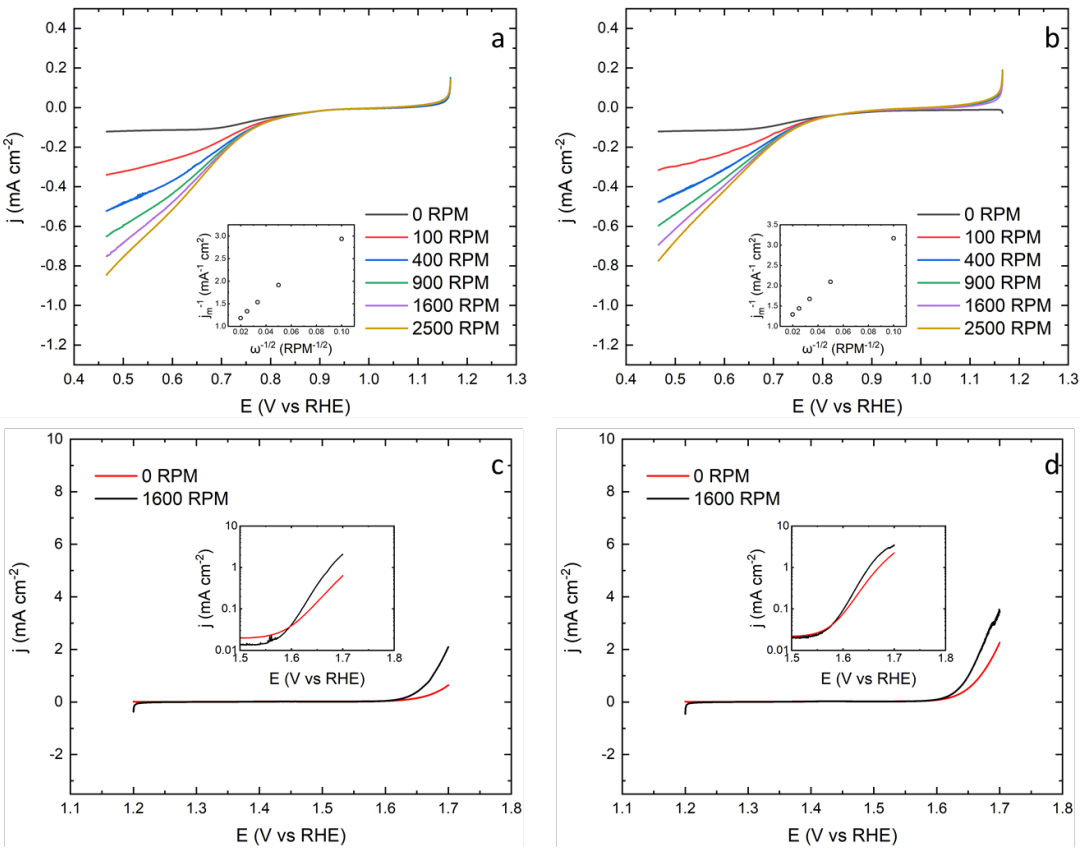

Figure 6.23 Cathodic linear sweeps at 5 mV s^{-1} for sample $x_{0.5}$ in 1 MKOH before (a) and after (b) dissolution step at various rotation speeds. Insets displays the Levich analysis plots at 0.5 V vs RHE. Linear sweeps in the OER region taken at 5 mV s^{-1} before (c) and after (d) for sample $x_{0.5}$ in 1 M KOH. Insets displays the exponential relationship between current and overpotential.

The linear sweeps for determination of oxygen reduction reaction kinetics for sample $x_{0.5}$ prior and after dissolution are displayed in Figure 6.23 a and b respectively. In both instances, an increase of net current with electrolyte convection was observed. The insets display the corresponding Koutecky-Levich analysis at 0.5V, which was found to yield a linear relationship. Prior to dissolution, the mass transport current determined

from the slope was 46.3 μmA cm^{-2}, and the kinetic current determined from the intercept was found to be 1.27 mA cm^{-2}.

After dissolution, the mass transport current determined from the slope was 43.1 μA cm^{-2}, and the kinetic current determined from the intercept was found to be 1.14 mA cm^{-2}. This correspond to a 10 % decrease in the kinetic current and a 6.9 % decrease in the diffusion controlled current after dissolution.

The linear sweeps for estimation of oxygen evolution reaction activity are displayed in Figure 6.23 c and d prior to and after dissolution respectively. Linear sweeps for both 0 and 1600 RPM are presented for easy comparison with literature values, but only results at 0 RPM will be considered. All linear sweeps clearly display much higher currents compared to the glassy carbon blank in Figure 6.14. Tafel slopes taken for the 0 RPM instances reveals values of 78 mV/decade prior to dissolution, and 72 mV/decade after dissolution. However, as seen in the inset of Figure 6.29 d, the current density of the oxygen evolution reaction after dissolution does not follow a Butler-Volmer relationship with overpotential, hence a Tafel slope value was difficult to determine. However, this data suggests that the activity for oxygen evolution has increased after dissolution.

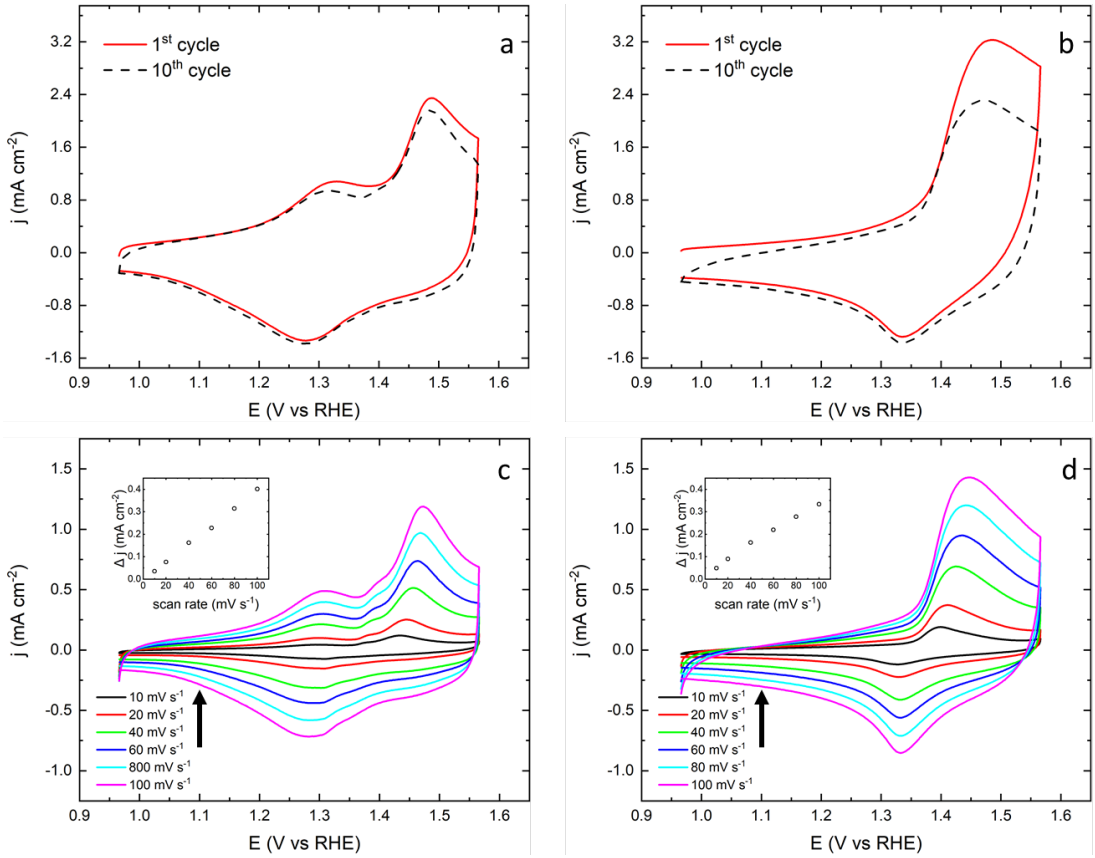

Figure 6.24 Stationary cyclic voltammograms of sample $x_{0.8}$ before (a) and after (b) dissolution step at 10 mV s^{-1} in 1 M KOH. Stationary cyclic voltammograms at various scan rates for sample $x_{0.8}$ before (c) and after (d) dissolution step in 1 M KOH. Inset plots the double layer current at 1.1 V versus the scan rate.

The cyclic voltammograms for sample $x_{0.8}$ is presented in Figure 6.24 a and b, prior to and after dissolution respectively. The voltammogram prior to dissolution exhibited an anodic peak at 1.31 and 1.48 V, and a cathodic peak at 1.27 V.

After dissolution, one anodic peak were found at 1.46 V, and a cathodic peak at 1.33 V. The characteristic peaks have altered significantly, suggesting that the material surface properties have significantly changed.

The capacitance measurements are presented in Figure 6.24 c and d, prior to and after dissolution respectively. The non-faradaic currents for capacitance determination were taken at 1.1 V, and the capacitive current display a linear trend against scan rate (inset). The capacitance prior to dissolution was found to be 4.01 µF cm^{-2}.

The capacitance after dissolution had a slope of 3.13 μF cm^{-2}. The relative surface area from capacitance measurements have decreased by 21%, which suggests that the material have either undergone surface restructuring or dissolution.

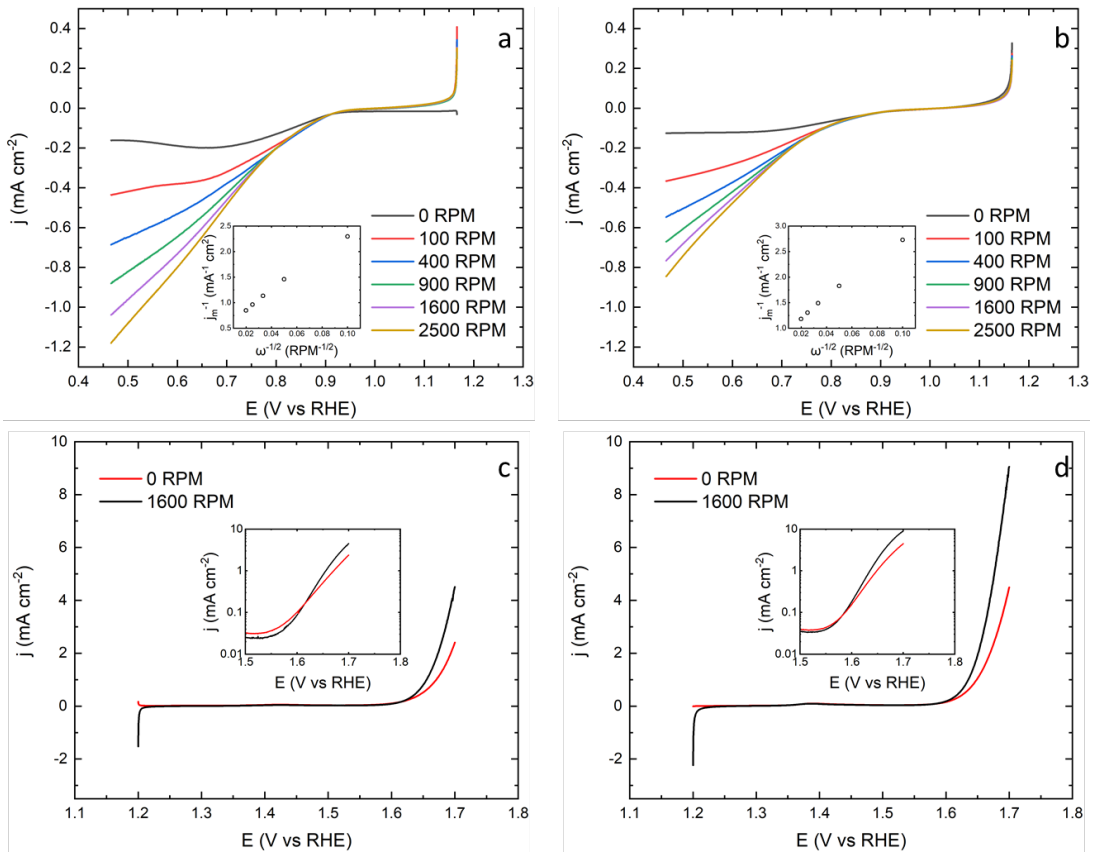

Figure 6.25 Cathodic linear sweeps at 5 mV s^{-1} for sample $x_{0.8}$ in 1 M KOH before (a) and after (b) dissolution step at various rotation speeds. Insets displays the Levich analysis plots at 0.5 V vs RHE. Linear sweeps in the OER region taken at 5 mV s^{-1} before (c) and after (d) for sample $x_{0.8}$ in 1 M KOH. Insets displays the exponential relationship between current and overpotential.

The linear sweeps for determination of oxygen reduction reaction kinetics for sample $x_{0.8}$ prior and after dissolution are displayed in Figure 6.25 a and b respectively. In both instances, an increase of net current with electrolyte convection was observed. The insets display the corresponding Koutecky-Levich analysis at 0.5V, which was found to yield a linear relationship. Prior to dissolution, the mass transport current determined

from the slope was 55.9 μA cm^{-2}, and the kinetic current determined from the intercept was found to be 1.92 mA cm^{-2}.

After dissolution, the mass transport current determined from the slope was 52.4 μA cm^{-2}, and the kinetic current determined from the intercept was found to be 1.20 mA cm^{-2}. This correspond to a 36 % decrease in the kinetic current and a 6.2 % decrease in the diffusion controlled current after dissolution.

The linear sweeps for estimation of oxygen evolution reaction activity are displayed in Figure 6.25 c and d prior to and after dissolution respectively. Linear sweeps for both 0 and 1600 RPM are presented for easy comparison with literature values, but only results at 0 RPM will be considered. All linear sweeps clearly display much higher currents compared to the glassy carbon blank in Figure 6.14. Tafel slopes taken for the 0 RPM instances reveals values of 75 mV/decade prior to dissolution, and 69 mV/decade after dissolution. However, as seen in the inset of Figure 6.25 d, the current density of the oxygen evolution reaction after dissolution does not follow a Butler-Volmer relationship with overpotential, hence a Tafel slope value was difficult to determine. However, this data suggests that the activity for oxygen evolution has increased after dissolution.

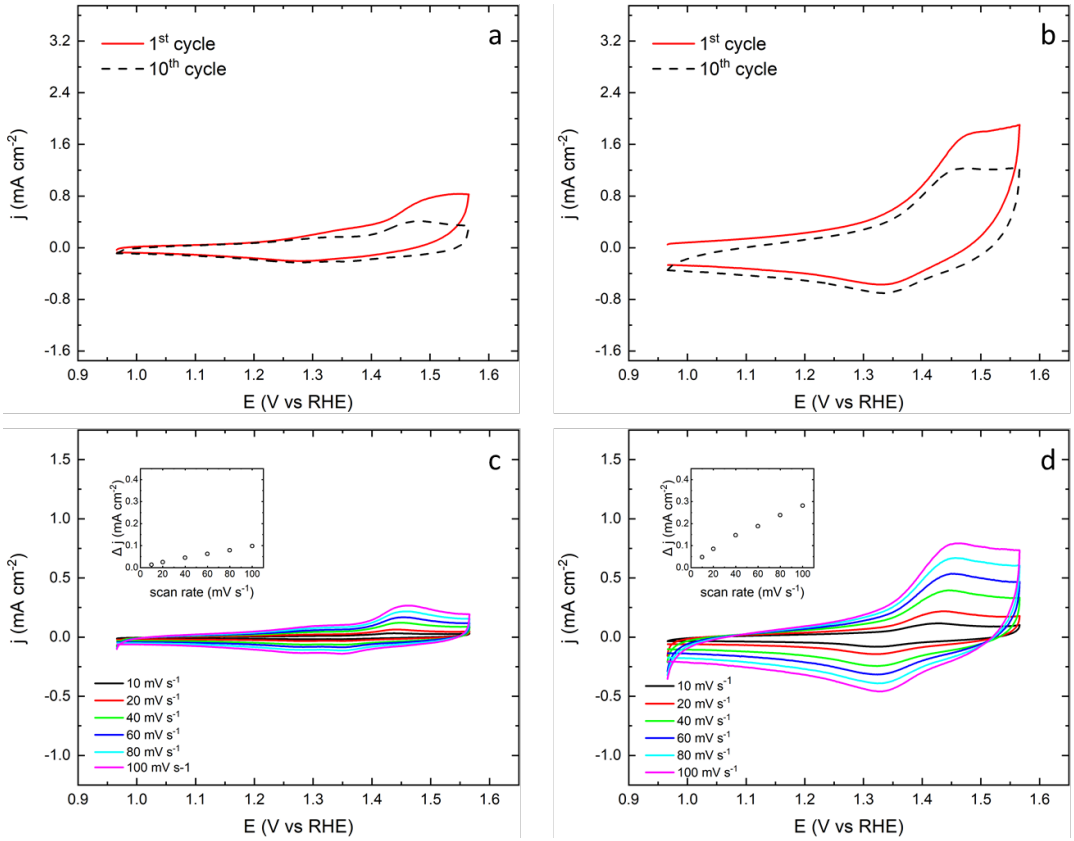

Figure 6.26 Stationary cyclic voltammograms of sample $x_{1.0}$ before (a) and after (b) dissolution step at 10 mV s^{-1} in 1 M KOH. Stationary cyclic voltammograms at various scan rates for sample $x_{1.0}$ before (c) and after (d) dissolution step in 1 M KOH. Inset plots the double layer current at 1.1 V versus the scan rate.

The cyclic voltammograms for sample $x_{1.0}$ is presented in Figure 6.26 a and b, prior to and after dissolution respectively. The voltammogram prior to dissolution exhibited an anodic peak at 1.32 and 1.47 V, and cathodic peaks at 1.35 V and 1.27 V.

After dissolution, one anodic peak was found at 1.46 V, and a cathodic peak at 1.33 V. The characteristic peaks have altered significantly, suggesting that the material surface properties have significantly altered.

The capacitance measurements are presented in Figure 6.26 c and d, prior to and after dissolution respectively. The non-faradaic currents for capacitance determination were

taken at 1.1 V, and the capacitive current display a linear trend against scan rate (inset). The capacitance prior to dissolution was found to be 0.92 μF cm^{-2}.

The capacitance after dissolution had a slope of 2.55 μF cm^{-2}. The relative surface area from capacitance measurements have increased by 277%, which suggests that the material have either undergone surface restructuring or dissolution.

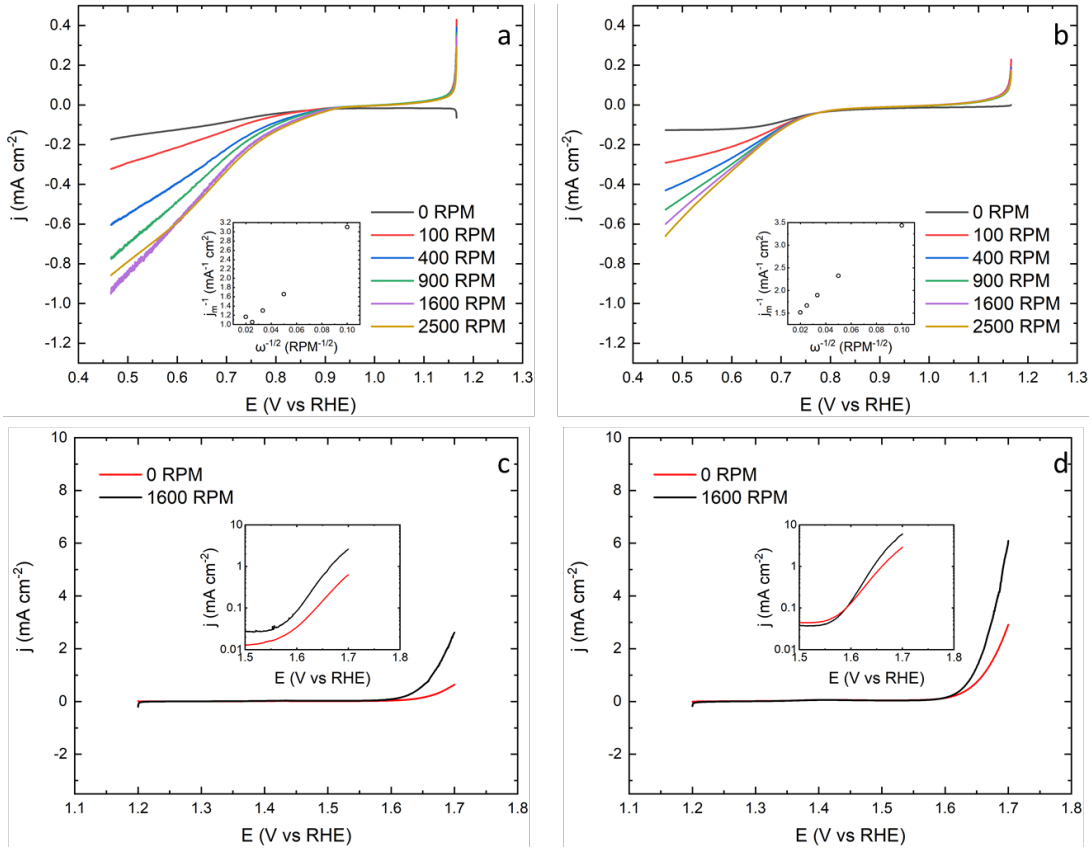

Figure 6.27 Cathodic linear sweeps at 5 mV s^{-1} for sample $x_{1.0}$ in 1 M KOH before (a) and after (b) dissolution step at various rotation speeds. Insets displays the Levich analysis plots at 0.5 V vs RHE. Linear sweeps in the OER region taken at 5 mV s^{-1} before (c) and after (d) for sample $x_{1.0}$ in 1 M KOH. Insets displays the exponential relationship between current and overpotential.

The linear sweeps for determination of oxygen reduction reaction kinetics for sample $x_{1.0}$ prior and after dissolution are displayed in Figure 6.27 a and b respectively. In both instances, an increase of net current with electrolyte convection was observed. The insets display the corresponding Koutecky-Levich analysis at 0.5V, which was found to yield a linear relationship. Prior to dissolution, the mass transport current determined

from the slope was 38.9 μA cm^{-2}, and the kinetic current determined from the intercept was found to be 2.10 mA cm^{-2}.

After dissolution, the mass transport current determined from the slope was 42.2 μA cm^{-2}, and the kinetic current determined from the intercept was found to be 0.92 mA cm^{-2}. This correspond to a 56 % decrease in the kinetic current and an 8.4 % increase in the diffusion controlled current after dissolution.

The linear sweeps for estimation of oxygen evolution reaction activity are displayed in Figure 6.27 c and d prior to and after dissolution respectively. Linear sweeps for both 0 and 1600 RPM are presented for easy comparison with literature values, but only results at 0 RPM will be considered. All linear sweeps clearly display much higher currents compared to the glassy carbon blank in Figure 6.14. Tafel slopes taken for the 0 RPM instances reveals values of 76 mV/decade prior to dissolution, and 78 mV/decade after dissolution. However, as seen in the inset of Figure 6.27 d, the current density of the oxygen evolution reaction after dissolution does not follow a Butler-Volmer relationship with overpotential, hence a Tafel slope value was difficult to determine. However, this data suggests that the activity for oxygen evolution has increased after dissolution.

6.3.6 Discussion

The data will be further discussed in this section to correlate the results and deduce any trends between changes in sample.

The structural information obtained from the PXRD diffractograms suggest that nickel has been incorporated into the Co_3O_4 lattice. The diffractograms presented in Figure 6.4 and 6.5 for the sintered samples display no prominent reflection peaks from anticipated side products like NiO, $Ni(OH)_2$, $Co(OH)_2$ or Co_2O_3 [225]. Diffractograms of nickel substituted samples exhibit the same peaks as commercial and synthesised Co_3O_4, suggesting that the lattice structure is intact. The magnified Figure 6.6 of the diffractograms reveal that the reflection peaks from nickel-containing samples exhibit a negative 2θ shift compared to pristine Co_3O_4[229], and that this shift increases with the relative concentration of nickel in the starting material during synthesis[219]. This effect is expected from lattice expansion when Co_3O_4 is doped with heteroatoms[220]. Further, no "doublets" could be found for any main reflection peak, which would be the case if

both phases of $NiCo_2O_4$ and Co_3O_4 were present, otherwise any doublet peaks are obscured by the broad reflection peaks.

Nickel doping of Co_3O_4 decreases the crystallite size which has been calculated from Scherrer's equation by using the full width half maximum (FWHM) value of the main (311) reflection of the diffractograms. The reflection peaks of the nickel containing samples are clearly broader than the pristine Co_3O_4 sample. Nickel has been reported to prevent crystallisation of Co_3O_4[216, 225], and this effect was found to increase with the degree of nickel doping of the samples. Because of the lower crystallinity of nickel-doped samples, Co_3O_4 samples containing nickel are expected to have smaller particle sizes[219].

The SEM micrographs show a transition in particle morphology as nickel content is increased in the samples. The nickel free sample contain mostly 2D-platelets clustered into rosette-like particles. Elongated morphology has been seen to disproportionally expose select crystal facets at the surface, and such effects have been seen by organic additives that selectively binds at and stops the growth at specific crystallographic sites[231]. The urea oxidising agent in the starting material may have a similar role for the particle growth of the Co_3O_4 samples.

With increased doping these large platelets were replaced with smaller and more numerous rod-shaped particles, in agreement with the decrease of crystallite size calculated from the diffractograms. In parallel with the increased nickel doping, the resulting particles move away from a hierarchical macro/microstructure to seemingly randomised particle aggregates, probably because the particles do not grow large enough to be affected by the shape-modifying urea.

Signature of nickel incorporation is displayed in the characteristic cyclic voltammograms in Figure 6.12. Two redox features from cobalt and one redox feature from nickel is expected to be seen from the cyclic voltammograms of the samples. First the oxidation of Co^{2+} to Co^{3+} at 0.86 V vs RHE[233, 234]:

$$Co_3O_4 + H_2O \rightarrow CoOOH + H^+ + e^-$$

The oxidation of Co^{3+} to Co^{4+} at 1.45 V vs RHE[233, 235]:

$$CoOOH \rightarrow CoO_2 + H^+ + e^-$$

And the oxidation of Ni^{2+} to Ni^{3+} at 1.40 V vs RHE[237, 238]:

$$\beta Ni(OH)_2 + OH^- \rightarrow \beta NiOOH + H_2O$$

The nickel-free sample has a prominent anodic peak at 1.53 V that can be assigned to the oxidation of Co^{3+} and a cathodic peak at 1.45 V which is consistent with reduction of Co^{4+}. A wide redox feature spanning a potential range around 1.3 V which may be due to the oxidation and reduction of Co^{2+}. The features remained unchanged after the dissolution protocol, suggesting that the surface did not undergo any structural changes.

The nickel doped samples display prominent anodic peaks at 1.31 V and 1.46 V prior to the dissolution protocol, which could be assigned to Co^{2+} and Co^{3+} oxidation[215]. The negative shift in the oxidation potential of Co^{3+} is an indication that nickel has been incorporated into the structure, as it has been reported to lower the energetic barrier for Co^{3+} oxidation[216]. The anodic peak at 1.53 V for the nickel-free sample shifts negative with increasing degree of nickel doping in the samples, to 1.50 V, 1.46 V, 1.48 V and 1.47 V, which further confirms this point.

Dissolution of cobalt enriched the nickel concentration at the surface of the electrode. The voltammograms for the nickel-containing samples $x_{0.4}$ and $x_{0.5}$ displayed less pronounced features for the Co^{2+} oxidation, whereas the Co^{2+} oxidation feature completely vanished from the $x_{0.8}$ and $x_{1.0}$ samples. The anodic peak at 1.5 V were also significantly wider for the last two samples, and the cathodic peak at 1.27 V had shifted to 1.33 V, which may be a signature of Ni^{3+}/Ni^{2+} redox instead.

There are voltammetric variations between the samples. The drop-casting procedure was optimised for the $x_{0.8}$ sample, and the significantly deviating morphologies in the other samples may have caused the less pronounced redox features. Since the morphologies are different across the samples, different planes may be exposed in different proprtions to the electrolyte causing the voltammetric signature to not be consistent across the samples[216].

Nickel doping may have affected the capacitance of the samples. The estimated double-layer capacitance increased with the degree of nickel doping, which could be due to smaller particle sizes as seen in the SEM micrographs and assumed from the smaller calculated crystallite sizes from the diffractograms.

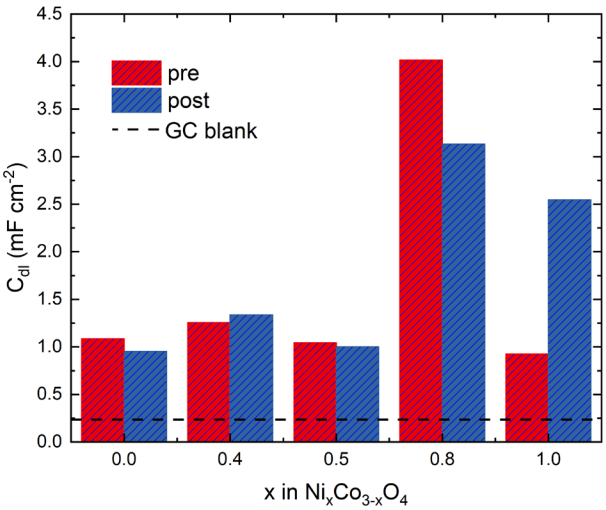

Figure 6.28 Capacitance before and after dissolution step for the samples as a function of nickel content of the original samples.

Figure 6.28 shows the change in capacitance from the dissolution test protocol. The capacitance pre-dissolution was in all cases at least four times that of the glassy carbon substrate, apart from the $x_{0.8}$ sample, which had an 16-fold increase in capacitance. However, typical capacitance values are 30-40 mF cm^{-2} [222], which is much greater than obtained for all samples. This could be due to the drop-casting method not being optimised for the samples, poor dispersion of the nanoparticles from the clusters or aggregates, or low degree of exposure of the surface area to the electrolyte.

Post-dissolution $x_{0.8}$ had a decrease of 25% and sample $x_{1.0}$ an increase by 300%. Samples $x_{0.0}$, $x_{0.4}$, $x_{0.5}$ only displayed very moderate changes in comparison. As the capacitance changes are not of the same sign, it is not certain that dissolution directly caused it, rather that the surface composition in the respective samples could have been altered and now contains different inherent capacitance properties.

For the oxygen reduction kinetics, only the kinetic current component of the Koutecky-Levich current is considered, to avoid contributions due to reactant transport since the linear sweeps did not reach steady state. As shown in Figure 6.29, prior to dissolution, there is a clear trend in increasing kinetic current as derived from the Koutecky-Levich equation when the nickel content of the samples is increased. Nickel doping has shown to increase the activity for ORR[214] at moderate concentrations, at either 5%[216] or 11%[224] of heteroatom doping depending on the synthesis route. This could be due to increased

conductivity of the nickel cobalt oxide particles[227 224], or the facilitating effect nickel has on the redox kinetics of cobalt[229].

Post-dissolution, the loss in kinetic current for oxygen reduction increases with the nickel content of the samples. From figure 6.29, the nickel-free sample displays nearly no change, while the $x_{0.4}$ and $x_{0.5}$ sample kinetic current has moderately decreased. The effect is even greater for $x_{0.8}$ and $x_{1.0}$ with a 55% decrease in the kinetic current. The sample surfaces may be too nickel-rich to facilitate ORR at a high rate. Notably, the post-dissolution kinetic currents of all nickel-containing samples are about equal that of the nickel-free cobalt oxide, but this may be coincidental, as NiO is not known to be a good oxygen reduction catalyst.

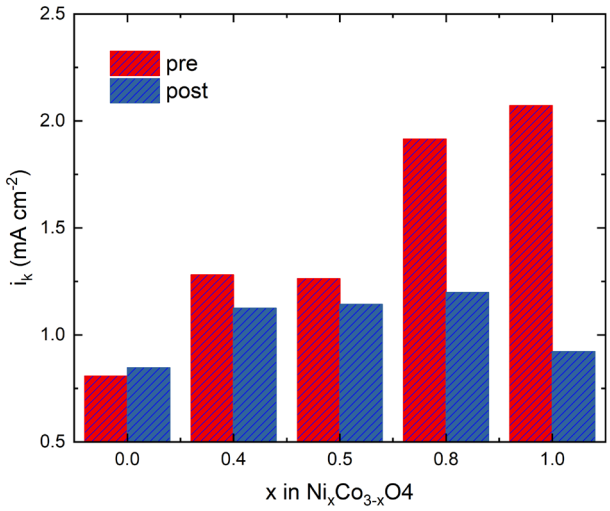

Figure 6.29 Kinetic current i_K at 0.5 V vs RHE before and after dissolution step as a function of nickel content.

Figure 6.30 shows the potential to reach a current density of 1 mA cm^{-2} before and after dissolution. The potential to reach j = 1 mA cm^{-2} shifted positive as nickel content increased. Further, the Tafel slopes increase from 50 to 70, 78, 75 and 76 mV/decade. This is contrary to some literature reports that states nickel doping increase OER activity[220 219] as the conductivity of the catalyst should increase, more -OH sites are available[220 239], and Co^{3+} is more easily oxidised due to elongation of the octahedral site Co-O bond[216]. It could also be due to formation of less {111} planes which are more catalytic towards OER[216]. It has been reported that nickel doping alters the OER mechanism from 1e$^-$ to 2e$^-$ [229], or that $NiCo_2O_4$ favours the 4e$^-$ mechanism[215], and this may contribute to the change in Tafel slopes.

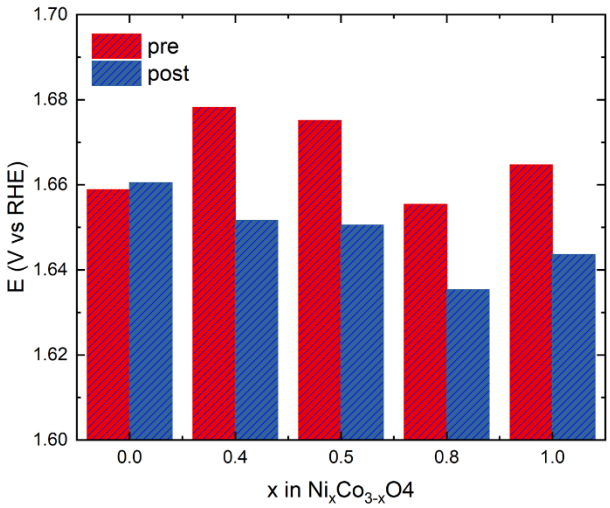

Figure 6.30 Potential at j = 1 mA cm^{-2} for the samples as a function of nickel content.

The pure cobalt oxide displayed very little change in the potential to reach j = 1 mA cm^{-2}, while all nickel-containing samples had a similar decrease of 25 mV. The Tafel slopes also decreased for all samples by about 4 mV/decade, which could be due to activation of the surface [229] as nickel is known to decrease the activation energy towards oxygen evolution compared to cobalt[231], and decrease the potential onset of Co^{4+} formation which is crucial for oxygen evolution [216] [214] [222]. However nickel itself does not oxidise[226]. Higher Ni^{3+} content is also known to improve catalytic activity[240] and increase the number of active sites rather than altering the mechanism[232] [224]. The non-linearity of the Tafel slopes suggests that the mechanism or reaction changes with overpotential[229].

Nickel doping may lead to a decrease in the stability of the cobalt oxide surface. Both in the electrochemical and the dissolution rate voltammograms cobalt is measurably dissolved into solution between 0.2-0.5 V, as seen in Figures 6.16 and 6.17. The potential onset of dissolution shifts to more positive potentials as the degree of nickel doping increases, suggesting a change in the stability with the degree of nickel doping. DFT calculations have shown that mixed nickel cobalt oxide surfaces have larger formation energy than nickel oxide[228], that makes it thermodynamically favourable for nickel to enrich at the top layers[226]. Long-term cycling of nickel cobalt oxide has shown formation of mixed amorphous-crystalline layers around 100 nm thick [220]. Figure 6.31 presents the integrated mass losses from the anodic scan from the on-line ICP-OES measurements. The “spikes” of cobalt

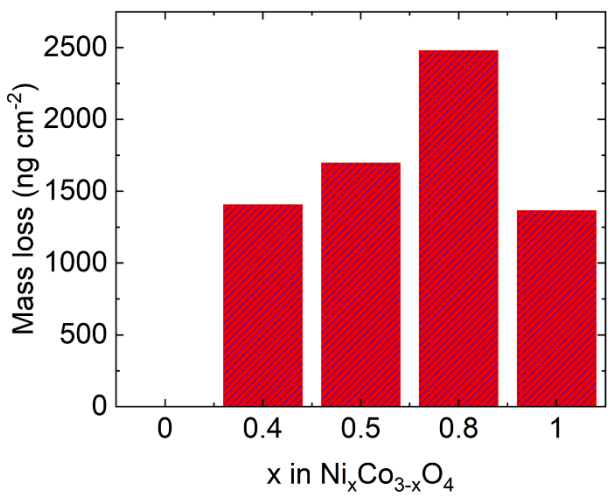

Figure 6.31 The integrated mass losses from the dissolution voltammograms (anodic scan only) of the observed dissolution rates of the samples as function of nickel content.

dissolution were omitted. The total mass loss for the voltammograms increase with the degree of nickel doping until $x_{0.8}$. The reason for less cobalt dissolution for $x_{1.0}$ sample could be because there is simply less cobalt available on the surface of the mixed oxide, aside from errors in the drop-casting method for electrode preparation. On the reverse sweep, cobalt dissolution is not reactivated, in other words the cobalt dissolution is not reversible. Part of the dissolved cobalt could have precipitated and passivated the surface, or all available cobalt atoms could have leeched out in the anodic sweep.

Mechanical particle detachment may have contributed to performance loss post-dissolution. In the oxygen evolution region spikes of cobalt occurred at random for each of the samples, however it is unlikely that this is due to chemical or electrochemical dissolution. First because these spikes were only observed under rapid bubble formation, which may have mechanically dislodged the catalyst particles, as the signal would be expected to have increased smoothly with the driving force behind the dissolution process.

No nickel dissolution rate above detection limits were observed for any of the samples, which may be due to the much lower solubility of Ni^{2+} and Ni^{3+} compared to cobalt ions in 1 M KOH, as seen in Chapter 5. On the other hand, nickel signals would be expected to appear in proportion with the cobalt dissolution rate signals in the OER region if bubbles were responsible for mechanical detachment of the sample particles. The relative sensitivity of cobalt and nickel was typically 4816 and 7181 intensity/ppm ratio determined from calibration curves, however the detection limits was 1.3 and 2.0 ng s^{-1} cm^{-2} for cobalt and nickel respectively as determined from standard deviation of the

blank signal. Hence, a higher nickel concentration in the electrolyte is required to detect any signal. On the other hand, it may be that there indeed were two phases of oxide formed in synthesis, $NiCo_2O_4$ and Co_3O_4, but this is difficult to determine by the PXRD results. Another explanation could be that nickel was not homogeneously distributed within the synthesised samples.

6.3.7 Effects of electrolyte pH and electrocatalyst loading

The pH of the solution is known to affect the solubility of ions, which is also the case for cobalt ions in alkaline solution. Pourbaix diagrams of cobalt indicate that as pH increases from pH 7, the solubility of cobalt also increases[241–244, 245], and this trend may also be seen with dissolution currents. As the 1 M KOH matrix is at the limit of stable operation for the ICP-OES instrument, dissolution rates for cyclic voltammograms in pH 14 was compared to cyclic voltammograms in pH 13. In Figure 6.38 it can be seen that dissolution rates for cobalt is not observed in pH 13. "Extrapolating" these findings to the KOH concentrations used in zinc-air batteries, which typically are in the range of 4-8 M KOH, one could assume that the cobalt mass loss would be even more severe for real world application batteries.

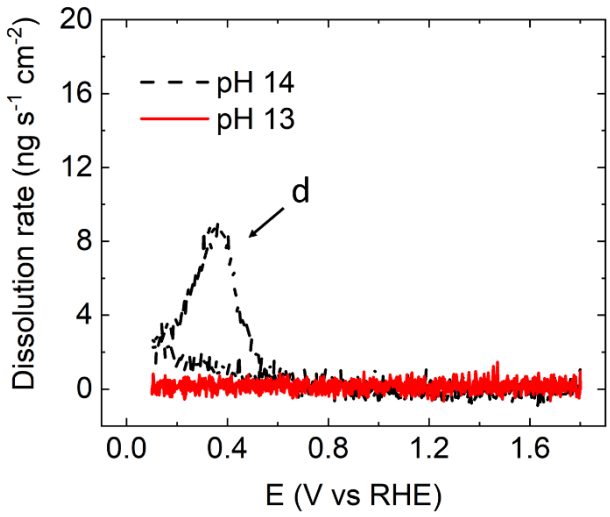

Figure 6.32 Effect of pH on potentiodynamic first-cycle dissolution rate.

Lastly, the effect of mass loading onto the fabricated electrodes were tested. Since the samples drop-casted consisted of mixed morphology and size, and contained a certain amount of binder, the transport of dissolved ions out of the film would be more convoluted

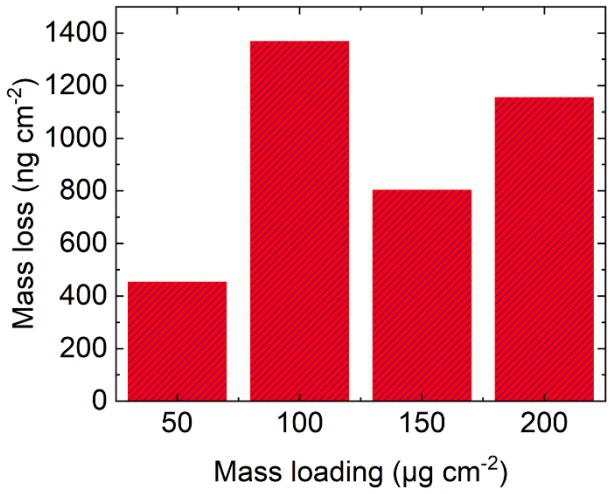

Figure 6.33 Effect of mass loading of drop-casted catalyst on dissolution rate.

compared to perfectly flat surfaces. In addition, a higher mass loading could potentially lead to higher dissolution rates and better elemental signal. In Figure 6.39, it can be seen that beyond a mass loading of 100 µg cm^{-2}, there was no gain in mass loss signal. However a clear trend can not be established with change in mass loading. It is however thinkable that this is due to the low conductivity of transition metal oxide, which would render the outmost particles practically electrochemically inactive. It could also be due to more small pores existing when the film thickness increases, such that dissolved species have longer and more convoluted paths to and from particles not on the very top surface of the film. Therefore, the mass loading used for this drop-casting formulation (100 µg cm^{-2}) in this investigation is seen to be in the optimal range for dissolution detection.

6.4 Conclusion and Summary

6.4.1 Conclusion

Heteroatom-substituted $Ni_xCo_{3-x}O_4$ were synthesised and tested for instability by on-line ICP-OES dissolution analysis. At high overpotentials for the oxygen reduction reaction for the bifunctional oxygen catalyst $Ni_xCo_{3-x}O_4$, cobalt undergoes dissolution which correlates to performance changes in the oxygen reduction reaction and the oxygen evolution reaction of the electrocatalysts. Cyclic voltammetry profiles may suggest that the electrochemical surface have been altered. This could be due to a straightforward dissolution of cobalt leaving behind a nickel-enriched surface, or a dissolution-deposition mechanism, where the re-deposited cobalt has a different structure to the initial material. The dissolution may not be a long-term phenomenon, as only first cycles were measured. Further it was found that nickel dissolution was not observed under any potential range.

6.4.2 Summary

Spinel nickel cobalt oxides $Ni_xCo_{3-x}O_4$ were synthesised and characterised by PXRD, SEM, and electrochemically. After deducing potential ranges that cause changes in the cyclic voltammetry profiles, dissolution in this range was confirmed by on-line metal dissolution detection. By benchmarking electrochemical activity before and after a dissolution step, it was found that the bifunctional oxygen catalyst had a significant decrease in oxygen reduction activity, and increase in oxygen evolution activity, and this change correlated with increased with nickel content.

7 Summary, Conclusion and Outlook

7.1 Conclusion and summary

The aim of this thesis was to design and fabricate a flow cell appropriate for downstream dissolution analysis with an ICP-OES. To approach this, a review was conducted of existing flow cell designs in literature. The effect of design elements for efficient throughput, to be able to conduct as many experiments as possible with minimised chance for error, and maximised quality of signal, in other words transport of dissolution products as efficiently as possible from the flow cell to the ICP-OES was assessed. A setup was from there created where transient dissolution analysis of energy storage materials was observed, and trends in material stability could be realised.

The on-line ICP-OES setup was realised by the combination of two separate parts: the electrochemical flow cell and the ICP-OES. The electrochemical flow cell was designed by adapting flow cells already used for dissolution analysis in literature. Incremental improvements was then made to optimise the flow cell design suit the requirements of the ICP-OES. The geometric working electrode area had to be increased by at least one order of magnitude compared to designs in literature (0.0079 cm^{-2}) while keeping the flow cell compartment volume to a minimum. Four cells 1-Vc, 2-Vc, 3-Lc and 4-Lc where fabriacted. A complex design was created for 4-Lc which combined the high throughput capabilities of the SDCM with the benefits of the low resistance AESEC cell. The oxygen exclusion management of the cell compared as good as or better to other cells due to integrated gas channels which could create efficient nitrogen gas shileds around the leak points of the cell. The design was realised by additive manufacturing techniques that could efficiently reproduce comlpex design features not possible by subtractive machining methods. Care was taken to ensure all materials of the flow cell assembly was compatible with alkaline electrolyte. The authenticity of the electrochemical response was tested by cyclic voltammetry on polycrystalline platinum, were instabilities in the current response wa solved by adding artificial resistance to the

working electrode. The flow properties of the cell was characterised by calculating Reynolds numbers and replenishing times of all cell iterations. The flow cells were coupled to the ICP-OES by downstream analysis and the efficiency of dissolution product transport was evaluated for all cell iterations, where the large durface area 4-Lc performed as well as the small surface area 1-Vc and 2-Vc due to optimisation of the 4-Lc flow compartment.

The key components of the ICP-OES for reliable analysis were identified. The effect of the nebuliser, spray chamber and the torch on the standard deviation of the dissolution signal was tested, which showed that the bore diameter of the torch had the most significant effect on the signal stability. By proper maintanance, the glass components of the ICP-OES remained in good condition in exposure with 1 M KOH, which was necesssary for long term operation. By calibration, the signal intensity between the electrochemical dissolution current and the ICP-OES dissolution signal correlated well in a zinc model test. The ICP-OES data had to be aligned to the timestamps of the potentiostat due to time dilation.

The stability of select positive electrode current collectors were investigated by performing cyclic voltammograms and anodic glavanostatic step experiments of silver, nickel, titanium, AISI 304 stainless steel and Hastelloy C-276 foils. It was shown that silver undergoes rapid dissolution once converted electrochemically to an oxidation state of 2, due to solubility of the oxide film. The certain observation of silver dissolution under oxygen evolution conditions in alkaline media was a novel finding. AISI 304 stainless steelunderwent iron and chromium dissolution due to oxidation of Fe(II) and Cr(II), however the magnitude was lower compared to silver. Hastelloy C-276 underwent chromium dissolution, but to a much lower degree compared to AISI304. Titanium underwent initial dissolution upon high polarisation, but was quickly passivated, probably due to growth of an inhibiting oxide layer. Nickel did not release any detectable dissolution within any experiments. It was therefore concluded that Nickel was the most stable current collector candidate from a dissolution perspective. The results were supported by published solubility data of solvated species of the elements found in these materials in 1 M KOH.

A range of $Ni_xCo_{3-x}O_4$ nickel cobalt oxides were synthesised to investigate the effect of heteroatom doping on stability. Heteroatom doping was confirmed by shifts in XRD

reflection peaks due to lattice expansion and widening of reflection peaks due to increasing short-order structuring as the amount of nickel substitution increased. By voltammetric characterisation the Co(III)/Co(IV) redox couple shifted to more negative potentials with the amount of heteroatom substitution. The novel finding was that dissolution voltammograms revealed that with increase of heteroatom substitution as the Co(III)/Co(II) reduction commenced at increasingly higher potentials. This was rationalised by the lower surface formation energy of nickel oxides compared to cobalt oxides, which could increase the driving force of cobalt to be depleted from the surface. Estimations of electrochemical kinetics before and after a dissolution protocol saw a trend of decrease in ORR kinetic current, change in relative capacitance and decrease in OER onset. The dissolution magnitude was dependent on pH and catalyst loading. Under OER current densities in the order 10 mA cm^{-2} sharp spikes of dissolution currents appeared, but these were rationalised to stem from mechanical particle detachment rather than chemical or electrochemical dissolution.

7.2 Outlook

The on-line dissolution detection achieved with the 4-Lc flow cell connected to the ICP-OES has demonstrated its capabilities to detect dissolution rates to below 1 ng s^{-1} cm^{-2}. It has shown that instability must be considered not just of the active energy conversion material, but also from supporting material in contact with the electrolyte. It has highlighted the need to consider the stability of supporting material as well as ative material that co-habitates a battery cell. Due to its versatility and high-throughput abilities and potential, materials for other types of energy conversion could also be investigated with this setup, including but not limited to intercalation materials, other types of heterogeneous catalysts and capacitors.

The authour hopes that the steps taken here to describe and discuss the fabrication routes to create flow cells for on-line monitoring will be helpful for other scientists, as such knowledge was found difficult to come by during this project. With more widespread availabilty by additive manufacturing, stability testing and on-line monitoring may become more readily available for other groups that wish to contribute to the understanding of efficient and durable energy conversion.

8 References

1 M. Winter and R. J. Brodd, *Chem. Rev.*, 2004, **104**, 4245–4269.

2 N. Armaroli and V. Balzani, *Energy Environ. Sci.*, 2011, **4**, 3193.

3 J. Garche and C. K. Dyer, *Encyclopedia of Electrochemical Power Sources*, Elsevier B.V, 2009.

4 P. Sapkota and H. Kim, *J. Ind. Eng. Chem.*, 2009, **15**, 445–450.

5 J. C. Meier, C. Galeano, I. Katsounaros, J. Witte, H. J. Bongard, A. A. Topalov, C. Baldizzone, S. Mezzavilla, F. Schüth and K. J. J. Mayrhofer, *Beilstein J. Nanotechnol.*, 2014, **5**, 44–67.

6 K. Desmond, *Innovators in Battery Technology: Profiles of 95 Influential Electrochemists*, McFarland & Company, 2016.

7 C. M. Lewandowski, N. Co-investigator and C. M. Lewandowski, *Lindens Handbook of Batteries 4th Edition*, 2015, vol. 1.

8 V. Caramia and B. Bozzini, *Mater. Renew. Sustain. Energy*, 2014, **3**, 28.

9 N. N. Greenwood and A. Earnshaw, *Chemistry of the Elements*, 1997.

10 S. Muller and O. Haas, *J. Appl. Electrochem.*, 1998, **28**, 305–310.

11 J. Goldstein, I. Brown and B. Koretz, *J. Power Sources*, 1999, **80**, 171–179.

12 Fluidic, http://fluidicenergy.com/technology/zinc-air-technology.

13 Eosenergystorage, http://www.eosenergystorage.com/products/.

14 ViZn Energy, http://www.viznenergy.com/.

15 NantEnergy, https://nantenergy.com/.

16 Varta, PowerOne, http://www.powerone-batteries.com/products/zink-luft-wireless-approved/.

17 H. Kim, G. Jeong, Y.-U. Kim, J.-H. Kim, C.-M. Park and H.-J. Sohn, *Chem. Soc. Rev.*, 2013, **42**, 9011–34.

18 M. Broussely, P. Biensan, F. Bonhomme, P. Blanchard, S. Herreyre, K. Nechev and R. J. Staniewicz, *J. Power Sources*, 2005, **146**, 90–96.

19 J. B. Goodenough and K. S. Park, *J. Am. Chem. Soc.*, 2013, **135**, 1167–1176.

20 I. Katsounaros, S. Cherevko, A. R. Zeradjanin and K. J. J. Mayrhofer, *Angew. Chemie Int. Ed.*, 2014, **53**, 102–121.

21 A. J. Bard, L. R. Faulkner, N. York, C. @bullet, W. Brisbane and S. E. Toronto, *ELECTROCHEMICAL METHODS Fundamentals and Applications*, 2nd edn., 1980.

22 K. A. Stoerzinger, M. Risch, B. Han and Y. Shao-Horn, *ACS Catal.*, 2015, **5**, 6021–6031.

23 V. Neburchilov, H. Wang, J. J. Martin and W. Qu, *J. Power Sources*, 2010, **195**, 1271–1291.

24 J. K. Nørskov, J. Rossmeisl, A. Logadottir, L. Lindqvist, J. R. Kitchin, T. Bligaard and H. Jónsson, *J. Phys. Chem. B*, 2004, **108**, 17886–17892.

25 I. C. Man, H. Y. Su, F. Calle-Vallejo, H. A. Hansen, J. I. Martínez, N. G. Inoglu, J. Kitchin, T. F. Jaramillo, J. K. Nørskov and J. Rossmeisl, *ChemCatChem*, 2011, **3**, 1159–1165.

26 P. Jovanovič, A. Pavlišič, V. S. Šelih, M. Šala, N. Hodnik, M. Bele, S. Hočevar and M. Gaberšček, *ChemCatChem*, 2014, **6**, 449–453.

27 Y. Li, M. Gong, Y. Liang, J. Feng, J. E. Kim, H. Wang, G. Hong, B. Zhang and H. Dai, *Nat Commun*, 2013, **4**, 1805.

28 S. Cherevko, N. Kulyk and K. J. J. Mayrhofer, *Nano Energy*, 2015, **29**, 275–298.

29 E. Pizzutilo, S. Geiger, J.-P. Grote, A. Mingers, K. J. J. Mayrhofer, M. Arenz and S. Cherevko, *J. Electrochem. Soc.*, 2016, **163**, F1510–F1514.

30 X. Han, X. Wu, C. Zhong, Y. Deng, N. Zhao and W. Hu, *Nano Energy*, 2017, **31**, 541–550.

31 S. Mezzavilla, S. Cherevko, C. Baldizzone, E. Pizzutilo, G. Polymeros and K. J. J. Mayrhofer, *ChemElectroChem*, 2016, **3**, 1524–1536.

32 A. A. Topalov, I. Katsounaros, M. Auinger, S. Cherevko, J. C. Meier, S. O. Klemm and K. J. J. Mayrhofer, *Angew. Chemie - Int. Ed.*, 2012, **51**, 12613–12615.

33 P. Marcus, *Corrosion Mechanisms in Theory and Practice*, 1995.

34 R. W. Staehle and H. Okada, *Passivity and Its Breakdown on Iron and Iron Base Alloys*, 1976.

35 M. Stern and A. L. Geary, *J. Electrochem. Soc.*, 1957, **104**, 56–63.

36 B. Cahan and R. Haynes, *J. Electroanal. Chem.*, 1969, **22**, 339–345.

37 J. O. M. Bockris, B. T. Rubin, A. Despic and B. Lovrecek, *Electrochim. Acta*, 1972, **17**, 973–999.

38 T. Tsuru, *Mater. Sci. Eng. A*, 1991, **146**, 1–14.

39 M. Bojinov, I. Betova, G. Fabricius, T. Laitinen, R. Raicheff and T. Saario, *Corros. Sci.*, 1999, **41**, 1557–1584.

40 I. Annergren, M. Keddam, H. Takenouti and D. Thierry, *Electrochim. Acta*, 1993, **38**, 763–771.

41 F. Huet, M. Keddam, X. R. Nóvoa and H. Takenouti, *Corros. Sci.*, 1996, **38**, 133–145.

42 B. Heine and R. Kirchheim, *Corros. Sci.*, 1990, **31**, 533–538.

43 C. S. O'Dell, G. W. Walker and P. E. Richardson, *J. Appl. Electrochem.*, 1986, **16**, 544–554.

44 Z. Wang and D. A. Scherson, , DOI:10.1149/1.2048488.

45 Y. Dongxing, W. Xiaoru, Y. Pengyuan and H. Benli, *Anal. Chim. Acta*, 1991, **243**, 65–69.

46 P. De Gelis, J. L. Caplan, R. Berneron and J. C. Charbonnier, in *Actes du 7e Congres European de Corrosion, Nice*, 1985.

47 K. Ogle, in *The Electrochemical Society Meetings Abstracts*, 1996, p. 218.

48 K. Ogle and S. Weber, 2000, **147**, 1770–1780.

49 M. Mokaddem, P. Volovitch and K. Ogle, *Electrochim. Acta*, 2010, **55**, 7867–7875.

50 L. Jiang, M. Wolpers, P. Volovitch and K. Ogle, *Surf. Coatings Technol.*, 2012, **206**, 3151–3157.

51 M. Serdechnova, P. Volovitch and K. Ogle, *Surf. Coatings Technol.*, 2012, **206**, 2133–2139.

52 V. Shkirskiy and K. Ogle, *Electrochim. Acta*, 2015, **168**, 167–172.

53 a Vogel and J. . Schultze, *Electrochim. Acta*, 1999, **44**, 3751–3759.

54 L. W. Smith and V. J. Pingel, *J. Electrochem. Soc.*, 1951, **98**, 48–50.

55 W. Brandl, *Electrochim. Acta*, 1992, **37**, 2263–2268.

56 T. Suter, T. Peter and H. Bohni, *Mater. Sci. Forum*, 1995, **192**–**194**, 25–40.

57 A. W. Hassel and M. M. Lohrengel, *Electrochim. Acta*, 1997, **42**, 3327–3333.

58 M. M. Lohrengel, A. Moehring and M. Pilaski, *Electrochim. Acta*, 2001, **47**, 137–141.

59 M. M. Lohrengel, C. Rosenkranz, I. Klüppel, A. Moehring, H. Bettermann, B. Van Den Bossche and J. Deconinck, *Electrochim. Acta*, 2004, **49**, 2863–2870.

60 M. M. Lohrengel and C. Rosenkranz, 2005, **47**, 785–794.

61 C. Rosenkranz, M. M. Lohrengel and J. W. Schultze, 2016, **50**, 2009–2016.

62 K. P. Rataj, C. Hammer, B. Walther and M. M. Lohrengel, *Electrochim. Acta*, 2013, **90**, 12–16.

63 N. Homazava, A. Ulrich, M. Trottmann and U. Kraehenbuehl, *J. Anal. At. Spectrom.*, 2007, **22**, 1122–1130.

64 N. Homazava, A. Shkabko, D. Logvinovich and U. Kra, 2008, **16**, 1066–1072.

65 A. Ulrich, N. Ott, A. Tournier-fillon, N. Homazava and P. Schmutz, *Spectrochim. Acta Part B At. Spectrosc.*, 2011, **66**, 536–545.

66 S. O. Klemm, J. C. Schauer, B. Schuhmacher and A. W. Hassel, *Electrochim. Acta*, 2011, **56**, 4315–4321.

67 S. O. Klemm, S. E. Pust, A. W. Hassel, J. Hüpkes and K. J. J. Mayrhofer, *J. Solid State Electrochem.*, 2012, **16**, 283–290.

68 M. Voith, G. Luckeneder and A. W. Hassel, 2012, 3473–3478.

69 M. Hafner, W. Burgstaller, A. I. Mardare and A. W. Hassel, *Thin Solid Films*, 2015, **580**, 36–44.

70 J. P. Kollender, A. I. Mardare and A. W. Hassel, *Electrochem. commun.*, 2017, **74**, 5–8.

71 A. K. Schuppert, A. A. Topalov, I. Katsounaros, S. O. Klemm and K. J. J. Mayrhofer, *J. Electrochem. Soc.*, 2012, **159**, F670–F675.

72 S. O. Klemm, A. A. Topalov, C. A. Laska and K. J. J. Mayrhofer, *Electrochem. commun.*, 2011, **13**, 1533–1535.

73 S. Cherevko, G. P. Keeley, N. Kulyk and K. J. J. Mayrhofer, *J. Electrochem. Soc.*, 2016, **163**, H228–H233.

74 N. Hodnik, C. Baldizzone, G. Polymeros, S. Geiger, J.-P. Grote, S. Cherevko, A.

Mingers, A. Zeradjanin and K. J. J. Mayrhofer, *Nat. Commun.*, 2016, **7**, 13164.

75 S. Cherevko, A. R. Zeradjanin, A. A. Topalov, N. Kulyk, I. Katsounaros and K. J. J. Mayrhofer, *ChemCatChem*, 2014, **6**, 2219–2223.

76 C. Baldizzone, S. Mezzavilla, H. W. P. Carvalho, J. C. Meier, A. K. Schuppert, M. Heggen, C. Galeano, J. D. Grunwaldt, F. Schüth and K. J. J. Mayrhofer, *Angew. Chemie - Int. Ed.*, 2014, **53**, 14250–14254.

77 A. a. Topalov, S. Cherevko, A. R. Zeradjanin, J. C. Meier, I. Katsounaros and K. J. J. Mayrhofer, *Chem. Sci.*, 2014, **5**, 631.

78 A. A. Topalov, A. R. Zeradjanin, S. Cherevko and K. J. J. Mayrhofer, *Electrochem. commun.*, 2014, **40**, 49–53.

79 S. Cherevko, A. A. Topalov, A. R. Zeradjanin, G. P. Keeley and K. J. J. Mayrhofer, *Electrocatalysis*, 2014, **5**, 235–240.

80 S. Geiger, S. Cherevko and K. J. J. Mayrhofer, *Electrochim. Acta*, 2015, **179**, 24–31.

81 S. Cherevko, G. P. Keeley, S. Geiger, A. R. Zeradjanin, N. Hodnik, N. Kulyk and K. J. J. Mayrhofer, *ChemElectroChem*, 2015, n/a-n/a.

82 G. P. Keeley, S. Cherevko and K. J. J. Mayrhofer, *ChemElectroChem*, 2016, **3**, 51–54.

83 S. Cherevko, A. A. Topalov, I. Katsounaros and K. J. J. Mayrhofer, *Electrochem. commun.*, 2013, **28**, 44–46.

84 S. Cherevko, A. A. Topalov, A. R. Zeradjanin, I. Katsounaros and K. J. J.

Mayrhofer, *RSC Adv.*, 2013, **3**, 16516.

85 S. Cherevko, A. R. Zeradjanin, G. P. Keeley and K. J. J. Mayrhofer, *J. Electrochem. Soc.*, 2014, **161**, H822–H830.

86 S. Cherevko, A. R. Zeradjanin, A. a. Topalov, G. P. Keeley and K. J. J. Mayrhofer, *J. Electrochem. Soc.*, 2014, **161**, H501–H507.

87 S. O. Klemm, A. Karschin, A. K. Schuppert, A. A. Topalov, A. M. Mingers, I. Katsounaros and K. J. J. Mayrhofer, *J. Electroanal. Chem.*, 2012, **677**–**680**, 50–55.

88 S. Cherevko, T. Reier, A. R. Zeradjanin, Z. Pawolek, P. Strasser and K. J. J. Mayrhofer, *Electrochem. commun.*, 2014, **48**, 81–85.

89 A. R. Zeradjanin, A. A. Topalov, Q. Van Overmeere, S. Cherevko, X. Chen, E. Ventosa, W. Schuhmann and K. J. J. Mayrhofer, *RSC Adv.*, 2014, **4**, 9579.

90 T. Reier, Z. Pawolek, S. Cherevko, M. Bruns, T. Jones, D. Teschner, S. Selve, A. Bergmann, H. N. Nong, R. Schl??gl, K. J. J. Mayrhofer and P. Strasser, *J. Am. Chem. Soc.*, 2015, **137**, 13031–13040.

91 S. Cherevko, S. Geiger, O. Kasian, A. Mingers and K. J. J. Mayrhofer, *J. Electroanal. Chem.*, 2016, **773**, 69–78.

92 S. Cherevko, S. Geiger, O. Kasian, A. Mingers and K. J. J. Mayrhofer, *J. Electroanal. Chem.*, 2016, **774**, 102–110.

93 M. J. Duarte, J. Klemm, S. O. Klemm, K. J. J. Mayrhofer, M. Stratmann, S. Borodin, a. H. Romero, M. Madinehei, D. Crespo, J. Serrano, S. S. a. Gerstl, P.

P. Choi, D. Raabe and F. U. Renner, *Science (80-.).*, 2013, **372**, 372–377.

94 J. Klemm, S. O. Klemm, M. J. Duarte, L. Rossrucker, K. J. J. Mayrhofer and F. U. Renner, *Corros. Sci.*, 2014, **89**, 59–68.

95 a. Pareek, G. N. Ankah, S. Cherevko, P. Ebbinghaus, K. J. J. Mayrhofer, a. Erbe and F. U. Renner, *RSC Adv.*, 2013, **3**, 6586.

96 L. Rossrucker, K. J. J. Mayrhofer, G. S. Frankel and N. Birbilis, *J. Electrochem. Soc.*, 2014, **161**, 115–119.

97 L. Rossrucker, A. Samaniego, J.-P. Grote, A. M. Mingers, C. A. Laska, N. Birbilis, G. S. Frankel and K. J. J. Mayrhofer, *J. Electrochem. Soc.*, 2015, **162**, C333–C339.

98 C. H. Choi, C. Baldizzone, J. P. Grote, A. K. Schuppert, F. Jaouen and K. J. J. Mayrhofer, *Angew. Chemie - Int. Ed.*, 2015, **54**, 12753–12757.

99 C. H. Choi, C. Baldizzone, G. Polymeros, E. Pizzutilo, O. Kasian, A. K. Schuppert, N. Ranjbar Sahraie, M. T. Sougrati, K. J. J. Mayrhofer and F. Jaouen, *ACS Catal.*, 2016, **6**, 3136–3146.

100 A. K. Schuppert, A. Savan, A. Ludwig and K. J. J. Mayrhofer, *Electrochim. Acta*, 2014, **144**, 332–340.

101 J. P. Grote, A. R. Zeradjanin, S. Cherevko, A. Savan, B. Breitbach, A. Ludwig and K. J. J. Mayrhofer, *J. Catal.*, 2016, **343**, 248–256.

102 O. Kasian, S. Geiger, P. Stock, G. Polymeros, B. Breitbach, A. Savan, A. Ludwig, S. Cherevko and K. J. J. Mayrhofer, *J. Electrochem. Soc.*, 2016, **163**,

F3099–F3104.

103 J. P. Kollender, J. Gasiorowski, N. S. Sariciftci, A. I. Mardare and A. W. Hassel, *J. Phys. Chem. C*, 2014, **118**, 16919–16926.

104 J. P. Kollender, J. Gasiorowski, N. S. Sariciftci, A. I. Mardare and A. W. Hassel, *Sci. Technol. Adv. Mater.*, 2014, **15**, 054201.

105 J. P. Kollender, M. Voith, S. Schneiderbauer, A. I. Mardare and A. W. Hassel, *J. Electroanal. Chem.*, 2015, **740**, 53–60.

106 J. P. Kollender, A. I. Mardare and A. W. Hassel, *Electrochim. Acta*, 2015, **179**, 32–37.

107 P. P. Lopes, D. Strmcnik, D. Tripkovic, J. G. Connell, V. Stamenkovic and N. M. Markovic, *ACS Catal.*, , DOI:10.1021/acscatal.5b02920.

108 P. P. Lopes, D. Tripkovic, P. F. B. D. Martins, D. Strmcnik, E. A. Ticianelli, V. R. Stamenkovic and N. M. Markovic, *J. Electroanal. Chem.*, , DOI:10.1016/j.jelechem.2017.09.047.

109 V. Shkirskiy, P. Maciel, J. Deconinck and K. Ogle, *J. Electrochem. Soc.*, 2016, **163**, 1–8.

110 N. Kulyk, S. Cherevko, M. Auinger, C. Laska and K. J. J. Mayrhofer, *J. Electrochem. Soc.*, 2015, **162**, H860–H866.

111 A. J. Bard and L. R. Faulkner, *Electrochemical Methods: Fundamentals and Applications*, Wiley, 2nd edn., 2001.

112 N. Kulyk, S. Cherevko, M. Auinger, C. Laska and K. J. J. Mayrhofer, *J.*

Electrochem. Soc., 2015, **162**, H860–H866.

113 B. Hwang, E.-S. Oh and K. Kim, *Electrochim. Acta*, 2016, **216**, 484–489.

114 Brandt, Technical Information, https://www.brand.cn.com/fileadmin/user/pdf/GK900/english/GK900_07_Technical_Info_e.pdf.

115 Gammarcil, Chemical Resistance PMMA, https://www.vink.fi/media/import/fi_Vink_MM_Kirkkaat_putket_Akryyliputket_PMMA_Kemiallinenkestavyys.pdf.

116 V. P. Polymers, .

117 Quickgasket, Chemical Resistance Chart, http://www.quickcutgasket.com/pdf/Chemical-Resistance-Chart.pdf.

118 P. Kjeldsen, *Water Res.*, 1993, **27**, 121–131.

119 Formlabs, Clear Material Datasheet, https://formlabs-media.formlabs.com/datasheets/Clear_Resin_Technical.pdf.

120 Formlabs Inc, Safety Data Sheet Clear Resin, https://formlabs-media.formlabs.com/datasheets/1801037-SDS-ENEU-0.pdf.

121 V. E. S. Gajewski, C. S. Pfeifer, N. R. G. Fróes-Salgado, L. C. C. Boaro and R. R. Braga, *Braz. Dent. J.*, 2012, **23**, 508–514.

122 J. G. Leprince, M. Hadis, A. C. Shortall, J. L. Ferracane, J. Devaux, G. Leloup and W. M. Palin, *Dent. Mater.*, 2011, **27**, 157–164.

123 V. Shkirskiy, P. Maciel, J. Deconinck and K. Ogle, *J. Electrochem. Soc.*, 2016,

163, 1–8.

124 I. I. Inc, Reference Electrodes, https://www.2in.com/products/reference/reference.html.

125 Celgard, Celgard(R) 3401 Microporous Membrane, www.celgard.com/literature.

126 P. Daubinger, J. Kieninger, T. Unmüssig and G. A. Urban, *Phys. Chem. Chem. Phys.*, 2014, **16**, 8392–8399.

127 S. J. Ashton, *Springer Theses*, , DOI:10.1007/978-3-642-30550-4.

128 M. C. Potter, *Fluid Mechanichs Demystified*, McGrawHill, 2009.

129 P. M. Sipos, G. Hefter and P. M. May, *J. Chem. Eng. Data*, 2000, **45**, 613–617.

130 D. A. Scherson, Y. V. Tolmachev, Z. Wang, J. Wang and A. Palencsar, *Electrochem. Solid-State Lett.*, 2008, **11**, F1.

131 Formlabs, .

132 R. Thomas, *Practical Guide to ICP-MS*, 2013.

133 A. Technologies, .

134 A. Technologies, .

135 A. Technologies, Agilent 5100 ICP-OES Dual View ICP-OES Supplies, http://www.chem.agilent.com/Library/brochures/5991-4734EN.pdf.

136 P. Elmer, *At. Spectrosc. A Guid. to Sel. Appropr. Tech. Syst.*, 2011, 2.

137 T. L. S. and R. A. Yost, *October*.

138 N. Le Corre and J. Yvon, 2017, 31–33.

139 G. Massari, *Stat. Discov.*, 2013, **1**, 1–12.

140 G. Wells, P. H and C. . Russ, Signal, Noise and Detection Limits in Mass Spectrometry, www.agilent.com/chem.

141 S. L. R. Ellison and M. Thompson, *amc Tech. briefs*, 2008, **133**, 992–997.

142 D. Lozano and M. Cantero, *Am. J. Clin. Pathol.*, 1997, **107**, 619.

143 S. T. Bashir, L. Yang, J. J. Liggat and J. L. Thomason, *J. Mater. Sci.*, 2018, **53**, 1710–1722.

144 R. Imhof and N. Petr, *October*, 1998, **145**, 3313–3319.

145 R. Brennan, J. Dulude and R. Thomas, *Spectrosc. (Santa Monica)*, 2015, **30**, 12–25.

146 D. Schröder, N. N. Sinai Borker, M. König and U. Krewer, *J. Appl. Electrochem.*, 2015, **45**, 427–437.

147 * Aroa R. Mainar1, 2, Olatz Leonet1, Miguel Bengoechea1, Iker Boyano1, Iratxe de Meatza1, Andriy Kvasha1, Abdelbast Guerfi3 and J. Alberto Blázquez1, *Int. J. energy Res.*, 2016, **40**, 1032–1049.

148 K. Ogle and S. Weber, *J. Electrochem. Soc.*, 2000, **147**, 1770.

149 J. B. Goodenough and K. S. Park, *J. Am. Chem. Soc.*, 2013.

150 C. P. P. Wong, T. C. K. Yang, S. Chong, J. C. Juan, G. T. Pan and C. M. Huang,

Ionics (Kiel)., 2019, **25**, 1689–1698.

151 Z. P. Cano, M. G. Park, D. U. Lee, J. Fu, H. Liu, M. Fowler and Z. Chen, *J. Phys. Chem. C*, 2018, **122**, 20153–20166.

152 T. H. You and C. C. Hu, *ACS Appl. Mater. Interfaces*, 2018, **10**, 10064–10075.

153 J. J. Han, N. Li and T. Y. Zhang, *J. Power Sources*, 2009, **193**, 885–889.

154 M. A. Kostowskyj, D. W. Kirk and S. J. Thorpe, *Int. J. Hydrogen Energy*, 2010, **35**, 5666–5672.

155 C. L. Lee, Y. L. Tsai, C. H. Huang and K. L. Huang, *Electrochem. commun.*, 2013, **29**, 37–40.

156 J. Ohyama, Y. Okata, N. Watabe, M. Katagiri, A. Nakamura, H. Arikawa, K. I. Shimizu, T. Takeguchi, W. Ueda and A. Satsuma, *J. Power Sources*, 2014, **245**, 998–1004.

157 X. Wei, D. Desai, G. G. Yadav, D. E. Turney, A. Couzis and S. Banerjee, *Electrochim. Acta*, , DOI:10.1016/j.electacta.2016.07.041.

158 M. Krebsz, J. P. Kollender and A. W. Hassel, *Phys. Status Solidi Appl. Mater. Sci.*, , DOI:10.1002/pssa.201600803.

159 S. Geiger, O. Kasian, A. M. Mingers, S. S. Nicley, K. Haenen, K. J. J. Mayrhofer and S. Cherevko, *ChemSusChem*, , DOI:10.1002/cssc.201701523.

160 P. Bonnick and J. R. Dahn, *J. Electrochem. Soc.*, , DOI:10.1149/2.023207jes.

161 M. Hepel and M. Tamkiewicz, *J. Electrochem. Soc.*, 1984, **131**, 1288–1294.

162 P. Stonehart and F. P. Portante, *Electrochim. Acta*, 1968, **13**, 1805–1814.

163 J. M. M. Droog and F. Huisman, *J. Electroanal. Chem.*, 1980, **115**, 211–224.

164 N. Sato and Y. Shimizu, *Electrochim. Acta*, 1973, **18**, 567–570.

165 B. Miller, *J. Electrochem. Soc.*, 1970, **117**, 491–499.

166 J. M. M. Droog, P. T. Alderliesten and G. A. Bootsma, *J. Electroanal. Chem.*, 1979, **99**, 173–186.

167 A. Vvedenskii, S. Grushevskaya, D. Kudryashov and S. Ganzha, *Surf. Interface Anal.*, 2008, **40**, 636–640.

168 D. A. Kudryashov, S. N. Grushevskaya and A. V. Vvedenskii, *Prot. Met.*, 2008, **44**, 301–309.

169 R. F. Amlie and P. Rüetschi, *J. Electrochem. Soc.*, 1961, **108**, 813.

170 T. P. Dirkse and B. Wiers, *J. Electrochem. Soc.*, 1959, **106**, 284–287.

171 I. S. Filimonenkov, G. A. Tsirlina and E. R. Savinova, *Electrochim. Acta*, 2019, **319**, 227–236.

172 A. Prusi and L. Arsov, *J. Solid State Electrochem.*, 2007, **11**, 355–360.

173 S. H. Bonilla and C. F. Zinola, *Electrochim. Acta*, 1998, **43**, 423–426.

174 E. M. Oliveira, C. E. B. Marino, S. R. Biaggio and R. C. Rocha-Filho, *Electrochem. commun.*, 2000, **2**, 254–258.

175 P. Vishnu Kamath and M. F. Ahmed, *J. Appl. Electrochem.*, 1993, **23**, 225–230.

176 C. V. D'Alkaine and M. A. Santanna, *J. Electroanal. Chem.*, 1998, **457**, 5–12.

177 C. Zhang and S. M. Park, *J. Electrochem. Soc.*, 1987, **134**, 2966–2977.

178 K. Micka and J. Cerny, *J. Power Sources*, 1989, **25**, 111–122.

179 R. D. Armstrong and I. Baurhoo, *J. Electroanal. Chem.*, 1972, **34**, 41–46.

180 D. M. Dražić and C. S. Hao, *Electrochim. Acta*, 1982, **27**, 1409–1415.

181 H. Neugebauer, A. Moser, P. Strecha and A. Neckel, *J. Electrochem. Soc.*, 1990, **137**, 1472–1475.

182 I. Song, D. Gervasio and J. H. Payer, *J. Appl. Electrochem.*, 1996, **26**, 1045–1052.

183 C. M. Abreu, M. J. Cristóbal, R. Losada, X. R. Nóvoa, G. Pena and M. C. Pérez, *Electrochim. Acta*, 2004, **49**, 3049–3056.

184 F. M. Julke, J. E. Rodríguez-yáñez and M. E. De, .

185 S. K. Tiwari, A. K. L. Singh and R. N. Singh, *J. Electroanal. Chem.*, 1991, **319**, 263–274.

186 L. De Micheli, C. A. Barbosa, A. H. P. Andrade and S. M. L. Agostinho, *Br. Corros. J.*, 2000, **35**, 297–300.

187 C. Jun, Y. Fengyuan and W. Jianzhang, *Ind. Lubr. Tribol.*, 2014, **66**, 9–14.

188 J. Chen, J. Wang, F. Yan, Q. Zhang and Q. Li, *Lubr. Sci.*, 2016, **28**, 67–80.

189 L. Freire, M. A. Catarino, M. I. Godinho, M. J. Ferreira, M. G. S. Ferreira, A. M. P. Simões and M. F. Montemor, *Cem. Concr. Compos.*, 2012, **34**, 1075–1081.

190 S. Lysgaard, M. K. Christensen, H. A. Hansen, J. M. García Lastra, P. Norby and T. Vegge, *ChemSusChem*, , DOI:10.1002/cssc.201800225.

191 H. L. Johnston and F. Cuta, *J. Am. Chem. Soc.*, 1933, **55**, 2311–2325.

192 T. P. Dirkse, *J. Electrochem. Soc.*, 1959, **106**, 453–457.

193 J. . McMillan, *Nature*, 1962, **195**, 594–595.

194 D. Rai, B. M. Sass and D. A. Moore, *Inorg. Chem.*, 1987, **26**, 345–349.

195 S. E. Ziemniak, M. E. Jones and K. E. S. Combs, *J. Solution Chem.*, 1998, **27**, 33–66.

196 K. Ishikawa, T. Yoshioka, T. Sato and A. Okuwaki, *Hydrometallurgy*, 1997, **45**, 129–135.

197 S. Licht, B. Wang and S. Ghosh, 1999, **285**, 1039–1043.

198 K. H. Gayer and A. B. Garrett, *J. Am. Chem. Soc.*, 1949, **71**, 2973–2975.

199 W. H. Zhu, J. J. Ke, H. M. Yu and D. J. Zhang, *J. Power Sources*, 1995, **56**, 75–79.

200 S. E. Ziemniak and M. A. Goyette, *J. Solution Chem.*, 2004, **33**, 1135–1159.

201 G. R. Wiese and T. W. Healy, *J. Colloid Interface Sci.*, 1975, **52**, 452–457.

202 K. G. Knauss, M. J. Dibley, W. L. Bourcier and H. F. Shaw, *Appl. Geochemistry*, 2001, **16**, 1115–1128.

203 S. M. Kramer, I. G. Gorichev, Y. A. Lainer, I. V. Artamonova and M. V. Terekhova, *Russ. Metall.*, 2014, **2014**, 704–707.

204 E. V. Shkol'nikov, *Russ. J. Phys. Chem. A*, 2016, **90**, 567–571.

205 P. Delahay, M. Pourbaix and P. Van Rysselberghe, *J. Electrochem. Soc.*, 1951, **98**, 65–67.

206 M. V. Ten Kortenaar, J. J. M. De Goeij, Z. I. Kolar, G. Frens, P. J. Lusse, M. R. Zuiddam and E. Der Van Drift, *J. Electrochem. Soc.*, 2001, **148**, 28–33.

207 B. Beverskog and I. Puigdomenech, *Corros. Sci.*, 1997, **39**, 43–57.

208 V. Shkirskiy, P. Keil, H. Hintze-Bruening, F. Leroux, T. Stimpfling, D. Dragoe, K. Ogle and P. Volovitch, *Corros. Sci.*, 2015, **99**, 31–41.

209 B. Beverskog and I. Puigdomenech, *Corros. Sci.*, 1997, **39**, 969–980.

210 N. V. Plyasunova, Y. Zhang and M. Muhammed, *Hydrometallurgy*, 1998, **48**, 43–46.

211 M. J. Muñoz-Portero, J. García-Antón, J. L. Guiñón and R. Leiva-García, *Corros. Sci.*, 2011, **53**, 1440–1450.

212 P. Mohammadian Samim and A. Fattah-alhosseini, *Anal. Bioanal. Electrochem.*, 2016, **8**, 717–731.

213 M. Rabe, C. Toparli, Y. H. Chen, O. Kasian, K. J. J. Mayrhofer and A. Erbe, *Phys. Chem. Chem. Phys.*, , DOI:10.1039/c9cp00911f.

214 J. Béjar, L. Álvarez-Contreras, J. Ledesma-García, N. Arjona and L. G. Arriaga, *J. Electroanal. Chem.*, 2019, **847**, 113190.

215 C. Jin, F. Lu, X. Cao, Z. Yang and R. Yang, *J. Mater. Chem. A*, 2013, **1**, 12170–12177.

216 W. Song, Z. Ren, S. Y. Chen, Y. Meng, S. Biswas, P. Nandi, H. A. Elsen, P. X. Gao and S. L. Suib, *ACS Appl. Mater. Interfaces*, 2016, **8**, 20802–20813.

217 Y. Liang, Y. Li, H. Wang, J. Zhou, J. Wang, T. Regier and H. Dai, *Nat. Mater.*, 2011, **10**, 780–786.

218 Y. J. Sa, K. Kwon, J. Y. Cheon, F. Kleitz and S. H. Joo, *J. Mater. Chem. A*, 2013, **1**, 9992–10001.

219 X. Zou, J. Su, R. Silva, A. Goswami, B. R. Sathe and T. Asefa, *Chem. Commun.*, 2013, **49**, 7522–7524.

220 N.-I. Kim, Y. J. Sa, S.-H. Cho, I. So, K. Kwon, S. H. Joo and J.-Y. Park, *J. Electrochem. Soc.*, 2016, **163**, F3020–F3028.

221 M. Prabu, K. Ketpang and S. Shanmugam, *Nanoscale*, 2014, **6**, 3173–3181.

222 M. Yang, W. Lu, R. Jin, X. C. Liu, S. Song and Y. Xing, *ACS Sustain. Chem. Eng.*, 2019, **7**, 12214–12221.

223 I. Spanos, A. A. Auer, S. Neugebauer, X. Deng, H. Tüysüz and R. Schlögl, *ACS Catal.*, 2017, **7**, 3768–3778.

224 X. Tong, X. Xia, C. Guo, Y. Zhang, J. Tu, H. J. Fan and X. Y. Guo, *J. Mater. Chem. A*, 2015, **3**, 18372–18379.

225 A. Lakehal, B. Benrabah, A. Bouaza, C. Dalache and B. Hadj, *Chinese J. Phys.*, 2018, **56**, 1845–1852.

226 X. Shi, S. L. Bernasek and A. Selloni, *J. Phys. Chem. C*, 2017, **121**, 3929–3937.

227 J. A. K. Tareen, A. Małecki, J. P. Doumerc, J. C. Launay, P. Dordor, M. Pouchard

and P. Hagenmuller, *Mater. Res. Bull.*, 1984, **19**, 989–997.

228 L. Fang, Z. Jiang, H. Xu, L. Liu, Y. guan, X. Gu and Y. Wang, *J. Catal.*, 2018, **357**, 238–246.

229 A. Singhal, A. Bisht and S. Irusta, *J. Electroanal. Chem.*, 2018, **823**, 482–491.

230 M. Lukaszewski, M. Soszko and A. Czerwiński, *Int. J. Electrochem. Sci.*, 2016, **11**, 4442–4469.

231 D. U. Lee, B. J. Kim and Z. Chen, *J. Mater. Chem. A*, 2013, **1**, 4754–4762.

232 G. A. El-Shobaky, A. M. Turky and A. M. Ghozza, *Adsorpt. Sci. Technol.*, 2002, **20**, 467–484.

233 R. BOGGIO, A. CARUGATF and S. TRASATTI, *J. Appl. Electrochem.*, 1987, **17**, 828–840.

234 E. B. Castro, C. A. Gervasi and J. R. Vilche, *J. Appl. Electrochem.*, 1998, **28**, 835–841.

235 K. M. Ismail and W. A. Badawy, *J. Appl. Electrochem.*, 2000, **30**, 1303–1311.

236 D. S. Hall, C. Bock and B. R. MacDougall, *J. Electrochem. Soc.*, 2013, **160**, F235–F243.

237 T. Nathan, A. Aziz, A. F. Noor and S. R. S. Prabaharan, *J. Solid State Electrochem.*, 2008, **12**, 1003–1009.

238 A. Seghiouer, J. Chevalet, A. Barhoun and F. Lantelme, *J. Electroanal. Chem.*, 1998, **442**, 113–123.

239 H. Shi and G. Zhao, *J. Phys. Chem. C*, 2014, **118**, 25939–25946.

240 Y. Liu, P. Liu, W. Qin, X. Wu and G. Yang, *Electrochim. Acta*, 2019, **297**, 623–632.

241 K. M. Ismail and W. A. Badawy, *J. Appl. Electrochem.*, 2000, **30**, 1303–1311.

242 A. Holewinski, J.-C. Idrobo and S. Linic, *Nat. Chem.*, 2014, **6**, 828–834.

243 W. K. Behl and J. E. Toni, *J. Electroanal. Chem.*, 1971, **31**, 63–75.

244 M. Grdeń and J. Jagiełło, *J. Solid State Electrochem.*, 2013, **17**, 145–156.

245 R. Parsons, *Atlas of electrochemical equilibria in aqueous solutions*, 1967, vol. 13.

9 Appendices

Appendix A

Prior to the flow cells described in Chapter 3, attempts were made to make a network-type flow cell system where each electrode is situated in its own compartment and connected by tubes filled with electrolyte. This design was inspired by Nesselberger et al. A render image of the cell schematic is provided below.

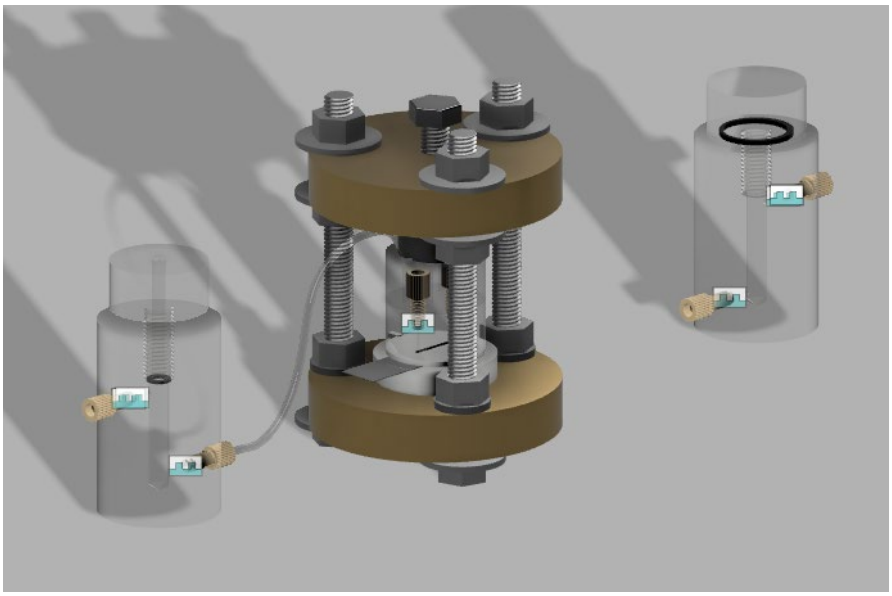

Parts were machined from acrylate. Reference and counter electrodes were held in separate compartments to minimize the chance of contamination. The flow channel was cut out of PTFE sheet, and pressed against the working electrode by a vice stage. The design was abandoned due to very large resistances between the electrodes and very demanding set-up procedure per experiment.

Another cell was attempted inspired by the AESEC, consisting of a flow compartment and a stagnant counter electrode compartment. The design was fabricated by SLA 3D printing.

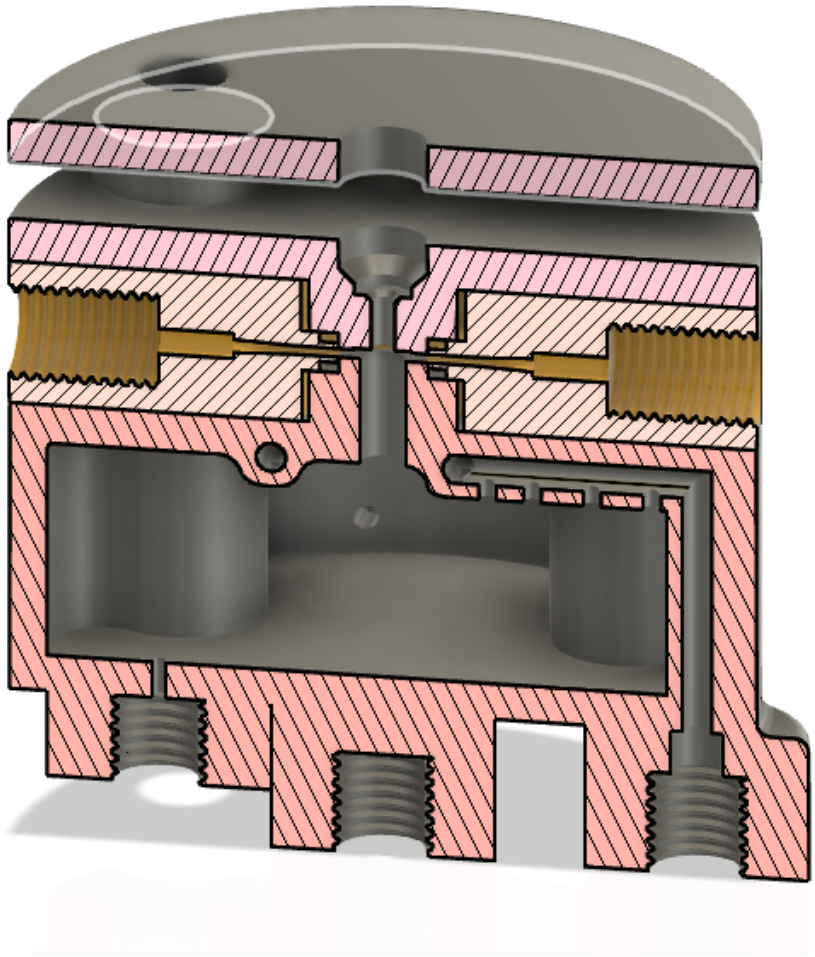

Despite good electrochemical signal and flow properties, this design was abandoned due to the long time needed to replace the working electrode, and its tendency to retain bubbles in the middle of the flow compartment.